November 2015

Responsive Supramolecular Assemblies Based on Amphiphilic Polymers and Hybrid Materials

Longyu Li
University of Massachusetts - Amherst

RESPONSIVE SUPRAMOLECULAR ASSEMBLIES BASED ON AMPHIPHILIC POLYMERS AND HYBRID MATERIALS

A Dissertation Presented

by

LONGYU LI

Submitted to the Graduate School of the
University of Massachusetts Amherst in partial fulfillment
of the requirements for the degree of

DOCTOR OF PHILOSOPHY

September 2015

Department of Chemistry

RESPONSIVE SUPRAMOLECULAR ASSEMBLIES BASED ON AMPHIPHILIC POLYMERS AND HYBRID MATERIALS

A Dissertation Presented

by

LONGYU LI

Approved as to style and content by:

_____
Sankaran Thayumanvan, Chair

_____
Min Chen, Member

_____
Kevin R. Kittilstved, Member

_____
Thomas J. McCarthy, Member

_____
Craig T. Martin, Department Head
Chemistry

DEDICATION

To my wife Zhu, my parents, and my elder sister

ACKNOWLEDGMENTS

It was very intense and difficult to have five years for PhD degree in Chemistry Department at University of Massachusetts Amherst. Without support and help from many people, this thesis would not have been achieved.

First of all, I am most grateful to my advisor and mentor, Professor Sankaran Thayumanavan, for his continuous guidance, support, and encouragement throughtout this process. Thank you for giving me the chance to come to Amherst and do research in such a great research group. I greatly appreciate the things he taught me in pursuing a scientific career, which will be definitely a source of wealth for my career in the future. Thank you for being a great advisor.

Next, I am deeply grateful to Professor Xinlin Yang, who was my advisor and mentor when I was an undergraduate student in Nankai Univeristy. Without his patience, guidance, and support, I would not have taken scientific career as my life goal, decided to come to USA, and finally finished my PhD degree. I also thank Professor Changchun Wang in Fudan Univeristy. He did not blame or stop me when I left his group for USA. He always treats me as his student and keeps encouraging me to work hard.

I would also like to thank my committee member Professor Min Chen, Professor Kevin R. Kittilstved, and Professor Thomas J. McCarthy for their valuable time and input to my research. Thank you for always allowing me to quickly fix the meeting time during my Prospectus, ORP and data defense. I especially thank Professor Kevin R. Kittilstved again for his great suggestions and help in my recent project about hollow metal-organic particles.

I also thank my past collaborators: Dr. Ja-Hyoung Ryu, Dr. Conghui Yuan, Dr. Alexander E. Ribbe, Kishore Raghupathi, Cunfeng Song, Dongming Zhou, Jiaming Zhuang, Priyaa Prasad, Mine Canakci, Mallory Gordon, and Matthew Jennings. I especially thank Dr. Ja-Hyoung Ryu for his initial help when I started my project in Thai group, and Dr. Conghui Yuan for being an unbelievable friend.

I would also like to take this opportunity to express my thanks to all the past and present Thai group members: Dr. Byron Collins, Dr. Deepak V. Dharmangadan, Dr. Ayyagari Venkata Subrahmanyam, Dr. Feng Wang, Dr. Jing Guo, Dr. Diego Amado Torres, Dr. Andrea Della Pelle, Dr. Bhooshan Popere, Dr. Ambata Poe, Dr. Wei bai, Dr. Mijanur Rahaman Molla, Hui Wang, Bin Liu, Huan He, and Bo Zhao, *etc* for their help. I am espically grateful to Hui Wang who joined Thai group at the same time and being there with me as one of my great friend.

I will not forget our group assistant Karen Hakala, and I thank her very much for her continuous help and support. Many thanks are also expressed to UMass staff, Weiguo Hu, Louis Raboin, Dennis Glick and J.M. Stowe.

I thank my classmates: Hui Wang, Xian Wang, Hanwei Zhao, Ying Jiang, Xuni Li, Kevin Dagbay, Jack Fuller, Timothy Gehan, Adam Gann, Devon McCarthy, Rubul Mout, Gustavo Elberto Epalza Sanchez, and so on. You all made me feel comfortable in USA.

I also need to thank all friends from Umass: Yinyong Li, Wenxu Zhang, Tao Feng, Changjiang Ye, Ran Liu, Songhua Liu, Yingqing Deng, Lin Gui, Sainan Lin, Dan Zhang, Yubo Huang, Zhe Zhang, Shengkai Li, Lei Zhang, Leqi Cui, Qingzhao Wang and Boqin Sun. Thank you all for the great time we had in the past five years. I will definitely remember the friendship with you all. May all your dreams and wishes come true!

I really want to thank my parents, Ping Sun and Changshu Li for always supporting without any conditions throughout my life. Although I can not become the doctor you wished, I wish this doctor degree still expresses my sincere thanks for your trust in me. I also thank my elder sister, Ting Li, for taking care of the family when I have been out of town since 2005. I thank her husband and little son for bringing more happinesses into the family. Wish I will hold him soon!

Finally I would like to thank my wife, Zhu Lin, for her patience and unconditional love. I must thank my father-in-law, Hongfeng Lin, and mother-in law, Shuping Xia for their trust. There are no words that can express the gratitude to my wife. Zhu, you are the apple of my eyes!

ABSTRACT

RESPONSIVE SUPRAMOLECULAR ASSEMBLIES BASED ON AMPHIPHILIC POLYMERS AND HYBRID MATERIALS

SEPTEMBER 2015

LONGYU LI, B.A., NANKAI UNIVERSITY

Ph.D., UNIVERSITY OF MASSACHUSETTS AMHERST

Directed by: Professor Sankaran Thayumanavan

The design and synthesis of responsive supramolecular assemblies are of great interest due to their applications in a variety of areas such as drug delivery and sensing. We have developed a facile method to prepare self-crosslinking disulfide-based nanogels derived from an amphiphilic random copolymer containing a hydrophilic oligo-(ethylene glycol)-based side-chain functionality and a hydrophobic pyridyl disulfide functional group. This thesis first provides a concept of studying the influence of Hofmeister ions on the size and guest encapsulation stability of a polymeric nanogel. The size and core density of nanogel can be fine-tuned through the addition of both chaotropes and kosmotropes during nanogel formation. We demonstrate that the change in core density can affect the guest encapsulation stability and stimuli-responsive character of the nanogel. Fluorescence resonance energy transfer (FRET) has been used as the tool to interrogate the guest-exchange process among varieties of host-guest assemblies, which has proved to be quite a robust method to gain insights regarding the guest encapsulation stability in these host assemblies. We studied the effect of host and guest environment upon the guest-exchange dynamics. By systematically comparing the behavior of pH-sensitive and pH-insensitive nanogels, we show that size, concentration, and hydrophobicity can all play a critical role in guest-exchange dynamics. More importantly, these studies reveal that the dominant mechanism of guest exchange can intimately depend on environmental factors. Nanocarriers that can be effectively transported across cellular membranes have potential in a variety of biomedical applications. We report a facile route to prepare nanogels, which generate surface charge with pH

as stimulus due to the slightly acidic conditions observed in the extracellular environment of solid tumor. We show that the pH at which the charge is generated, *i.e.* the isoelectric point (pI) of the nanogel, can be easily adjusted. Intracellular delivery of these nanogels was greatly enhanced in an acidic pH environment due to the surface charge generation. This study demonstrates the versatile nature of the nanogels to introduce specific functionalities with relative ease to achieve desired functional behavior. Further, we have taken advantage of photo-induced heterodisulfide metathesis to develop a reagent-free synthetic method to generate self-crosslinking disulfide-based nanogels crosslinked polymer nanoparticles.

In addition, we report on a simple method to prepare monodisperse polymeric nanoparticles through sequential boronate esterification of boronic acids and bifunctional catechols under ambient conditions. Our results suggest that the initial polymer formation, serving as the nucleus for monodisperse nanoparticle assembly, involves a cooperative polymerization, wherein the dative bond between the nitrogen in the imine building blocks and the boron in the boronate ester plays a critical role. The dynamic nature of the dative interaction in this equilibrium self-assembly has been shown to endow these nanoparticles with thermal responsive characteristics. Further, hollow metal-organic nanoparticles (MOPs) were synthesized from these polymeric nanoparticles using a simple metal-comonomer exchange process in a single step. The Kirkendall effect has been identified as the underlying mechanism for the formation of these hollow MOPs, which also allows a unique opportunity to tune the shell thickness of the MOPs. The generality of the methodology is evident from that it is applied for a variety of metal ions with different coordination geometries.

TABLE OF CONTENTS

Page

ACKNOWLEDGMENTS v

ABSTRACT vii

LIST OF TABLES xv

LIST OF FIGURES xvi

LIST OF SCHEMES xxiii

CHAPTER

1. INTRODUCTION 1

1.1 Introduction 1

1.2 Simple nanogels based on amphiphilic random copolymers 2

1.3 Complex polymeric aggregates based on amphiphilic random copolymers 9

1.4 Thesis overview 13

1.5 References 16

2. EFFECT OF HOFMEISTER IONS ON THE SIZE AND ENCAPSULATION STABILITY OF POLYMER NANOGELS 19

2.1 Introduction 19

2.2 Results and Discussion 20

2.2.1 Effect of Hofmeister ions on the LCST of polymers 20

2.2.2 Effect of Hofmeister ions on the size of nanogels 22

2.2.3 Effect of Hofmeister ions on the encapsulation stability of nanogels 24

2.2.4 Effect of Hofmeister ions on the release behavior of nanogels 29

2.3 Summary 29

2.4 Experimental 30

2.4.1 General 30

2.4.2 Synthesis of Random Copolymer. 31

2.4.3 Synthesis of Nanogels Containing DiI/DiO. 31

2.4.4 Dynamic Light Scattering Measurement. 32

2.5 References 32

3. ENVIRONMENT-DEPENDENT GUEST EXCHANGE IN SUPRAMOLECULAR HOSTS 35

3.1 Introduction 35

3.2 Results and Discussion 37

3.2.1 Design and synthesis of nanogels 37

3.2.2 Collision-based mechanism for control nanogels NG-C 38

3.2.3 pH-dependent guest-exchange mechanism 39

3.3 Summary 47

3.4 Experimental 47

3.4.1 General Methods 47

3.4.2 Synthesis of Random Copolymer 48

3.4.3 Preparation of Nanogels Contaning DiI/DiO 49

3.4.4 Mixing of Nanogel-Encapsulated Dyes 49

3.5 References 50

4. SURFACE CHARGE GENERATION IN NANOGELS FOR ACTIVATED CELLULAR UPTAKE AT TUMOR-RELEVANT PH 53

4.1 Introduction 53

4.2 Results and Discussion 54

4.2.1 Design and synthesis of pH-sensitive nanogels 54

4.2.2 Effect of monomer ratio on pI 58

4.2.3 Effect of crosslink density on pI 60

4.2.4 Effect of preparation condition on pI 61

4.2.5 pH-dependent cellular uptake 62

4.2.6 Encapsulation capability and redox-responsive behavior 64

4.3 Summary 67

4.4 Experimental 68

4.4.1 General 68

4.4.2 Synthesis of random copolymer P1-P4 69

4.4.3 Synthesis of random copolymer P5 without DPA units 69

4.4.4 Synthesis of random copolymer with primary amine groups 70

4.4.5 Encapsulation of DiI/DiO in nanogels 70

4.4.6 Synthesis of fluorescein-labeled DPA nanogels 70

4.4.7 DLS measurement 70

4.4.8 Dye exchange experiment 71

4.4.9 DiI release experiment 71

4.4.10 Confocal experiments 71

4.5 References 72

5. PHOTOINDUCED HETERODISULFIDE METATHESIS FOR REAGENT-FREE SYNTHESIS OF POLYMER NANOPARTICLES 76

5.1 Introduction 76

5.2 Results and Discussion 77

5.2.1 Photo-induced disulfide metathesis of 2-hydroxyethyl-*o*-pyridyl disulfide 77

5.2.2 Preparation of nanogels via photo-induced crosslinking reaction 82

5.2.3 Encapsulation capability and redox-responsive behavior 85

5.3 Summary 86

5.4 Experimental 87

5.4.1 General Methods 87

5.4.2 Synthesis of 2-hydroxyethyl 2-pyridyl disulfide (PDS-OH) and 2-thiopyridone 88

5.4.3 Synthesis of PDS monomer 88

5.4.4 Synthesis of random copolymer containing PDS groups 89

5.4.5 Time-dependent ^{1}H NMR measurement 90

5.4.6 Nanoparticles preparation 90

5.4.7 Determination of crosslinking density 90

5.4.8 Redox-responsive guest release experiment 91

5.4.9 FRET experiment 91

5.5 References 91

6. THERMORESPONSIVE POLYMERIC NANOPARTICLES: NUCLEATION FROM COOPERATIVE POLYMERIZATION DRIVEN BY DATIVE BONDS 95

6.1 Introduction 95

6.2 Results and Discussion 96

6.2.1 Design and preparation of nanoparticles 96

6.2.2 Mechanism study of the particle formation 101

6.2.3 Responsive behavior of BNP based on dative N→B bond 108

6.3 Summary 110

6.4 Experimental 111

6.4.1 General Procedures 111

6.4.2 Synthesis of Im-Ca 111

6.4.3 Synthesis of Im-BA 112

6.4.4 Synthesis of mono-Im-Ca 113

6.4.5 Synthesis of Im-Ca2 113

6.4.6 Synthesis of Im-Ca6 114

6.4.7 Synthesis of St-BA and St-Ca 114

6.4.8 Synthesis of tetraethyl (1,4-phenylenebis(methylene))bis(phosphonate) 115

6.4.9 Protection of 4-formylphenylboronic acid 115

6.4.10 Protection of 3, 4-dihydroxybenzaldehyde 116

6.4.11 Synthesis of St-BA 116

6.4.12 Synthesis of St-Ca 117

6.4.13 Preparation of Nanoparticles via dropwise addition 118

6.4.14 Stability of nanoparticles in solution and in solid state. 119

6.5 References 121

7. HOLLOW METAL ORGANIC NANOPARTICLES FROM POLYMERIC NANOPARTICLES USING KIRKENDALL EFFECT 125

7.1 Introduction 125

7.2 Results and Discussion 126

7.2.1 Preparation and characterization of hollow metal organic nanoparticles (MOPs) 126

7.2.2 General method for hollow metal organic nanoparticles (MOP) 129

7.2.3 Electron paramagnetic resonance spectroscopy characterization 131

7.2.4 Mechanism study of the hollow MOP formation 132

7.3 Summary 138

7.4 Experimental 138

7.4.1 General 138

7.4.2 Synthesis of Im-Ca 139

7.4.3 Synthesis of Im-BA 140

7.4.4 Preparation of Hollow Metal-Organic Particles 140

7.4.5 Preparation of Hollow Fe@C particles 140

7.4.6 Adsorption of methylene blue (MB) from aqueus solution 141

7.4.7 Release of methylene blue (MB) from Fe@C particles 141

7.5 References 141

8. SUMMARY AND FUTURE DIRECTIONS 144

8.1 Summary 144

8.2 Future directions 147

8.2.1 Redox-activatable ^{19}F-MRI nanoprobe 147

8.2.2 Hollow carbon particles loaded with metal nanoparticles 152

8.3 References 156

BIBLIOGRAPHY 160

LIST OF TABLES

Table Page

Table 2.1 Sizes of the Polymer Aggregates and Nanogels.....23

Table 2.2 Leakage coefficient of nanogels made in different conditions.....25

Table 3.1 Leakage coefficient of 0.10 mg/mL NG of at different pH values. 40

Table 3.2 Leakage coefficient of NG of different concentrations (0.05 mg/mL, 0.10 mg/mL and 0.15 mg/mL) at different pH values (8.0, 7.1, 6.1 and 5.1). 45

Table 3.3 Leakage coefficient of NG-C of different concentrations (0.05 mg/mL, 0.10 mg/mL and 0.15 mg/mL) at different pH values (8.0, 7.1, 6.1 and 5.1).....46

Table 4.1 Characteristics of $PEGMA_x$-co-DPA_y-co-PDS_z copolymers (P1–P4). 57

Table 5.1 Calculated crosslinking densities for nanogels. 84

Table 8.1 Characteristics of $PEGMA_x$-co-$PDSMA_y$-co-$TFEMA_z$ copolymers (P1–P4) 149

Table 8.2 T2 measurement 150

LIST OF FIGURES

Figure Page

Figure 1.1 Schematic representation of drug release via disassembly of amphiphilic polymer micelle triggered by GSH (reproduced with permission from reference[21]). 2

Figure 1.2 (a) Structure of the polymer precursors and nanogels: (*i*) cleavage of specific amount of PDS group by DTT, and (*ii*) nanogel formation by inter/intrachain cross-linking. (b) Schematic representation of the preparation of the biodegradable nanogels (reproduced with permission from reference[22]). 3

Figure 1.3 (a) Mixed nanogels encapsulated DiI/DiO and FRET behavior. (b) Fluorescence emission spectra of mixed NG1 encapsulated DiI/DiO. (c) Plot of FRET ratio vs time (reproduced with permission from reference[24]). 4

Figure 1.4 (a) Schematic Representation of the One-Pot Synthesis of T-NGs, (b) Chemical Structure of Polymer and T-NGs, and (c) Cysteine-Containing Targeting Ligands (reproduced with permission from reference[25]). 5

Figure 1.5 Structures of the nanogel's polymer precursor and tri-Arginine peptide as well as nanogel−protein complexation by complementary electrostatic interactions (reproduced with permission from reference[26]). 6

Figure 1.6 (a) BSA modification with SATP linker, (b) NG-DiI–BSA conjugate formation. (BSA structure PDB: 3V03) (reproduced with permission from reference[29]). 7

Figure 1.7 Schematic representation of design and synthesis of the cross-linked polymer nanogels (reproduced with permission from reference[30]). 8

Figure 1.8 a) Schematic representation of the polymer nanoparticle with surface functionalization and guest binding abilities, b) Synthesis of Polymer Precursor and the Nanoparticle (reproduced with permission from reference[31]). 9

Figure 1.9 Schematic representation of the polymer structure, the coating and decoating processes (reproduced with permission from reference[32]). 10

Figure 1.10 Schematic representation of the composite nanostructure assembly and stimuli-sensitive disassembly (reproduced with permission from reference[33]).....11

Figure 1.11 Schematic representation of nanocluster formation at physiological pH and reversal at lower pH (reproduced with permission from reference[36]). 13

Figure 2.1 Schematic illustration of the possibility of varying size and encapsulation stability in polymeric nanogels using Hofmeister ions. 20

Figure 2.2 (a) LCST trend of polymer in salts with different anions solution, the salt concentration is 30 mM/mL (b)LCST trend of polymer in salts with different cations solution, the salt concentration is 30 mM/mL (c) LCST trend of polymer in Na_2SO_4 solution with different concentrations (d) LCST trend of polymer in NaSCN solution with different concentrations. All the concentration of polymer solution is 10 mg/mL. 22

Figure 2.3 Size of polymer aggregates (a) in Na_2SO_4 solution (b) in NaSCN solution; Size of nanogels after dialysis (c) made in Na_2SO_4 solution (d) made in NaSCN solution. 23

Figure 2.4 Fluorescence emission spectra of mixed NGs encapsulated DiI/DiO, (a) NG made in 100 mM Na_2SO_4(aq), (b) NG made in 100 mM NaSCN(aq). (c) Comparing the dynamics of leakage/interchange of NGs made in different solution. 24

Figure 2.5 Absorbance of the nanogel loaded with DiI after the addition of Na_2SO_4 or NaSCN. Nanogel was made in salt free water, and concentration of both the measured nanogel solutions is 0.2 mg/mL. (a-b) Nanogels with 6% crosslinking degree, (c-d) Nanogels with 13% crosslinking degree, (e-f) Nanogels with 25% crosslinking degree. 26

Figure 2.6 Change in morphology of the nanogels due to the presence of salts (a) nanogel without salts (b) nanogel after adding Na_2SO_4 (c) nanogel after adding NaSCN from AFM(height mode). 27

Figure 2.7 Analysis of the nanogel AFM height images of the nanogels (a) in the absence of salt (b) in the presence of Na_2SO_4 (c) in the presence of NaSCN. 28

Figure 2.8 GSH-induced (10mM) DiI release rate from the nanogels made in different salt solutions. 29

Figure 3.1 Schematic representation of two possible mechanisms for guest-exchange between cross-linked nanogels. a) Collision – Exchange – Separation Mechanism, also called as Collision- based mechanism b) Exit – Re - entry Mechanism, also called as Diffusion-based mechanism. 36

Figure 3.2 Size distribution of nanogel at different pH values via DLS measurements. a) NG with 30% crosslinking density, b) NG-C with 20% crosslinking density. 38

Figure 3.3 Fluorescence evolution when NG-C containing DiI and DiO are mixed in solutions at pH 7.1. a) 0.05 mg/mL, b) 0.10 mg/mL, c) 0.15 mg/mL. d) Comparison of the dynamics of guest-exchange between NG-C with different concentration at pH 7.1. 39

Figure 3.4 Fluorescence evolution when NG containing DiI and DiO are mixed in solutions at different pH values. a) pH 8.0, b) pH 6.4, c) pH 5.1. d) Guest-exchange rates between NG at different pH values. The concentration of each nanogel was 0.10 mg/mL. 40

Figure 3.5 Comparison of the dynamics of guest-exchange between NG-C with 0.10 mg/mL at different pH values. 42

Figure 3.6 Effect of pH on the hydrophobicity. a) Fluorescence emission spectrum measured for nanogel NG-C loading 2 wt% pyrene and b) calculated I_1/I_3 ratios for nanogels at different pH values, (black, NG; red, NG-C). 43

Figure 3.7 Comparison of the dynamics of guest-exchange between NG of different concentrations (0.05 mg/mL, 0.10 mg/mL and 0.15 mg/mL) at a) pH 8.0, b) pH 7.1, c) pH 6.1 and d) pH 5.1.....44

Figure 3.8 Comparison of the dynamics of dye exchange between NG-C of different concentrations (0.05 mg/mL, 0.10 mg/mL and 0.15 mg/mL) at a) pH 8.0, b) pH 7.1, c) pH 6.1 and d) pH 5.1.....46

Figure 4.1 Synthetic scheme and NMR spectrum of PEGMA-co-DPA-co-PDS random copolymer with PEGMA: DPA: PDS = 0.28: 0.36: 0.36 (P2) in $CDCl_3$.....57

Figure 4.2 Change in the zeta potential of nanogels as a function of pH. NG1 - NG4 were made by using P1-P4 at pH 10. All nanogel crosslinking densities were 100%, achieved by adding 50 mol% DTT with respect to PDS groups.....59

Figure 4.3 Change in the zeta potential of nanogels with different crosslinking density as a function of pH. All three nanogels were made by using P1 at pH10, and the crosslinking density was varied by using appropriate amount of DTT.....60

Figure 4.4 Change in the zeta potential of nanogels as a function of pH. NG1-x nanogels were made by using P1 at different pHs, represented as NG1-x where x stands for the pH at which the nanogel was prepared. Crosslinking density in all nanogels was fixed at 100%. For comparison, nanogel without DPA units (NG5) was prepared; structure of NG5 is also shown.....62

Figure 4.5 (a) and (b) are confocal images of NG2, containing DiI at pH 7.4 and 6.5 respectively, after incubation with HeLa cells for 2 hours. The nanogels used were 100% crosslinked. Cells were imaged using a 63 × oil-immersion objective. Within each image set, left panel is the red channel that shows DiI emission; middle panel is the DIC image, and right panel is an overlap of both. 63

Figure 4.6 (a) and (b) are confocal images of the control nanogel NG5 (without DPA units) loaded with DiI at pH 7.4 and 6.5 respectively after incubation with HeLa cells for 2 hours. The nanogels used were made from polymer without DPA units. Cells were imaged using a 63 × oil-immersion objective. Within each image set, left panel is the red channel that shows DiI emission; middle panel is the DIC image, and right panel is an overlap of both images.....63

Figure 4.7 Encapsulation stability of nanogel at different pH (a-d). DiI release experiment, a) at pH 6.0, b) at pH 7.4. FRET experiment based DiI/DiO exchange, c) at pH 6.0, d) at pH 7.4; DiI release experiment in the presence of 5mM DTT in solution, e) at pH 6, f) pH 7.4. The nanogels used were made from P2 (100% crosslinked). 65

Figure 4.8 Absorption spectra for DiI release experiment at a) pH 6.0 with 5 mM DTT and b) pH 7.4 with 5mM DTT.....66

Figure 4.9 (a) and (b) are confocal images of fluorescein-labeled DPA nanogel at pH 7.4 and 6.5 after incubation with HeLa cells for 2 hours. The concentration of the nanogels used was 1mg/mL. Cells were imaged using a 63 × oil-immersion objective. Within each image set, left panel is the green channel that shows FITC emission; middle panel is the DIC image, and right panel is an overlap of both. 67

Figure 5.1 Time-dependent ^{1}H NMR spectra of the photo-induced reaction of 2-hydroxyethyl 2-pyridyl disulfide (PDS-OH, **1**). Control spectra of bis(2-hydroxyethyl) disulfide (DPDS, **2**), 2, 2'-dipyridyl disulfide (**3**) and 2-thiopyridone were also included. The concentration was 2.5 mg/mL. The final product after photoirradiation was determined to be pyridine-2-sulfonic acid (**4**). 78

Figure 5.2 Concentration dependent of reaction rate of PDS under photoirradiation. 79

Figure 5.3 Time-dependent ^{1}H NMR spectra of the photo-induced disulfide metathesis of 2-hydroxyethyl 2-pyridyl disulfide (PDS-OH, **1**) under anaerobic condition. Control spectra of bis(2-hydroxyethyl) disulfide (**2**), 2, 2'-dipyridyl disulfide (DPDS, **3**) and 2-thiopyridone were also included. The concentration was 2.5 mg/mL. 80

Figure 5.4 Time-dependent ^{1}H NMR spectra of 2, 2'-dipyridyl disulfide (DPDS) under the photoirradiation without O_2. 81

Figure 5.5 DLS sizes in hydrodynamic diameter, a) micelle aggregates prepared with polymer solutions with different concentrations, b) nanogels prepared with polymer solutions with different concentrations, the photoirradiation time was 2 h for all samples. 83

Figure 5.6 a) Absorption spectra of pyridothione in UV-vis. Pyridothione, which is a byproduct by the reaction between PDS with DTT and shows characteristic absorption at 343 nm wavelength, is monitored in each nanogel (2 mg/mL) prepared. b) Time dependent crosslinking density of the nanogels with different concentrations of polymer solution, from 1 mg/mL to 10 mg/mL. 84

Figure 5.7 Dye release from the nanogels prepared via photoirradiation for 2 h in response to varied GSH concentrations, a) 0 mM, b) 10 mM. Sample concentration was 0.1 mg/mL. FRET experiment based DiI/DiO exchange, c) micelle aggregates, d) nanogels prepared via photoirradiation for 1 h, e) nanogels prepared via photoirradiation for 2 h. Sample concentration was 0.1 mg/mL. 86

Figure 6.1 Synthesis and characterization of boronate nanoparticle (**BNP**). a) Scheme presents the syntheses of **Im-Ca** and **Im-BA** monomers, as well as polymer P1 via the polyboronate esterification between **Im-Ca** and **Im-BA**. b) TEM image of the **BNP**, the scale bar is 500 nm. c) SEM image of the **BNP**, the scale bar is 5μm. Conditions: dropwise added 1 mL 5 mg/mL **Im-Ca** methanol solution into 1 mL 5 mg/mL **Im-BA** methanol solution with stirring at room temperature. The TEM and SEM samples were taken immediately after the addition. d) FTIR spectra of molecule **Im-BA**, **Im-Ca** and solid **BNP**, and e) Zoomed-in FTIR spectra from (d). 97

Figure 6.2 Particle size and absorption characteristics variation. a) DLS of the **BNP** prepared with different monomer concentration in methanol. TEM images of the **BNP**, prepared with different monomer concentration in methanol, b) 1.5 mg/mL, c) 3.0 mg/mL, d) 5 mg/mL. The scale bar is 500 nm. e) Normalized absorption spectra for **Im-BA**, **Im-Ca** and **BNP** prepared with different monomer concentration in methanol. Temporal evolution of absorption spectra for **BNP** prepared with f) 3 mg/mL in methanol, g) 5 mg/mL in methanol. All samples were prepared by adding 0.01 mL reaction mixture into 1 mL methanol. 98

Figure 6.3 PXRD pattern of the **BNP**. A broad bump at about 2θ=20 was resulted from crystalline parts of polymers. 99

Figure 6.4 Absorption spectra for **Im-BA** and **Im-Ca** as the time. The concentration for both solutions is 0.02 mg/mL. 100

Figure 6.5 Mechanism study of the particle formation. a) Photographs of the **BNP** solution with different ratios of **Im-Ca** into **Im-BA** in methanol. b) DLS of the **BNP** prepared with different addition volumes of **Im-Ca** into 1 mL of **Im-BA** solution. TEM images of the corresponding solutions, c) 0.10 mL **Im-Ca** + 1.0 mL **Im-BA**, d) 0.30 mL **Im-Ca** + 1.0 mL **Im-BA**, e) 0.65 mL **Im-Ca** + 1.0 mL **Im-BA**, f) 1.0 mL **Im-Ca** + 1.0 mL **Im-BA**. The scale bar is 500 nm. Absorption spectra of the reaction mixture with different initial concentrations during the dropwise addition, g) 1 mg/mL, h) 2 mg/mL, i) 3 mg/mL. Note that there were flat lines between 500 and 525 nm, because samples had an absorbance of more than dynamic range of instrument. 102

Figure 6.6 Solid ^{11}B-NMR spectra of **Im-BA**, boronate ester from 4-formylphenylboronic acid and 3,4-dihydroxybenzaldehyde, and solid BNP. 105

Figure 6.7 UV-vis spectra of a), **St-BA, St-Ca, Im-BA** and **Im-Ca** in ethanol; b), their one to one mixture in ethanol. 106

Figure 6.8 a)Typical photos of the mixtures using **Im-BA** react with **Im-Ca2** and **Im-Ca6** in methanol, and their TEM pictures of BNP using b) **Im-Ca2**, c) **Im-Ca6**. The scale bar is 500 nm. 106

Figure 6.9 Solvent effects on the particle formation. TEM images of the **BNP** prepared with methanol (M) and DMSO (D) mixture solution, a) M/D=4/1, b) M/D=6/1, c) M/D=9/1, d) Pure M. The scale bar is 500 nm. 107

Figure 6.10 Responsive behavior of **BNP** based on dative N→B bond. a) Photographs of the **BNP** with the addition of pyridine, imidazole, 4-dimethylaminopyridine, b) Photographs of the **BNP** with changing temperature and their TEM images of the **BNP**, c) before heating, d) after first heat-cool cycle, e) after second heat-cool cycle, f) after third heat-cool cycle. The scale bars are 500 nm. 108

Figure 6.11 TEM images of the **BNP**, a) before the heating and cooling at room temperature for b) 1 min, c) 5 mins, d) 10 mins. 110

Figure 6.12 Aging of the **BNP** in methanol. TEM images of the samples taken after a) 5 mins after the mixing, size is 330 nm, b) 3 days after the mixing, size is 320 nm. The scale bar is 500 nm. 119

Figure 6.13 NMR spectra showing stability of the imine bond as time.....120

Figure 6.14 TGA curves of **Im-BA, Im-Ca** and solid **BNP**.....121

Figure 7.1 a) TEM image of the **BNP**; b) TEM image of the hollow Fe^{3+}-**MOP**; c) SEM image of the hollow Fe^{3+}-**MOP**; Inset is a SEM image of one broken hollow Fe^{3+}-**MOP**. All the scale bar is 500 nm.....127

Figure 7.2 a) EELS mapped images of **BNP**; b) EELS mapped images of hollow Fe^{3+}-**MOP**; All the scale bar is 500 nm.....127

Figure 7.3 Fe, C, N and O line-scanned EELS profiles of two nanoparticles in Figure 1f. EELS images and line-scan profiles confirm the hollow structure of hollow Fe^{3+}-**MOP**.....128

Figure 7.4 Bright-field STEM images and EDS maps of hollow Fe^{3+}-**MOP**, element C and Fe included.....129

Figure 7.5 a) TEM image of the hollow Cu^{2+}-**MOP** by adding Cu^{2+}; b) TEM image of the hollow Sn^{4+}-**MOP** adding Sn^{4+}; c) TEM image of the hollow Al^{3+}-**MOP** adding Al^{3+}; All the scale bar is 500 nm.....130

Figure 7.6 a) Bright-field STEM images and EDS maps of hollow Sn^{4+}-**MOP**, element C and Sn included; b) HAADF STEM images and EDS maps of dual Fe^{3+}/Sn^{4+}-hollow **MOP**, element C, Fe and Sn included. 130

Figure 7.7 EPR spectra of **BNP** and hollow **MOP**. 295 K, X-band (9.8 GHz) EPR spectrum measured at room temperature for **BNP** (black), hollow Al^{3+}-**MOP** (green), hollow Fe^{3+}-**MOP** (blue), dual hollow Fe^{3+}/Al^{3+}-**MOP** (red) (starting composition was 0.05 mol fraction of $FeCl_3/AlCl_3$). Inset: $g' \sim 9.6$ transition of the dual hollow Fe^{3+}/Al^{3+}-**MOP**s on an expanded scale. 132

Figure 7.8 TEM images taken at a) 0 min, b) 20 min, c) 1 h and d) 6 h after the addition of $FeCl_3$ into **BNP**; the scale bar is 500 nm. Conditions: 0.1 mL $FeCl_3$ methanol solution was added into 1 mL BNP methanol solution prepared using 3 mg/mL **Im-BA** and **Im-Ca**, the ratio of Fe^{3+} to Im-Ca was 1/2. The TEM samples were taken by drop-casting. The scale bar is 500 nm.....133

Figure 7.9 Time dependent TEM measurement, taken after 30 min, 1 h, and 2 h. Conditions: 0.1 mL $SnCl_4$ methanol solution was added into 1 mL **BNP** methanol solution prepared using 3 mg/mL **Im-BA** and **Im-Ca**, the ratio of Sn^{4+} to Im-Ca was 1/2. The TEM samples were taken by drop-casting. The scale bar is 500 nm.....133

Figure 7.10 The thickness of shell could be tuned by changing the ratio of Fe^{3+} to Im-Ca, a) 1/8, b) 1/2, c) 3/4.However, when the ratio increased up to 1/1, only solid **MOP**s were observed as shown TEM in figure d). EDS maps of solid Fe^{3+}-**MOP**, element C (e) and Fe (f) included. , all scale bar is 500 nm except e) and f) with 250 nm scale bar.....134

Figure 7.11 The size of hollow **MOP** could be varied by tuning the size of **BNP** used, a, d) 1.5 mg/mL monomers, b, e) 3.0 mg/mL monomers, c, f) 5.0 mg/mL monomers. The ratio of Fe^{3+} to Im-Ca was 1/2; all scale bar is 500 nm. 135

Figure 7.12 Preparation and application of hollow Fe@C particles. TEM measurement of a) hollow Fe@C particles after the temperature thermal treatment of **MOP**s, b) hollow carbon particles after the acid treatment of Fe@C; c) Optical photograph of the MB solution without (left) and with (right) the addition of Fe@C applying an external magnet; d) UV-vis absorption measurement before and after the magnetic separation. 136

Figure 7.13 HAADF STEM images and EDX line scanning data.....137

Figure 8.1 Schematic representation of the functionalities for an effective drug delivery system after the injection. 144

Figure 8.2 a) pH-activatable ON/OFF ^{19}F-MRI nanoprobes from ionizable diblock copolymers. At pH > pK_a, the hydrophobic segments selfassemble into a micelle core leading to ^{19}F signal suppression as a result of restricted polymer chain motion. Upon pH activation (pH < pK_a), micelle disassembly leads to dissociated unimers and a strong ^{19}F signal. b) Structural formula of three representative diblock copolymers containing different pH responsive segments and ^{19}F reporter moieties, their pKa values and ^{19}F chemical shifts (in ppm, relative to trifluoroacetic acid, or TFA), respectively, are shown in parenthesis (reproduced with permission from reference[15]). 148

Figure 8.3 GPC results of P1-P3. 149

Figure 8.4 Typical NMR spectrum of P2. 150

Figure 8.5 ^{19}F NMR spectra were taken for all three polymers before and after the addition of GSH in water containing 10% D_2O. 151

Figure 8.6 Hollow carbon particles loaded with metal nanoparticles (M@Fe), a) Fe@C, b) Cu@C, c) Sn@C. 152

Figure 8.7 XRD results of M@C. Typical peaks were marked. 153

Figure 8.8 TGA result, a) **MOP**s and **BNP** in N_2, b) M@C in air. 154

Figure 8.9 The time-dependent absorption spectra of the reaction solution in the presence of 0.3 mg of Cu@C. 155

LIST OF SCHEMES

Scheme Page

Scheme 2.1 Structure of the polymer and the nanogel containing OEG units. 21

Scheme 3.1 Structure of polymers **P1** and **P2**; nanogels **NG-C** and **NG**; and the dye molecules DiO and DiI. 37

Scheme 4.1 Schematic illustration and chemical structure of polymeric nanogels for pH-induced surface charge generation and activated cellular uptake. 55

Scheme 5.1 Hypothesized reaction scheme of photo-induced disulfide metathesis of 2-pyridyl disulfide (PDS-OH) 78

Scheme 5.2 Scheme of photo-induced chemistry reaction of PDS-OH. 79

Scheme 5.3 Scheme of photo-induced chemistry reaction of 2-pyridyl disulfide (PDS-OH) under anaerobic condition. 81

Scheme 5.4 Representation of photo-induced crosslinking reaction of random copolymers containing PDS groups. 82

Scheme 6.1 Structure of **St-Ca**, **St-BA**, **Im-Ca2** and **Im-Ca6.** 106

Scheme 6.2 Synthesis of **Im-Ca**. 111

Scheme 6.3 Synthesis of **Im-BA**. 112

Scheme 6.4 Synthesis of mono-**Im-Ca**. 113

Scheme 6.5 Synthesis of **Im-Ca2**. 113

Scheme 6.6 Synthesis of **Im-Ca6**. 114

Scheme 6.7 Synthesis of tetraethyl (1,4-phenylenebis(methylene))bis(phosphonate). 115

Scheme 6.8 Protection of 4-formylphenylboronic acid. 115

Scheme 6.9 Protection of 3, 4-dihydroxybenzaldehyde. 116

Scheme 6.10 Synthesis of **St-BA**. 116

Scheme 6.11 Synthesis of **St-Ca**. 117

Scheme 7.1 Scheme presents the syntheses of BNP via **Im-Ca** and **Im-BA**, and the preparation of hollow **MOP** by adding metal chloride salts to the **BNP** solution. 126

Scheme 7.2 Schematic illustration showing the transformation of solid polymer nanoparticles to hollow or solid metal organic particles, depending on the relative diffusivities. 134

Scheme 8.1 Synthetic scheme of $PEGMA_x$-co-$PDSMA_y$-co-$TFEMA_z$ random copolymer. 149

CHAPTER 1

INTRODUCTION

Li, L.; Raghupathi, K.; Song, C.; Prasad, P.; Thayumanavan, S. Self-assembly of random copolymers. *Chem. commun.* **2014**, *50*, 13417-13432. - Reproduced by permission of The Royal Society of Chemistry

http://pubs.rsc.org/en/content/articlehtml/2014/cc/c4cc03688c

1.1 Introduction

Self-assembly of amphiphilic copolymers are of great interest for many decades because these materials are able to offer a rich variety of morphologies and transitions as well as their potential applications in many fields, such as biomedical, micro-electronic, photoelectric and optical materials.[1–5] Significant progress has been made in the design and synthesis of a variety of amphiphilic copolymers owing to advances in controlled polymerization techniques, such as nitroxide mediated radical polymerization (NMP), atom transfer radical polymerization (ATRP), reversible addition–fragmentation chain transfer polymerization (RAFT) and ring-opening mediated radical polymerization (ROMP).[6–11] Copolymers can be broadly classified into two categories: block copolymers and random copolymers. In the case of block copolymers, the monomers are arranged systematically in the form of blocks where each block is a repetition of a certain monomer species, whereas in the case of random copolymers different monomeric components of the polymer are randomly arranged where the probability of finding a given monomeric unit at any given location on the polymer is independent of the nature of the adjacent units. Until recently, much focus has been directed towards understanding the self-assembly of block copolymers, due to their unique and excellent assembly behaviours.[12–17] However, their synthetic methods can be tedious and time-consuming, as it involves sequential controlled polymerization or post-polymerization treatments such as grafting, substitution, hydrolysis and ‘‘click’’ chemistries.[18–20] Compared to block copolymers, preparation of random copolymers is

relatively easy, as they are typically achieved in a one step co-polymerization of two (or more) different monomers. Therefore, it is intriguing to highlight the supramolecular capabilities of amphiphilic random copolymers in self-assembly.

1.2 Simple nanogels based on amphiphilic random copolymers

Our group has had a longstanding interest in using random copolymers for self-assembly. Amphiphilic random copolymers, containing triethylene glycol as the hydrophilic part and an alkyl chain connected by the disulfide bond as the hydrophobic part, were prepared by free radical polymerization.[21] These polymers were able to form micelle-like nanoassemblies in water and encapsulate hydrophobic guests inside their core (Figure 1.1). These nanoassemblies disintegrate in the presence of a reducing environment, leading to the release of encapsulated guest molecules. This stimuli responsive behavior is due to the cleavage of the disulfide bond that connects the hydrophobic moiety to the polymer backbone. Thus, under the reducing conditions, the self-assembling amphiphilic polymer is converted to a hydrophilic polymer that no longer has the ability to self-assemble, leading to the release of guest molecules.

Figure 1.1 Schematic representation of drug release via disassembly of amphiphilic polymer micelle triggered by GSH (reproduced with permission from reference[21]).

Considering that micelle-type assemblies can be destabilized upon dilution, strategies to crosslink the core of these nanoassemblies have been developed. Apart from retaining their structural integrity upon dilution, these nanogels can also stably encapsulate guest molecules and release them only in response to a redox trigger, such as glutathione (GSH).[22, 23] The nanogel is

based on a random copolymer that contains hydrophilic oligoethylene glycol (OEG) and hydrophobic pyridyldisulfide (PDS) units as side chain functionalities. This random copolymer forms nanoaggregates in water; addition of a deficient amount of dithiothreitol (DTT) to this solution leads to an intra/inter polymer chain disulfide exchange reaction to afford the core crosslinked polymeric assembly (Figure 1.2). Hydrophobic guest molecules were stably encapsulated inside, while they were released in a reducing environment due to the redox-sensitive disulfide bonds. The size of these polymeric aggregates could be tuned by varying the properties of the polymer, such as molecular weight of the polymer and the relative percentages of OEG units and PDS units incorporated into the polymer. Because the procedure for the nanogel with high encapsulation stability is quite simple and release of guest molecules is tunable, this polymer nanogel scaffold holds great potential for drug delivery, especially for chemotherapeutics.

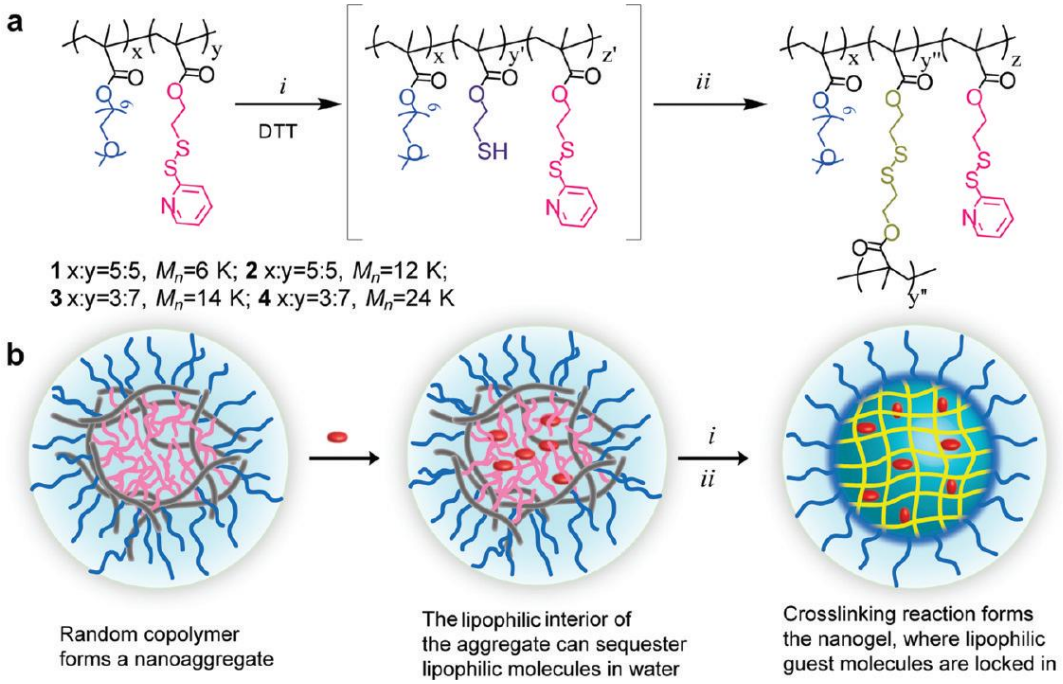

Figure 1.2 (a) Structure of the polymer precursors and nanogels: (*i*) cleavage of specific amount of PDS group by DTT, and (*ii*) nanogel formation by inter/intrachain cross-linking. (b) Schematic representation of the preparation of the biodegradable nanogels (reproduced with permission from reference[22]).

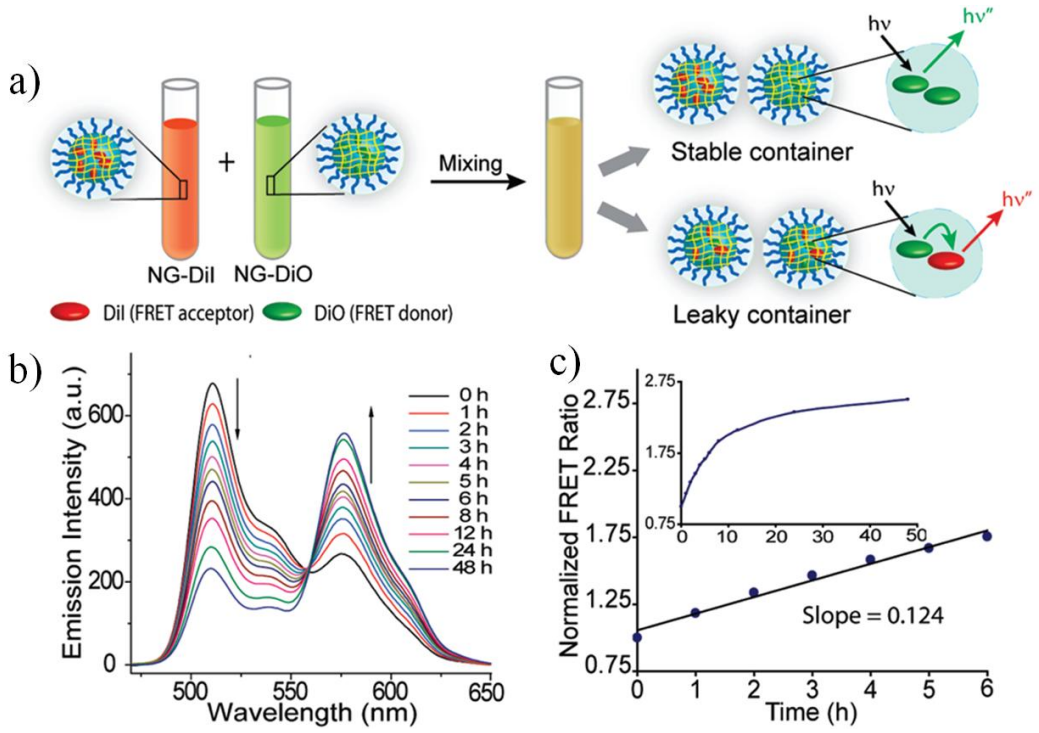

Figure 1.3 (a) Mixed nanogels encapsulated DiI/DiO and FRET behavior. (b) Fluorescence emission spectra of mixed **NG1** encapsulated DiI/DiO. (c) Plot of FRET ratio vs time (reproduced with permission from reference[24]).

To monitor the guest exchange dynamics, which can provide insight into the encapsulation stability of these nanogels, a fluorescence resonance energy transfer (FRET) based method was developed.[24] A lipophilic FRET pair, 3,3′-dioctadecyloxacarbocyanine perchlorate (DiO, donor) and 1,1′-dioctadecyl-3,3,3′,3′-tetramethylindocarbocyanine perchlorate (DiI, acceptor) were independently encapsulated inside nanogels. As shown Figure 1.3a, if the encapsulation stability of dye molecules is pretty high, the two dye molecules will continue to be in two separate nanogels when the nanogels containing the dye molecules were mixed in solution. No FRET would be observed because the distance between the two dye molecules is much higher than their Förster radius. However, it is likely that the dye molecules will equilibrate between the two containers, if the dye molecules are not stably encapsulated, causing DiI and DiO molecules to occupy the same container, resulting in the increased FRET (Figure 1.3b). The FRET ratio $I_a/(I_d + I_a)$, where I_a and I_d are the fluorescence intensities of the acceptor (DiI) and the donor (DiO)

respectively, was plotted against time. The slope of the linear fit is defined as the leakage coefficient (Λ), which shows the dynamics of the guest exchange (Figure 1.3c). It showed that the encapsulation stability of nanogels depends on the degree of cross-linking.

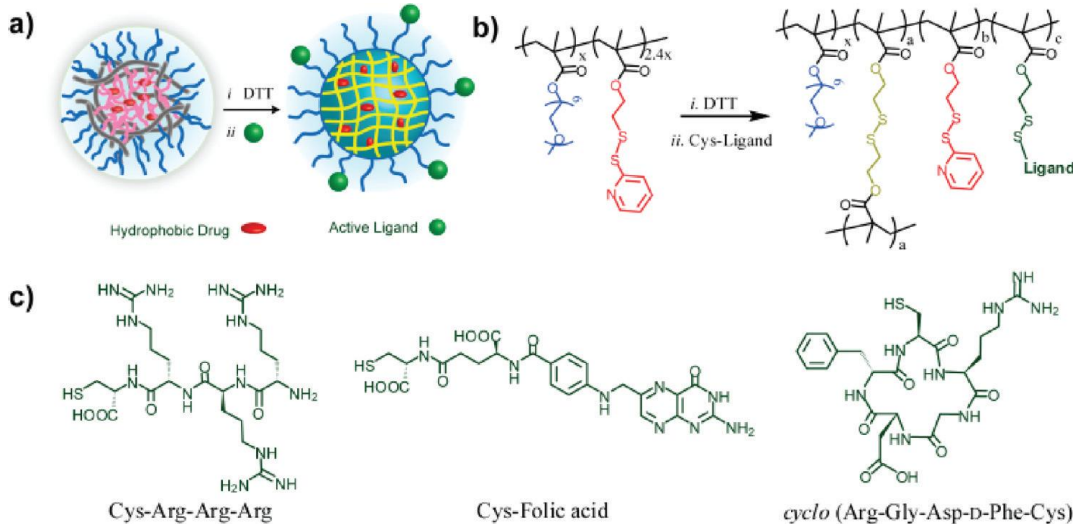

Figure 1.4 (a) Schematic Representation of the One-Pot Synthesis of T-NGs, (b) Chemical Structure of Polymer and T-NGs, and (c) Cysteine-Containing Targeting Ligands (reproduced with permission from reference[25]).

The unique advantage of these assemblies made from random copolymers is that the surface of our nanogel can be conveniently functionalized by free thiol containing molecules via thiol–disulfide exchange.[25] Unlike the block copolymer assemblies where the hydrophobic units are completely buried in the interior, random copolymer aggregates have a certain portion of surface exposed functional hydrophobic PDS moieties, which have been exploited for nanogel decoration with cysteine-modified ligands including folic acid, cyclic arginine-glycine-aspartic acid (cRGD) peptide, and cell-penetrating peptide (Figure 1.4). The results showed that these functionalized nanogels caused rapid uptake by the cells, whereas the unfunctionalized nanogels are taken up very poorly by various cells. RGD-modified nanogels were selective uptake by cells over-expressing integrin and folic-acid decorated nanogels were selective uptake by cells over-expressing FRs. Nanogels with cell-penetrating peptides caused rapid nonspecific uptake by the cells, independent of the receptor.

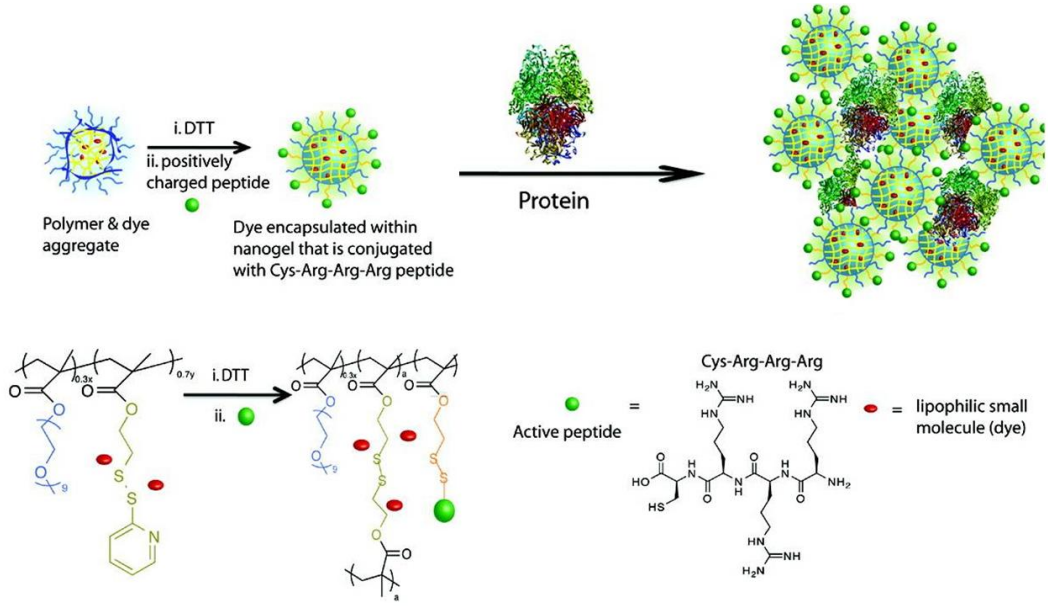

Figure 1.5 Structures of the nanogel's polymer precursor and tri-Arginine peptide as well as nanogel−protein complexation by complementary electrostatic interactions (reproduced with permission from reference[26]).

Supramolecular nanoassemblies, which are capable of binding and delivering either lipophilic small molecules or hydrophilic molecules, are of great interest. These polymeric nanogels indeed could not only be used to deliver hydrophobic drugs, but also be used to bind proteins on their surface through electrostatic interactions, resulting in the concurrent delivery of proteins and hydrophobic small molecules (Figure 1.5).[26] Tri-arginine was chosen as the functional group due to two reasons: (*i*) providing the positively charged surface to bind to the negatively charged surface of protein; (*ii*) exhibiting cell penetrating peptide characteristics for efficient uptake by cells.[27, 28] It showed that complexation of the protein with the nanogel does not alter the activity of the protein. The complex exhibits efficient uptake by cells, where both the lipophilic small molecule and the protein are concurrently taken up by the cells. The conjugation of protein at the nanogel exterior by covalent attachment was also determined.[29] After modification with a thiol linker, the protein was readily conjugated to the nanogels via disulfide

exchange reactions with pyridyl disulfide moieties at the nanogel exterior (Figure 1.6). The results further suggest that this nanogel system is a simple and effective platform for development of sophisticated drug delivery systems. From the application standpoint, the results indicate the possibility to combine therapeutic proteins and antibodies to the nanogels, which are important for selective targeting of the nanogels.

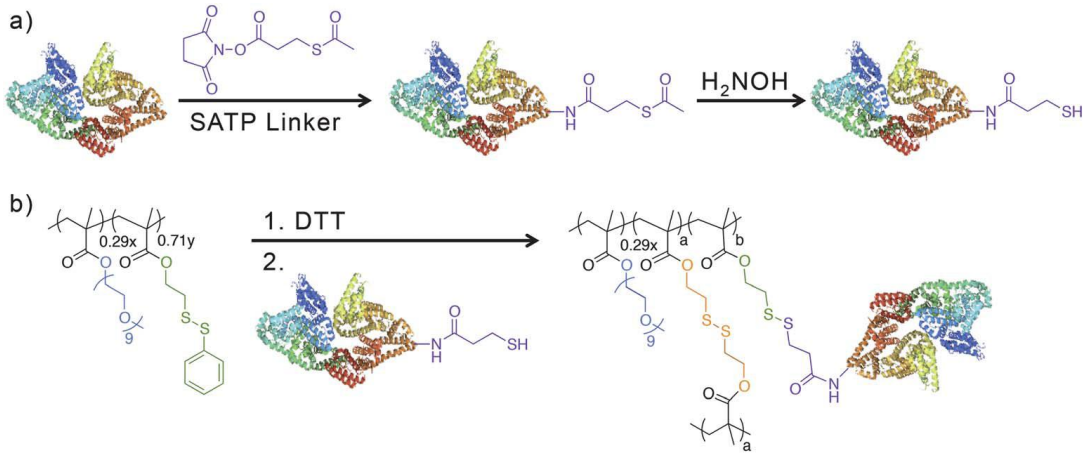

Figure 1.6 (a) BSA modification with SATP linker, (b) NG-DiI–BSA conjugate formation. (BSA structure PDB: 3V03) (reproduced with permission from reference[29]).

Besides disulfide cross-linked systems, a simple reaction between the lipophilic activated PFP ester and diamines was also used to achieve polymeric nanogels (Figure 1.7).[30] Amphiphilic random copolymers with polyethylene glycol methacrylate (PEGMA) as the hydrophilic unit and the pentafluorophenyl acrylate (PFPA) as the lipophilic unit were synthesized. The addition of diamine into the polymer solution could cause inter- and intrachain cross-linking amidation reactions to afford the nanogel, wherein the lipophilic guest molecules were encapsulated within the cross-linked interiors. Both THF and water can be used as the solvent for the nanogel formation. The size of the nanogel can be tuned via the change in polymer concentration.

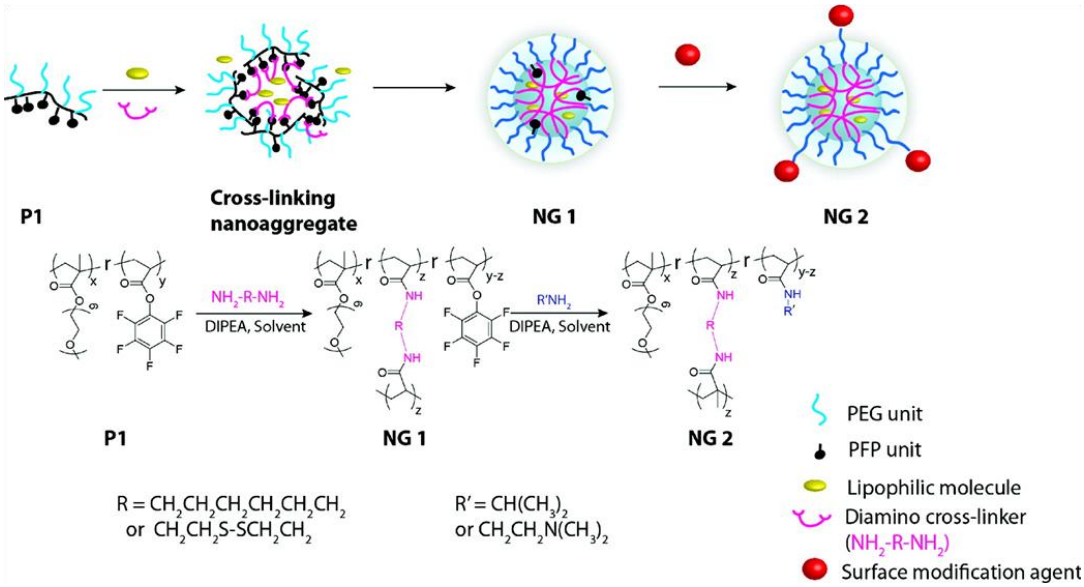

Figure 1.7 Schematic representation of design and synthesis of the cross-linked polymer nanogels (reproduced with permission from reference[30]).

Polymer nanoparticles were also prepared using amphiphilic random copolymers containing 2-aminoethyl methacrylamide and 3-(9-methylcoumarinoxy)propyl methacrylamide (Figure 1.8).[31] These copolymers self-assembled in to a micelle aggregate in water, where the hydrophilic amino functional groups are exposed on the surface, while the coumarin moieties are buried in the hydrophobic interior. The coumarins groups can undergo photochemically driven [2 + 2] cylcoaddition reaction, resulting in the inter- and intrachain cross-linking reaction to achieve the polymer nanoparticles. Hydrophobic guest molecules can be noncovalently encapsulated, while the amine functionality can be used as a handle for surface functionalization of the nanoparticles. Since the pH of the solution changes the hydrophilic−lipophilic balance of the polymer, leading to the formation of polymer aggregates with different sizes, polymer nanoparticles wtih different sizes can be achieved by simply photochemically locking these aggregates.

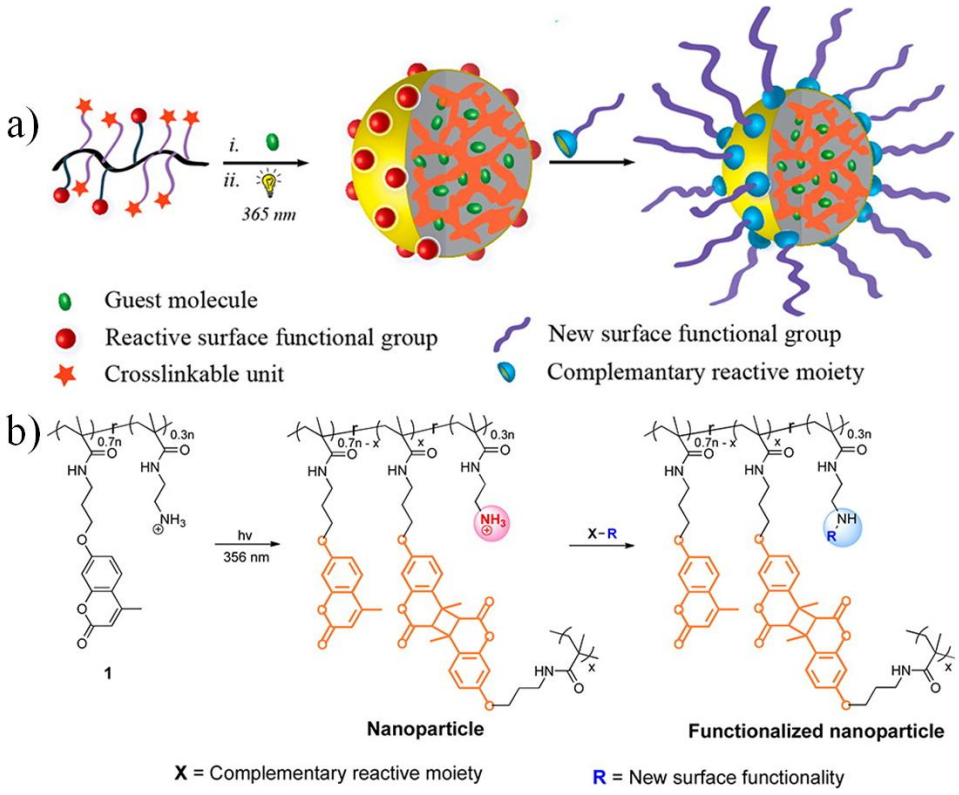

Figure 1.8 a) Schematic representation of the polymer nanoparticle with surface functionalization and guest binding abilities, b) Synthesis of Polymer Precursor and the Nanoparticle (reproduced with permission from reference[31]).

1.3 Complex polymeric aggregates based on amphiphilic random copolymers

In order to prepare smart materials that have additional features such as stealth characteristics and stable encapsulation of guest molecules in addition to stimuli responsive behavior towards multiple environmental triggers, multiple polymers or polymer assemblies have been integrated to form self-assembled structures.

To mask the surface properties *viz*., surface charge on the nanoparticle surface and increase the guest encapsulation stability, polymer coating on nanogels were achieved through electrostatic complementarity (Figure 1.9).[32] First a polycationic nanogel was achieved using intra-aggregate self-crosslinking strategy with PDS functionalities using amphiphilic random copolymer containing pyridyldisulfide units, quaternary ammonium moieties and N-isopropyl acrylamide units. These disulfide crosslinked nanoassemblies were coated with a pH-sensitive

anionic polymer through the electrostatic interactions. This resulted in masking of the positive surface charge of the nanogel and also led to an increase in the encapsulation stability of the non-covalently sequestered guest molecules inside the nanogels. The pH-sensitivity of the coating polymer is such that there is a charge conversion in the polymer in response to lower pH. The pH-induced charge conversion causes electrostatic repulsion between the coating polymer and the polymer nanogel to reveal the positive charge on the nanogel surface. Moreover, the encapsulation stability of the nanogel is also weakened due to the pH-induced decoating, which is further accentuated using a redox stimulus.

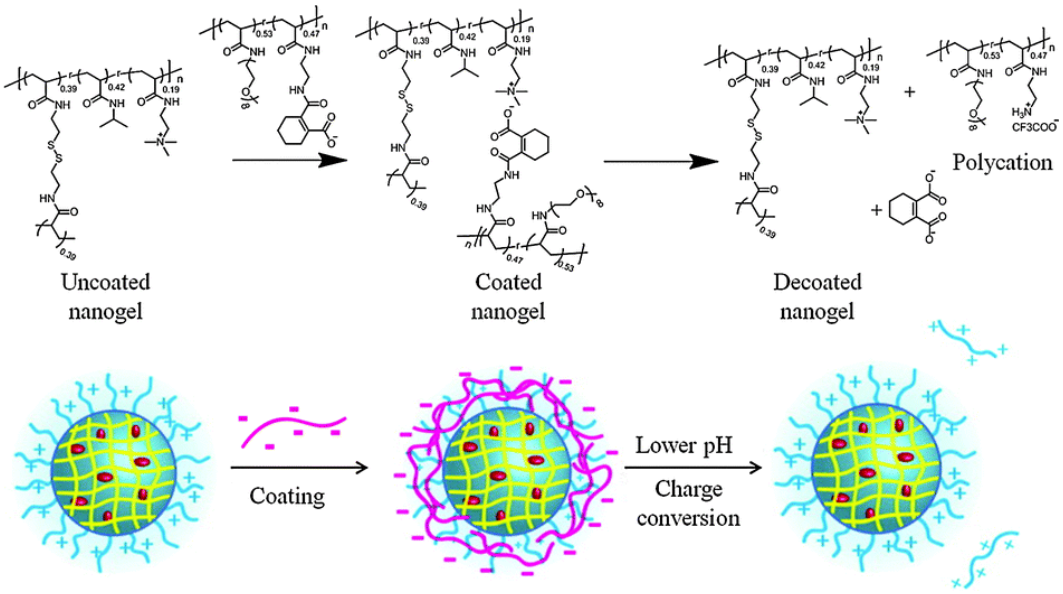

Figure 1.9 Schematic representation of the polymer structure, the coating and decoating processes (reproduced with permission from reference[32]).

Nanocomposites can also be formed by integration of more than one pre-formed nanostructures. For example, the combination of two independent supramolecular assemblies resulted in a novel, dynamic composite nanostructure (Figure 1.10).[33] These composite structures are developed by using polymeric micelles from a block copolymer (poly(2-(diisopropylamino)ethylmethacrylate-b-2-aminoethyl methacrylate hydrochloride)) and nanogels formed from a random copolymer poly(oligoethyleneglycol monomethylether methacrylate-co-

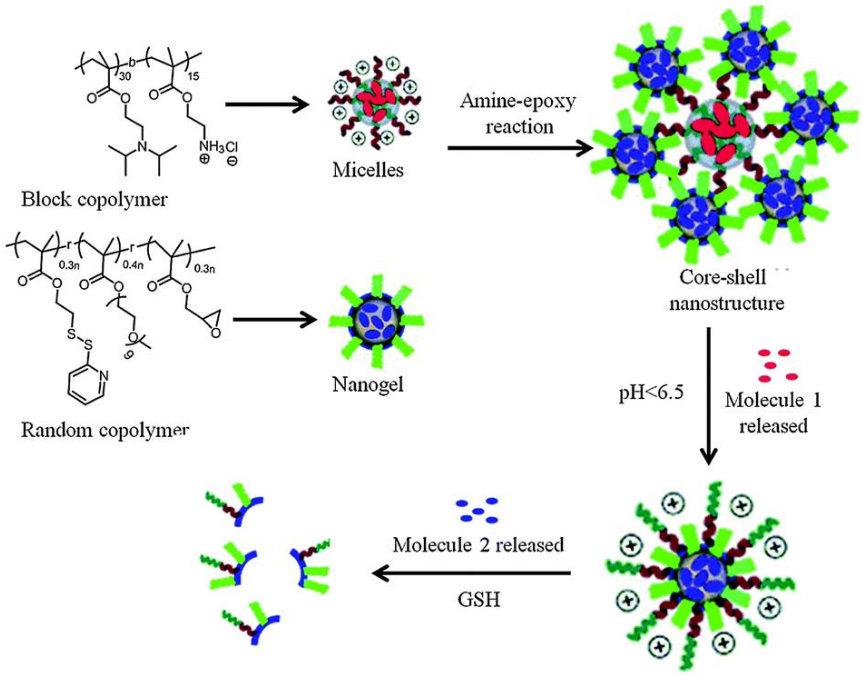

Figure 1.10 Schematic representation of the composite nanostructure assembly and stimuli-sensitive disassembly (reproduced with permission from reference[33]).

glycidylmethacrylate-co-pyridyldisulfide ethyl methacrylate). These two supramolecular assemblies were integrated together by utilizing the covalent reaction between primary amines on the surface of the micellar assemblies and epoxide functionalities present on the nanogel surface to produce a composite nanostructure between the two nanoassemblies. The diisopropylamine (DIPA) block, which constitutes the hydrophobic core of the polymer micelle, endows the composite assembly with pH sensitivity. Under physiologically neutral pH (around pH 7.4 or higher) the DIPA block would be mostly unprotonated and therefore would be hydrophobic. However, when the pH is lowered below 6.5, these functional groups are protonated, which convert the hydrophobic core to a hydrophilic one, causing a disassembly of micellar aggregates. The nanogels on the other hand are redox responsive. In the composite assembly, each of these assemblies retains their individual stimulus-responsive characteristics. But, there exists a synergy. Since the composite nanostructure is formed based on a reactive self-assembly event, when the micelle at the core of this composite assembly breaks, the disassembled polymer chain becomes covalently attached to the nanogel. This feature endows the nanogel with a positively charged

surface that was previously unavailable on the nanogel. The pH-induced charge generation that leads to rapid cellular uptake and the possibility of encapsulating and releasing two different molecules at two different times and locations potentially lend themselves for applications in cancer therapy.

Considering the significant role that the size of drug delivery vehicles plays in enhanced permeability and retention (EPR) effect based tumour targeting,[34, 35] it is interesting to be able to design composite nanostructures that change size in response to microenvironments that are unique to cancer tissues. For example, a larger nanoparticle size is desired for tumour homing, while much smaller nanoparticle sizes are desired for tissue penetration. This combined with the fact that the tumour pH is lower; it is interesting to design a system that exhibits one size at neutral pH and reduces in size when subjected to lower pH conditions. Accordingly, a system of complex aggregates was designed to exhibit variations in size and charge in response to slight changes in pH.[36]

This design involves preparation of stimuli responsive nanoclusters by crosslinking multiple nanoparticles, utilizing the pH sensitive dynamic covalent imine bond between them (Figure 1.11). This is achieved by reversibly crosslinking the nanoassemblies using a small molecule crosslinker. These nanogels are prepared using self-crosslinked nanogel system with a slight modification by using a random copolymer poly(oligoethyleneglycol monomethylether methacrylate-co-aminoethyl methacrylate hydrochloride-co-pyridyldisulfide ethyl methacrylate). The interparticle crosslinking between these nanogels was achieved by reacting the nanogels with a calculated amount of hexaethyleneglycol dibenzaldehyde crosslinker at pH 7.4. This results in the formation of nanoclusters due to the imine formation. These nanoclusters break down into smaller nanogel particles at slightly acidic pH 6.5, presumably due to hydrolysis of imine bonds. This also leads to a simultaneous exposure of free primary amines to present positive charges on the nanogel surface that accelerate cellular uptake.

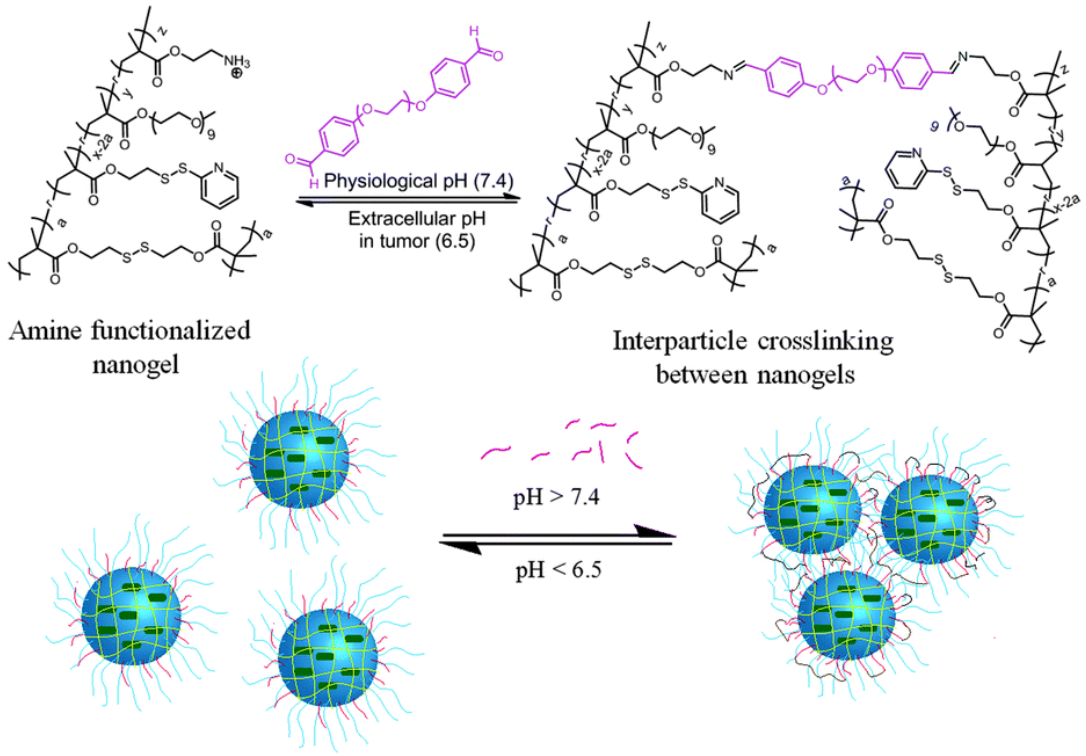

Figure 1.11 Schematic representation of nanocluster formation at physiological pH and reversal at lower pH (reproduced with permission from reference[36]).

1.4 Thesis overview

This thesis work focuses on responsive supramolecular assemblies based on amphiphilic random copolymers. In Chapter 2, influence of Hofmeister ions has been investigated on the size and guest encapsulation stability of a polymeric nanogel. While variations in macroscopic phase transitions have been observed in response to the presence of salts, changes in the size and host−guest behavior of polymeric aggregates in the presence of salts have not been explored in any detail. The size and core density of nanogel can be fine-tuned through the addition of both chaotropes and kosmotropes during nanogel formation. The change in core density affects the guest encapsulation stability and stimuli-responsive character of the nanogel. These studies not only have practical applications in areas such as drug delivery and sensing but also have

fundamental implications in the future design and syntheses of polymer nanoassemblies and nanoparticles.

The guest-exchange mechanism in supramolecular hosts was studied to probe the possible pathways for guest exchange in these polymeric nanogels in Chapter 3. Dynamic exchange of guest molecules, encapsulated in host assemblies, is a phenomenon in supramolecular chemistry that has important implications in several applications. While the mechanism of exchange in micellar assemblies has been previously investigated, the effect of host and guest environment upon the guestexchange dynamics has received little attention, if any. By systematically comparing the behavior of pH-sensitive nanogels along with pH-insensitive nanogels as a control, size, concentration, and hydrophobicity can all play a critical role in guest-exchange dynamics. More importantly, these studies reveal that the dominant mechanism of guest exchange can intimately depend on environmental factors.

Nanocarriers that can be effectively transported across cellular membranes have potential in a variety of biomedical applications. Among these, materials that are capable of changing their surface properties and thus gain entry into a cell, in response to a specific tissue environment, are of particular interest. In Chapter 4, a facile route was designed to prepare nanogels, which generate surface charge with pH as stimulus. This is achieved by designing a polymeric nanogel containing 2-diisopropylamino (DPA) moieties. The pH at which the charge is generated, *i.e.* the isoelectric point (pI) of the nanogel, can be adjusted by varying the percentage of DPA units in the nanogel, its preparation process and crosslinking density. Intracellular delivery of these nanogels was greatly enhanced in an acidic pH environment due to the surface charge generation. This study demonstrates the versatile nature of the nanogels to introduce specific functionalities with relative ease to achieve desired functional behavior.

Photo-crosslinking chemistry has significant importance owing to its advantages, such as no crosslinking agents or reaction catalysts are needed and the photo-crosslinking procedure can be

easily tuned by turning on or off the light. However, the problem is that the de-crosslinking for the current methods always involves the use of high-energy ultra-violet (UV) or visible light, which limits the practical application of these nanocarriers. In Chapter 5, photoinduced heterodisulfide metathesis of pyridyl disulfide (PDS) functionalities is an irreversible reaction. The micelle aggregates based on random copolymer containing PDS can be successfully crosslinked to form polymer nanoparticles based on redox-responsive disulfide bonds. Since the crosslinks generated here are biologically relevant, this method could also have implications in generating new materials of interest in biology and medicine.

This thesis also describes a novel and facile approach to generate well-defined, hollow metal-organic nanoparticles (MOPs) from polymeric organic nanoparticles. In Chapter 6, polymeric organic nanoparticles were prepared through sequential boronate esterification of boronic acids and bifunctional catechols under ambient conditions. The nucleation step involves the cooperative polymerization, wherein the covalent dative interaction between nitrogen in imine and boron center from boronate ester was used as the secondary. In Chapter 7, these polymeric organic nanoparticles based on boronate ester were extended to prepare the hollow MOPs using a simple metal-comonomer exchange process in a single step. The Kirkendall effect has been identified as the underlying mechanism for the formation of these hollow MOPs. This non-reciprocal diffusion process based effect has not been utilized for hollow metal-organic composites, which are of great interest in a variety of applications because of their low density and high surface area.

Finally, in Chapter 8 general conclusions and several future research directions are provided. We hope that our work will have some impact on the design of responsive supramolecular assemblies based on amphiphilic polymers. Our ability to reliably generate organic-inorganic hybrid nanoparticles using polymeric nanostructure templates will open up a fount of opportunities for hybrid materials nanotechnology.

1.5 References

1. Ikkala, O.; ten Brinke, G. Functional materials based on self-assembly of polymeric supramolecules. *Science*, **2002**, *295*, 2407–2409.

2. Janata, J.; Josowicz, M. Conducting polymers in electronic chemical sensors. *Nat. Mater*., **2003**, *2*, 19–24.

3. Zotti, G.; Vercelli, B.; Berlin, A. Monolayers and multilayers of conjugated polymers as nanosized electronic components. *Acc. Chem. Res.*, **2008**, *41*, 1098–1109.

4. Aida, T.; Meijer, E. W.; Stupp, S. I. Functional supramolecular polymers. *Science*, **2012**, *335*, 813–817.

5. Rösler, A.; Vandermeulen, G. W. M.; Klok, H.-A. Advanced drug delivery devices via self-assembly of amphiphilic block copolymers. *Adv. Drug Delivery Rev.*, **2012**, *64*, 270–279.

6. Nakatani, K.; Ogura, Y.; Koda, Y.; Terashima, T.; Sawamoto, M. Sequence-regulated copolymers via tandem catalysis of living radical polymerization and in situ transesterification. *J. Am. Chem. Soc.*, **2012,** *134*, 4373–4383.

7. Hawker, C. J.; Bosman, A. W.; Harth, E. New polymer synthesis by nitroxide mediated living radical polymerizations. *Chem. Rev.*, **2001**, *101*, 3661–3688.

8. Moad, G.; Rizzardo, E.; Thang, S. H. Living radical polymerization by the RAFT process–a third update. *Aust. J. Chem.*, **2012**, *65*, 985–1076.

9. Hilf, S.; Kilbinger, A. F. M. Functional end groups for polymers prepared using ring-opening metathesis polymerization. *Nat. Chem.*, **2009**, *1*, 537–546.

10. Matyjaszewski, K.; Tsarevsky, N. V. Macromolecular engineering by atom transfer radical polymerization. *J. Am. Chem. Soc.*, **2014,** *136*, 6513–6533.

11. Rosebrugh, L. E.; Marx, V. M.; Keitz, B. K.; Grubbs, R. H. Synthesis of highly *cis*, syndiotactic polymers via ring-opening metathesis polymerization using ruthenium metathesis catalysts. *J. Am. Chem. Soc.*, **2013**, *135*, 10032–10035.

12. Kim, J. K.; Yang, S. Y.; Lee, Y.; Kim, Y. Functional nanomaterials based on block copolymer self-assembly. *Prog. Polym. Sci.*, **2010**, *35*, 1325–1349.

13. Zhang, Q.; Ko, N. R.; Oh, J. K. Recent advances in stimuli-responsive degradable block copolymer micelles: synthesis and controlled drug delivery applications. *Chem. Commun.*, **2012**, *48*, 7542–7552.

14. Ge, Z.; Liu, S. Functional block copolymer assemblies responsive to tumor and intracellular microenvironments for site-specific drug delivery and enhanced imaging performance. *Chem. Soc. Rev.*, **2013**, *42*, 7289–7325.

15. Ruzette, A.-V.; Leibler, L. Block copolymers in tomorrow's plastics. *Nat. Mater.*, **2005**, *4*, 19–31.

16. Mai, Y.; Eisenberg, A. Self-assembly of block copolymers. *Chem. Soc. Rev.*, **2012**, *41*, 5969–5985.

17. Kim, H. -C.; Park, S.-M.; Hinsberg, W. D. Block copolymer based nanostructures: materials, processes, and applications to electronics. *Chem. Rev.*, **2009**, *110*, 146–177.

18. Quémener, D.; Davis, T. P.; Barner-Kowollik, C.; Stenzel, M. H. RAFT and click chemistry: A versatile approach to well-defined block copolymers. *Chem. Commun.*, **2006**, *42*, 5051–5053.

19. Wong, C. -H.; Zimmerman, S. C. Orthogonality in organic, polymer, and supramolecular chemistry: from Merrifield to click chemistry. *Chem. Commun.*, **2013**, *49*, 1679–1695.

20. Johnson, J. A.; Lu, Y. Y.; Burts, A. O.; Lim, Y. -H.; Finn, M. G.; Koberstein, J. T.; Turro, N. J.; Tirrell, D. A.; Grubbs, R. H. Core-clickable PEG-branch-azide bivalent-bottle-brush polymers by ROMP: grafting-through and clicking-to. *J. Am. Chem. Soc.*, **2010**, *133*, 559–566.

21. Ryu, J. -H.; Roy, R.; Ventura, J.; Thayumanavan, S. Redox-sensitive disassembly of amphiphilic copolymer based micelles. *Langmuir* **2010**, *26*, 7086–7092.

22. Ryu, J. -H.; Chacko, R. T.; Jiwpanich, S.; Bickerton, S.; Babu R. P.; Thayumanavan, S. Self-cross-linked polymer nanogels: a versatile nanoscopic drug delivery platform. *J. Am. Chem. Soc.*, **2010**, *132*, 17227–17235.

23. Ryu, J. -H.; Jiwpanich, S.; Chacko, R.; Bickerton S.; Thayumanavan, S. Surface-functionalizable polymer nanogels with facile hydrophobic guest encapsulation capabilities. *J. Am. Chem. Soc.*, **2010**, *132*, 8246–8247.

24. Jiwpanich, S.; Ryu, J. -H.; Bickerton, S.; Thayumanavan, S. Noncovalent encapsulation stabilities in supramolecular nanoassemblies. *J. Am. Chem. Soc.*, **2010**, *132*, 10683-10685.

25. Ryu, J. -H.; Bickerton, S.; Zhuang, J.; Thayumanavan, S. Ligand-decorated nanogels: fast one-pot synthesis and cellular targeting. *Biomacromolecules* **2012**, *13*, 1515-1522.

26. González-Toro, D. C.; Ryu, J. -H.; Chacko, R.; Zhuang, J.; Thayumanavan, S. Concurrent binding and delivery of proteins and lipophilic small molecules using polymeric nanogels. *J. Am. Chem. Soc.*, **2012**, *134*, 6964-6967.

27. Rothbard, J. B.; Jessop, T. C.; Lewis, R. S.; Murray, B. A.; Wender, P. A. Role of membrane potential and hydrogen bonding in the mechanism of translocation of guanidinium-rich peptides into cells. *J. Am. Chem. Soc.* **2004**, *126*, 9506−9507.

28. Nakase, I.; Takeuchi, T.; Tanaka, G.; Futaki, S. Methodological and cellular aspects that govern the internalization mechanisms of arginine-rich cell-penetrating peptides. *Adv. Drug Delivery Rev.* **2008**, *60*, 598−607.

29. Matsumoto, N. M.; González-Toro, D. C.; Chacko, R. T.; Maynard, H. D.; Thayumanavan. S. Synthesis of nanogel–protein conjugates. *Polym. Chem.*, **2013**, *4*, 2464-2469.

30. Zhuang, J.; Jiwpanich, S.; Deepak, V. D.; Thayumanavan, S. Facile preparation of nanogels using activated ester containing polymers. *ACS Macro Lett.*, **2012**, *1*, 175−179.

31. Wang, H.; Zhuang, J.; Thayumanavan, S. Functionalizable Amine-Based Polymer Nanoparticles. *ACS Macro Lett.* **2013**, *2*, 948−951.

32. Zhuang, J.; Chacko, R. T.; Amado Torres, D. F.; Wang, H.; Thayumanavan, S. Dual Stimuli-Dual Response Nanoassemblies Prepared from a Simple Homopolymer. *ACS Macro Lett.* **2014**, *3*, 1−5.

33. Yuan, C.; Raghupathi, K.; Popere, B. C.; Ventura, J.; Dai, L.; Thayumanavan, S. Composite supramolecular nanoassemblies with independent stimulus sensitivities. *Chem. Sci.*, **2014**, *5*, 229-234.

34. Maeda, H.; Wu, J.; Sawa, T.; Matsumura Y.; Hori, K. Tumor vascular permeability and the EPR effect in macromolecular therapeutics: a review. *J. Controlled Release*, **2000**, *65*, 271-284.

35. Maeda, H.; Fang, J.; Inutsuka T.; Kitamoto, Y. Vascular permeability enhancement in solid tumor: various factors, mechanisms involved and its implications. *Int. Immunopharmacol.*, **2003**, *3*, 319–328.

36. Raghupathi, K.; Li, L.; Ventura, J.; Jennings M.; Thayumanavan, S. pH responsive soft nanoclusters with size and charge variation features. *Polym. Chem.*, **2014**, *5*, 1737–1742.

CHAPTER 2

EFFECT OF HOFMEISTER IONS ON THE SIZE AND ENCAPSULATION STABILITY OF POLYMER NANOGELS

2.1 Introduction

Inorganic salts have the ability to enhance solubilization or precipitate proteins in an aqueous solution, based on a phenomenon observed by Hofmeister in the late 19th century.[1–3] While biological applications of these findings are well-established,[4–6] its implications in chemical applications are relatively underexplored.[7] For example, it has been shown that addition of salts can significantly alter the lower critical solution temperature (LCST) of water-soluble polymers and that the effect is dependent on the nature of the salt; that is, they follow the Hofmeister series.[8–11] The LCST behavior, or the macroscopic phase separation of the polymer from the aqueous phase, is attributed to the reduced hydrogen bonding driven interaction between water and the polymer at elevated temperatures. While it is well-studied in macroscopic hydrogels and surfaces,[12,13] we do not know of any studies that take advantage of the subtle changes that are likely to occur due to altered hydration or dehydration of functional groups in the presence of Hofmeister ions in nanosized gels. We have been interested in probing this phenomenon, with fine-tuning the size and guest encapsulation stability in oligo(ethylene glycol)-functionalized polymer nanogels as the context.

We hypothesized that although LCST transitions in polymers are often sharp, it is likely that there are also subtle changes in the aggregation states of these polymers at temperatures well below their LCST. Considering that Hofmeister ions could influence LCST, it is also likely that these ions would influence these aggregation states and thus the nanogel itself. We then

envisaged the possibility of tuning the size and the host−guest properties of polymer nanogels by simply varying the nature and concentration of the salt ions in the aqueous solution in which they are prepared (illustrated in Figure 2.1).

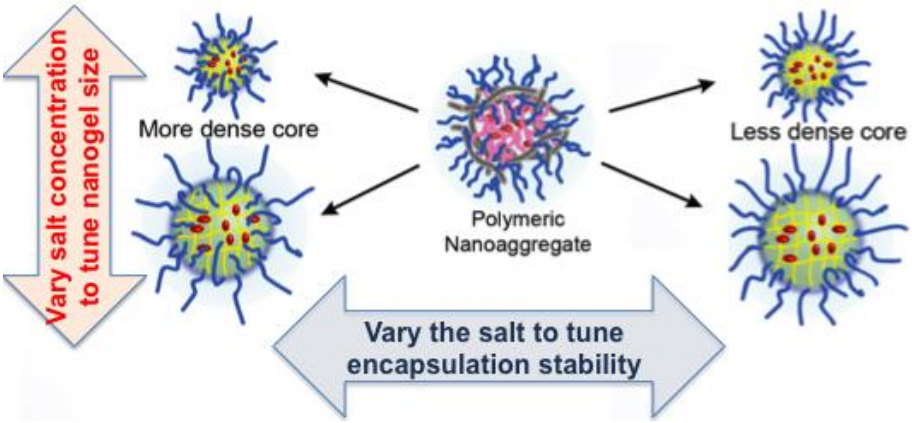

Figure 2.1 Schematic illustration of the possibility of varying size and encapsulation stability in polymeric nanogels using Hofmeister ions.

In this paper, we use a recently reported set of polymer nanogels derived from an amphiphilic random copolymer.[14,15] This polymer precursor was based on a hydrophilic oligo-(ethylene glycol)-functionalized comonomer and a hydrophobic pyridyl disulfide-functionalized comonomer. The key feature here was that the size of the amphiphilic aggregate is fully retained in the chemically crosslinked nanogel, suggesting that there was minimal or no inter-aggregate crosslinking and that the intra-aggregate crosslinking dominated the nanogel formation. This feature made this an ideal system to test our hypothesis for ion-based control over size and guest encapsulation stability in polymer nanogels.

2.2 Results and Discussion

2.2.1 Effect of Hofmeister ions on the LCST of polymers

To investigate the possibilities of size control and encapsulation stability variations by use of Hofmeister ions, it is essential that these polymers do exhibit an LCST behavior. Oligo(ethylene glycol)-based polymers and assemblies have been shown to exhibit LCST, because these

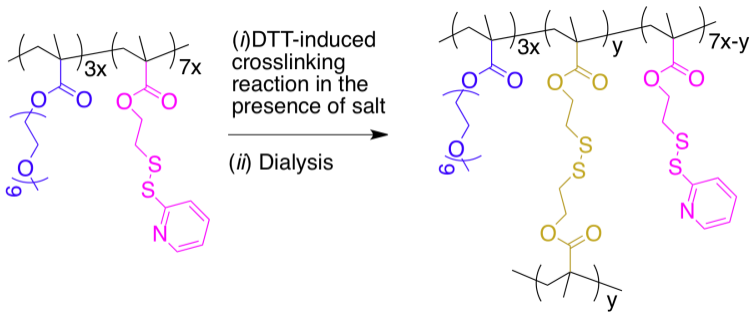

Scheme 2.1 Structure of the polymer and the nanogel containing OEG units.

functionalities can dehydrate at elevated temperatures.[16–19] To probe our polymer nanogel precursor, we first screened the cloud point of a precursor polymer, containing 30% OEG methacrylate and 70% PDS derived methacrylate (Scheme 2.1) in the presence of several salts. We used dynamic light scattering (DLS) at different temperatures to assess the onset of cloud point in the aqueous solution. While variation of cations had no effect on the cloud point (Figure 2.2b), Figure 2.2a shows that the LCST decreases with the addition of anion and LCST trend follows the Hofmeister series $SCN^- > Cl^- > SO_4^{2-}$. Note that one would expect the cloud point to increase in NaSCN, since this is a salting-in chaotropic anion. However, at low SCN^- concentrations, the cloud point onset decreased, relative to water (Figure 2.2a). Nonetheless, there are several indications that this behavior is indeed consistent with the Hofmeister effect on these amphiphilic polymer aggregates: (*i*) This anomalous behavior has been previously observed with chaotropic anions at low salt concentrations due to the pyridine groups in the polymer. The pyridine will be partially quaternized due to the weak acid-base interaction. Thus the ion-pairing between pyridinium cations and anions could screen the electrostatic repulsion inside and among the polymers, thereby promoting the salting-out behavior.[20] To test if our results are consistent with those observations, we tested the cloud point at a much higher salt concentration of 1 M NaSCN (Figure 2.2d). The polymer did exhibit a much higher cloud point temperature, consistent with the salting-in capability of this anion. (*ii*) Increase in concentration of the salt ions affords higher cloud points with chaotropic (salting-in) anions and lower cloud point transitions in

kosmotropic (salting-out) anions (Figure 2.2c, d). (*iii*) Contrary to the effect of high concentrations of SCN^-, polymers precipitate out at ambient temperatures in the presence of a high concentration of salting-out anions (SO_4^{2-}).

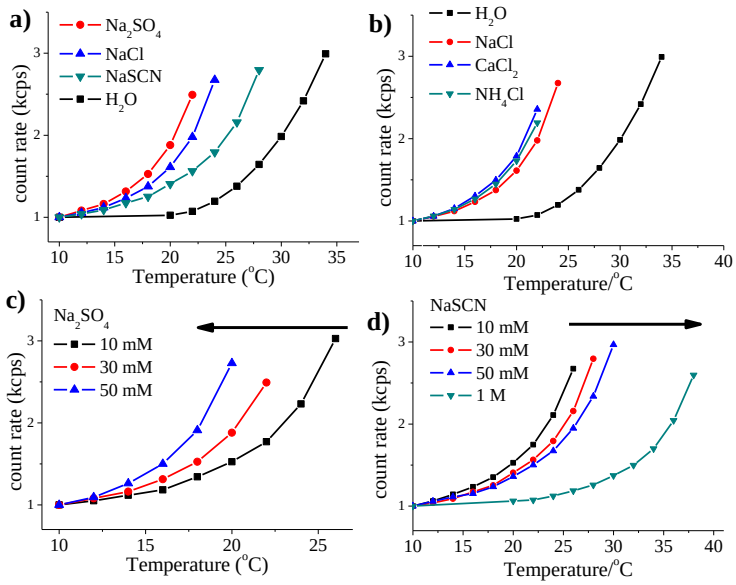

Figure 2.2 (a) LCST trend of polymer in salts with different anions solution, the salt concentration is 30 mM/mL (b) LCST trend of polymer in salts with different cations solution, the salt concentration is 30 mM/mL (c) LCST trend of polymer in Na_2SO_4 solution with different concentrations (d) LCST trend of polymer in NaSCN solution with different concentrations. All the concentration of polymer solution is 10 mg/mL.

2.2.2 Effect of Hofmeister ions on the size of nanogels

Encouraged by these observations, we investigated the possibility of varying the size of the nanogels based on salt concentrations. We have previously observed that the size of the self-crosslinking nanogels, formed from the DTT-induced disulfide exchange, is determined by the size of the amphiphilic aggregate formed in the aqueous phase.[15] Therefore, we hypothesized that the sizes of nanogels made in Na_2SO_4 solution would be larger even below the LCST, since SO_4^{2-} shows the salting-out effect. Indeed, as shown in Figure 2.3 and Table 2.1, the nanogel sizes can be varied systematically from 8 to 24 nm by simply varying the Na_2SO_4 concentration. Also, note that there is a systematic change in the size of the amphiphilic aggregate, which translates to size tunability in the nanogel. At concentrations above 100 mM Na_2SO_4, the polymer precipitated out

of solution. On the other hand, while the size of the aggregate itself did not change, size of the final nanogel increased with NaSCN concentration. We attribute this to the possibility that SCN^- renders the polymer more soluble, which results in less stable aggregates in solution. This loose aggregation could induce interaggregate crosslinking, resulting in larger size of the nanogel. For example, the nanogel size jumped to about 97 nm, while the polymer aggregate was still only about 11 nm.

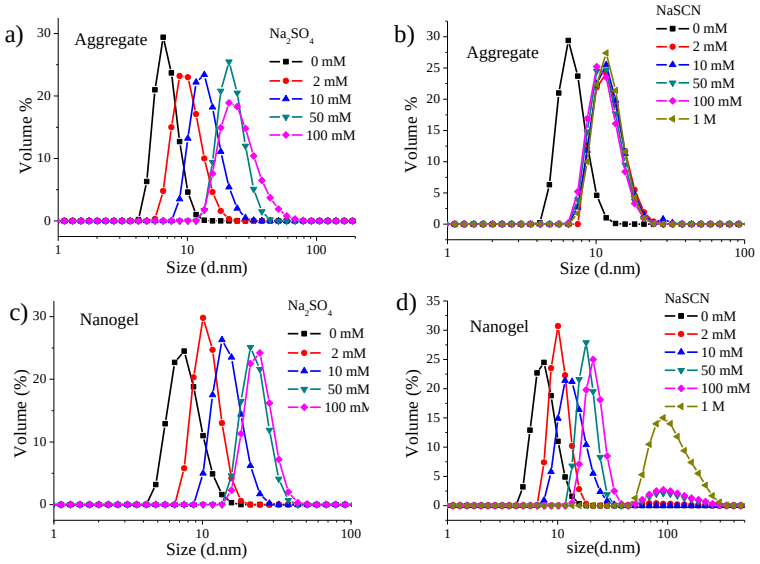

Figure 2.3 Size of polymer aggregates (a) in Na_2SO_4 solution (b) in NaSCN solution; Size of nanogels after dialysis (c) made in Na_2SO_4 solution (d) made in NaSCN solution.

Table 2.1 Sizes of the Polymer Aggregates and Nanogels

Salt	Concentration	Size of polymer aggregates /nm	Size of nanogel /nm
None	0 mM	7 ±0.4	8 ±0.2
Na_2SO_4	2 mM	9 ±0.4	10 ±0.3
	10 mM	13 ±0.3	14 ±0.4
	50 mM	22 ±0.3	22 ±0.4
	100 mM	22 ±0.2	24 ±0.3
NaSCN	2 mM	11 ±0.4	10 ±0.1
	10 mM	11 ±0.3	13 ±0.3
	50 mM	11 ±0.4	19 ±0.5
	100 mM	10 ±0.6	21 ±0.4
	1M	11 ±0.4	97 ±1.0

2.2.3 Effect of Hofmeister ions on the encapsulation stability of nanogels

If the hypotheses suggested above were correct and nanogel sizes increased with salt concentration in both cases, we conceived that it should follow that the guest encapsulation stability of nanogels formed in the presence of kosmotropic anions (Na_2SO_4) should be considerably different from those formed in the presence of chaotropic anions (NaSCN) at similar size and crosslink density. Note that kosmotropic anions would dehydrate the OEG units, making some of these units behave as if they are hydrophobic. These OEG units would be tucked within the hydrophobic interiors of the nanogels during their synthesis. When these nanogels are redistributed in saltless water solution, these OEG units are likely to be rehydrated and present themselves on the surface. This structural reorganization is likely to make the nanogel interior more porous, thus making the nanogels leaky. With NaSCN nanogels, on the contrary, the guest encapsulation stability should increase with salt concentration used during the nanogel preparation.

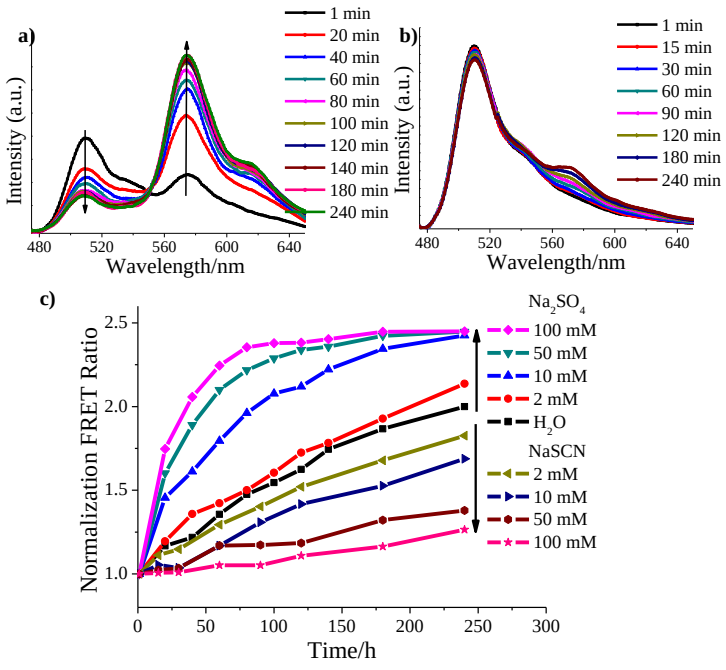

Figure 2.4 Fluorescence emission spectra of mixed NGs encapsulated DiI/DiO, (a) NG made in 100 mM Na_2SO_4(aq), (b) NG made in 100 mM NaSCN(aq). (c) Comparing the dynamics of leakage/interchange of NGs made in different solution.

We used a recently reported fluorescence resonance energy transfer (FRET) based method to measure the leakage coefficient (Λ) and gain insights regarding the guest encapsulation stability in these nanogels.[21] For this purpose, we prepared nanogels at identical crosslink densities (6% crosslinked) containing 1 wt % FRET donor dye (DiO) or FRET acceptor dye (DiI) as the guest molecule at different salt concentrations. Figure 2.4a shows that there is a rapid evolution of FRET with time in the nanogels prepared with Na_2SO_4, compared to those prepared without salt. On the other hand, the nanogels prepared with NaSCN exhibited little change in FRET ratio with time and thus very high encapsulation stability (Figure 2.4b). The extent of encapsulation stability can be systematically tuned. For example, the nanogels made from 2 mM and 100 mM Na_2SO_4 solution exhibited Λ values of 0.0092 and 0.0393 min^{-1}, respectively, while those from NaSCN solutions exhibited Λ values of 0.0034-0.0011 min^{-1} (Figure 2.4c and Table 2.2).

Table 2. 2 Leakage coefficient of nanogels made in different conditions

	Concentration	Λ*/min^{-1}
Pure water	0 mM	0.0057
Na2SO4	2 mM	0.0092
	10 mM	0.0129
	50 mM	0.0227
	100 mM	0.0393
NaSCN	2 mM	0.0034
	10 mM	0.003
	50 mM	0.0016
	100 mM	0.0011

To further test this, we first prepared the nanogels with three different crosslink densities (6%, 13%, and 25%) in salt-free water. We then tested their encapsulation stability directly by monitoring the absorption spectrum of the guest molecule, DiI. Here we measure the leakage and precipitation of the dye molecule, instead of the dynamic exchange of the dye molecule. Since the nanogel is already prepared in water, the solution that contains Na_2SO_4 should dehydrate the

exposed OEG groups, thus rendering the nanogel less leaky. On the contrary, NaSCN should render the nanogels more leaky, because more OEG units will be hydrated and become more exposed to the solvent, thereby leaving the core of the nanogel less dense. Indeed, Figure 2.5 shows that this is indeed the case. In all three nanogels, there is no leakage of the dye molecules in the presence of Na_2SO_4. However, the 6% and 13% crosslinked nanogels were leaky in the presence of NaSCN, while the 25% crosslinked one encapsulates the guest molecule sufficiently tightly that it was unperturbed by the presence of the SCN^- anions. A similar trend was observed for the nanogels with DiO as the guest molecule (Figure 2.5).

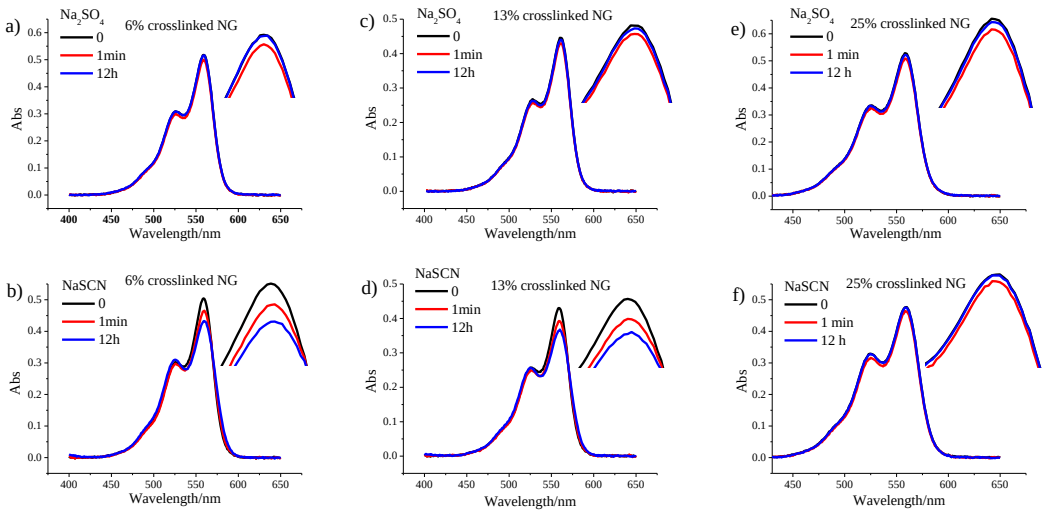

Figure 2.5 Absorbance of the nanogel loaded with DiI after the addition of Na_2SO_4 or NaSCN. Nanogel was made in salt free water, and concentration of both the measured nanogel solutions is 0.2 mg/mL. (a-b) Nanogels with 6% crosslinking degree, (c-d) Nanogels with 13% crosslinking degree, (e-f) Nanogels with 25% crosslinking degree.

We rationalize the above results on the basis of salt dependent dehydration or rehydration of the OEG units: NaSCN would rehydrate the OEG units and thus render any buried OEG units to be presented at the surface. This rehydration should leave behind a relatively hollow interior. To further test this possibility, we investigated the nanogels by atomic force microscopy (AFM). If Na_2SO_4 and NaSCN dehydrate and rehydrate the nanogels, respectively, then the density of the nanogel from the former salt should be denser. If this were the case, it is possible that the

nanogels are more rigid in the presence of Na_2SO_4 and therefore would not collapse on a solid surface. On the other hand, NaSCN should cause these nanogels to collapse on the surface. We examined this possible difference via AFM height images. Figure 2.6b shows the height profile obtained from these nanogels in the presence of Na_2SO_4. Although they are obtained from the same sample, the height of the nanogels is greater in the presence of Na_2SO_4 (Figure 2.6b) and lesser in the presence of NaSCN (Figure 2.6c), compared to the salt-free nanogels (Figure 2.6a). In addition to the height images in Figure 2.6, more quantitative analyses of the heights of the nanogels in these images are shown in the Figure 2.7. These results support our hypotheses that Na_2SO_4 rigidifies the nanogels and NaSCN loosens the nanogels, due to the differential hydration of the OEG units.

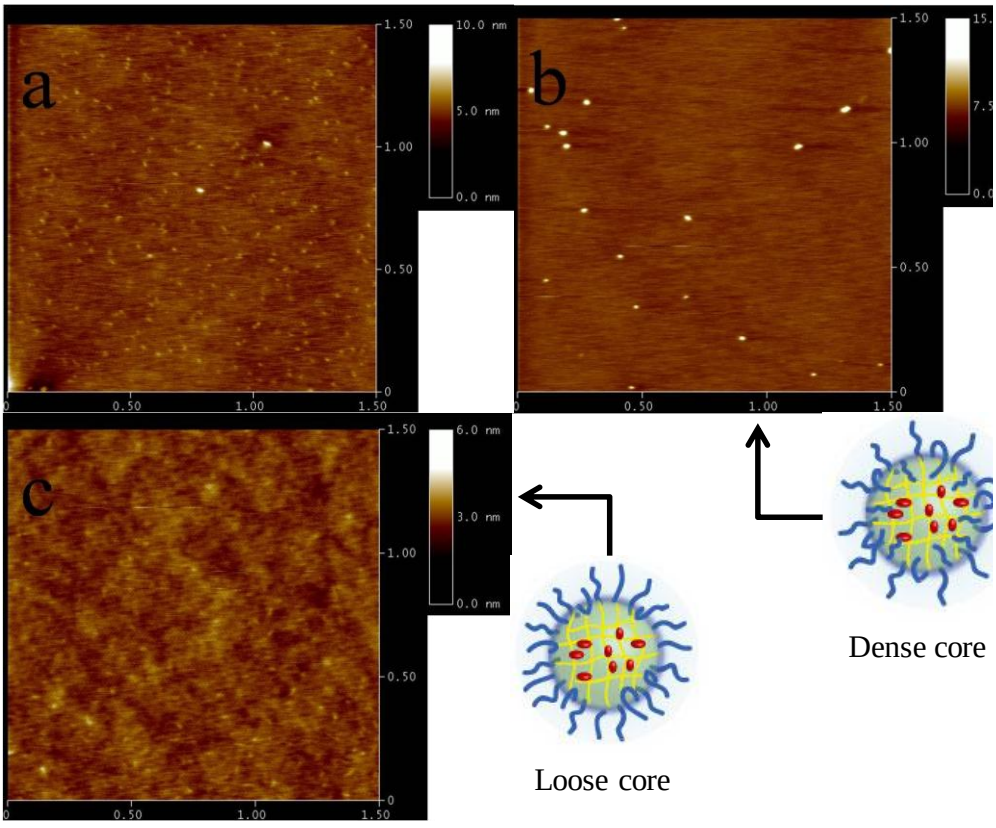

Figure 2.6 Change in morphology of the nanogels due to the presence of salts (a) nanogel without salts (b) nanogel after adding Na_2SO_4 (c) nanogel after adding NaSCN from AFM(height mode).

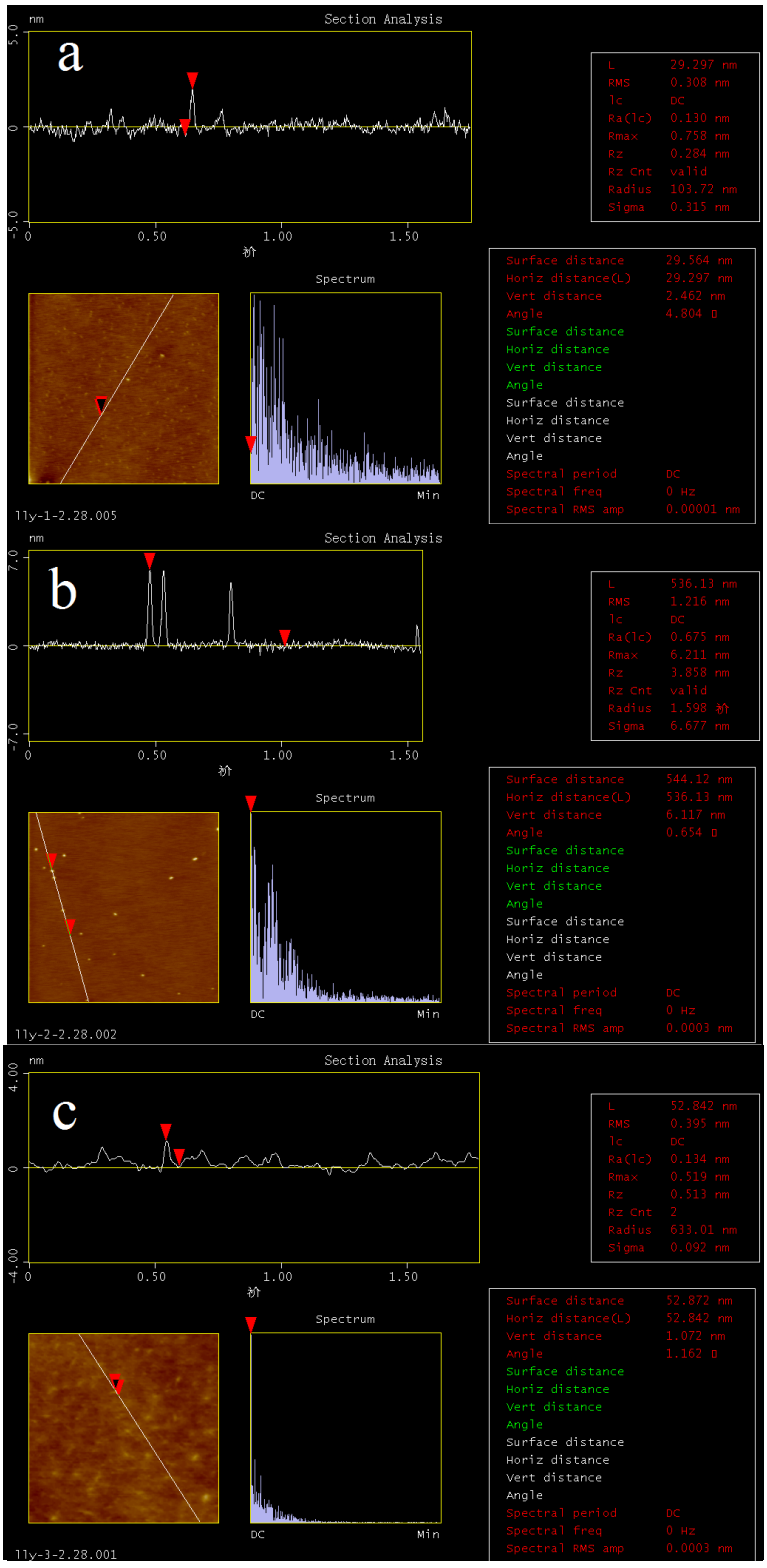

Figure 2.7 Analysis of the nanogel AFM height images of the nanogels (a) in the absence of salt (b) in the presence of Na_2SO_4 (c) in the presence of NaSCN.

2.2.4 Effect of Hofmeister ions on the release behavior of nanogels

Finally, we tested the relative release rate of the guest molecules from nanogels prepared under different salt conditions in the presence of a stimulus. Note that the disulfide bonds, which form crosslinked network inside nanogels, make them susceptible to an uncrosslinking reaction in the presence of glutathione (GSH). This led us to test whether the nanogels prepared under various salt conditions would exhibit differential guest release rates in the presence of GSH. For this, we prepared a series of nanogels in the presence of 30 mM Na_2SO_4, NaOAc, NaCl, or NaSCN. All nanogels were prepared at 25% crosslink density to ensure significant guest encapsulation stability in the absence of GSH, and the loading of DiI was 1 wt %. When these nanogels were subjected to 10 mM GSH concentration, the release rates observed were indeed consistent with the Hofmeister series, which followed the order Na_2SO_4> NaOAc > NaCl > no salt > NaSCN, as shown in Figure 2.8.

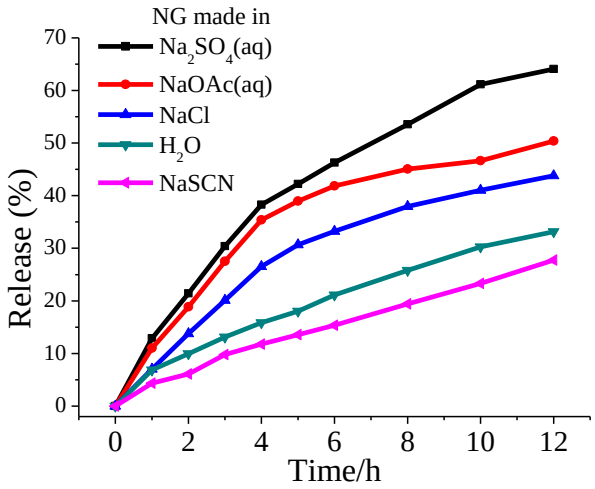

Figure 2.8 GSH-induced (10mM) DiI release rate from the nanogels made in different salt solutions.

2.3 Summary

In summary, we have demonstrated the following: (*i*) There are subtle differences in the aggregation states of OEG-functionalized amphiphilic polymers in aqueous phase, endowed by

the presence of various salts. (*ii*) While anions provide variations as predicted by the Hofmeister effect, variation in cations does not affect the aggregation of the polymer. (*iii*) In the case of kosmotropic SO_4^{2-}, the size of the nanogel can be systematically varied with concentration, since the size is determined by the aggregate size. (*iv*) In the case of chaotropic anion SCN^-, interaggregate crosslinking occurs due to the rather loose nature of the aggregates. (*v*) Encapsulation stability of guest molecules is dependent on the nature of the salt used for preparation of the nanogels; chaotropic anions afford nanogels with greater guest encapsulation stability. (*vi*) Salt-dependent hydration of the OEG units in the nanogel causes variations in density, which then determine the leaky character of the nanogel. From a practical perspective, utilizing Hofmeister ions provides unprecedented control in fine-tuning the size of the polymer nanogel. In addition to size, we have concurrent control over altering the guest encapsulation stabilities. These studies not only have practical applications in areas such as drug delivery and sensing but also have fundamental implications in the future design and syntheses of polymer nanoassemblies and nanoparticles.

2.4 Experimental

2.4.1 General

2,2′-Dithiodipyridine, 2-mercaptoethanol, poly(ethylene glycol) monomethyl ether methacrylate (MW 450), D,L-dithiothreitol (DTT), 1,1′-dioctadecyl-3,3,3′,3′-tetramethylindocarbocyanine perchlorate (DiI), 3,3′-dioctadecyloxacarbocyanine perchlorate (DiO), 4-cyano-4-(phenylcarbonothioylthio)pentanoic acid, and other conventional reagents were obtained from commercial sources and were used as received, unless otherwise mentioned. Pyridyl disulfide ethyl methacrylate (PDSEMA) was prepared by a previously reported procedure.[22] ^{1}H NMR spectra were recorded on a 400 MHz Bruker NMR spectrometer with the residual proton resonance of the solvent as the internal standard. Chemical shifts are reported in parts per million (ppm). Molecular weights of the polymers were estimated by gel-permeation

chromatography (GPC) with a refractive index detector, with poly(methyl methacrylate) (PMMA) as a standard . Dynamic light scattering (DLS) measurements were performed on a Malvern Nanozetasizer. UV−visible absorption spectra were recorded on a Varian (model EL 01125047) spectrophotometer. Fluorescence spectra were obtained from a Jasco FP-6500 spectrofluorometer. Atomic force microscopy (AFM) images were collected on a Digital Instruments Nanoscope III in tapping mode under ambient conditions by use of silicon cantilievers (spring constant 0.58 N/m).

2.4.2 Synthesis of Random Copolymer.

Polymers were prepared by reversible addition−fragmentation chain transfer (RAFT) polymerization. A mixture of 4-cyano-4-(phenylcarbonothioylthio)pentanoic acid (3.0 mg, 0.02 mmol), PDSEMA (1.25 g, 4.9 mmol), poly(ethylene glycol) monomethyl ether methacrylate (1.0 g, 2.1 mmol), and 2,2′-azobis(isobutyronitrile) (AIBN; 2.5 mg, 0.014 mmol) was dissolved in tetrahydrofuran (THF) (5 mL) and degassed by performing three freeze−pump−thaw cycles. The reaction mixture was sealed and then transferred into a preheated oil bath at 65 ℃ for 10 h. To remove unreactive monomers, the resultant mixture was precipitated in cold ethyl ether (20 mL) to yield the random copolymer as a waxy liquid. GPC (THF) M_n, 13 kDa; polydispersity, 1.3. ^{1}H NMR (400 MHz, $CDCl_3$) δ 8.46, 7.68, 7.11, 4.35-4.09, 3.94-3.37, 3.03, 2.04-1.64, 1.43-0.87. The molar ratio between two blocks was determined by integrating the methoxy proton in the poly-(ethylene glycol) unit and the aromatic proton in the pyridine and was found to be 3:7 (PEO:PDSEMA).

2.4.3 Synthesis of Nanogels Containing DiI/DiO.

As shown in Scheme 1, the polymer (10 mg) was dissolved in 1 mL of water or salt solution. A 0.02 mL DiI stock solution (5 mg/mL) or 0.04 mL DiO stock solution (2.5 mg/mL) in acetone was added into the polymer solution. The mixture was stirred overnight at room temperature, open to the atmosphere to allow the organic solvent to evaporate. Then, to control the

crosslinking density of nanogel (6%, 13%, and 25% by molar equivalents), a measured amount of DTT (0.4, 0.8, and 2.0 μmol for 10, 20, and 50 mol % against PDS groups, respectively) was added. After 4 h of stirring, any insoluble DiI/DiO residue was removed by filtration and pyridothione was removed from the nanogel solution by extensive dialysis through a membrane with a molecular weight cutoff of 7000 g/mol.

2.4.4 Dynamic Light Scattering Measurement.

Dynamic light scattering experiments were performed by using a Malvern Nanozetasizer. The scattered light is detected at an angle of 173 °. For cloud point measurement, the polymer (10 mg/mL) in water or salt solution was used. The temperature was increased from 10 to 60 ℃ in 2 ℃ increments. Equilibration time at each temperature was 10 min. Above the LCST, the polymer chains collapse into a globule and produce a more compressed particle with a higher refractive index, so scattering intensity was monitored as a function of temperature to determine the LCST behavior of polymer solution. For size distribution measurement, we used the polymer (10 mg/mL) or nanogel (1 mg/mL) solution in water or each salt solution, which contains a specific salt concentration. The measurement was kept constant at 25 ℃ throughout the experiment. Dust was eliminated by filtering the solution through 0.45 μm membrane filter. Nanogel Encapsulated Dye Mixing. A solution of nanogel containing DiI (100 μL) was mixed with a solution of nanogel containing DiO (100 μL) in a cuvette, and then Milli-Q water (800 μL) was added to adjust the volume. The fluorescence intensity was recorded (λ_{exc} = 450 nm).

2.5 References

1. Hofmeister, F. On the understanding of the effects of salts, second report. On irregularities in the precipitating effect of salts and their relationship to their physical behavior. *Arch. Exp. Pathol. Pharmocol.* **1888**, 24, 247-260.

2. Von Hippel, P. H.; Wong. K. Y. Neutral salts: the generality of their effects on the stability of macromolecular conformations. *Science* **1964**, 145, 577-580.

3. Baldwin, R. L. How Hofmeister ion interactions affect protein stability. *Biophys. J.* **1996**, 71, 2056-2063.

4. Arakawa, T.; Timasheff, S. N. Preferential interactions of proteins with salts in concentrated solutions. *Biochem*istry. **1982**, 21, 6545-6552.

5. Pinna, M. C.; Bauduin, P.; Touraud, D.; Monduzzi, M.; Ninham, B. W.; Kunz, W. Hofmeister effects in biology: effect of choline addition on the salt-induced super activity of horseradish peroxidase and its implication for salt resistance of plants. *J. Phys. Chem. B*, **2005**, 109, 16511-16514.

6. Nostro, P. L.; Ninham, B. W. Hofmeister phenomena: an update on ion specificity in biology. *Chem. Rev*. **2012**, 112, 2286-2322.

7. Zhang, Y. J.; Cremer, P. S. Chemistry of Hofmeister anions and osmolytes. *Ann. Rev. Phys. Chem.* **2010**, 61, 63-83.

8. Zhang, Y. J.; Furyk, S.; Bergbreiter, D. E.; Cremer, P. S. Specific ion effects on the water solubility of macromolecules: PNIPAM and the Hofmeister Series. *J. Am. Chem.Soc.* **2005**, 127, 14505–14510.

9. Magnusson, J. P.; Khan, A.; Pasparakis, G.; Saeed, A. O.; Wang, W. X.; Alexander, C. Ion-sensitive isothermal responsive polymers prepared in water. *J. Am. Chem. Soc.* **2008**, 130, 10852–10853.

10. Suwa, K.; Yamamoto, K.; Akashi, M.; Takano, K.; Tanaka, N.; Kunugi, S. Effects of salt on the temperature and pressure responsive properties of poly(N-vinylisobutyramide) aqueous solutions. *Colloid Polym. Sci.* **1998**, 276, 529-533.

11. Zhang, Y.; Furyk, S.; Sagle, L. B.; Cho, Y.; Bergbreiter, D. E.; Cremer, P. S. Effects of Hofmeister anions on the LCST of PNIPAM as a function of molecular weight. *J. Phys. Chem. C.* **2007**, 111, 8916-8924.

12. He, Y.; Shao, Q.; Chen, S. F.; Jiang, S. Y. Water mobility: a bridge between the Hofmeister series of ions and the friction of zwitterionic surfaces in aqueous environments. *J. Phys. Chem. C.* **2011**, 115, 15525–15531.

13. Swann, J. M. G.; Bras, W.; Topham, P. D.; Howse, J. R.; Ryan, A. J. Effect of the Hofmeister anions upon the swelling of a self-assembled ph-responsive hydrogel. *Langmuir* **2010**, 26, 10191–10197.

14. Ryu, J. -H.; Jiwpanich, S.; Chacko, R.; Bickerton, S.; Thayumanavan, S. Surface-functionalizable polymer nanogels with facile hydrophobic guest encapsulation capabilities. *J. Am. Chem. Soc.* **2010**, 132, 8246-8247.

15. Ryu, J. -H.; Chacko, R. T.; Jiwpanich, S.; Bickerton, S.; Babu, R. P.; Thayumanavan, S. Self-cross-linked polymer nanogels: a versatile nanoscopic drug delivery platform. *J. Am. Chem. Soc.* **2010**, 132, 17227-17235.

16. Lutz, J. -F. Thermo-switchable materials prepared using the OEGMA-platform. *Adv. Mater.* **2011**, 23, 2237-2243.

17. Lutz, J. F.; Akdemir, O.; Hoth, A. Point by point comparison of two thermosensitive polymers exhibiting a similar LCST: is the age of poly(NIPAM) Over? *J. Am. Chem. Soc.* **2006**, 128, 13046-13047.

18. Qin, S.; Geng, Y.; Discher, D. E.; Yang, S. Temperature-controlled assembly and release from polymer vesicles of poly(ethylene oxide)-*block*- poly(*N*-isopropylacrylamide). *Adv. Mater.* **2006**, 18, 2905-2909.

19. Aathimanikandan, S. V.; Savariar, E. N.; Thayumanavan, S. Temperature-sensitive dendritic micelles. *J. Am. Chem. Soc.* **2005**, 127, 14922-14929.

20. Liu, X. Y.; Mu, X. R.; Liu, Y.; Liu, H. J.; Chen, Y.; Cheng, F.; Jiang, S. C. Hyperbranched polymers with thermoresponsive property highly sensitive to ions. *Langmuir* **2012**, 10, 4867-4876.

21. Jiwpanich, S.; Ryu J. -H.; Bickerton S.; Thayumanavan S. Noncovalent encapsulation stabilities in supramolecular nanoassemblies. *J. Am. Chem. Soc.* **2010**, 132, 10683–10685.

22. Ghosh, S.; Basu, S.; Thayumanavan, S. Simultaneous and reversible functionalization of copolymers for biological application. *Macromolecules* **2006**, 39, 5595-5597.

CHAPTER 3

ENVIRONMENT-DEPENDENT GUEST EXCHANGE IN SUPRAMOLECULAR HOSTS

3.1 Introduction

Nanocontainers that can bind and hold hydrophobic molecules have attracted significant interest due to implications in areas such as self-healing materials and drug delivery.[1−3] Among the factors that are taken into account while arriving at a molecular design for these containers, encapsulation stability is often considered a critical one.[4,5] Encapsulation itself is often defined by the loading capacity of the host, *i.e.*, the amount of guest molecule that a host assembly can hold. This capacity is dictated by the thermodynamic distribution coefficient of the guest molecule between the host and the solvent.[6−8] A feature that has not received much attention involves the guest exchange dynamics. This is important, as this is a direct and arguably the most rigorous indicator of encapsulation stability of a host assembly.[9] Considering the diversity of the environments that a supramolecular assembly encounters in a typical biological system, it is important that we understand the influence of these external environmental factors upon encapsulation stability. In this paper, we show that the mechanism of guest-exchange dynamics and thus the factors that affect encapsulation stability can greatly vary with environmental changes.

Three limiting scenarios exist for the mechanism of guestexchange: (*i*) collision−exchange−separation mechanism, (*ii*) exit−re-entry mechanism, and (*iii*) fission−recombination mechanism.[10−16] The first mechanism is collision-based, where the guest exchange occurs only because of a collision between two host assemblies. The rate of this process mostly depends on the effective collision frequency. The second pathway is diffusion-based,

where the guest-exchange rate depends on the ability of guest to exit and enter from the host assemblies. The third mechanism involves fragmentation of the host assembly into two smaller entities as the first step, followed by a recombination to regain the original host assembly. To simplify the possibilities, we chose to use host assemblies that are based on cross-linked polymer nanogels, which do not lend themselves to the third possibility. The cross-linking feature of nanogels obviates the fission possibility, and thus, the third mechanism can be ruled out in this case. The two viable pathways for the host assembly are illustrated in Figure 1. Between these pathways, although the kinetic orders of these mechanisms are different, it is difficult to quantify the order of a molecular exchange process, as this is not a chemical reaction. Here, we design a series of experiments to probe the possible pathways for guest exchange in these polymeric nanogels.

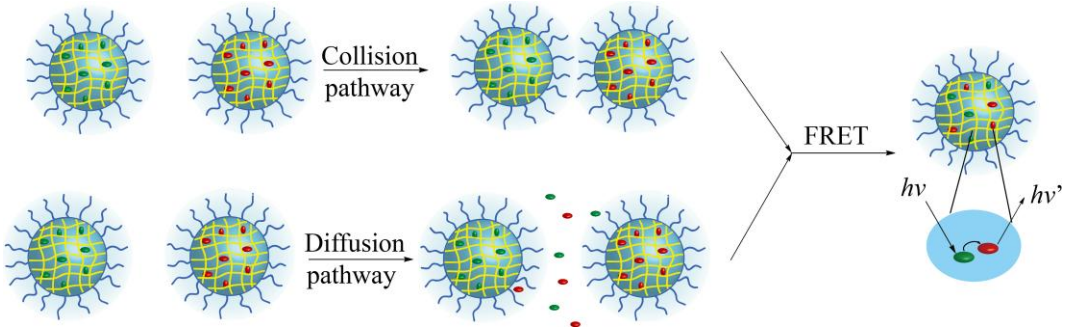

Figure 3.1 Schematic representation of two possible mechanisms for guest-exchange between cross-linked nanogels. a) Collision-Exchange-Separation Mechanism, also called as Collision- based mechanism b) Exit-Re-entry Mechanism, also called as Diffusion-based mechanism.

We use the recently reported fluorescence resonance energy transfer (FRET) as the tool to interrogate the guest-exchange process,[17] which has proved to be quite a robust method for a variety of host-guest assemblies.[18–25] Briefly, a hydrophobic FRET pair, 3,3′-dioctadecyloxacarbocyamine perchlorate (donor) and 1,1′-dioctadecyl-3,3,3′,3′-tetramethylindocarbocyanine perchlorate (acceptor), were independently encapsulated in otherwise similar nanogel hosts. When these solutions were mixed, the emission spectrum of the

mixed solution in response to donor excitation at 450 nm was monitored over time. No FRET would be observed if the two dye molecules are stably encapsulated and continue to be in their separate nanocontainers, since the distance between the two dye molecules is much higher than their Förster radii. On the other hand, if the guest exchange between the host and its surroundings was significant, the extent of FRET would evolve, as the guest composition in the nanogel changes over time.

3.2 Results and Discussion

3.2.1 Design and synthesis of nanogels

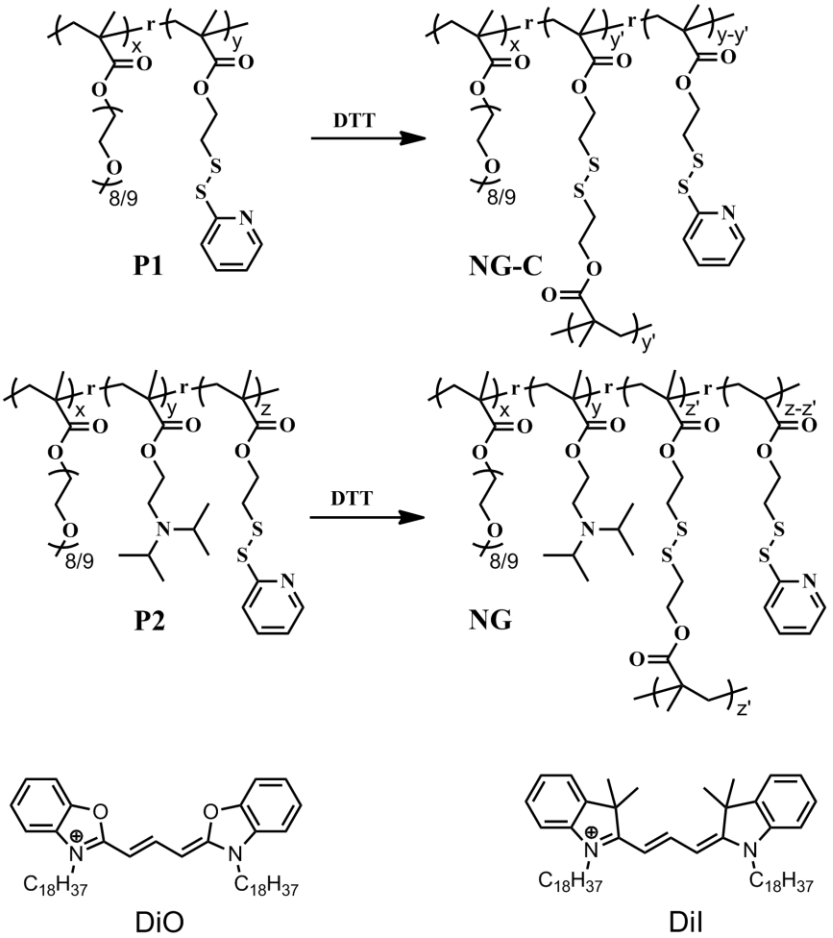

Scheme 3.1 Structure of polymers **P1** and **P2**; nanogels **NG-C** and **NG**; and the dye molecules DiO and DiI.

Two cross-linked polymeric nanogels were used in this study. The first nanogel (NG-C) is based on a random copolymer (P1), formed from a hydrophilic oligoethylene glycol (OEG) functionalized methacrylate monomer and a hydrophobic pyridyl disulfide (PDS) functionalized methacrylate monomer (Scheme 3.1). The second nanogel (NG) and its precursor (P2) contain a diisopropylamine (DPA) functionalized methacrylate as a comonomer in addition to the OEG- and the PDSfunctionalized monomers.[26] The size of these two types of nanogels at neutral pH was found to be very similar (Figure 3.2).

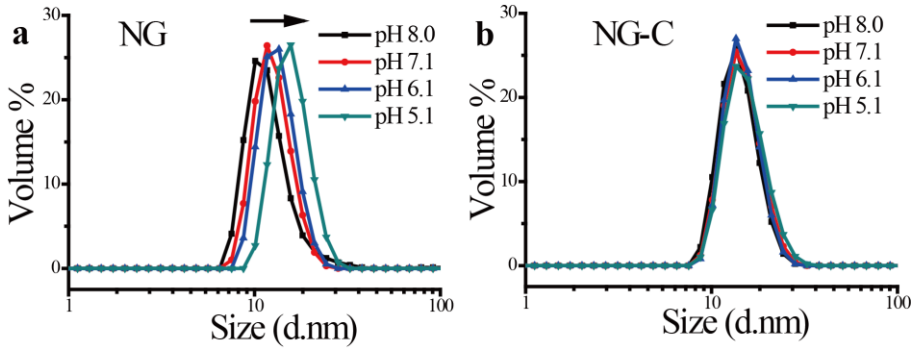

Figure 3.2 Size distribution of nanogel at different pH values via DLS measurements. a) **NG** with 30% crosslinking density, b) **NG-C** with 20% crosslinking density.

3.2.2 Collision-based mechanism for control nanogels NG-C

First, we were interested in understanding the mechanism of guest exchange in the control nanogel NG-C, which is not sensitive to the external environment, as this provides the baseline for our study. Among the collision- and diffusion-based pathways, the former pathway should clearly depend on the concentration of the nanogel. One would expect strong and positive correlations between the collision frequency and the concentration of nanogels in solution. We used the FRET based method, which provided a measure of the dye exchange rate in the form of the leakage coefficient (Λ), which can be obtained as the initial slope of the linear fit (earlier four points in the linear regime) by plotting the FRET ratio $I_a/(I_a + I_d)$ against time, where I_a and I_d are the fluorescence intensities of the acceptor (DiI) and the donor (DiO) respectively. The

concentrations of the nanogels were varied as 0.05, 0.10, and 0.15 mg/mL for both NG-C containing DiI and NG-C containing DiO at pH 7.1. Figure 3.3c shows that there was indeed a faster evolution of FRET with time in the nanogels with a concentration of 0.15 mg/mL, compared to those with a concentration of 0.05 mg/mL (Figure 3.3a) and 0.10 mg/mL (Figure 3.3b). Λ values of 0.0192, 0.0284, and 0.0315 min^{-1} were observed for the concentrations of 0.05, 0.1, and 0.15 mg/mL, respectively, indicating that the guest exchange between nanogels indeed increased with increasing concentration (Figure 3.3d). These data provide the initial evidence that the guest exchange in these control nanogels happens via the collision-based mechanism as the dominant pathway.

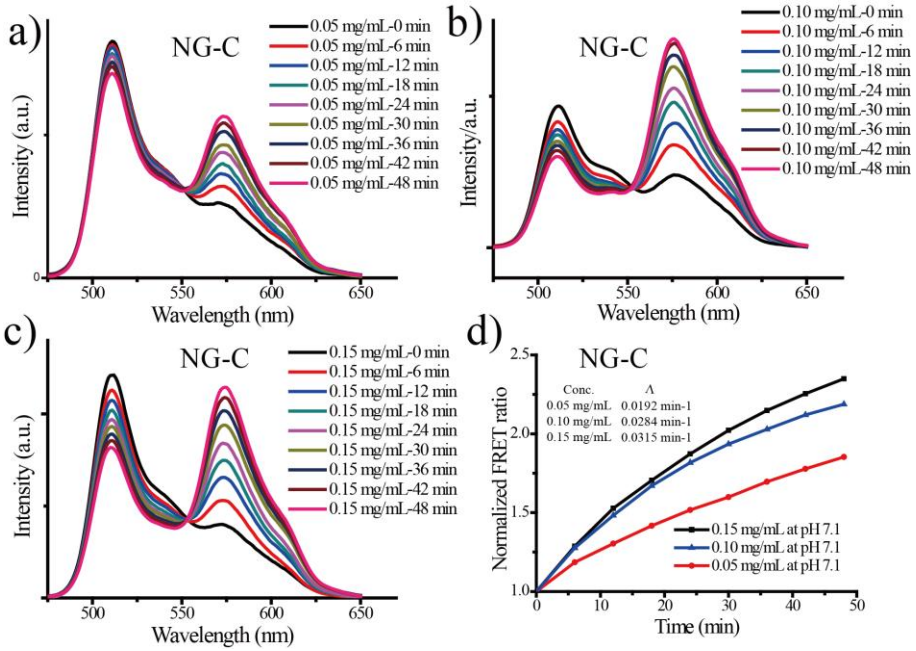

Figure 3.3 Fluorescence evolution when **NG-C** containing DiI and DiO are mixed in solutions at pH 7.1. a) 0.05 mg/mL, b) 0.10 mg/mL, c) 0.15 mg/mL. d) Comparison of the dynamics of guest-exchange between **NG-C** with different concentration at pH 7.1.

3.2.3 pH-dependent guest-exchange mechanism

Additionally, the size of the nanogel would also impact guest exchange, if the collision-based mechanism was the dominant mechanism for guest exchange, since the collision frequency

would be affected by the size of nanogels. The pH-sensitive nature of the DPA moieties endows NG with pH-dependent size variations in this nanogel. The size of NG increases with decreasing pH, while the size of NG-C does not change with pH (Figure 3.2). Figure 3.2a shows that the sizes of NG increased from 10 to 18 nm when the pH changed from 8.0 to 5.1. The observed size increase in NG is attributed to the protonation of the DPA units, which presumably results in the swelling of the nanogels due to electrostatic repulsion between these positively charged DPA groups inside. As the size of NG varies with pH, we expected that the dye-exchange rate would also change with the pH.

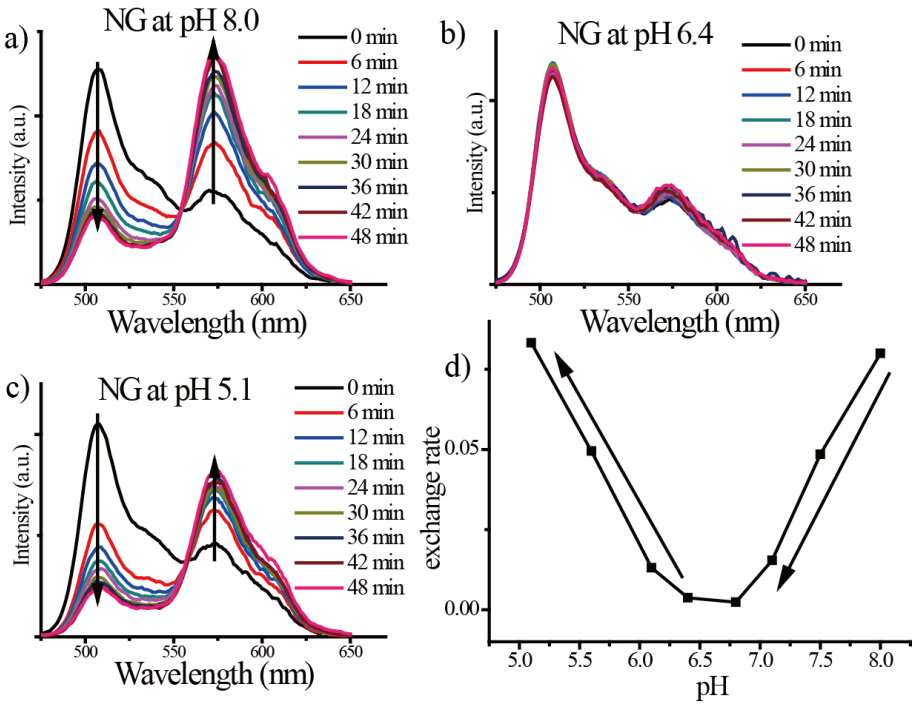

Figure 3.4 Fluorescence evolution when **NG** containing DiI and DiO are mixed in solutions at different pH values. a) pH 8.0, b) pH 6.4, c) pH 5.1. d) Guest-exchange rates between **NG** at different pH values. The concentration of each nanogel was 0.10 mg/mL.

Table 3. 1 Leakage coefficient (min^{-1}) of 0.10 mg/mL NG of at different pH values.

pH 5.1	0.0833	pH 6.8	0.0023
pH 5.6	0.0495	pH 7.1	0.0154
pH 6.1	0.0131	pH 7.5	0.0485
pH 6.4	0.0037	pH 8.0	0.08

Figure 3.4a shows that there is a rapid evolution of FRET with time for NG at pH 8.0. On the other hand, NG at pH 6.4 exhibits little change in FRET ratio with time and thus shows very slow dye exchange (Figure 3.4b). Thus, the exchange rate indeed decreased from a Λ value of 0.080 min^{-1} at pH 8.0 to 0.004 min^{-1} at pH 6.4 (Figure 3.4d and table 3.1). These results are consistent with the collision-based mechanism, as the size of NG indeed affected the rate of guest exchange, providing further evidence that the dominant guest exchange in nanogels might happen via the collision-based mechanism. It should be noted, however, that while the collision frequency is expected to decrease with increase in size, because of the slower diffusion (via the Stokes−Einstein equation), it is also known that the collision frequency can increase with an increase in size.[27] One possible explanation is that the number of effective collisions, *i.e.*, collisions that result in guest exchange, decrease with an increase in size. This is reasonable, as the effect of the reduced diffusion could potentially reduce the effective collisions. This explanation is consistent with the results but remains provisional, as there are no established quantitative relationships to this effect at this point.

Interestingly, however, an unexpected change in the FRET evolution occurs below pH 6.4, even though the size-increase is observed through the entire pH range from 8.0 to 5.1. From pH 6.4 to 5.1, the FRET evolution was found to increase (Figure 3.4c). Figure 3.4d shows that the exchange rate systematically increases with decreasing pH from 6.4 to 5.1. The Λ value of 0.004 min^{-1} at pH 6.4 increased back to 0.083 min^{-1} at pH 5.1 (table 3.1). Since the size of the nanogel increases with decreasing pH, including at this pH range, these results are not consistent with the collision-based mechanism. Therefore, it is possible that the diffusion-based pathway is the dominant operating mechanism in this scenario, providing the first indication that there might be an environment-dependent change in mechanism. However, a few alternating possibilities need to be considered prior to reaching this conclusion.

First, it is possible that the dye molecules themselves have a certain pH-dependent solubility

and thus is affecting the guest molecule exchange in the collision state. To test this possibility, we investigated the pH-dependence of guest-exchange dynamics in NG-C, where the size of the nanogel does not change with pH. Figure 3.5a,b shows that there was indeed similar evolution of FRET with time in the nanogels at pH 8.0 and 7.1, while a slightly faster FRET evolution was observed at pH 6.1 (Figure 3.5). We attribute the small pH-dependence to the possibility that the solubility of DiI and DiO molecules may vary at different pH values. The solubility may be improved a bit at low pH due to the presence of tertiary amine (Scheme 3.1), leading to easier dye exchange during the collision. Note that we do not observe any significant dye loss in the nanogel during our FRET experiments, which suggests that the repulsion between these positively charged dyes and protonated NG at lower pH might be very small. Two features are noteworthy in these results: first, the magnitude of difference in exchange dynamics is too small compared to those observed with NG and, therefore, does not account for the results observed with NG. Second, the guest-exchange kinetics continues to increase with pH and there is no change in the trend after pH 6.4. These results suggest that the results observed in NG are not due to the inherent difference in dye molecule behavior at different pH values.

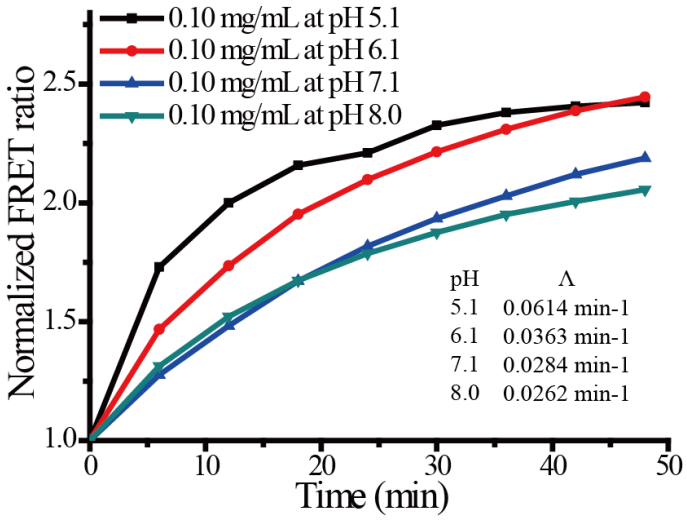

Figure 3.5 Comparison of the dynamics of guest-exchange between **NG-C** with 0.10 mg/mL at different pH values.

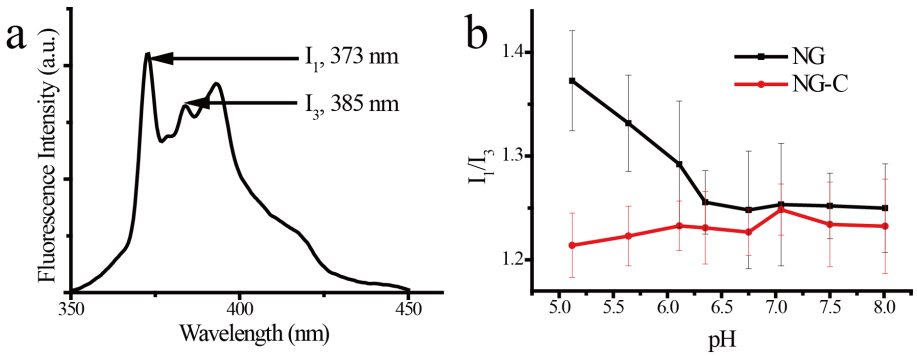

Figure 3.6 Effect of pH on the hydrophobicity. a) Fluorescence emission spectrum measured for nanogel **NG-C** loading 2 wt% pyrene and b) calculated I_1/I_3 ratios for nanogels at different pH values, (black, **NG**; red, **NG-C**).

We hypothesized next that the observed change in pH dependence trend at pH 6.4 could perhaps be explained by a change in the hydrophobicity of the nanogel interior, i.e., the host properties. It is reasonable to anticipate that the protonation of DPA groups would decrease the hydrophobicity of the nanogel.[28] Pyrene's fluorescence properties are greatly dependent on its microenvironment.[29, 30] Specifically, the ratio of the intensities between the first and the third peaks (I_1/I_3) in the pyrene emission spectrum can be used to determine the polarity of the dye's microenvironment. The value of this ratio can range from 1.9 in polar solvents to 0.6 in certain hydrocarbon solvents. We utilized this dye as the guest molecule to probe the hydrophobicity of the microenvironment within the nanogel interiors. Aqueous buffer solutions of NG containing 2 wt% pyrene were prepared for this purpose at different pH values. A sample fluorescence spectrum of nanogel is shown in Figure 3.6a. The hydrophobicity of nanogel at different pH values was studied by calculating the intensity ratio of the first and third emission peaks of pyrene, commonly referred to as the I_1/I_3 ratio. Figure 3.6b shows the variations in I_1/I_3 of pyrene encapsulated in NG at different pH values. When the pH was reduced from 8.0 to about 6.4, the I_1/I_3 remained constant around 1.25. This value suggests that the nanogel interior is quite hydrophobic. However, when the pH was further decreased, a steady increase in the I_1/I_3 value was observed, suggesting that the microenvironment of the dye is becoming increasingly polar. The I_1/I_3 ratio at pH 5.1 was found to be about 1.37. On the contrary, pyrene in the control

nanogel NG-C (that lacks the DPA units) did not exhibit any discernible change in the I_1/I_3 ratio over the same pH range of 5.1-8.0, suggesting that the hydrophobicity of these nanogels was not pH-dependent.

While the environment inside NG was quite hydrophobic between pH 8.1 and 6.4, it became less hydrophobic when the pH value decreased from 6.4 to 5.1, which indicates that the ability of NG at these pH values to encapsulate the DiI or DiO molecules could be greatly depleted. Our studies with the control nanogel NG-C also suggest that the solubility of these dye molecules can be slightly improved at lower pH. Therefore, the dye might be able to exit one nanogel and diffuse through the solvent to re-enter another; *i.e.*, the diffusion-based mechanism is possible in this case. Thus, these results suggest that the guest exchange is primarily based on the collision based mechanism from pH 8.0 to 6.4, but changes to a diffusion-based mechanism below pH 6.4.

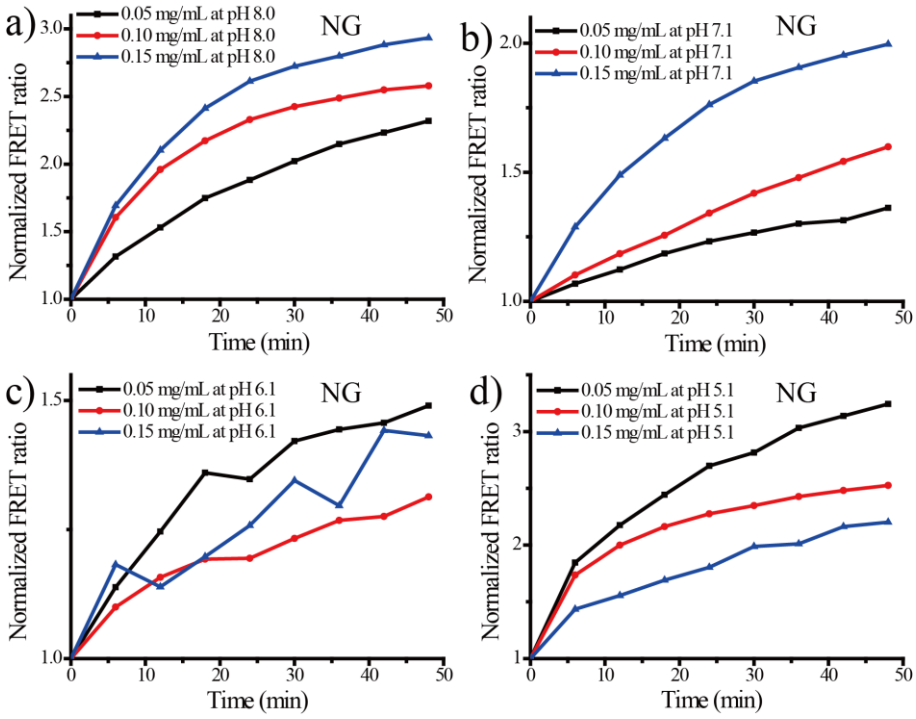

Figure 3.7 Comparison of the dynamics of guest-exchange between **NG** of different concentrations (0.05 mg/mL, 0.10 mg/mL and 0.15 mg/mL) at a) pH 8.0, b) pH 7.1, c) pH 6.1 and d) pH 5.1

To further test this possibility, we investigated the effect of nanogel concentration on the guest-exchange rate at different pH values in NG (table 3.2). We varied the concentrations of NG samples (0.05, 0.1, and 0.15 mg/mL) and studied their FRET evolution at pH 5.1, 6.1, 7.1, and 8.0. Figure 3.7a, b shows that the exchange rates increase with nanogel concentration at both pH 7.1 and 8.0. This suggests that the guest exchange at these pH values indeed occurred mostly via the collision-based mechanism. However, while there is no clear trend at pH 6.1 (Figure 3.7c), the guest-exchange rate became slower with increasing concentration at pH 5.1, as Λ values of 0.098, 0.083, and 0.046 min^{-1} were observed for nanogel concentrations of 0.05, 0.1, and 0.15 mg/mL, respectively (Figure 3.7d). Note that in a diffusion-based mechanism, the diffusion rate of dye out from the nanogel should depend on the concentration of nanogels in solution. At higher concentrations, the concentration of the host nanogel is higher while the concentration of the dye is very low at all these concentrations. In this case, the driving force for the guest molecules to diffuse into the solvent from the host nanogel is lower at higher host concentrations. Therefore, the observed decrease in guest-exchange rate with the increasing nanogel concentration supports the assertion that a diffusion-based mechanism is dominant at pH 5.1.

Table 3.2 Leakage coefficient of **NG** of different concentrations (0.05 mg/mL, 0.10 mg/mL and 0.15 mg/mL) at different pH values (8.0, 7.1, 6.1 and 5.1).

Concentration	Leakage coefficient (Λ) (min^{-1})			
	pH 8.0	pH 7.1	pH 6.1	pH 5.1
0.05 mg/mL	0.0442	0.0101	0.0119	0.0981
0.10 mg/mL	0.08	0.0154	0.0131	0.0833
0.15 mg/mL	0.0918	0.0408	0.0126	0.0464

If our hypotheses were correct, it should also follow that there should not be any change in the mechanism of guest exchange in NG-C, as the hydrophobicity of its interior does not change with pH. To perform this control experiment, we investigated the pH-dependent trends at different concentrations of NG-C. The concentration dependence of guest exchange was similar

for this nanogel at all pH values. Indeed, the FRET evolution increased with concentration at all four pH values (Figure 3.8 and table 3.3), indicating that the guest-exchange rate indeed increased with the increasing concentration. This suggests that the operating mechanism is collision-based and is not dependent on pH in the pH-insensitive nanogel NG-C. The results from the control nanogel are consistent with our conclusions for the pH-sensitive nanogels NG.

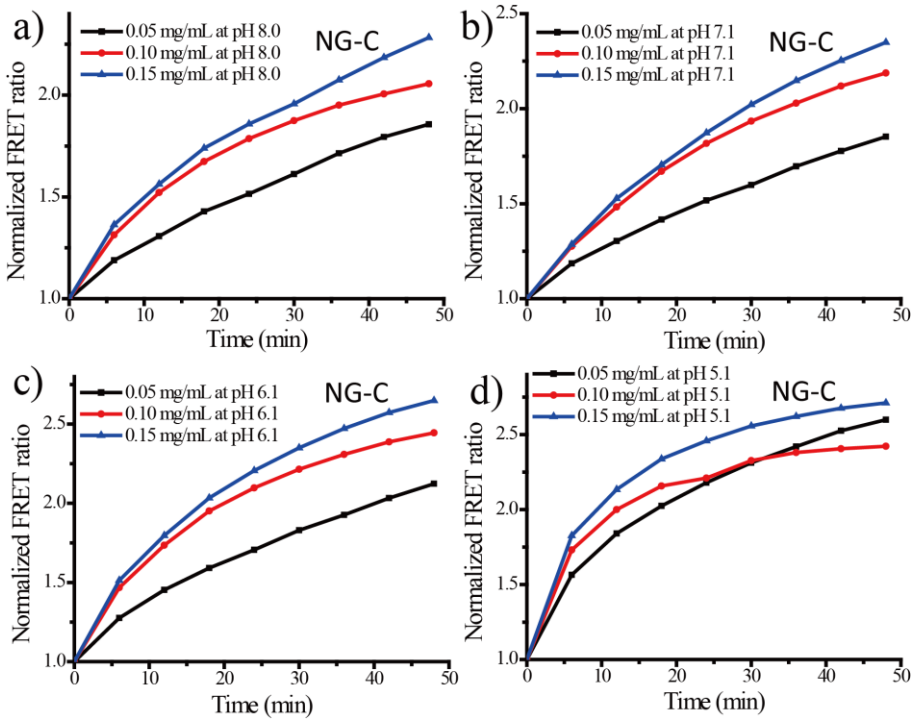

Figure 3.8 Comparison of the dynamics of dye exchange between **NG-C** of different concentrations (0.05 mg/mL, 0.10 mg/mL and 0.15 mg/mL) at a) pH 8.0, b) pH 7.1, c) pH 6.1 and d) pH 5.1.

Table 3.3 Leakage coefficient of **NG-C** of different concentrations (0.05 mg/mL, 0.10 mg/mL and 0.15 mg/mL) at different pH values (8.0, 7.1, 6.1 and 5.1).

Concentration	Leakage coefficient (Λ) (min^{-1})			
	pH 8.0	pH 7.1	pH 6.1	pH 5.1
0.05 mg/mL	0.0195	0.0192	0.0259	0.0558
0.10 mg/mL	0.0262	0.0284	0.0363	0.0614
0.15 mg/mL	0.0302	0.0315	0.0407	0.0719

3.3 Summary

In summary, we have designed a series of experiments to study the guest-exchange mechanism in pH-sensitive nanogels along with pH-insensitive nanogels as a control. We have shown that the dominant mechanism for guest exchange in these pH insensitive nanogel hosts is collision-based. Perhaps, the most important take-home message of this work is that the mechanism of guest exchange in the pH-sensitive host-guest assemblies can change on the basis of the microenvironment of the host. When the nanogel interior is hydrophobic, the collision-based mechanism is the dominant pathway. However, when the interior is sufficiently hydrophilic, the dominant mechanism changes to a diffusion-based one. From an even broader perspective, it is important to recognize that both the intrinsic factors, such as size and interior environment of the host assemblies, and the extrinsic factors, such as pH and concentration, can have significant impact on encapsulation stability. From the application standpoint, these findings could have implications in many areas. For example, in drug delivery applications, the drug-loaded nanocarrier experiences both concentration and environmental changes upon biodistribution to diseased tissues. The mechanistic variations in two different environments provide insights into molecular designs that can afford stable encapsulation in one environment and release of the molecules in another.[31,32] Similarly, the results from this study may also provide new opportunities for designing nanoreactors[33,34] in which catalysts encapsulated in a host can be used to reversibly turn a chemical reaction on or off, because of the environment-dependent diffusion of reactant molecules.

3.4 Experimental

3.4.1 General Methods

2,2′-Dithiodipyridine, 2-mercaptoethanol, poly(ethylene glycol) monomethyl ether methacrylate (PEGMA, Mw 450 g/mol), 2-(diisopropylamino)ethyl methacrylate (DPA), D,L-dithiothreitol (DTT), 1,1′-dioctadecyl-3,3,3′,3′-tetramethylindocarbocyanine perchlorate (DiI),

3,3′-dioctadecyloxacarbocyanine perchlorate (DiO), 4-cyano-4-(phenylcarbonothioylthio)pentanoic acid, and other conventional reagents were obtained from commercial sources and were used as received without further purification. 2,2′-Azobis(isobutyronitrile) (AIBN) was purified by recrystallization from ethanol. Pyridyl disulfide ethyl methacrylate (PDSEMA) was prepared using a previously reported procedure.[35] Phosphate buffer solutions were prepared by using monosodium phosphate and disodium phosphate. The buffer strength was constant at 10 mM. The pH value was determined via the Accumet AB 15/15+ benchtop pH meter. ^{1}H NMR spectra were recorded on a 400 MHz Bruker NMR spectrometer using the residual proton resonance of the solvent as the internal standard. Chemical shifts are reported in parts per million (ppm). Molecular weights of the polymers were estimated by gel permeation chromatography (GPC) using PMMA standard with a refractive index detector. Dynamic light scattering (DLS) measurements were performed using a Malvern Nanozetasizer. UV−visible absorption spectra were recorded on a Varian (model EL 01125047) spectrophotometer. The fluorescence spectra were obtained from a JASCO FP-6500 spectrofluorimeter. Transmission electron microscopy (TEM) images were taken using a JEOL 2000FX at 200 kV. All experiments were carried out at ambient temperature, unless otherwise mentioned.

3.4.2 Synthesis of Random Copolymer

Random copolymer P2, containing DPA groups, was synthesized according to a previously reported procedure.[26] A mixture of 4-cyano-4-(phenylcarbonothioylthio)pentanoic acid (12.0 mg, 0.043 mmol), PDSMA (150.0 mg, 0.588 mmol), PEGMA (215.0 mg, 0.453 mmol), DPAMA (130.0 mg, 0.609 mmol), and AIBN (1.5 mg, 0.010 mmol) was dissolved in THF (1.0 mL) and degassed by performing three freeze-pump-thaw cycles. The reaction mixture was sealed and then transferred into a preheated oil bath at 65 ℃ and stirred for 10 h. To remove unreacted monomers, the resultant mixture was precipitated in cold diethyl ether (20 mL) and redispersed in

THF three times to yield the random copolymer P2 as a waxy solid. GPC (THF) Mn: 10.6 kDa. Đ: 1.44. ^{1}H NMR (400 MHz, $CDCl_3$) δ: 8.46, 7.67, 7.10, 4.35-4.09, 3.94-3.37, 3.02, 2.62, 2.04-1.64, 1.43-0.87. The molar ratio (PDS/PEG/DPA) was determined to be 34%/28%/38% by integrating the methoxy protons in the polyethylene glycol unit (δH_d = 3.37 ppm), the aromatic protons in the pyridine (δH_a = 8.46, δH_b = 7.67, δH_c = 7.10), and the methylene protons next to the nitrogen in DPA units (δH_e = 2.62, δH_f = 3.02).

3.4.3 Preparation of Nanogels Contaning DiI/DiO

Polymer (10 mg) was dissolved in 1 mL of water, and the pH was adjusted to around 10 through the addition of NaOH aqueous solution (1 M). Then 0.04 mL of DiI in acetone stock solution (5 mg/mL) or 0.08 mL of DiO in acetone stock solution (2.5 mg/mL) was added into the polymer solution (0.2 mg of each dye for 10 mg of polymer in 1 mL of water). The final dye concentration was about 0.2 mmol/L. The mixed solution was stirred overnight at room temperature, open to the atmosphere to allow the organic solvent to evaporate. Then a measured amount of DTT (0.2 μmol for 15 mol % against PDS groups) was added. After stirring for 4 h, insoluble DiI/DiO was removed by filtration and the pyridothione byproduct was removed from the nanogel solution by extensive dialysis using a membrane with a molecular weight cutoff of 7000 g/mol. Finally, nanogel stock solutions with a concentration of 1 mg/mL were prepared for further studies.

3.4.4 Mixing of Nanogel-Encapsulated Dyes

Nanogel containing DiI and nanogel containing DiO were mixed in phosphate buffer solution at ambient temperature and at a certain pH value such that the total volume was 1 mL. The pH did not change after mixing. The fluorescence spectra were recorded using a 450 nm excitation wavelength. At the same time, absorption spectra were also measured for all samples to ensure that there is no loss of dye molecules due to precipitation. The FRET ratio $I_a/(I_a + I_d)$, where I_a and I_d are the fluorescence intensities of the acceptor (DiI) and the donor (DiO),

respectively, was plotted against time to show the dynamics of the dye exchange in nanogel solution. The leakage coefficients (Λ) were calculated on the basis of the slopes from four earlier points in the linear regime. In the case of very fast guest exchange, the time frame for obtaining these four data points is shorter.

3.5 References

1. Allen, T. M.; Cullis, P. R. Drug delivery systems: entering the mainstream. *Science* **2004**, *303*, 1818-1822.

2. Peer, D.; Karp, J. M.; Hong, S.; Farokhzad, O. C.; Margalit, R.; Langer, R. Nanocarriers as an emerging platform for cancer therapy. *Nat. Nanotechnol.* **2007**, *2*, 751-760.

3. Oh, J. K.; Drumright, R.; Siegwart, D. J.; Matyjaszewski, K. The development of microgels/nanogels for drug delivery applications. *Prog. Polym. Sci.* **2008**, *33*, 448-477.

4. Savic, R.; Eisenberg, A.; Maysinger, D. Block copolymer micelles as delivery vehicles of hydrophobic drugs: Micelle-cell interactions. *J. Drug Target.* **2006**, *14*, 343-355.

5. Liu, K. C.; Yeo, Y. Extracellular stability of nanoparticulate drug carriers. *Arch. Pharmacal Res.* **2014**, *37*, 16-23.

6. Kumar, R.; Chen, M. H.; Parmar, V. S.; Samuelson, L. A.; Kumar, J.; Nicolosi, R.; Yoganathan, S.; Watterson, A. C. Supramolecular assemblies based on copolymers of PEG600 and functionalized aromatic diesters for drug delivery applications. *J. Am. Chem. Soc.*, **2004**, *126*, 10640-10644.

7. Pan, L.; He, Q.; Liu, J.; Chen, Y.; Ma, M.; Zhang, L.; Shi, J. Nuclear-targeted drug delivery of TAT peptide-conjugated monodisperse mesoporous silica nanoparticles. *J. Am. Chem. Soc.* **2012**, *134*, 5722-5725.

8. Shen, Y.; Jin, E.; Zhang, B.; Murphy, C. J.; Sui, M.; Zhao, J.; Wang, J.; Tang, J.; Fan, M.; Kirk, E. V.; Murdoch, W. J. Prodrugs forming high drug loading multifunctional nanocapsules for intracellular cancer drug delivery. *J. Am. Chem. Soc.*, **2010**, *132*, 4259-4265.

9. Zhu, J.; Tan, M.; Zhang, L.; Yin, Q. Elongation flow-triggered morphology transitions of dendritic polyethylene amphiphilic assemblies: host−guest implications. *Soft Matter*, **2014**, *10*, 6506-6513.

10. Rharbi, Y.; Winnik, M. A. Solute exchange between surfactant micelles by micelle fragmentation and fusion. *Adv. Colloid Interface Sci.* **2001**, *89*, 25-46.

11. Piñeiro, L.; Freire, S.; Bordello, J.; Novo, M.; Al-Soufi, W. Dye exchange in micellar solutions. Quantitative analysis of bulk and single molecule fluorescence titrations. *Soft Matter* **2013**, *9*, 10779-10790.

12. Rharbi, Y.; Li, M.; Winnik, M. A.; Hahn, K. G. Temperature dependence of fusion and fragmentation kinetics of Triton X-100 Micelles. *J. Am. Chem. Soc*. **2000**, *122*, 6242-6251.

13. Rharbi, Y.; Chen, L.; Winnik, M. A. Exchange mechanisms for sodium dodecyl sulfate micelles: high salt concentration. *J. Am. Chem. Soc*. **2004**, *126*, 6025-6034.

14. Novo, M.; Felekyan, S.; Seidel, C. A.; Al-Soufi, W. Dye-exchange dynamics in micellar solutions studied by fluorescence correlation spectroscopy. *J. Phys. Chem. B* **2007**, *111*, 3614-3624.

15. Bordello, J.; Novo, M.; Al-Soufi, W. Exchange-dynamics of a neutral hydrophobic dye in micellar solutions studied by fluorescence correlation spectroscopy. *J. Colloid Interface Sci.* **2010**, *345*, 369-376.

16. Gehlen, M. H.; De Schryver, F. C. Time-resolved fluorescence quenching in micellar assemblies. *Chem. Rev.* **1993**, *93*, 199-221.

17. Jiwpanich, S.; Ryu, J. -H.; Bickerton, S.; Thayumanavan, S. Noncovalent encapsulation stabilities in supramolecular nanoassemblies. *J. Am. Chem. Soc.* **2010**, *132*, 10683-10685.

18. Lu, J.; Owen, S. C.; Shoichet, M. S. Stability of self-assembled polymeric micelles in serum. *Macromolecules* **2011**, *44*, 6002-6008.

19. Dong, H.; Shu, J. Y.; Dube, N.; Ma, Y.; Tirrell, M. V.; Downing, K. H.; Xu, T. 3-Helix micelles stabilized by polymer springs. *J. Am. Chem. Soc.* **2012**, *134*, 11807-11814.

20. Kim, K.; Bae, B.; Kang, Y. J.; Nam, J.-M.; Kang, S.; Ryu, J. -H. Natural polypeptide-based supramolecular nanogels for stable noncovalent encapsulation. *Biomacromolecules* **2013**, *14*, 3515-3522.

21. Zou, P.; Chen, H.; Paholak, H. J.; Sun, D. Noninvasive fluorescence resonance energy transfer imaging of in vivo premature drug release from polymeric nanoparticles. *Mol. Pharmaceutics* **2013**, *10*, 4185-4194.

22. Dan, K.; Rajdev, P.; Deb, J.; Jana, S. S.; Ghosh, S. Remarkably stable amphiphilic random copolymer assemblies: A structure–property relationship study. *J. Polym. Sci. A Polym. Chem.* **2013**, *51*, 4932-4943.

23. Li, L.; Ryu, J. -H.; Thayumanavan, S. Effect of Hofmeister ions on the size and encapsulation stability of polymer nanogels. *Langmuir* **2013,** *29*, 50-55.

24. Fuller, J. M.; Raghupathi, K. R.; Ramireddy, R. R.; Subrahmanyam, A. V.; Yesilyurt, V.; Thayumanavan, S. Temperature-sensitive transitions below LCST in amphiphilic dendritic assemblies: host–guest implications. *J. Am. Chem. Soc.* **2013**, *135*, 8947-8954;

25. Swaminathan, S.; Fowley, C.; McCaughan, B.; Cusido, J.; Callan, J. F.; Raymo. F. M. Intracellular guest-exchange between dynamic supramolecular hosts. *J. Am. Chem. Soc.*, **2014**, *136*, 7907-7913.

26. Li, L.; Raghupathi, K.; Yuan, C.; Thayumanavan, S. Surface charge generation in nanogels for activated cellular uptake at tumor-relevant pH. *Chem. Sci.* **2013**, *4*, 3654-3360.

27. Gjaltema, A.; Van Loosdrecht, M. C. M.; Heijnen, J. Abrasion of suspended biofilm pellets in airlift reactors: Effect of particle size. *J. Biotechnol. Bioeng.* **1997**, *55*, 206-215

28. Yu, S.; Hu, J.; Pan, X.; Yao, P.; Jiang, M. Stable and pH-sensitive nanogels prepared by self-assembly of chitosan and ovalbumin. *Langmuir* **2006**, *22*, 2754-2759.

29. Kalyanasundaram, K.; Thomas, J. Environmental effects on vibronic band intensities in pyrene monomer fluorescence and their application in studies of micellar systems. *J. Am. Chem. Soc.* **1977**, *99*, 2039-2044.

30. Bickerton, S.; Jiwpanich, S.; Thayumanavan, S. Interconnected roles of scaffold hydrophobicity, drug loading, and encapsulation stability in polymeric nanocarriers. *Mol. Pharmaceutics* **2012**, *9*, 3569-3578.

31. Du, J. Z.; Sun, T. M.; Song, W. J.; Wu, J.; Wang, J. A tumor-acidity-activated charge-conversional nanogel as an intelligent vehicle for promoted tumoral-cell uptake and drug delivery. *Angew. Chem. Int. Ed.*, **2010**, *49*, 3621-3626.

32. Poon, Z.; Chang, D.; Zhao, X. Y.; Hammond, P. T. Layer-by-layer nanoparticles with a pH-sheddable layer for in vivo targeting of tumor hypoxia. *ACS Nano.*, **2011**, *5*, 4284-4292.

33. Wang, X.; Liu, G.; Hu, J.; Zhang, G.; Liu, S. Concurrent block copolymer polymersome stabilization and bilayer permeabilization by stimuli-regulated traceless crosslinking. *Angew. Chem. Int. Ed.*, **2014,** *53*, 3138-3142.

34. Yuan, C.; Luo, W.; Zhong, L.; Deng, H.; Liu, J.; Xu, Y.; Dai, L. Au @ polymer nanostructures with tunable permeability shells for selective catalysis. *Angew. Chem. Int. Ed.* **2011**, *51*, 3515-3519.

35. Ghosh, S.; Basu, S.; Thayumanavan, S. Simultaneous and reversible functionalization of copolymers for biological applications. *Macromolecules* **2006**, *39*, 5595-5597.

CHAPTER 4

SURFACE CHARGE GENERATION IN NANOGELS FOR ACTIVATED CELLULAR UPTAKE AT TUMOR-RELEVANT PH

Li, L.; Raghupathi, K.; Yuan, C.; Thayumanavan, S. Surface charge generation in nanogels for activated cellular uptake at tumor-relevant pH. *Chem. Sci.* **2013**, *4*, 3654-3360. - Reproduced by permission of The Royal Society of Chemistry

http://pubs.rsc.org/en/content/articlehtml/2013/sc/c3sc50899d

4.1 Introduction

Nanocarriers with cationic surface charge are readily internalized by the cells because of their higher affinity for the negatively charged phospholipid bilayer of cell membranes.[1,2] Since cellular internalization can often be a stumbling block in therapeutic approaches, positively charged nanoparticles are often used to enhance cellular uptake.[3] However, the positively charged nature of carriers may also induce non-specific interactions in serum, leading to their severe aggregation and rapid clearance from the circulation by the reticuloendothelial system following systemic administration.[4] To address this problem, recent efforts have been dedicated to the development of stimuli-responsive charge conversional nanoparticles.[5–7] Typically, it is desirable that the surface charge of nanoparticles be neutral or even negatively charged under normal physiological conditions. Then, under the aberrant conditions that simulate the disease site, the surface charge of these environment responsive nanoparticles become positive. The hypothesis is that such a change could result in rapid uptake of the nanocarriers by the cells.

Environmental stimuli that were exploited in the development of stimuli-responsive drug delivery systems include pH,[8–10] temperature,[11–13] enzymatic expression,[14–16] redox reaction, [17–19] and light.[20–22] Many of these designs were motivated by the environment around solid tumors and thus have been targeted to ultimately impact cancer therapy. Among these, pH responsiveness is most frequently utilized, because the extracellular pH (pH_e) of tumor tissue (~6.5) is slightly

lower than that of normal tissue and blood (~7.4), which is due to the hypoxia-induced production of excess lactic acid in the tumor microenvironments.[23–25] For example, nanocarriers that are capable of reversing the surface charge from negative to positive at pH_e have been designed, where the pH-induced cleavage of the amide bond between an amino and 2,3-dimethylmaleic anhydride causes the charge conversion.[26–28] Similarly, nanoparticles containing a pH-sensitive outer stealth layer have been designed using layer-by-layer techniques. In this case, the nanoparticle sheds a layer in response to acidity and reveals a charged nanoparticle surface that can be readily internalized by tumor cells.[29]

In this manuscript, we report on a system that contains a few important and new complementary features. In our design, we stipulated that: (*i*) the system should be a charge generation process (neutral to positive), instead of a charge conversion process (negative to positive). This design has the potential to further reduce non-specific binding, prior to the charge-generation step; (*ii*) the charge generation should be rapid; (*iii*) the pH-induced charge-generation step is reversible, i.e. the surface charge is environment-dependent, but not permanent; (*iv*) the scaffold that exhibits these features should be nanoscale and be able to non-covalently bind hydrophobic guest molecules; and (*v*) the charge-generation step should not produce any small molecule by-products. Polymer nanogels have the potential to satisfy these requirements and thus afford pH-activated cellular uptake.

4.2 Results and Discussion

4.2.1 Design and synthesis of pH-sensitive nanogels

To afford pH-activated cellular uptake and satisfy the requirements above, we utilize our recently reported self-crosslinking disulfide-based nanogels as the scaffold.[30–33] Disulfide based nanogels systems have gained significant interest because of their triggered encapsulated guest release capabilities in the cytosol.[34] Our polymeric disulfide nanogels can be achieved by taking advantage of amphiphilic random copolymers that form nanoscale aggregates and by trapping

them as nanogels through a crosslinking reaction in the hydrophobic component of the amphiphilic assembly. In our current work, we have developed a series of random copolymers by copolymerizing 2-(diisopropylamino) ethyl methacrylate (DPA), polyethyleneglycol methacrylate (PEGMA) and 2-(pyridyldisulfide) ethyl methacrylate (PDSMA) monomers. Nanogels were generated by crosslinking the pyridyl disulfide (PDS) moieties within the hydrophobic interior of the amphiphilic aggregates.

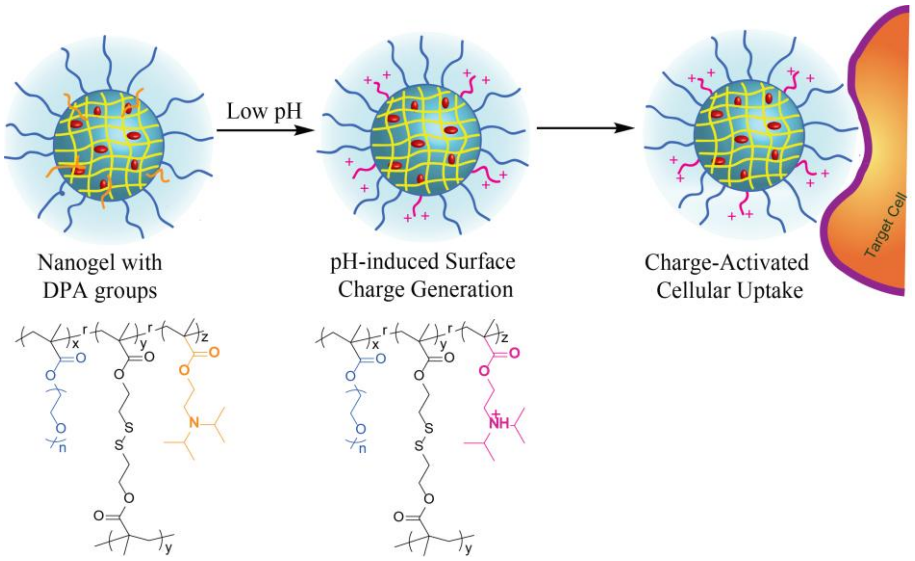

Scheme 4.1 Schematic illustration and chemical structure of polymeric nanogels for pH-induced surface charge generation and activated cellular uptake.

Our design hypothesis is that the DPA moieties are hydrophobic and are buried within the interior of the nanogels at neutral pH, but are protonated at pH_e to generate a positively charged surface (Scheme 4.1), thus providing an opportunity for activated cellular uptake. The main reason for choosing the diisopropylamino moiety, as the pH-sensitive moiety, is its pK_a. The pK_a of the protonated form of the amine is around 6.2, which suggests that at neutral pH this amine will be mostly unprotonated and thus will be hydrophobic. However, at a pH of 6.2, about 50% of the functional groups would be protonated. We anticipate this protonation event to be rapid and reversible; the transformation also should not provide any byproducts. Moreover, we expected that the protonation event to render the DPA functional group to be sufficiently hydrophilic to be

displayed on the surface of the nanogel. In fact, such a pH-dependent change in hydrophobicity has been utilized to disassemble amphiphilic block copolymer micelles, where the DPA units are incorporated within the hydrophobic component of the assembly.[35,36] In our case, we were interested in retaining the nanoscale structure, but only change the surface charge of the assembly. We hypothesized that incorporation of the DPA within the crosslinked polymeric nanostructure should make this a possibility, as shown in Scheme 1. Note also that the nanogel surface would be decorated with PEG moieties, which is likely to be charge neutral. Therefore, the pH-induced presentation of the protonated DPA moieties on the surface should convert the assembly from a charge neutral nanogel to a positively charged one. Finally, since these polymeric nanostructures are assembled from an amphiphilic aggregate, executing the crosslinking reaction in the presence of hydrophobic guest molecules provides the opportunity to incorporate them within the nanogel interior. Thus, the targeted polymer nanogel has the potential to satisfy all the design criteria mentioned above.

The PEGMA-co-DPAMA-co-PDSMA copolymers were synthesized by a reversible addition-fragmentation chain transfer (RAFT) polymerization reaction (Figure 4.1). Four different copolymers with varying comonomer compositions were targeted. Copolymers P1-P4 were synthesized by simply varying the feed ratio of the monomers during the polymerization. Copolymer P4 differs from the polymers P1-P3, as P4 is synthesized by using a PEGMA with shorter length polyethyleneglycol side chain (~350 g/mol). After polymerization, the polymers were purified by precipitation in hexane, filtered, and washed to remove unreacted monomers. The polymers were characterized by NMR and GPC. We used the characteristic resonances of PDS (δH_a = 8.46, δH_b = 7.67, δH_c = 7.10), PEGMA (δH_d = 3.37 ppm) and DPA (δH_e = 2.62, δH_f = 3.02 ppm) moieties to calculate the relative ratios of the monomer incorporated in the polymer (Figure 4.1). The number-average molecular weights (M_n) and dispersity ($Đ = M_w/M_n$) of the copolymers were evaluated by GPC. The results are summarized in Table 4.1.

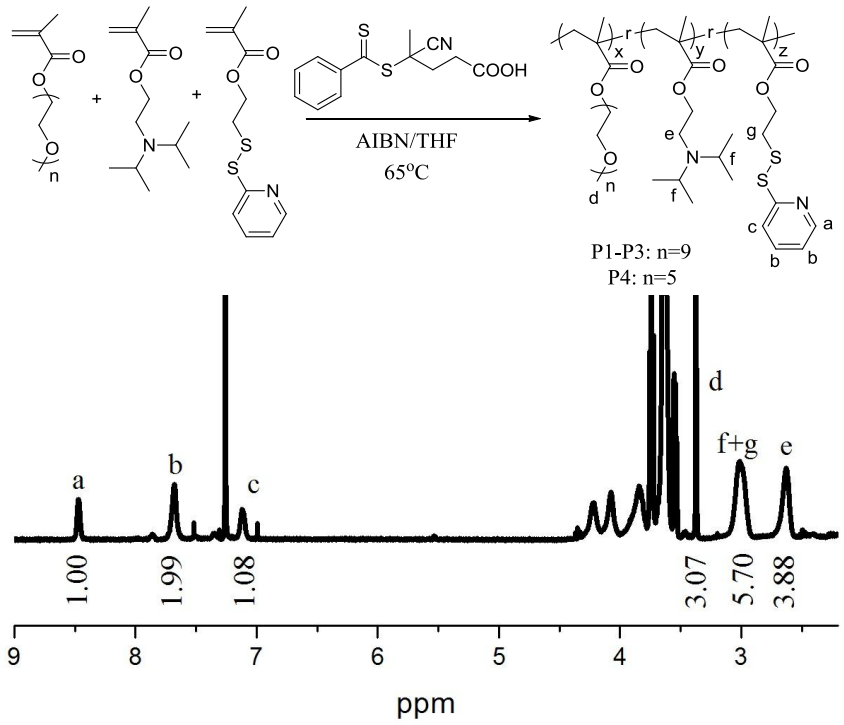

Figure 4.1 Synthetic scheme and NMR spectrum of PEGMA-co-DPA-co-PDS random copolymer with PEGMA: DPA: PDS = 0.28: 0.36: 0.36 (P2) in $CDCl_3$

Table 4.1 Characteristics of $PEGMA_x$-co-DPA_y-co-PDS_z copolymers (P1–P4).

Sample code	*x/y/z*[a]	M_n(kDa)[b]	Đ[b]
P1	0.28/0.19/0.53	8.26	1.29
P2	0.28/0.36/0.36	10.2	1.34
P3	0.26/0.49/0.25	8.36	1.23
P4[c]	0.26/0.32/0.42	12.3	1.51

[a] Calculated weight ratio by ^{1}H NMR
[b] Determined by GPC in THF using PMMA as standards
[c] The molecular weight of PEGMA is 350 g/mol

Next, these polymers were converted into the corresponding nanogels, NG1-NG4, by first dispersing these polymers in aqueous phase. The nanoscale aggregates are locked-in as nanogels by generating intra-aggregate disulfide crosslinks. The crosslinking reaction is executed by adding a calculated amount of dithiothreitol (DTT), which cleaves the disulfide bond of corresponding amount of PDS moieties. The free thiols generated in this process then react with remaining PDS functionalities in the polymer chain (both intra- and interchain) to provide the

crosslinked polymer nanogel. The intra-aggregate nature of the crosslinking reaction insures that the nanogel size is tightly controlled by the size of the nanoscale aggregate. In all our nanogels, we used about 50% DTT (relative to the PDS units) to cause the PDS units to be exhausted in the crosslinking reaction; the extent of the PDS cleavage is conveniently monitored by the absorption peak that corresponds to the 2-thiopyridone by-product.

Next, we investigated the pH-dependent charge-generation features in these nanogels through zeta potential measurements. The zeta potential of the PEG-decorated nanogel at neutral pH is negative. Although this seems surprising, there have been several reports that suggest that the surface charge of PEG-decorated nanostructures are indeed negative.[37,38] The origins of this charge are not clear. Upon decreasing the pH of the solution, the surface charge of the nanogel changes to positive with the transition from negative to positive charge at a pH ~ 6.2. Considering that there is no formal charge in the PEG moieties, we hesitate to ascertain that the generation of the pH induced positive charge generation as charge-conversional. Nonetheless, the apparent negative surface charge of the PEG moieties on the surface of the nanogel served as a useful starting point for us to conveniently ascertain the pH at which the surface charge of the nanogel becomes positive.

4.2.2 Effect of monomer ratio on pI

We first hypothesized that the pH at which the surface charge is generated in the nanogel can be conveniently tuned by simply altering the ratio of DPA unit in the copolymer. To test this possibility, we used the nanogels NG1-NG3 and investigated their isoelectric point (pI). Due to the apparent negative charge on the PEG surface, we named the pH at which the surface charge of the nanogel becomes neutral as the nanogel's pI. We found that the pI indeed increased with the ratio of DPA in the copolymer, as shown in Figure 4.2. The pI of the NG1 was found to be 6.2, while those of the NG2 and NG3 were found to be 6.7 and 6.8 respectively. These results are taken to suggest that the surface charge generation is driven by the protonation induced charge

build-up within the interior of the nanogel. After a certain charge build-up, the electrostatic repulsion is likely relieved by presenting the protonated DPA units on the surface of the nanogel. This change is achieved at higher pH in the case of larger number of DPA units, because the critical charge built-up can be achieved within the nanogel interior relatively quickly.

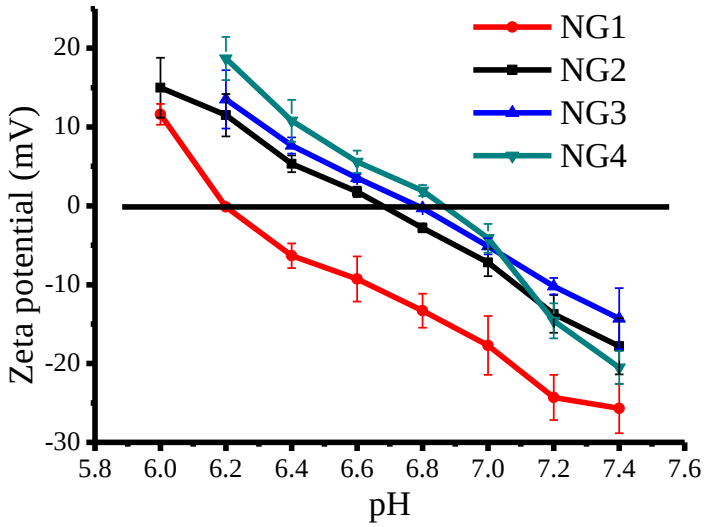

Figure 4.2 Change in the zeta potential of nanogels as a function of pH. NG1-NG4 were made by using P1-P4 at pH 10. All nanogel crosslinking densities were 100%, achieved by adding 50 mol% DTT with respect to PDS groups.

Next, we were interested in investigating the effect of length of OEG units on the charge conversion. It is reasonable that OEG moieties can be used to shield the DPA units. If this were the case, then the length of the OEG functionalities should affect the pI of the nanogel. To test this possibility, we used the nanogel NG4, which differs from other nanogels only in the length of OEG units; these are shorter. We found that the pI of the nanogel from NG4 was indeed slightly higher than those of NG2 and NG3, even though the relative ratio of DPA units was smaller in the case of NG4. Note however that in the case of NG4, there is also another factor that is concurrently changed, *viz.* crosslink density due to the percentage of the PDS units in the polymer P4.

4.2.3 Effect of crosslink density on pI

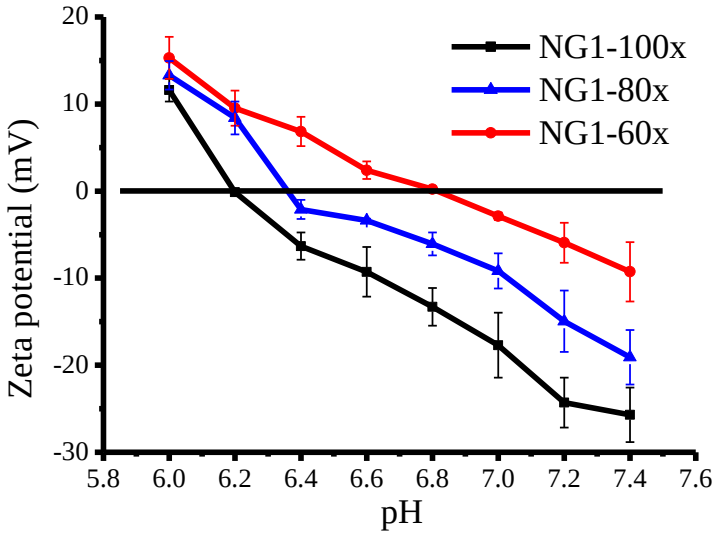

Figure 4.3 Change in the zeta potential of nanogels with different crosslinking density as a function of pH. All three nanogels were made by using P1 at pH 10, and the crosslinking density was varied by using appropriate amount of DTT.

Note that the crosslink density of NG4 is higher than that of NG2 and NG3 in the experiment above. The pI of NG4 is higher than those of NG2 and NG3. However, if crosslink density were to have an effect on the pI, we anticipated that the nanogels with lower crosslinking density to exhibit higher pI. This is because the DPA groups that are buried inside the core can be more easily presented on the nanogel surface upon protonation, when the crosslink density is lower, due to the greater flexibility of the polymer chains.[39] To test this further, nanogels of three different crosslink densities were prepared using the polymer P1 by adding different amounts of dithiothreitol (DTT) (30, 40 and 50 mol% against the precursor PDS groups) during the crosslinking reaction. These nanogels were labeled as NG1-60x, NG1-80x, and NG1-100x respectively, indicating the percent crosslink densities in each of the nanogels. When examining the change in surface charge with pH (Figure 4.3), the pI for the NG1-60x is much higher than that of NG1-80x, which was higher than that of NG1-100x. These results suggest that: (*i*) the pH-induced surface presentation of the DPA units, buried in the core of the nanogel when hydrophobic and unprotonated, is influenced by the flexibility of the polymer chains; and (*ii*) the

higher pI of NG4, compared to NG2 and NG3, is not due to the crosslink density variation and is indeed due to the shorter OEG units on the surface of NG4.

Considering our observations above, we were next interested in investigating the effect of nanogel preparation conditions upon its pI; more specifically the pH of the solution at which the crosslinking reaction was carried out. If the chain flexibility is indeed the reason for the observed variation in pI, then it should follow that at same crosslink densities, the percentage of the hydrophobic and unprotonated DPA units presented on the surface vs. the core of the nanogel should influence the nanogel's pI. This presentation can be tuned because: (*i*) if the pH were lower during the crosslinking step of the nanogel preparation, there will be a greater percentage of DPA units that are protonated and therefore hydrophilic to be presented on the surface (the pKa of the protonated DPA tertiary amine moiety is ~ 6.2); (*ii*) although at neutral pH, the originally protonated DPA units would be unprotonated and hydrophobic, it is unlikely that these units can be tucked inside the core of the nanogel after crosslinking; and (*iii*) the longer OEG units, compared to the DPA moieties, can allow for the unprotonated and hydrophobic DPA units to be presented outside the nanogel and yet not exhibit significant hydrophobicity induced aggregation.

4.2.4 Effect of preparation condition on pI

To test this possibility, we synthesized nanogels at pH 5, 6, 8, and 10 using P1 and 50% DTT to obtain NG1-5, NG1-6, NG1-8, and NG1-10 respectively. After syntheses, all these nanogels were brought to identical solution conditions through extensive dialysis. Then, we investigated the charge-generation possibility of the nanogel by measuring the zeta potential at different pHs (Figure 4.4). Indeed, we found the pI of the nanogel to be dependent on the preparative conditions. For example, the pI for NG1-8 was found to be ~ 6.4, while the pI of the NG1-5 and NG1-10 were found to be 6.5 and 6.2 respectively. We were also interested in ascertaining that the observed differences are not due to any adventitious effects and are indeed due to the DPA units. For this purpose, we also prepared a structurally similar nanogel NG5, but

without the DPA units. The zeta potential of the nanogel without DPA units remained at ~10 mV at whole pH range. This clearly suggests that the observed pH-dependence is indeed due to the DPA units in the nanogel.

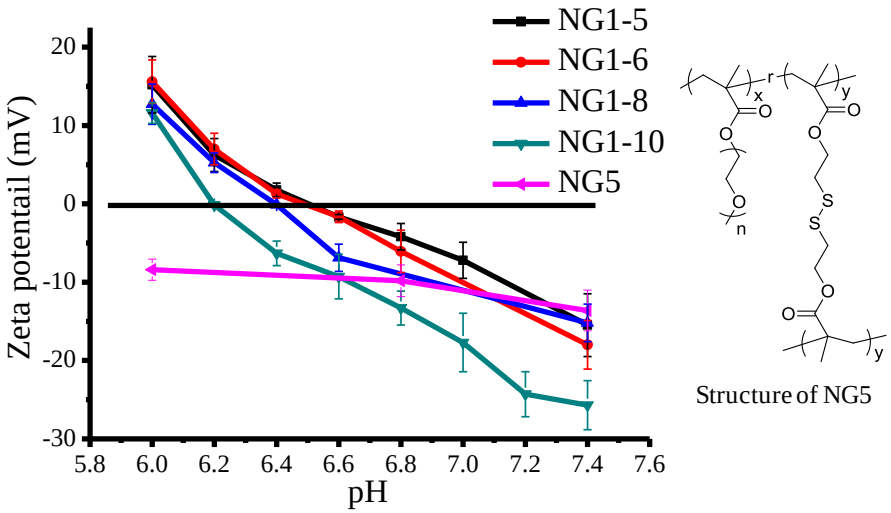

Figure 4.4 Change in the zeta potential of nanogels as a function of pH. NG1-x nanogels were made by using P1 at different pHs, represented as NG1-x where x stands for the pH at which the nanogel was prepared. Crosslinking density in all nanogels was fixed at 100%. For comparison, nanogel without DPA units (NG5) was prepared; structure of NG5 is also shown.

4.2.5 pH-dependent cellular uptake

One of the key motivations in altering surface charges in response to pH is the ability to demonstrate pH-dependent cellular uptake. Since the change in surface charge is close to the slightly acidic tumor extracellular environment (the so-called pH_e), exploration of this possibility is relevant. For this approach to be useful in applications such as drug delivery, it is also essential that these nanogels are able to carry a hydrophobic cargo. A key advantage of the self-crosslinking nanogels is that these scaffolds can non-covalently and stably encapsulate hydrophobic guest molecules. We used 1,10-dioctadecyl- 3, 3,30,30-tetramethylindocarbocyanine perchlorate (DiI) as the guest molecule due to its hydrophobicity and fluorescence emission wavelength that is suitable for studying the cellular uptake using confocal laser scanning microscopy (CLSM). We investigated the internalization behavior of DiI-encapsulated NG2 at

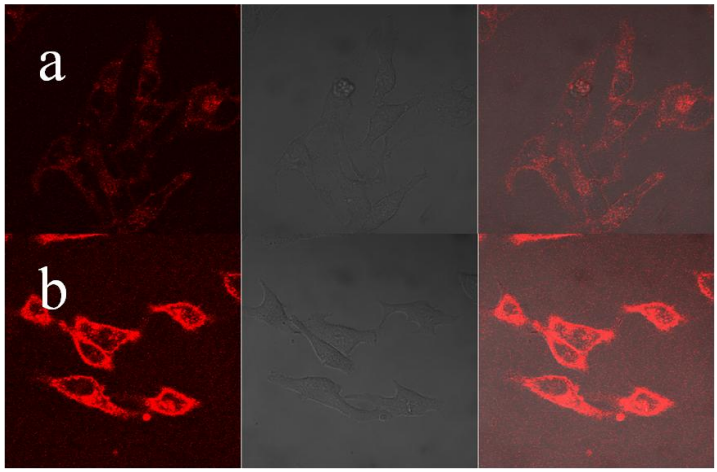

Figure 4.5 (a) and (b) are confocal images of NG2, containing DiI at pH 7.4 and 6.5 respectively, after incubation with HeLa cells for 2 hours. The nanogels used were 100% crosslinked. Cells were imaged using a 63 × oil-immersion objective. Within each image set, left panel is the red channel that shows DiI emission; middle panel is the DIC image, and right panel is an overlap of both.

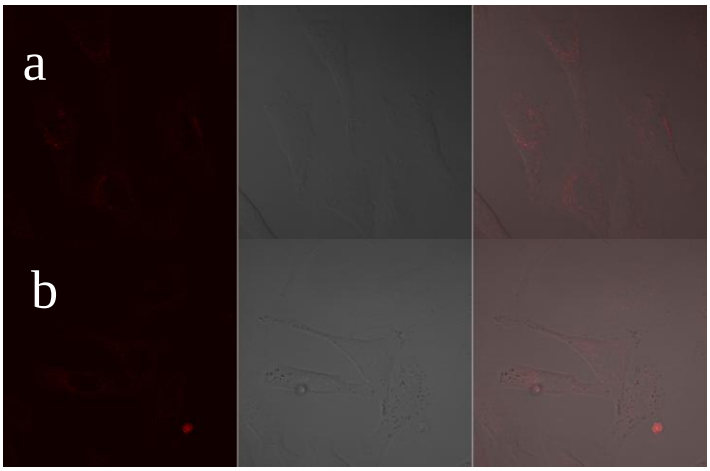

Figure 4.6 (a) and (b) are confocal images of the control nanogel **NG5** (without DPA units) loaded with DiI at pH 7.4 and 6.5 respectively after incubation with HeLa cells for 2 hours. The nanogels used were made from polymer without DPA units. Cells were imaged using a 63 × oil-immersion objective. Within each image set, left panel is the red channel that shows DiI emission; middle panel is the DIC image, and right panel is an overlap of both images.

the normal extracellular pH of 7.4 and pHe of 6.5 with the HeLa cell line. Significantly different cellular uptake was observed for the DPA nanogels under these conditions. As shown in Figure 4.5, the red fluorescence is significantly higher at pH 6.5, compared to pH 7.4. We attributed this difference to the possibility that the DPA nanogel would become positively charged upon the protonation of DPA groups at lower pH and thus enhance the cellular internalization. First, we

wanted to confirm that this is indeed due to the DPA moieties. Therefore, we carried out cellular internalization experiments with NG5 at both pHs for the same amount of time (2 hours). At both pH 7.4 and 6.5, very little internalization was observed (Figure 4.6). These results support our assertion that the pH-induced surface charge change can affect cellular uptake due to the DPA units.

The results above do not necessarily show that the difference in fluorescence is due to the cellular uptake differences, because it is possible that the DiI leaks out at lower pH (in response to DPA protonation). This small molecule can then be rapidly taken up by the cells, as DiI is hydrophobic.[33,40] In this case, difference in cellular uptake is not necessary to explain the difference in fluorescence observed at different pH. We carried out two different sets of experiments to gain further insight: (*i*) we tested the stability of encapsulation at different pH; and (*ii*) we covalently attached a fluorophore to the nanogel, where the leakage of the fluorophore possibility is circumvented.

4.2.6 Encapsulation capability and redox-responsive behavior

To test encapsulation stability at different pH, we prepared DiI-incorporated nanogel solutions and monitored their fluorescence over time at pH 7.4 and 6.0. We found the fluorescence to be unchanged even over a 24 hours time period (Figure 4.7a and b). This suggests that although the surface charge of the nanogels change with pH, their host–guest capabilities do not change with pH. Note that this assay is based on the expectation that any leaked dye from the nanogel will precipitate out of solution. However, since these nanogels also have certain amphiphilic character, it is also possible that there is a driving force to keep the dye molecules within its interiors at both pHs. Therefore, to more rigorously test whether there is a stable encapsulation of the guest molecules within the nanogel, we utilized a recently developed fluorescence resonance energy transfer (FRET) experiment.[41] Here, we prepare two different solutions one with a FRET donor and another with a FRET acceptor. When these solutions are

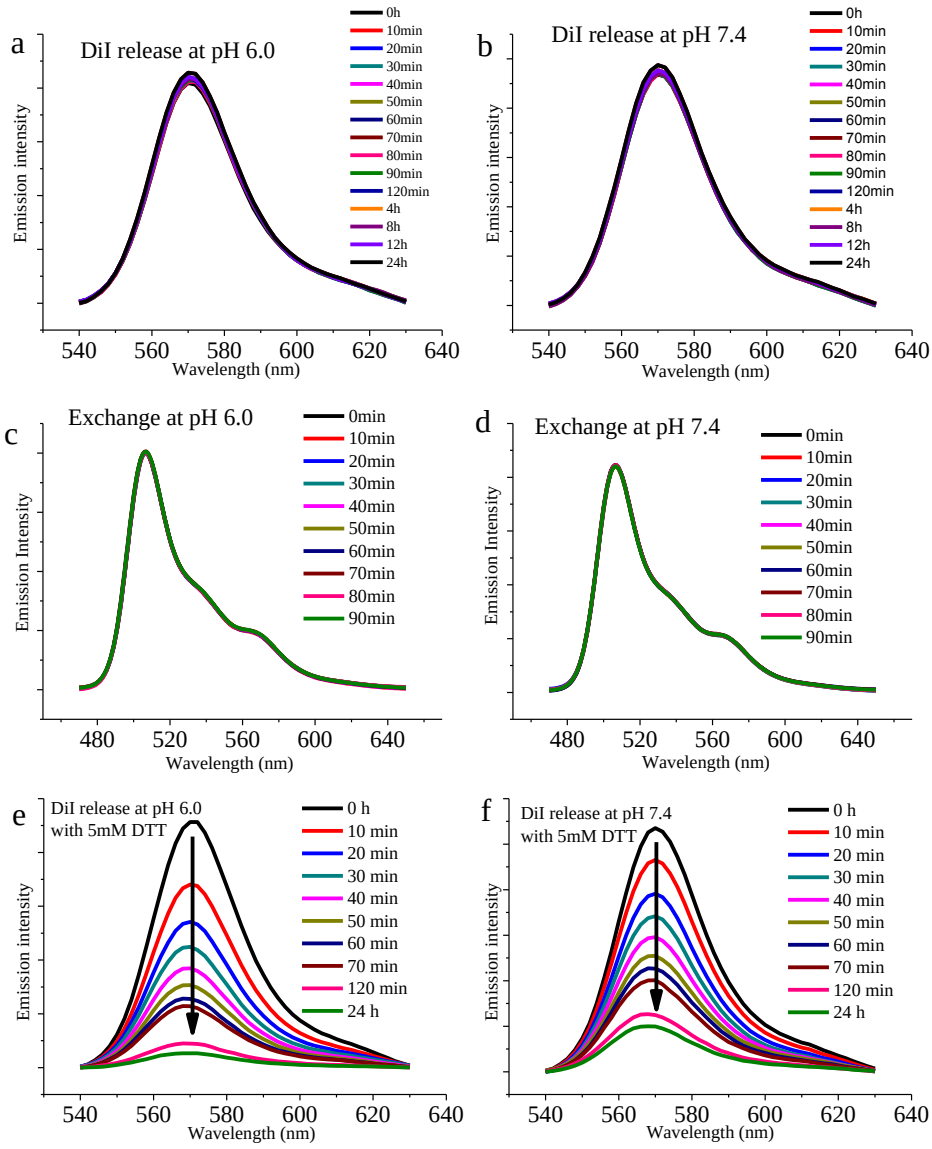

Figure 4.7 Encapsulation stability of nanogel at different pH (a-d). DiI release experiment, a) at pH 6.0, b) at pH 7.4. FRET experiment based DiI/DiO exchange, c) at pH 6.0, d) at pH 7.4; DiI release experiment in the presence of 5 mM DTT in solution, e) at pH 6, f) pH 7.4. The nanogels used were made from P2 (100% crosslinked).

mixed, if the extent of FRET increases with time, then the nanogel is leaky. If there is no change in FRET, then the encapsulation is stable. In this experiment, the measure of encapsulation stability is independent of the ability of the nanogel to solubilize the dye molecules through amphiphilic driving forces. 3, 3'-Dioctadecyloxacarbocyanine perchlorate (DiO) is a well-known higher energy FRET donor partner for DiI. The FRET evolution was investigated at both pH 7.4

and 6.0, where we found that the extent of FRET did not change over a 24 hours time period (Figure 4.7c and d). This confirms that the guest molecules are indeed stably encapsulated, independent of whether the DPA units are protonated or not.

While stable encapsulation is desirable, it is also important that these guest molecules be released in response to a specific stimulus. Since these are disulfide-based crosslinks, the nanogels are sensitive to reactive thiols such as DTT and glutathione. In the presence of 5 mM DTT, the nanogels were found to be quite leaky, with a large extent of the guest molecules released within 2 hours (Figure 4.7e and f). Again, this feature was found to be independent of the pH. To insure that the observed change is not an adventitious pH response to fluorescence, we also monitored the absorbance of the solution under these conditions. Similar results were observed for the DiI release, via absorption spectra (see Figure 4.8).

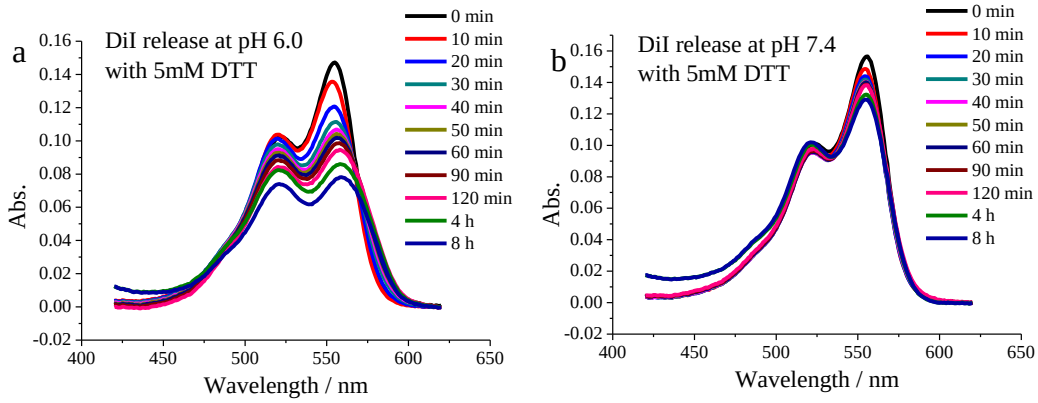

Figure 4.8 Absorption spectra for DiI release experiment at a) pH 6.0 with 5 mM DTT and b) pH 7.4 with 5 mM DTT.

Finally, to further confirm that the pH-dependent internalization is indeed due to change in surface charge, nanogels with covalently attached fluorescein were prepared and incubated with the HeLa cells for 2 hours, at both pH 6.5 and pH 7.4. From the optical microscopy images, it is clear that the cells treated with nanogels at pH 6.5 exhibit much higher cellular uptake, compared to the same nanogels at pH 7.4 (Figure 4.9). These results confirm that the difference in fluorescence images at two different pHs, with the DiI-encapsulated nanogels, is not due to the

non-covalently encapsulated guest leakage. These results also support our assertion that the difference in cellular uptake is indeed due to the greater nanogel uptake at pH 6.5, most likely due to the difference in surface charge. These results also suggest that the current nanogel system can be used in drug delivery via both physical encapsulation and chemical conjugation.

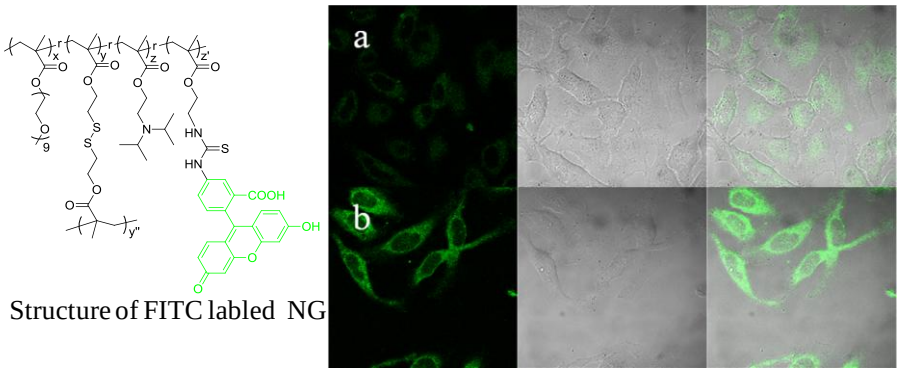

Structure of FITC labled NG

Figure 4.9 (a) and (b) are confocal images of fluorescein-labeled DPA nanogel at pH 7.4 and 6.5 after incubation with HeLa cells for 2 hours. The concentration of the nanogels used was 1mg/mL. Cells were imaged using a 63 × oil-immersion objective. Within each image set, left panel is the green channel that shows FITC emission; middle panel is the DIC image, and right panel is an overlap of both.

4.3 Summary

In summary, we report on a nanogel that is capable of transforming into a positively charged nanogel at a pH that is relevant to the slightly acidic tumor extracellular environment. We have shown that: (*i*) the co-incorporation of DPA units to PEG based nanogels can lead to effective pH-dependent charge generation; (*ii*) the pI of the DPA nanogel can be systematically tuned by varying the (a) percentage DPA units present in the nanogel, (b) percentage of DPA units that are initially exposed on the nanogel surface, and (c) crosslink density; (*iii*) the charge generation process can be utilized to enhance cellular uptake at pHe, compared to the normal extracellular pH. It is remarkable that this charge generation event results in enhanced cellular uptake, even though the length of the OEG units are much higher than the side chains that contain the DPA moieties; and (*iv*) non-covalently encapsulated guest molecules are stably encapsulated at both pH and are thus effectively taken up by the cells at lower pH without any leakage. Considering

that there exist a number of ternary amines with very different pK_a from 5 to 7, it is also possible to prepare nanogels with diverse pI. Thus, the surface charge can be selectively modulated not only for cellular uptake, but also for different endocytic compartments such as early endosomes (pH 5.9-6.2) and lysosomes (5.0-5.5). Overall, the reported facile synthetic method for preparing the pH_e-responsive charge generation nanogels, combined with stable encapsulation and tunable pI, should open up new avenues for the design of the next generation nanogels.

4.4 Experimental

4.4.1 General

2,2′-dithiodipyridine, 2-mercaptoethanol, polyethylene glycol monomethylether methacrylate (MW 450 g/mol and 350 g/mol) (OEG), 2-(diisopropylamino) ethyl methacrylate (DPA), D,L-dithiothreitol (DTT), 1,1'-dioctadecyl-3,3,3',3'-tetramethyl indocarbocyanine perchlorate (DiI) and 3,3'-dioctadecyloxacarbocyanine perchlorate (DiO), 4-cyano-4-(phenylcarbonothioylthio)pentanoic acid, fluorescein isothiocyanate (FITC) and other conventional reagents were obtained from commercial sources and were used as received, unless otherwise mentioned. Polymers were synthesized using RAFT polymerization and then purified by precipitation. Pyridyl disulfide ethyl methacrylate (PDS) was prepared using a previously reported procedure.[42] ^{1}H-NMR spectra were recorded on a 400 MHz Bruker NMR spectrometer using the residual proton resonance of the solvent as the internal standard. Chemical shifts are reported in parts per million (ppm). Molecular weights of the polymers were estimated by gel permeation chromatography (GPC) using PMMA standard with a refractive index detector and THF as the elution. Dynamic light scattering (DLS) measurements and zeta potential measurements were performed using a Malvern Nanozetasizer. UV-visible absorption spectra were recorded on a Varian (model EL 01125047) spectrophotometer. The fluorescence spectra were obtained from a JASCO FP-6500 spectrofluorimeter.

4.4.2 Synthesis of random copolymer P1-P4

A mixture of 4-cyano-4-(phenylcarbonothioylthio) pentanoic acid (5.9 mg, 0.021 mmol), PDS (107.4 mg, 0.421 mmol), polyethylene glycol monomethyl ether methacrylate (100 mg, 0.21 mmol), 2-(diisopropylamino) ethyl methacrylate (27mg, 0.126 mmol) and AIBN (0.7 mg, 0.00421 mmol) was dissolved in THF (0.5 mL) and degassed by performing three freeze-pump-thaw cycles. The reaction mixture was sealed and then transferred into a pre-heated oil bath at 65 ℃ and stirred for 10 h. To remove unreactive monomers, the resultant mixture was precipitated in cold ethyl ether (20 mL) to yield the random copolymer **P1** as a waxy solid. GPC (THF) M_n: 8.3 KDa. D: 1.3. ^{1}H NMR (400 MHz, $CDCl_3$) δ: 8.46, 7.67, 7.10, 4.35-4.09, 3.94-3.37, 3.02, 2.62, 2.04-1.64, 1.43-0.87. Other polymers **P2-P4** were prepared by a similar method using the appropriate molar ratio of the co-monomers. The molar ratio between three monomer units was determined by integrating the methoxy protons in the polyethylene glycol unit, the aromatic protons in the pyridine and methylene protons contacted to amino groups.

4.4.3 Synthesis of random copolymer P5 without DPA units

A mixture of 4-cyano-4-(phenylcarbonothioylthio)pentanoic acid (3.0 mg, 0.02 mmol), PDS (1.25 g, 4.9 mmol), polyethylene glycol monomethyl ether methacrylate (1.0 g, 2.1 mmol) and AIBN (2.5 mg, 0.014 mmol) was dissolved in THF (5 mL) and degassed by performing three freeze-pump-thaw cycles. The reaction mixture was sealed and then transferred into a pre-heated oil bath at 65 ℃ and stirred for 10 h. To remove unreactive monomers, the resultant mixture was precipitated in cold ethyl ether (20 mL) to yield the random copolymer as a waxy liquid. GPC (THF) M_n: 13 kDa; PD: 1.3. ^{1}H NMR (400 MHz, $CDCl_3$) δ: 8.46, 7.68, 7.11, 4.35-4.09, 3.94-3.37, 3.03, 2.04-1.64, 1.43-0.87. The molar ratio between two monomer units was determined by integrating the methoxy protons in the polyethyleneglycol unit and the aromatic protons in the pyridine and found to be 3:7 (PEG:PDS).

4.4.4 Synthesis of random copolymer with primary amine groups

A mixture of 4-cyano-4-(phenylcarbonothioylthio) pentanoic acid (5.5 mg), PDS (75 mg), polyethylene glycol monomethyl ether methacrylate (107 mg), 2-(diisopropylamino) ethyl methacrylate (65 mg), 2-Aminoethyl methacrylate hydrochloride (4mg) and AIBN (0.6 mg) was dissolved in DMF (0.5 mL) and degassed by performing three freeze-pump-thaw cycles. The reaction mixture was sealed and then transferred into a pre-heated oil bath at 65 ℃ and stirred for 10 h. To remove unreactive monomers, the resultant mixture was precipitated in cold ethyl ether (20 mL) to yield the random copolymer as a waxy solid.

4.4.5 Encapsulation of DiI/DiO in nanogels

The polymer (10 mg) was dissolved in 1 mL water. To this solution, either a 0.02 mL of DiI stock solution (5mg/mL in acetone) or 0.04 mL DiO stock solution (2.5 mg/mL in acetone) was added into the polymer solution. The pH was adjusted by adding drops of HCl or NaOH solution (1M). The mixed solution was stirred overnight at room temperature, open to the atmosphere allowing the organic solvent to evaporate. Then a measured amount of DTT was added. After stirring for 4 hours, insoluble DiI/DiO was removed by filtration and pyridinethione was removed from the nanogel solution by extensive dialysis using a membrane with a molecular weight cutoff of 7,000 g/mol.

4.4.6 Synthesis of fluorescein-labeled DPA nanogels

The blank DPA nanogel was made by using amine group containing polymer (10 mg/mL) using the procedures outlined above. Then excess FITC was added into the nanogel solution. After stirring for 24 hours, excess FITC was removed from the nanogel solution by extensive dialysis using a membrane with a molecular weight cutoff of 7,000 g/mol.

4.4.7 DLS measurement

Dynamic light scattering experiments were performed by using a digital correlator and goniometer. The light source was solid-stat laser system, operating at 514 nm. For size

measurements, the nanogels in deionized water (1 mg/mL) was kept constant at 25 ℃ throughout the experiment. Dust was eliminated by filtering the solution through 0.45 μm polycarbonate filter. All measurements were done at a correlation time of 30 seconds. For zeta potential measurements, the pH was adjusted by adding drops of HCl or NaOH solution (1M). The nanogels solution was also kept constant at 25 ℃ throughout the experiment.

4.4.8 Dye exchange experiment

A solution of nanogel containing DiI (100 μL) was mixed with a solution of nanogel containing DiO (100 μL) in a cuvette, and then milliQ water (800 μL) was added to adjust the volume. The fluorescence spectra were recorded using the excitation wavelength of 450 nm.

4.4.9 DiI release experiment

A solution of nanogel containing DiI (100 μL) was mixed with a buffer solution with pH 6 or 7.4 (800 μL) in a cuvette, and then DTT stock solution (100 μL) was added. The fluorescence spectra were recorded using the excitation wavelength of 530 nm.

4.4.10 Confocal experiments

Confocal experiments were done using Zeiss510 META confocal laser scanning microscope. 100k HeLa cells were incubated in glass bottomed dishes, purchased from Mat tek corp, at 37 ℃ overnight in 5% CO_2 incubator allowing the cells stick to the bottom of dish. Then, the nutrient medium was taken out and cells were washed with 5 mL of pH 7.4 PBS buffer. In one of the confocal dish, the pH of 1 mL of nutrient media was adjusted to 6.5. Then, 100uL of 1mg/mL solution of pH sensitive nanogels were added to each of the confocal dishes maintained at pH 6.5 and at pH 7.4. The cells were incubated for 2 hrs at 37 ℃ and the florescence was observed at 560 nm by laser excitation at 543 nm for the DiI encapsulated nanogels and florescence was observed at 501nm by exciting at 480nm for fluorescein-attached nanogels. All images were taken using 63x oil immersion objective.

4.5 References

1. Mutsaers, S. E.; John M. P. Surface charge of macrophages and their interaction with charged particles. *J. Leukocyte Biol.*, **1988**, *44*, 17-26.

2. Richard, J. P.; Melikov, K.; Vives, E.; Ramos, C.; Verbeure, B.; Gait, M. J.; Chernomordik, L. V.; Lebleu, B. Cell-penetrating peptides A reevaluation of the mechanism of cellular uptake. *J. Biol. Chem.*, **2003**, *278*, 585-590.

3. Ulbrich, K.; Subr, V. Polymeric anticancer drugs with pH-controlled activation. *Adv. Drug Delivery Rev*. **2004**, *56*, 1023-1050;

4. Lee, H. J.; Pardridge, W. M. Monoclonal antibody radiopharmaceuticals: cationization, pegylation, radiometal chelation, pharmacokinetics, and tumor imaging. *Bioconjugate Chem.* **2003**, *14*, 546-553;

5. Gu, J.; Cheng, W. P.; Liu, J.; Lo, S. Y.; Smith, D.; Qu, X.; Yang, Z. pH-triggered reversible stealth polycationic micelles. *Biomacromolecules* **2008**, *9*, 255-262;

6. Gao, Y.; Yang, C.; Liu, X.; Ma, R.; Kong, D.; Shi, L. A multifunctional nanocarrier based on nanogated mesoporous silica for enhanced tumor-specific uptake and intracellular delivery. *Macromol Biosci.* **2012**, *12*, 251-259;

7. Ding, C. X.; Gu, J. X.; Qu, X. Z.; Yang, Z. Z. Preparation of multifunctional drug carrier for tumor-specific uptake and enhanced intracellular delivery through the conjugation of weak acid labile linker. *Bioconjugate Chem.* **2009,** *20*, 1163-1170;

8. Bae, Y.; Fukushima, S.; Harada, A.; Kataoka, K. Design of environment-sensitive supramolecular assemblies for intracellular drug delivery: Polymeric micelles that are responsive to intracellular pH change. *Angew. Chem., Int. Ed.*, **2003,** *42*, 4640-4643.

9. Griset, A. P.; Walpole, J.; Liu, R.; Gaffey, A.; Colson Y. L.; Grinstaff, M. W. Expansile nanoparticles: synthesis, characterization, and in vivo efficacy of an acid-responsive polymeric drug delivery system. *J. Am. Chem. Soc.*, **2009**, *131*, 2469-2471;

10. Liu, S.; Weaver, J. V. M.; Tang, Y.; Billingham, N. C.; Armes, S. P.; Tribe. K. Synthesis of shell cross-linked micelles with pH-responsive cores using ABC triblock copolymers. *Macromolecules*, **2002,** *35*, 6121-6131.

11. Choi, S. W.; Zhang, Y.; Xia, Y. N. A temperature-sensitive drug release system based on phase-change materials. *Angew. Chem., Int. Ed.*, **2010**, *49*, 7904-7908.

12. Bikram, M; West, J. L. Thermo-responsive systems for controlled drug delivery. *Expert Opin Drug Deliv.* **2008**, *10*, 1077-1091;

13. Nakayama, M.; Okano, T.; Miyazaki, T.; Kohori, F.; Sakai, K.; Yokoyama, M. Molecular design of biodegradable polymeric micelles for temperature-responsive drug release. *J. Controlled Release*, **2006**, *115*, 46–56.

14. Lee, Y.; Fukushima, S.; Bae, Y.; Hiki, S.; Ishii, T.; Kataoka, K. A protein nanocarrier from charge-conversion polymer in response to endosomal pH. *J. Am. Chem. Soc.* **2007,** *129*, 5362-5363;

15. Xiong, M. H.; Bao, Y.; Yang, X. Z.; Wang, Y. C.; Sun, B. L.; Wang, J. lipase-sensitive polymeric triple-layered nanogel for on-demand drug delivery. *J. Am. Chem. Soc.,* **2012**, *134*, 4355-4362;

16. Wang, C.; Chen, Q.S.; Wang, Z. Q.; Zhang, X. An enzyme-responsive polymeric superamphiphile. *Angew. Chem. Int. Ed.,* **2010**, *49*, 8612-8615;

17. Dong, W.; Kishimura, A.; Anraku, Y.; Chuanoi, S.; Kataoka, K. Monodispersed polymeric nanocapsules: spontaneous evolution and morphology transition from reducible hetero-PEG PICmicelles by controlled degradation. *J. Am. Chem. Soc.,* **2009**, *131*, 3804-3805.

18. Liu, J. Y.; Pang, Y.; Huang, W.; Zhu, Z. Y.; Zhu, X. Y.; Zhou, Y. F.; Yan, D. Y. Redox-responsive polyphosphate nanosized assemblies: a smart drug delivery platform for cancer therapy. *Biomacromolecules*, **2011**, *12*, 2407-2415;

19. Cerritelli, S.; Velluto, D.; Hubbell, J. A. PEG-SS-PPS: reduction-sensitive disulfide block copolymer vesicles for intracellular drug delivery. *Biomacromolecules*, **2007**, *8*, 1966-1972.

20. Tong, R.; Hemmati, H. D.; Langer, R.; Kohane, D. S. Photoswitchable nanoparticles for triggered tissue penetration and drug delivery. *J. Am. Chem. Soc.*, **2012**, *134*, 8848-8855;

21. McCoy, C. P.; Rooney, C.; Edwards, C. R.; Jones, D. S.; Gorman, S. P. Light-triggered molecule-scale drug dosing devices. *J. Am. Chem. Soc.*, **2007**, *129*, 9572-9573;

22. Hu, L. C.; Yonamine, Y.; Lee, S. H.; Van der Veer, W. E.; Shea, K. J. Light-triggered charge reversal of organic-silica hybrid nanoparticles. *J. Am. Chem. Soc.*, **2012**, *134*, 11072-11075;

23. Yamagata, M.; Hasuda, K.; Stamato, T.; Tannock, I. F. The contribution of lactic acid to acidification of tumours: studies of variant cells lacking lactate dehydrogenase. *Br. J. Cancer,* **1998**, *77*, 1726-1731;

24. Helmlinger, G.; Schell, A.; Dellian, M.; Forbes, N. S.; Jain, R. K. Acid production in glycolysis-impaired tumors provides new insights into tumor metabolism. *Clin. Cancer Res.* **2002**, *8*, 1284-1291;

25. Vander, H. M. G.; Cantley, L. C.; Thompson, C. B. Understanding the Warburg effect: the metabolic requirements of cell proliferation. *Science*, **2009**, *324*, 1029-1033;

26. Du, J. Z.; Sun, T. M.; Song, W. J.; Wu, J.; Wang, J. A tumor-acidity-activated charge-conversional nanogel as an intelligent vehicle for promoted tumoral-cell uptake and drug delivery. *Angew. Chem. Int. Ed.*, **2010**, *49*, 3621-3626;

27. Du, J. Z.; Du, X. J.; Mao, C. Q.; Wang, J. Tailor-made dual pH-sensitive polymer_doxorubicin nanoparticles for efficient anticancer drug delivery. *J. Am. Chem. Soc.*, **2011**, *133*, 17560-17563;

28. Yuan, Y. Y.; Mao, C. Q.; Du, X. J.; Du, J. Z.; Wang, F.; Wang, J. Surface charge switchable nanoparticles based on zwitterionic polymer for enhanced drug delivery to tumor. *Adv. Mater.*, **2012**, *24*, 5476-5480;

29. Poon, Z.; Chang, D.; Zhao, X. Y.; Hammond, P. T. Layer-by-layer nanoparticles with a pH-sheddable layer for in vivo targeting of tumor hypoxia. *ACS Nano*, **2011**, *5*, 4284-4292;

30. Ryu, J. -H.; Chacko, R.; Jiwpanich, S.; Bickerton, S.; Babu, R. P.; Thayumanavan, S. Self-crosslinked polymer nanogels: a versatile nanoscopic drug delivery platform. *J. Am. Chem. Soc.* **2010**, *132*, 17227-17235;

31. Ryu, J. -H.; Jiwpanich, S.; Chacko, R.; Bickerton, S.; Thayumanavan, S. Surface-functionalizable polymer nanogels with facile hydrophobic guest encapsulation capabilities *J. Am. Chem. Soc.* **2010**, *132*, 8246-824;

32. Gonz áez-Toro, D. C.; Ryu, J. -H.; Chacko, R. T.; Zhuang, J. M.; Thayumanavan, S. Concurrent binding and delivery of proteins and lipophilic small molecules using polymeric nanogels. *J. Am. Chem. Soc.*, **2012**, *134*, 6964-6967;

33. Ryu, J. H.; Bickerton, S.; Zhuang, J. M.; Thayumanavan, S. Ligand-decorated nanogels: fast one-pot synthesis and cellular targeting. *Biomacromolecules*, **2012**, *13*, 1515-1522;

34. Oh, J. K.; Siegwart, D. J.; Lee, H.; Sherwood, G.; Peteanu, L.; Hollinger, J. O.; Kataoka, K.; Matyjaszewski, K. Biodegradable nanogels prepared by atom transfer radical polymerization as potential drug delivery carriers: synthesis, biodegradation, in vitro release, and bioconjugation. *J. Am. Chem. Soc.*, **2007**, *129*, 5939-5945.

35. Hu, Y. Q.; Kim, M. S.; Kim, B. S.; Lee, D. S. Synthesis and pH-dependent micellization of 2-(diisopropylamino)ethyl methacrylate based amphiphilic diblock copolymers via RAFT polymerization. *Polymer*, **2007,** *48*, 3437-3443;

36. Du, J. Z.; Tang, Y. Q.; Lewis, A. L.; Armes, S. P. pH-Sensitive vesicles based on a biocompatible zwitterionic diblock copolymer. *J. Am. Chem. Soc.*, **2005**, *127*, 17982-17983;

37. Radovic-Moreno, A. F.; Lu, T. K.; Puscasu, V. A.; Yoon, C. J.; Langer, R.; Farokhzad, O. C. Surface charge-switching polymeric nanoparticles for bacterial cell wall-targeted delivery of antibiotics. *ACS Nano*, **2012,** *6*, 4279-4287.

38. Bahadur, K. C. R.; Xu, P. Multicompartment intracellular self-expanding nanogel for targeted delivery of drug cocktail. *Adv. Mater.*, **2012**, *24*, 6479-6483.

39. Li, L.; Ryu, J. -H.; Thayumanavan, S. Effect of Hofmeister ions on the size and encapsulation stability of polymer nanogels. *Langmuir*, **2013**, *29*, 50-55.

40. Li, Y.; Song, Y.; Zhao, L.; Gaidosh, G.; Laties, A. M.; Wen, R. Direct labeling and visualization of blood vessels with lipophilic carbocyanine dye DiI. *Nat. Protoc.*, **2008,** *3*, 1703-1708.

41. Jiwpanich, S.; Ryu, J. H.; Bickerton, S.; Thayumanavan, S. Noncovalent encapsulation stabilities in supramolecular nanoassemblies. *J. Am. Chem. Soc.*, **2010**, *132*, 10683-10685;

42. Ghosh, S.; Basu, S.; Thayumanavan, S. Simultaneous and reversible functionalization of copolymers for biological applications. *Macromolecules* **2006**, *39*, 5595-5597.

CHAPTER 5

PHOTOINDUCED HETERODISULFIDE METATHESIS FOR REAGENT-FREE SYNTHESIS OF POLYMER NANOPARTICLES

Li, L.; Song, C.; Jennings, M.; Thayumanavan, S. Photoinduced heterodisulfide metathesis for reagent-free synthesis of polymer nanoparticles. *Chem. commun.* **2015**, *51*, 1425-1428. - Reproduced by permission of The Royal Society of Chemistry

http://pubs.rsc.org/en/content/articlehtml/2015/cc/c4cc08000a

5.1 Introduction

Metathesis reactions have found utility in many synthetic and supramolecular chemistry strategies. For example, diene metathesis has found use in the syntheses of polymers and small molecules,[1-7] while strategies such as imine[8-13] and hydrazone[14-18] metathesis reactions have found use in supramolecular chemistry and dynamic combinatorial chemistry, among others. All these reactions are reversible under the reaction conditions and this provides the opportunity to obtain the thermodynamically favorable structures, under a given set of conditions. For example, the host identification process for a guest molecule in a dynamic combinatorial chemistry reaction is driven by the templation by the guest molecule to select for a specific host structure among the myriad possibilities. Disulfide metathesis reactions have also been used in this context both by Mother Nature for stabilizing the desired protein secondary and tertiary structures[19-21] and for identifying optimal host geometries in supramolecular chemistry.[22-25] More recently, the photolabile nature of disulfides has been exploited to produce bulk hydrogels from oligomeric disulfidemolecules and polymeric disulfides.[24] Although this has provided very interesting materials in their own respect, this observation also indicates a rather uncontrolled nature of photoinduced disulfide metathesis reactions. We sought to develop a photoinduced disulfide metathesis reaction that can provide greater control such that we can achieve well defined, crosslinked polymeric nanostructures and have outlined our findings in this chapter.

Photochemically driven reactions are interesting, because these are reagentless reactions. Photoreactions, based on the dimerization of thymine[26] and coumarin[27-29] or benzophenone moieties,[30] have been used quite extensively. The dimerization reactions are reverted by a higher energy photochemical irradiation, while the reactive radicals generated from benzophenone often provide irreversible products. The photoinduced disulfide formation reaction has the potential of being initiated by a photochemical reaction, but being reverted by a biologically relevant stimulus, such as the redox potential of the intracellular environment.[31-35]

Photochemical reactivity of disulfides has been known for several decades.[36-42] Disulfides are thought to undergo homolytic cleavage, giving thio radicals, which can attack nearby disulfide bonds, resulting in disulfide exchange under photoirradiation.[24, 37, 40] We were interested in exploring this photoinduced metathesis of disulfide molecules containing pyridyl disulfide (PDS) units. PDS units are well known for their unreactive byproduct, pyridothione, formed during disulfide exchange reactions, which provides the opportunity for reliably generating unsymmetrical disulfides.[43, 44] However, it is not clear whether such a possibility exists in a photochemical disulfide metathesis reaction. In fact, ultraviolet (uv) irradiation of 2,2'-dipyridyldisulfide (DPDS) results in the formation of pyridine-2- sulfonic acid, presumably due to oxidation.[45, 46] This suggests that hydrogen abstraction by the thio radical is much slower than the oxidation reaction. Considering that pyridyl groups are relatively electron poor compared to the alkyl groups, we were also concerned that the homolytic cleavage of the disulfide bond between an alkyl group and a pyridyl group will result in the formation of two sulfonic acids.

5.2 Results and Discussion

5.2.1 Photo-induced disulfide metathesis of 2-hydroxyethyl-*o*-pyridyl disulfide

To investigate the possibility, we first used the photochemical reaction of 2-hydroxyethyl-*o*-pyridyl disulfide (PDS-OH, 1) as amodel system. A solution of 2.5 mg/mL of 1 in CD_3OD was irradiated using a UV lamp (15W) equipped with a 350 nm light source. If this reaction were a

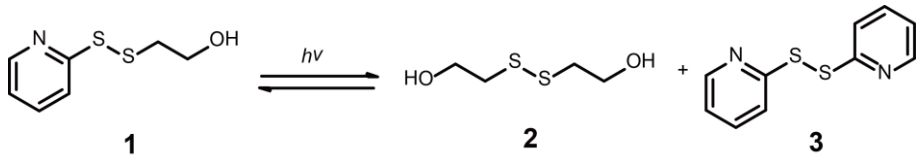

Scheme 5.1 Hypothesized reaction scheme of photo-induced disulfide metathesis of 2-pyridyl disulfide (PDS-OH).

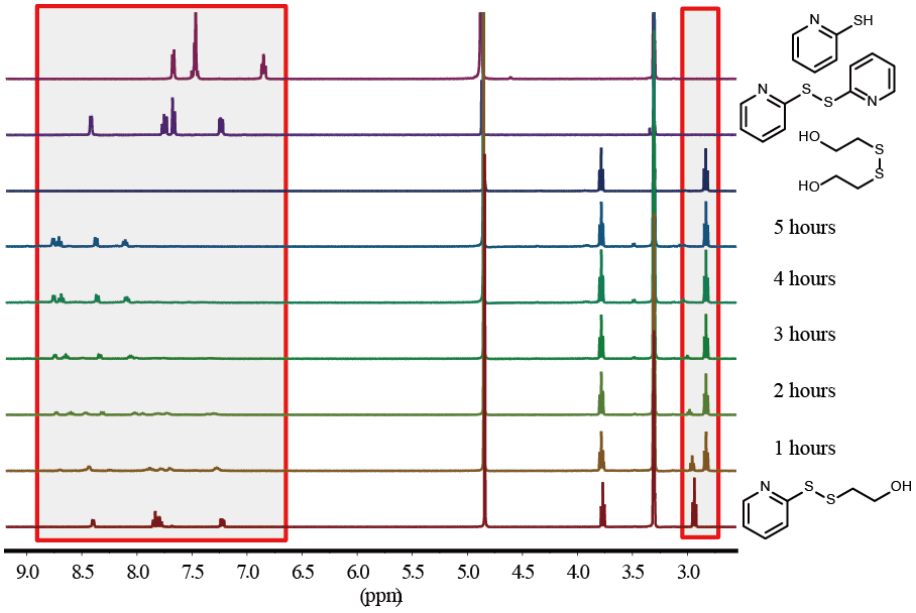

Figure 5.1 Time-dependent 1H NMR spectra of the photo-induced reaction of 2-hydroxyethyl 2-pyridyl disulfide (PDS-OH, **1**). Control spectra of bis(2-hydroxyethyl) disulfide (DPDS, **2**), 2, 2'-dipyridyl disulfide (**3**) and 2-thiopyridone were also included. The concentration was 2.5 mg/mL. The final product after photoirradiation was determined to be pyridine-2-sulfonic acid (**4**).

purely disulfide exchange reaction due to thio radical formation and then recombination, molecule 1 would have been in equilibrium with bis(2-hydroxyethyl) disulfide (2) and DPDS (3). Ideally, a statistical ratio of 2 : 1 : 1 of products 1-3 would be obtained (Scheme 5.1). However, the starting material 1 was being continuously consumed with a concurrent increase in the concentration of 2. As shown in the ^{1}H NMR spectra over the irradiation time (Figure 5.1), the integrated signal intensity of the triplet at 2.94 ppm, arising from the CH_2 protons attached to sulfur in 1, decreased with the corresponding increase in the intensity of the triplet at 2.83 ppm (the same CH_2 protons in 2). Finally, the disappearance of the peak at 2.94 ppm showed that no starting material (1) remained in the reaction mixture. Also, there is no evidence of the formation

of DPDS (3) in the reaction mixture. However, we did find that the formation of 2 was accompanied by the formation of pyridine-2-sulfonic acid (4) (Scheme 5.2). Finally, we found that the percent conversion in this reaction was lower at higher concentrations (Figure 5.2). This is typical of photochemical reactions as the fluence of light was kept the same in all these reactions. Two features are readily discerned from these observations: (*i*) no equilibrium is observed in this photoinduced disulfide metathesis and (*ii*) while the pyridylthio radical is readily oxidized, the alkylthio radical undergoes a radical recombination reaction to produce 2. These initial observations are encouraging for the use of heterodisulfides containing PDS units for controlled polymer nanoparticle synthesis.

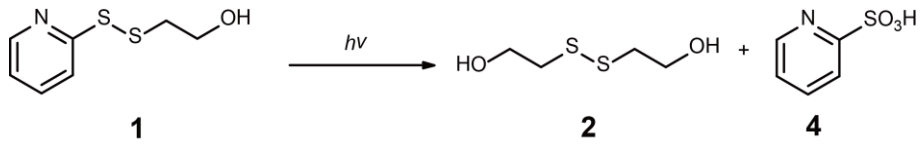

Scheme 5.2 Scheme of photo-induced chemistry reaction of PDS-OH.

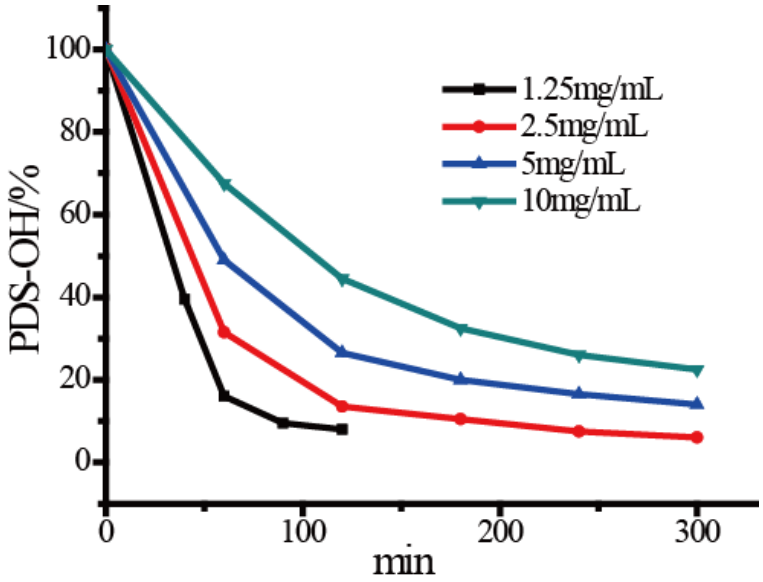

Figure 5.2 Concentration dependent of reaction rate of PDS under photoirradiation.

Prior to utilizing this in nanoparticle synthesis however, we were interested in investigating the reasons for the observed oxidation of the pyridylthio radical. Presumably, this oxidation is

caused by the oxygen in the reaction mixture. To check this hypothesis, we excluded oxygen from the reaction by performing three freeze-pump-thaw cycles. Analysis of the PDS-OH (1) photochemical reaction under these conditions shows that the product generation has become seemingly slower than that in the reaction where oxygen was not rigorously removed (Figure 5.3).

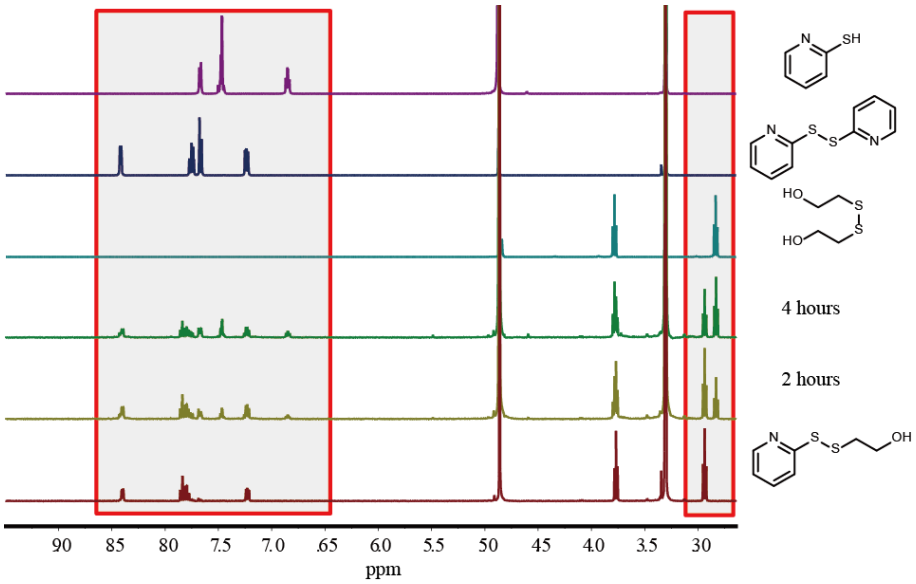

Figure 5.3 Time-dependent 1H NMR spectra of the photo-induced disulfide metathesis of 2-hydroxyethyl 2-pyridyl disulfide (PDS-OH, **1**) under anaerobic condition. Control spectra of bis(2-hydroxyethyl) disulfide (**2**), 2, 2'-dipyridyl disulfide (DPDS, **3**) and 2-thiopyridone were also included. The concentration was 2.5 mg/mL.

Even after 4 hours of irradiation, there was still 50% of starting material 1 left in the reaction, consistent with a reaction in equilibrium. Note that the starting material 1 was completely consumed in about 2 hours without oxygen exclusion. In addition to the expected DPDS (3) product, there were additional peaks in the aromatic region for this reaction mixture, as shown in Figure 5.3. NMR analysis of this reaction mixture indicates that the formation of the byproduct in this reaction is indeed due to hydrogen abstraction by the pyridylthio radical to generate pyridothione (Scheme 5.3). In fact, we have shown that direct irradiation of DPDS (3), after the freeze–pump–thaw cycles, cleanly produces pyridothione rather than 4 (Figure 5.4). Several observations are noteworthy here: (*i*) the thio radical from pyridine undergoes oxidation to form pyridine-2-sulfonic acid (4) under ambient conditions; (*ii*) this reaction can be mitigated by

rigorously excluding oxygen from the reaction mixture; and (*iii*) in the absence of oxygen, the pyridylthio radical undergoes both radical recombination (evidenced by the formation of DPDS from 1) and hydrogen abstraction (evidenced by the formation of pyridothione from 1 and from DPDS irradiation).

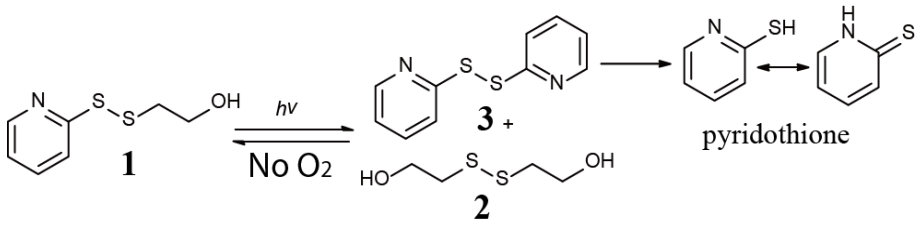

Scheme 5.3 Scheme of photo-induced chemistry reaction of 2-pyridyl disulfide (PDS-OH) under anaerobic condition.

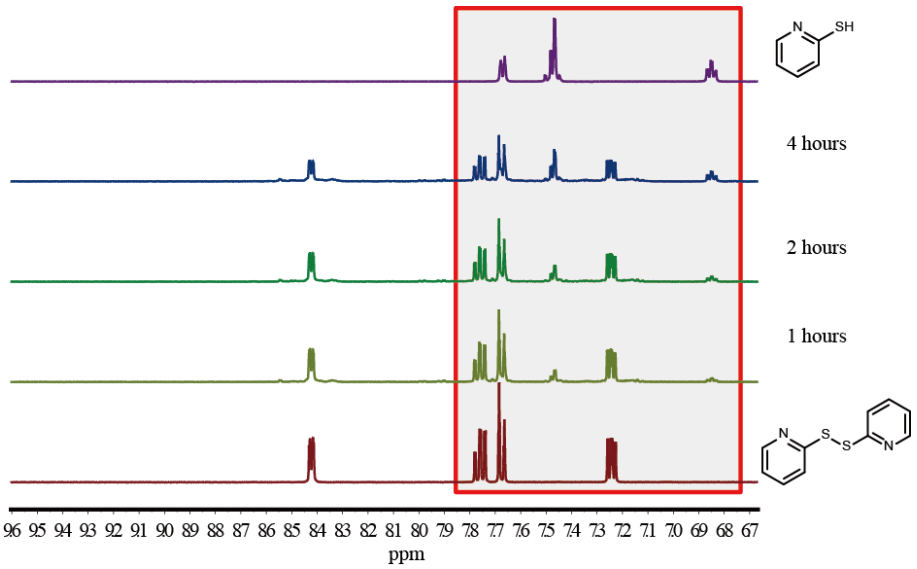

Figure 5.4 Time-dependent ^{1}H NMR spectra of 2, 2'-dipyridyl disulfide (DPDS) under the photoirradiation without O_2.

Overall, photochemical irradiation of PDS-OH (1) results in the homolytic cleavage of the disulfide bond to generate a pyridyl and an aliphatic thio radical. The aliphatic radical undergoes rapid recombination to generate the corresponding disulfide. However, the stability provided by resonance in the thiopyridyl radical seems to be sufficient to slow down radical recombination or hydrogen abstraction, but is not sufficient to inhibit oxidation to the corresponding sulfonic acid 4. In the absence of the oxidative pathway, this radical ultimately undergoes radical recombination

and hydrogen abstraction. These latter processes also provide the opportunity for the photochemical reaction of 1 to be in equilibrium and thus slow down the conversion of the starting material to the product. In other words, the oxidized byproduct serves to drive the equilibrium towards the right in the reaction of 1. Therefore, in reactions where we need the thiopyridyl byproduct to be continuously removed, the reaction should be carried out without excluding oxygen (vide infra).

5.2.2 Preparation of nanogels via photo-induced crosslinking reaction

Encouraged by these observations, we then envisaged the possibility of utilizing this methodology for preparing crosslinked polymer nanoparticles. We wanted to test this for a well-characterized polymer and polymer nanoparticles so that the validation of this methodology is robust. A 3 : 7 random copolymer of the oligoethylene glycol methacrylate monomer (5) and the PDS-ethylmethacrylatemonomer (6), shown as structure 7 in Scheme 5.4, has been shown to form micelle-like assemblies in water.[33, 44, 47] These assemblies have been previously shown to be also crosslinked to form polymer nanogels, triggered by the thiol exchange reaction with dithiothreitol (DTT).

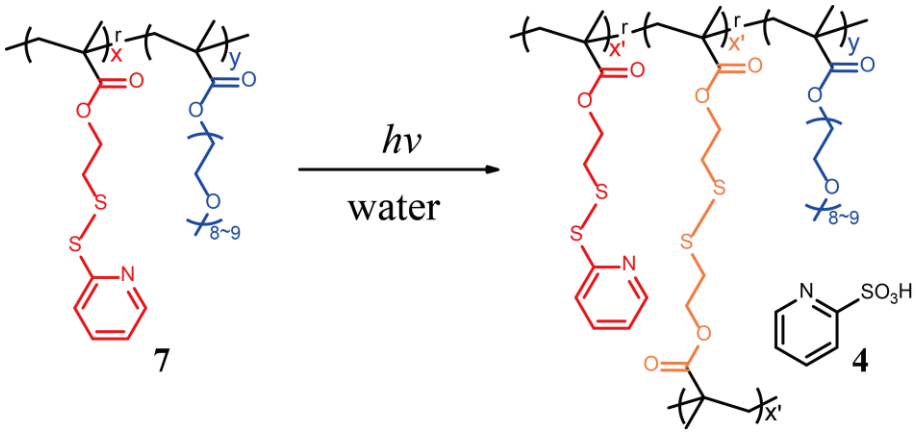

Scheme 5.4 Representation of photo-induced crosslinking reaction of random copolymers containing PDS groups.

A solution of polymer 7 (1 mg/mL) in water was found to aggregate to form assemblies with a hydrodynamic diameter of 9 nm, as discerned by dynamic light scattering (Figure 5.5). This

solution was subjected to irradiation in a photochemical reaction chamber at 350 nm for 2 hours. At this time, the size of the assemblies was assessed by DLS again and was found to be 13 nm, which is close to the size of the aggregates prior to crosslinking (Figure 5.5b). This observation suggests that the disulfide metathesis occurs sufficiently fast such that the crosslinking reaction is mostly intra-aggregate. The slight increase in the size could be the result of a small amount of inter-aggregate crosslinking or the swelling that is likely to occur in crosslinked nanoparticles, when the hydrophobic components are reduced. Alternatively, this increase in the size could also be attributed to the adventitious heating that occurs during photochemical irradiation of the sample. This latter possibility is consistent with the increase in the size of PEG-based assemblies at higher temperatures.[44, 47]

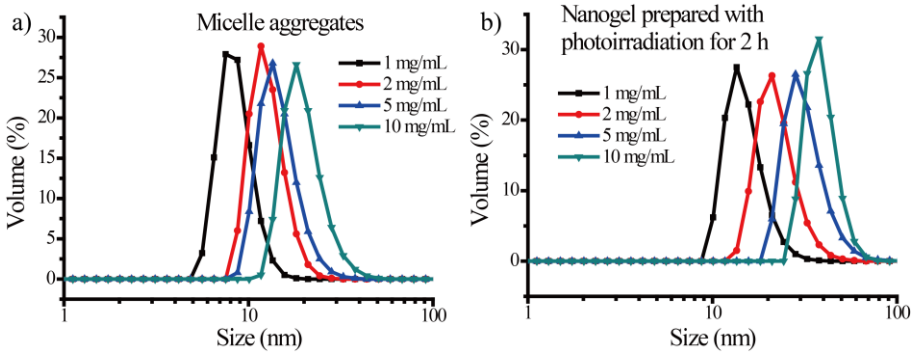

Figure 5.5 DLS sizes in hydrodynamic diameter, a) micelle aggregates prepared with polymer solutions with different concentrations, b) nanogels prepared with polymer solutions with different concentrations, the photoirradiation time was 2 h for all samples.

If it is indeed due to temperature variations and not due to the inter-aggregate reaction, we should be able to systematically tune the size of the nanoparticles by varying the concentration of the polymer. Indeed, when we varied the sample concentrations from 1 mg/mL to 10 mg/mL, the size of the micelle aggregates increased from 9 nm to 20 nm with increasing concentrations (Figure 5.5a). Upon irradiation, the size of the nanogels was only slightly increased from 20 nm to 38 nm even at a concentration of 10 mg/mL (Figure 5.5b). If the observed increase in the size at 1 mg/mL were due to inter aggregate crosslinking, then with an increase in the concentration

by an order of magnitude, the size of the nanoparticles should have been substantially increased or even formed bulk gels. Instead, there was only a slight increase in size. This suggests that the observed increase in the size upon crosslinking is most likely due to the increase in solution temperature, and the photoinduced crosslinking is predominantly intra-aggregate.

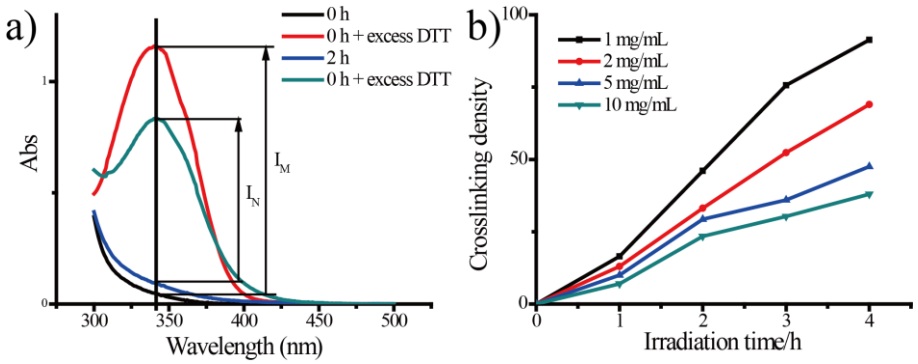

Figure 5.6 a) Absorption spectra of pyridothione in UV-vis. Pyridothione, which is a byproduct by the reaction between PDS with DTT and shows characteristic absorption at 343 nm wavelength, is monitored in each nanogel (2 mg/mL) prepared. b) Time dependent crosslinking density of the nanogels with different concentrations of polymer solution, from 1 mg/mL to 10 mg/mL.

Table 5.1 Calculated crosslinking densities for nanogels.

	Crosslinking density/%			
concentration	1 h	2 h	3 h	4 h
1 mg/mL	16	46	76	91
2 mg/mL	13	33	52	69
5 mg/mL	10	29	36	48
10 mg/mL	7	23	30	38

Next, we were interested in estimating the crosslink density in the nanoparticles. We utilized the residual PDS units present in the polymer nanoparticles to estimate this. According to our analysis, upon using the small molecule model system mentioned above, the pyridylthio radical gets converted to pyridine-2-sulfonic acid 4. The unreacted PDS in the polymer can be treated

with a thiol to reliably generate pyridothione, which can be readily monitored spectroscopically due to its distinct absorption peak at 343 nm.[43] The concentration of pyridothione generated then gives us the amount of unreacted PDS in the mixture. As shown in Figure 5.6a, there was very little difference between the absorption spectra before and after photoirradiation. However, the addition of excess DTT into both samples resulted in a significant difference between the intensities of the absorption peak at 343 nm due to the difference in the extent of pyridothione generated. The crosslinking density was then calculated using the ratio of these intensities. If I_N is the increased intensity at 343 nm of the irradiated sample obtained by adding excess DTT, while I_M is that of the unirradiated sample, then the crosslinking density was calculated from I_N/I_M. Thus, the crosslinking density of the nanoparticles was found to be 33% after photoirradiation for 2 hours, when the concentration of the polymer was 2 mg/mL. The crosslinking density could be systematically varied using different irradiation times, as shown in Figure 5.6b and table 5.1. Interestingly, the crosslink density scales much slower with irradiation time at higher concentrations (Figure 5.6b). This might seem to be counterintuitive at first, because reactions seem to be slower at higher concentrations. This is indeed consistent with photochemical reactions between small molecules (Figure 5.2), because we are measuring the percent conversion of the starting material and the reagent here is light, which is constant at all different concentrations.

5.2.3 Encapsulation capability and redox-responsive behavior

To test if the difference in the extent of PDS generation is indeed due to crosslinking, we incorporated hydrophobic guest molecules inside these nanogels prior to the photoirradiation. With the dye molecules, DiI, incorporated into the nanoparticles, the guest molecules were found to be stably encapsulated in the nanoparticles over a time period of 24 hours, even after a 10-fold dilution (Figure 5.7a). However, when glutathione (GSH) was added to this solution at 10 mM concentration, the guest molecules seem to be releasing over time (Figure 5.7b).

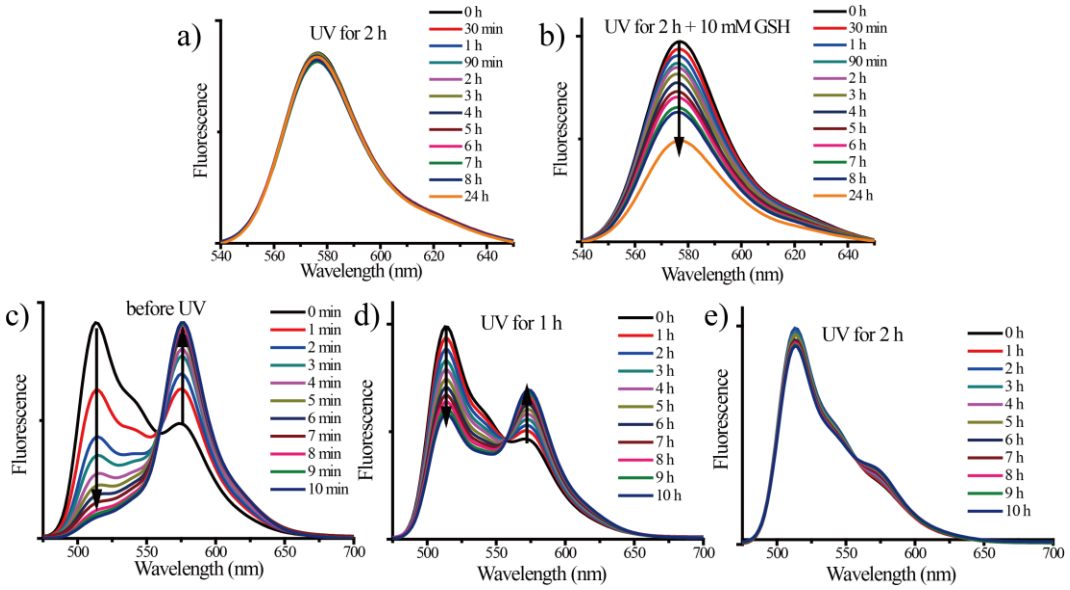

Figure 5.7 Dye release from the nanogels prepared via photoirradiation for 2 h in response to varied GSH concentrations, a) 0 mM; b) 10 mM. Sample concentration was 0.1 mg/mL. FRET experiment based DiI/DiO exchange, c) micelle aggregates; d) nanogels prepared via photoirradiation for 1 h; e) nanogels prepared via photoirradiation for 2 h. Sample concentration was 0.1 mg/mL.

To further confirm that the encapsulation stability could be easily tuned by simply varying the irradiation time, a fluorescence resonance energy transfer (FRET) based encapsulation stability assay was carried out.[48] In this experiment, a faster FRET evolution suggests leaky nanoparticles, while an unchanged FRET over time suggests stably encapsulated guests inside the nanoparticles. Indeed, we observed that there was a rapid evolution of FRET with time in the micelle aggregates without any photoirradiation (Figure 5.7c), compared to that in the nanoparticles prepared after 1 hour of irradiation (Figure 5.7d). The evolution of FRET was even slower after 2 hours of irradiation (Figure 5.7e), suggesting that the encapsulation stability can indeed be tuned by varying the irradiation time.

5.3 Summary

In summary, we have demonstrated that: (*i*) PDS-containing asymmetrically substituted disulfides can be homolytically cleaved by photochemical irradiation; (*ii*) although the alkyl substituted thio radical consistently undergoes radical recombination, the reactivity of the

pyridylthio radical is dependent on the presence of oxygen; (*iii*) in the presence of oxygen, the pyridylthio radical gets converted to pyridine-2-sulfonic acid, while it undergoes hydrogen abstraction or radical recombination in deoxygenated solutions; (*iv*) the oxidation reaction also provides a pathway for driving the equilibrium towards the desired product; (*v*) this feature was used for the reagentless synthesis of crosslinked polymer nanoparticles; (*vi*) the size of the nanoparticles can be conveniently varied by tuning the size of the nanoaggregates, because the photo-induced crosslinking was predominantly intra-aggregate; and (*vii*) the crosslink density and encapsulation stability of these nanoparticles can be simply varied by altering the irradiation time. In addition to the typical advantages of a reagentless reaction, the fact that this reaction is carried out in water and that the byproduct of this reaction is a highly water-soluble sulfonic acid that can be easily removed by dialysis suggests that this methodology offers a promising new approach for nanoparticle synthesis. Since the crosslinks generated here are biologically relevant, this method could also have implications in generating new materials of interest in biology and medicine.

5.4 Experimental

5.4.1 General Methods

2,2-Dithiodipyridine, 2-mercaptoethanol, polyethyleneglycol monomethylether methacrylate (PEGMA, M_W 450 g/mol), D,L-dithiothreitol (DTT), 1,1'-dioctadecyl-3,3,3',3'-tetramethylindocarbocyanine perchlorate (DiI) and 3,3'-dioctadecyloxacarbocyanine perchlorate (DiO), 4-Cyano-4-(phenylcarbonothioylthio)-pentanoic acid and other conventional reagents were obtained from commercial sources and were used as received without further purification. The 2,2'-azobisisobutyronitrile (AIBN) was purified by recrystallization from ethanol. ^{1}H-NMR spectra were recorded on a 400 MHz Bruker NMR spectrometer using the residual proton resonance of the solvent as the internal standard. Chemical shifts are reported in parts per million (ppm). Molecular weights of the polymers were estimated by gel permeation chromatography (GPC) using PMMA standard with a refractive index detector. Dynamic light scattering (DLS)

measurements were performed using a Malvern Nanozetasizer. UV-visible absorption spectra were recorded on a Varian (model EL 01125047) spectrophotometer. The fluorescence spectra were obtained from a JASCO FP-6500 spectrofluorimeter.

5.4.2 Synthesis of 2-hydroxyethyl 2-pyridyl disulfide (PDS-OH) and 2-thiopyridone

PDS-OH was synthesized according to the previous report.[49] 2, 2'-dipyridyl disulfide (DPDS) (10.3 g, 0.047 mol) was dissolved in 100 mL of methanol. Then 1.2 mL of glacial acetic acid, used as catalyst, was added. To this mixture, a solution of mercaptoethanol (4.4 g, 0.056 mol, 4 mL) in 100 mL methanol was added drop-wise at room temperature with continuous stirring. Once the addition was over, the reaction mixture was stirred at room temperature overnight. The stirring was stopped; solvent was evaporated to get the crude product as yellow oil which was purified by flash column chromatography using silica gel as stationary phase and mixture of ethyl acetate/hexane as eluent. When the polarity of the eluent was increased to 40% ethyl acetate/hexane, the desired product came out as colorless oil. Yield : 80 % ^{1}H NMR: (CD_3OD, 400 MHz), δ (ppm): 8.40 (m, 1H, aromatic proton ortho-N), 7.84 (m, 1H, aromatic proton meta-N), 7.80 (m, 1H, aromatic proton para-N), 7.22 (m, 1H, aromatic proton, ortho-disulfide linkage), 3.77(t, 2H, -CH_2OH), 2.94 (t, 2H, -SS-CH_2-).

2-thiopyridone can also be prepared at the same time by continually increasing the polarity of the eluent up to 55% ethyl acetate/hexane to get the desired product. After concentrating the solution, light yellow Needle-shaped crystals were got. ^{1}H NMR: (CD_3OD, 400 MHz), δ (ppm): 7.67 (m, 1H), 7.47 (m, 2H), 6.85 (m, 1H).

5.4.3 Synthesis of PDS monomer

PDS monomer was also synthesized according to the previous report.[49] To a solution of PDS-OH (12 g, 64.1 mmol) in 50 mL of dry dichloromethane was added 7.8 g (76.9 mmol) of triethylamine. The mixture was firstly cooled in an ice-bath. To this cold mixture, a solution of methacryloyl chloride (6.7 g, 64.1 mmol) in 25 mL dichloromethane was then added drop-wise

with continuous stirring. After the addition was over the reaction mixture was stirred at room temperature overnight. The stirring was stopped and the reaction mixture was washed with 3x100 mL distilled water and then with 100 mL of brine. The organic layer was collected, dried over anhydrous Na_2SO_4 and concentrated to get the crude product as yellow oil. It was purified by column chromatography using silica gel as stationary phase and mixture of ethyl acetate/hexane as eluent. The pure product was collected at 30 % ethylacetate/hexane. Yield: 80 % ^{1}H NMR: ($CDCl_3$, 400 MHz), δ (ppm): 8.52 (m, 1H, aromatic proton ortho-N), 7.62-7.83 (m, 2H, aromatic proton meta-N and para-N), 7.15 (m, 1H, aromatic proton, orthodisulfide linkage), 6.23 (d, 1H, vinylic proton, cis-ester), 5.65(d, 1H, vinylic proton, trans-ester) 4.41 (t, 2H, -S-S-CH_2CH_2O-), 3.13 (t, 2H, -S-S-CH_2CH_2O-), 1.91(s, 3H, methyl proton of the methacryloyl group).

5.4.4 Synthesis of random copolymer containing PDS groups

Random copolymers were prepared by reversible addition−fragmentation chain transfer (RAFT) polymerization.[47] A mixture of 4-cyano-4-(phenylcarbonothioylthio)pentanoic acid (24 mg, 0.086 mmol), poly(ethylene glycol) monomethyl ether methacrylate (0.4 g, 0.84 mmol), PDS (0.537 g, 2.1 mmol), and 2,2′-azobis(isobutyronitrile) (AIBN; 2.8 mg, 0.017 mmol) was dissolved in tetrahydrofuran (THF) (2 mL) and degassed by performing three freeze-pump-thaw cycles. The reaction mixture was sealed and then transferred into a preheated oil bath at 65 ℃ for 10 h. To remove unreactive monomers, the resultant mixture was precipitated in cold ethyl ether (20 mL) to yield the random copolymer as a waxy liquid. GPC (THF) M_w, 12 kDa; polydispersity, 1.2. ^{1}H NMR (400 MHz, $CDCl_3$) δ 8.46, 7.68, 7.11, 4.35-4.09, 3.94-3.37, 3.03, 2.04-1.64, 1.43-0.87. The molar ratio between two blocks was determined by integrating the methoxy proton in the poly-(ethylene glycol) unit and the aromatic proton in the pyridine and was found to be 1:2.70 (PEO:PDS).

5.4.5 Time-dependent ^{1}H NMR measurement

In 5mm NMR tubes, 1 mL of samples with different concentrations was added. ^{1}H-NMR spectra were recorded on a 400 MHz Bruker NMR spectrometer using the residual proton resonance of the solvent as the internal standard. These tubes were put inside UV chamber (SYLVANIA F15T8/350/BL, 15w). After each 1 hour's photoirradiation, another NMR spectrum for each sample was taken with the same parameters. The integrations of peak at 2.94 ppm and peak at 2.83 ppm were used to determine the percent of remaining PDS-OH.

5.4.6 Nanoparticles preparation

1 mL of polymer solution of different concentrations was added to a 7 mL vial. These vials were then put inside an UV chamber (SYLVANIA F15T8/350/BL, 15w). After photoirradiation for certain times, nanoparticles with different sizes were formed in solutions. The crosslinking density could be determined by taking some volume of polymer solution from the above solutions into cuvettes for UV-vis measurement. The concentration of these samples was all 0.1 mg/mL. Absorption spectra were taken first. Then, excess DTT were added into these samples and then the solution was observed using absorption spectroscopy again after 3 hours, during which all PDS functionalities could be changed to 2-thiopyridine by DTT.

5.4.7 Determination of crosslinking density

In 7mL small glass vial, 1 mL of polymer solution with different concentrations was added. From them, certain volume of polymer solution was taken and then added into cuvettes for UV-vis measurement. The volume was made to 1 mL by adding water. The concentration of these samples was all 0.1 mg/mL. Absorption spectra were taken. Excess DTT were added into these samples, one more absorption spectra were taken after 3 hours, during which all PDS functionalities could be changed to 2-thiopyridine by DTT.

Then these vials were put inside UV chamber (SYLVANIA F15T8/350/BL, 15w). After each 1 hour's photoirradiation, certain volume of polymer solution was taken from the above

solutions and then added into cuvettes for UV-vis measurement. The volume was made to 1 mL by adding water. The concentration of these samples was all 0.1 mg/mL. Absorption spectra were taken. Excess DTT were added into these samples, one more absorption spectra were taken after 3 hours, during which all PDS functionalities could be changed to 2-thiopyridine by DTT.

5.4.8 Redox-responsive guest release experiment

A solution of nanogel containing DiI (100 μL) was mixed with water (800 μL) in a cuvette, and then GSH stock solution (100 μL) was added. The fluorescence spectra were recorded using the excitation wavelength of 530 nm.

For control experiment, A solution of nanogel containing DiI (100 μL) was mixed with water (900 μL) in a cuvette. The fluorescence spectra were recorded using the excitation wavelength of 530 nm.

5.4.9 FRET experiment

A solution of nanogel containing DiI (100 μL) was mixed with a solution of nanogel containing DiO (100 μL) in a cuvette, and then milliQ water (800 μL) was added to adjust the volume. The fluorescence spectra were recorded using the excitation wavelength of 450 nm.

5.5 References

1. Fu, G. C.; Nguyen, S. T.; Grubbs, G. H. Catalytic ring-closing metathesis of functionalized dienes by a ruthenium carbene complex. *J. Am. Chem. Soc.* **1993,** *115,* 9856-9857;

2. La, D. S.; Alexander, J. B.; Cefalo, D. R.; Graf, D. D.; Hoveyda, A. H.; Schrock, R. R. Mo-catalyzed asymmetric synthesis of dihydrofurans. Catalytic kinetic resolution and enantioselective desymmetrization through ring-closing metathesis. *J. Am. Chem. Soc.* **1998,** *120,* 9720-9721;

3. Connon, S. J.; Blechert, S.. Recent developments in olefin cross-metathesis. *Angew. Chem. Int. Ed.* **2003,** *42,* 1900-1923;

4. Mutlu, H.; de Espinosa, L. M.; Meier, M. A. R. Acyclic diene metathesis: a versatile tool for the construction of defined polymer architectures. *Chem. Soc. Rev.* **2011**, *40,* 1404-1445;

5. Wagener, K. B., Boncella, J. M.; Nel, J. G. Acyclic diene metathesis (ADMET) polymerization. *Macromolecules* **1991**, *24,* 2649-2657;

6. Lu, Y.-X.; Guan, Z. Olefin metathesis for effective polymer healing via dynamic exchange of strong carbon–carbon double bonds. *J. Am. Chem. Soc.* **2012,** *134,* 14226-14231;

7. Koh, M. J.; Khan, R. K. M.; Torker, S.; Hoveyda, A. H. Broadly applicable Z- and diastereoselective ring-opening/cross-metathesis catalyzed by a dithiolate Ru complex. *Angew. Chem. Int. Ed.* **2014**, *53*, 1968-1972.

8. Oh, K.; Jeong, K.-S.; Moore, J. S. Folding-driven synthesis of oligomers. *Nature* **2001**, *414*, 889-893;

9. Nishinaga, T.; Tanatani, A.; Oh, K.; Moore, J. S. The size-selective synthesis of folded oligomers by dynamic templation. *J. Am. Chem. Soc.* **2002**, *124*, 5934-5935;

10. Cantrell, G. K.; Meyer, T. Y. Catalytic CN bond formation by metal-imide-mediated imine metathesis. *J. Am. Chem. Soc.* **1998**, *120*, 8035-8042;

11. Meyer, C. D.; Joiner, C. S.; Stoddart, J. F. Template-directed synthesis employing reversible imine bond formation. *Chem. Soc. Rev.* **2007,** *36*, 1705-1723;

12. Janeliunas, D.; van Rijn, P.; Boekhoven, J.; Minkenberg, C. B.; van Esch, J. H.; Eelkema, R. Aggregation-driven reversible formation of conjugated polymers in water. *Angew. Chem. Int. Ed.* **2013**, *52*, 1998-2001;

13. Taynton, P.; Yu, K.; Shoemaker, R. K.; Jin, Y.; Qi, H. J.; Zhang, W. Heat- or water- driven malleability in a highly recyclable covalent network polymer. *Adv. Mater.* **2014**, *26*, 3938–3942.

14. Hirsch, A. K. H.; Buhler, E.; Lehn, J. -M. Biodynamers: self-organization-driven formation of doubly dynamic proteoids. *J. Am. Chem. Soc.* **2012**, *134*, 4177-4183.

15. Folmer-Andersen, J. F.; Lehn, J. -M. Thermoresponsive dynamers: thermally induced, reversible chain elongation of amphiphilic poly (acylhydrazones). *J. Am. Chem. Soc.* **2011**, *133*, 10966-10973.

16. Barrell, M. J.; Campaña, A. G.; von Delius, M.; Geertsema, E. M.; Leigh, D. A. Light-driven transport of a molecular walker in either direction along a molecular track. *Angew. Chem. Int. Ed.* **2011**, *50*, 285-290;

17. Dirksen, A.; Dirksen, S.; Hackeng, T. M.; Dawson. P. E.. Nucleophilic catalysis of hydrazone formation and transimination: implications for dynamic covalent chemistry. *J. Am. Chem. Soc.* **2006**, *128*, 15602-15603;

18. Chung, M.-K.; Hebling, C. M.; Jorgenson, J. W.; Severin, K.; Lee, S. J.; Gagné, M. R. Deracemization of a dynamic combinatorial library induced by (−)-cytidine and (−)-2-thiocytidine. *J. Am. Chem. Soc.* **2008**, *130*, 11819-11827.

19. Markus, G.; Karush, F. The disulfide bonds of human serum albumin and bovine γ-globulin1. *J. Am. Chem. Soc.* **1957**, *79*, 134-139;

20. Rueping, M.; Jaun, B.; Seebach, D. NMR Structure in methanol of a β-hexapeptide with a disulfide clamp. *Chem. Commun.* **2000**, *22*, 2267-2268;

21. Wedemeyer, W. J.; Welker, E.; Narayan, M.; Scheraga, H. A. Disulfide bonds and protein folding. *Biochemistry* **2000**, *39*, 4207-4216.

22. Otto, S.; Furlan, R. L. E.; Sanders, J. K. M. Dynamic combinatorial libraries of macrocyclic disulfides in water. *J. Am. Chem. Soc.* **2000**, *122,* 12063-12064;

23. Otto, S.; Furlan, R. L. E.; Sanders, J. K. M. Selection and amplification of hosts from dynamic combinatorial libraries of macrocyclic disulfides. *Science* **2002**, *297,* 590-593;

24. Li, J.; Carnall, J.; Stuart, M. C. A.; Otto, S. Hydrogel formation upon photoinduced covalent capture of macrocycle stacks from dynamic combinatorial libraries. *Angew. Chem. Int. Ed.* **2011**, *50,* 8384-8386;

25. Basak, D.; Kumar, R.; Ghosh, S. Telechelic poly(disulfide)s and related block copolymer. *Macromol. Rapid Commun.*, **2014**, *35,* 1340-1344.

26. Kuang, H.; He, H.; Hou, J.; Xie, Z.; Jing, X.; Huang, Y. Thymine modified amphiphilic biodegradable copolymers for photo-cross-linked micelles as stable drug carriers. *Macromol. Biosci.* **2013**, *13,* 1593-1600.

27. Chung, J. W.; Lee, K.; Neikirk, C.; Nelson, C. M.; Priestley, R. D. Photoresponsive coumarin-stabilized polymeric nanoparticles as a detectable drug carrier. *Small* **2012**, *8,* 1693-1700;

28. He, J.; Tong, X.; Zhao, Y. Photoresponsive nanogels based on photocontrollable cross-links. *Macromolecules* **2009**, *42,* 4845-4852;

29. Jiang, J.; Qi, B.; Lepage, M.; Zhao, Y. Polymer micelles stabilization on demand through reversible photo-cross-linking. *Macromolecules* **2007**, *40,* 790-792.

30. Kim, J. S.; Youk, J. H. Preparation of core cross-linked micelles using a photo-cross-linking agent. *Polymer* **2009,** *50,* 2204-2208.

31. Chakravarthi, S.; Jessop, C. E.; Bulleid, N. J. The role of glutathione in disulphide bond formation and endoplasmic-reticulum-generated oxidative stress. *EMBO reports* **2006**, *7,* 271-275;

32. Luo, Z.; Cai, K.; Hu, Y.; Zhao, L.; Liu, P.; Duan, L.; Yang, W. Mesoporous silica nanoparticles end‐capped with collagen: redox‐responsive nanoreservoirs for targeted drug delivery. *Angew. Chem. Int. Ed.* **2011**, *50,* 640-643;

33. Ryu, J.-H.; Jiwpanich, S.; Chacko, R.; Bickerton, S.; Thayumanavan, S. Surface-functionalizable polymer nanogels with facile hydrophobic guest encapsulation capabilities. *J. Am. Chem. Soc.* **2010**, *132,* 8246-8247;

34. Li, L.; Raghupathi, K.; Yuan, C.; Thayumanavan, S. Surface charge generation in nanogels for activated cellular uptake at tumor-relevant pH. *Chem. Sci.* **2013**, *4,* 3654-3660;

35. Kabanov, A. V.; Vinogradov, S. V. Nanogels as pharmaceutical carriers: finite networks of infinite capabilities. *Angew. Chem. Int. Ed.* **2009**, *48,* 5418-5429.

36. Milligan, B.; Rivett, D. E.; Savige, W. E. The photolysis of dialkyl sulphides, disulphides, and trisulphides. *Aust. J. Chem.* **1963**, *16,* 1020-1029;

37. Nelander, B.; Sunner, S. Cogwheel effect in dialkyl disulfides. *J. Am. Chem. Soc.* **1972**, *94*, 3576-3577;

38. Lee, Y. R.; Chiu, C. L.; Lin, S. M. Ultraviolet photodissociation study of CH_3SCH_3 and CH_3SSCH_3. *J. Chem. Phys.* **1994**, *100*, 7376-7384;

39. Gupta, D.; Knight, A. R. Reactions of thiyl radicals. XIII. Photochemically induced exchange reactions of liquid alkyl disulfides. *Can. J. Chem.* **1980**, *58*, 1350-1354;

40. Otsuka, H.; Nagano, S.; Kobashi, Y.; Maeda, T.; Takahara, A. A dynamic covalent polymer driven by disulfide metathesis under photoirradiation. *Chem. Commun.* **2010**, *46*, 1150-1152;

41. Robert-Banchereau, E.; Lacombe, S.; Ollivier, J. Solution reactivity of thiyl radicals with molecular oxygen: Unsensitized photooxidation of dimethyldisulfide. *Tetrahedron Lett.* **1995**, *36*, 8197-8200;

42. Robert-Banchereau, E.; Lacombe, S.; Ollivier, J. Unsensitized photooxidation of sulfur compounds with molecular oxygen in solution. *Tetrahedron* **1997**, *53*, 2087-2102.

43. Kakizawa, Y.; Harada, A.; Kataoka, K. Environment-sensitive stabilization of core-shell structured polyion complex micelle by reversible cross-linking of the core through disulfide bond. *J. Am. Chem. Soc.* **1999**, *121*, 11247-11248;

44. Ryu, J. -H.; Chacko, R. T.; Jiwpanich, S.; Bickerton, S.; Babu, R. P.; Thayumanavan, S. Self-cross-linked polymer nanogels: a versatile nanoscopic drug delivery platform. *J. Am. Chem. Soc.* **2010,** *132*, 17227-17235.

45. Adam, W.; Grimm, G. N.; Marquardt, S.; Saha-Möller, C. R. Are pyridinethiones reliable photochemical oxyl-radical sources for photobiological studies? The importance of secondary photolysis products in the guanine oxidation of 2'-deoxyguanosine and cell-free DNA. *J. Am. Chem. Soc.* **1999**, *121*, 1179-1185;

46. Lobana, T. S.; Kinoshita, I.; Kimura, K.; Nishioka, T.; Shiomi, D.; Isobe, K. Pyridine-2-sulfonates as versatile ligands for the synthesis of novel coordinative and hydrogen-bonded supramolecules. *Eur. J. Inorg. Chem.* **2004**, *2004*, 356-367;

47. Li, L.; Ryu, J. -H.; Thayumanavan, S. Effect of hofmeister ions on the size and encapsulation stability of polymer nanogels. *Langmuir* **2013**, *29*, 50-55.

48. Jiwpanich, S.; Ryu, J. -H.; Bickerton, S.; Thayumanavan, S. Noncovalent encapsulation stabilities in supramolecular nanoassemblies. *J. Am. Chem. Soc.* **2010**, *132*, 10683-10685.

49. Ghosh, S.; Basu, S.; Thayumanavan, S. Simultaneous and reversible functionalization of copolymers for biological applications. *Macromolecules* **2006**, *39*, 5595-5597.

CHAPTER 6

THERMORESPONSIVE POLYMERIC NANOPARTICLES: NUCLEATION FROM COOPERATIVE POLYMERIZATION DRIVEN BY DATIVE BONDS

6.1 Introduction

Cooperative polymerization, also called nucleation-elongation (N-E) polymerization, has become a new and interesting paradigm in the field of supramolecular materials.[1-3] Although it has been observed and relatively well studied in biological systems (*e.g.* actin, tubulin, bacterial flagellin, and tobacco mosaic virus),[4, 5] these are not common in artificial material assemblies. It is believed that systems governed by the N-E mechanism can provide access to materials with novel properties, which are otherwise not available with classical synthetic polymerization techniques.[6-8] For example, although a polymer is achieved through a condensation-type reaction, the N-E system could produce polymers with substantially high molecular weights even when the stoichiometry of the monomers is imbalanced.[9] The molecular origin of cooperative growth of supramolecular polymers is regarded as the result of secondary interaction between units, which usually involves a non-covalent interaction arising due to electronic (both short-range polarization and longer-range electrostatic effects), structural (*e.g.* helix formation and allosteric conformational changes), or hydrophobic effects.[1] However, there are no reports on utilizing dative bonds, a covalent interaction, as the driving force for the cooperative polymerization. Demonstration of such a possibility will greatly expand the repertoire of nucleation-elongation polymerization in materials science, as exemplified in this report.

Boronate ester formation is the reaction between boronic acids and diols to form boronate esters, which is a covalent, yet reversible, bonding interaction. Recently, considerable attention has been devoted to the use of this dynamic ester formation as a popular strategy to build boron-containing multicomponent systems, including self-assembling macrocycles[10, 11], capsules[12, 13], covalent organic frameworks[14, 15], reversible linear polymers[16, 17] and particles[18, 19]. On the other hand, it is well known that boronate esters can act as Lewis acids, which enable them to form donor–acceptor complexes with N-donor ligands through a so-called coordinative or dative N→B bond[20-23] and have been exploited to achieve several self-assembled systems[24-27].

In this paper, we report on a simple method to prepare monodisperse polymeric nanoparticles through sequential boronate esterification of boronic acids and bifunctional catechols under ambient conditions. We find that the nucleation step for the formation of the particle involves a N-E polymerization step, wherein the dative bond between the nitrogen in the imine building blocks and the boron in the boronate ester plays a critical role. The controlled polymerization induced nucleation of the particle formation also allows a unique opportunity for significant control over the size of the self-assembled nanoparticles. Since the dative covalent B-N bond is relatively weak, these boronate nanoparticles exhibit a unique reversible, thermal responsive behavior. We expect that this finding will have a considerable impact on the development of dynamic supramolecular materials.

6.2 Results and Discussion

6.2.1 Design and preparation of nanoparticles

To introduce the imine building blocks, we designed two monomers based on boronic acid and on catechol, which were synthesized through a simple condensation reaction between a *p*-phenylenediamine and an aryl carboxaldehyde (Figure 6.1a). The latter molecule was based on 4-formyl-phenylboronic acid or 3, 4-dihydroxybenzaldehyde to obtain the boronic acid monomer **Im-BA** or the catechol monomer **Im-Ca** respectively. When a methanol solution of **Im-BA** was

added dropwise to a methanol solution of **Im-Ca**, the resultant mixture became deeper in color compared to the monomer solutions and a turbid suspension. Analyses of these mixtures using transmission electron microscopy (TEM) and scanning electron microscopy (SEM) (Figure 6.1b and 6.1c) revealed formation of spherical and monodisperse nanoparticles with a smooth surface. In the case of the nanoparticles shown in Figure 6.1, the concentrations of the **Im-BA** and **Im-Ca** were 13.4 mM (5.0 mg/mL). We also noticed that the size and dispersity of the particles is independent of the order of addition of the two solutions.

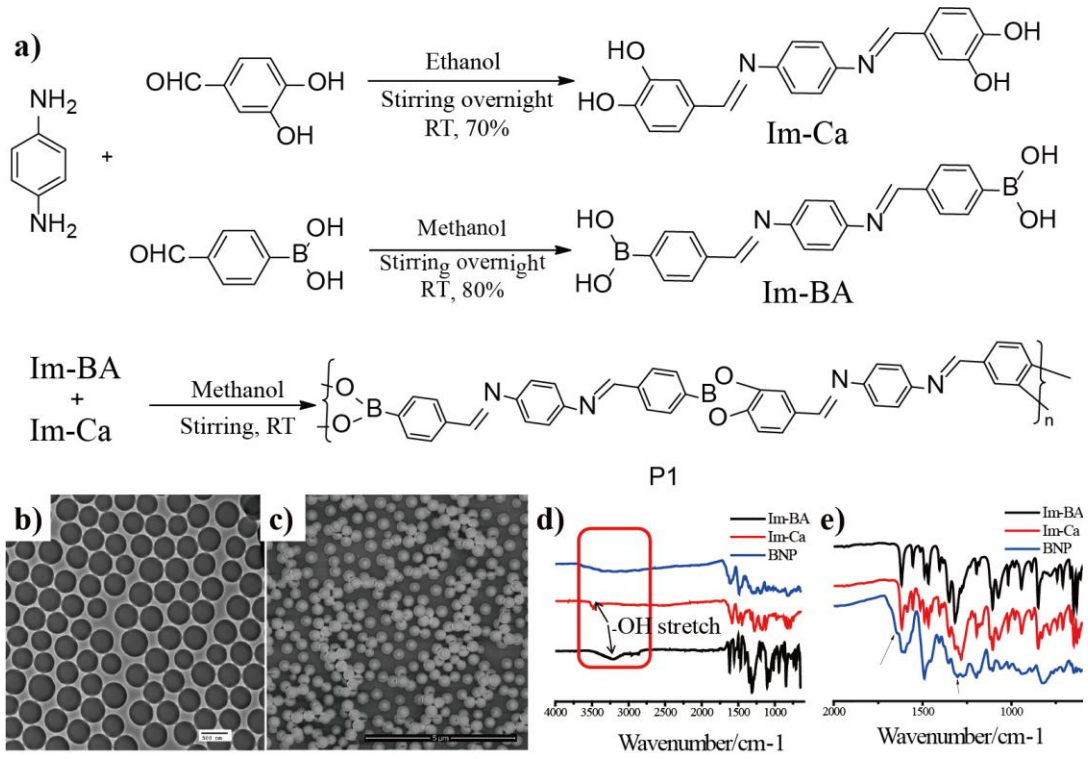

Figure 6.1 Synthesis and characterization of boronate nanoparticle (**BNP**). a) Scheme presents the syntheses of **Im-Ca** and **Im-BA** monomers, as well as polymer P1 via the polyboronate esterification between **Im-Ca** and **Im-BA**. b) TEM image of the **BNP**, the scale bar is 500 nm. c) SEM image of the **BNP**, the scale bar is 5μm. Conditions: dropwise added 1 mL 5 mg/mL **Im-Ca** methanol solution into 1 mL 5 mg/mL **Im-BA** methanol solution with stirring at room temperature. The TEM and SEM samples were taken immediately after the addition. d) FTIR spectra of molecule **Im-BA**, **Im-Ca** and solid **BNP**, and e) Zoomed-in FTIR spectra from (d).

Considering the chemical structure of both starting molecules, we hypothesized that the observed nanoparticles are composed of boronate ester polymer P1, which are formed through

sequential boronate esterification. To test this, we first investigated the particles using infrared absorption spectroscopy (Figure 6.1d-6.1e). Contrary to the starting **Im-BA** and **Im-Ca** monomers, the product nanoparticles did not exhibit a distinct peak for the hydroxyl stretch frequencies at 3470 and 3217 cm^{-1}, suggesting the formation of the dehydrated boronate ester products. Moreover, the peak corresponding to B-O stretch in boronate ester was also observed at 1350 cm^{-1}.[29, 30] Similarly, the new peak centered at 1658 cm^{-1} is regarded as an IR marker for the formation of phenylboronate ester.[31]

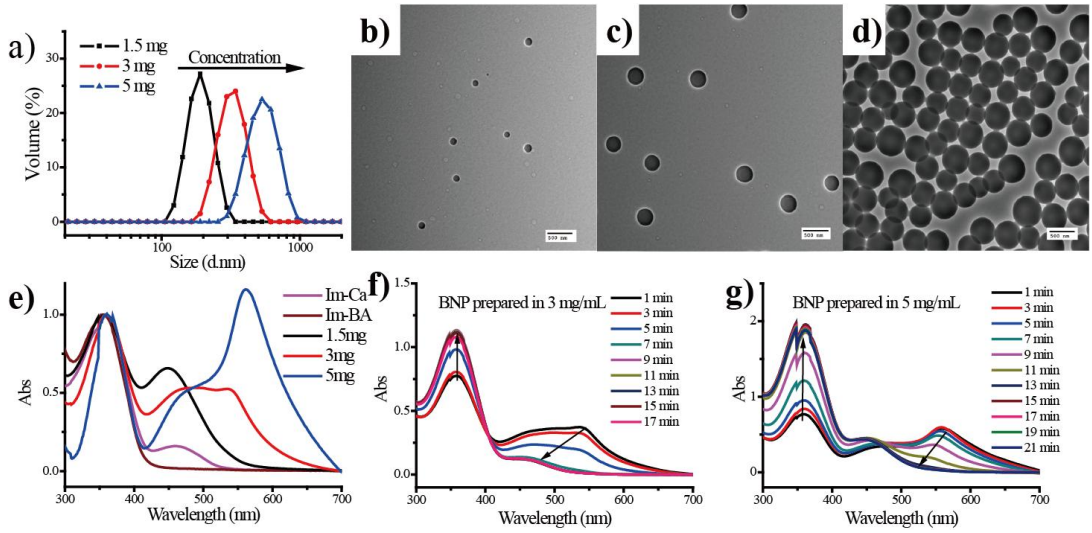

Figure 6.2 Particle size and absorption characteristics variation. a) DLS of the **BNP** prepared with different monomer concentration in methanol. TEM images of the **BNP**, prepared with different monomer concentration in methanol, b) 1.5 mg/mL, c) 3.0 mg/mL, d) 5 mg/mL. The scale bar is 500 nm. e) Normalized absorption spectra for **Im-BA**, **Im-Ca** and **BNP** prepared with different monomer concentration in methanol. Temporal evolution of absorption spectra for **BNP** prepared with f) 3 mg/mL in methanol, g) 5 mg/mL in methanol. All samples were prepared by adding 0.01 mL reaction mixture into 1 mL methanol.

Remarkably, we found that the size of these monodisperse particles can be tuned by simply altering the concentrations of the monomers used for the polymer formation. The spherical nanoparticles were about 150 nm in size, when the concentrations of the monomers were about 4.0 mM (1.5 mg/mL). This size could be increased to 300 nm and 500 nm, while maintaining the monodispersity of the nanoparticles, when the concentrations were increased to 8.0 mM (3.0

mg/mL) and 13.4 mM (5.0 mg/mL) respectively. Thus, we found that the sizes of the polymer nanoparticles systematically increase with concentration. The rather uniform dispersity of the particles is evident from the TEM images shown in Figure 6.2. These results were also consistent with the size measurements in solution using dynamic light scattering (DLS) (Figure 6.2a). Lack of diffraction peaks, except for an ill-defined broad peak at about 2θ=20, in powder X-ray diffraction (PXRD) (Figure 6.3) suggests that these particles were mostly amorphous. Interestingly, there is a need for a critical concentration, below which there was no discernible nanoparticle formation. We noticed that particles could not be formed when the initial concentration of both monomers (1:1 ratio) was lower than 1.0 mg/mL, as discerned from TEM. The poor correlation function, observed in DLS, further confirmed this assertion.

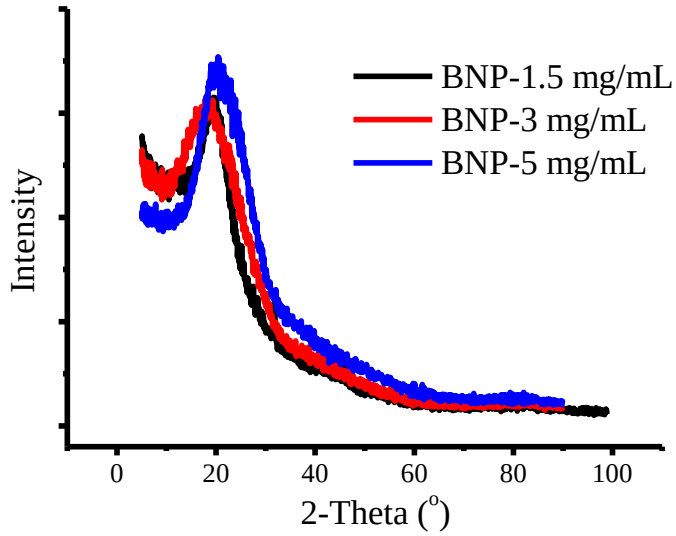

Figure 6.3 PXRD pattern of the **BNP**. A broad bump at about 2θ=20 was resulted from crystalline parts of polymers.

The absorbance spectra for these particles in methanol are also shown in the Figure 6.2e. Compared to the starting **Im-BA** and **Im-Ca**, the nanoparticle solutions exhibit new peaks at longer wavelengths. This is taken to be an indicator for the formation of boronate ester between **Im-BA** and **Im-Ca**, which could lead to a longer π-conjugated polymer. Conjugated systems extending through the boronate ester is reasonable. For example, poly (dioxaborole)s, in which

the empty p-orbitals on the boron atoms and the lone pairs of electrons on the oxygen atoms are in conjugation with the phenyl rings[32-36], are considered to provide an opportunity for extending π-conjugation and thus have attracted attention as a novel class of conjugated polymers. The red shift in the new peak, resulting from the polymerization reaction, increased with concentration. In a condensation polymerization, it is reasonable to assume that the polymer length increases with increasing concentration and therefore it is reasonable that the increase in red shift is taken to be an indicator of the resultant increase in π-conjugation. Unfortunately, we could not measure the molecular weight of the polymer from the resultant nanoparticles by size-exclusion chromatography because of the disassembly in response to dilution.

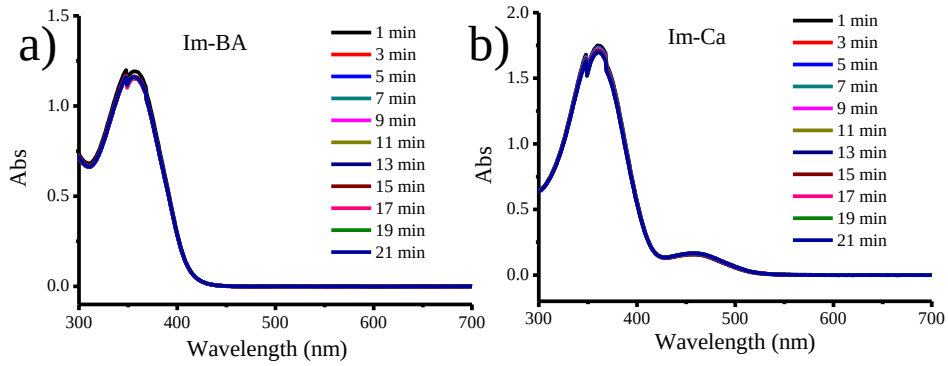

Figure 6.4 Absorption spectra for **Im-BA** and **Im-Ca** as the time. The concentration for both solutions is 0.02 mg/mL.

As shown in Figure 6.2f and 6.2g, a time-dependent blue shift in the low energy peaks was also observed upon large dilution (about 100 times), along with the expected commensurate decrease in the absorption intensity. We attributed this to the dynamic nature of the boronate ester bonds and the dilution-induced depolymerization. To insure that imines are not unstable under these conditions, the same time-dependent absorption measurements were carried out for both molecules **Im-BA** and **Im-Ca** by themselves at an even higher dilution and no change in the absorption spectra was observed (Figure 6.4). This suggests that the observed change in absorption spectra was indeed due to the reversibility of the boronate ester. It should be noted

however that the hydrolytic stability of the imine bonds did compromise the nanoparticle morphology, when these were left in solution over a long time (over three days). Nonetheless, these nanoparticles were found to be stable in both morphology and size over several months in the solid state (see Experimental section).

6.2.2 Mechanism study of the particle formation

It has been reported that micron-sized particles can be prepared by adding 1.0 equiv pyridine into a 1:1 mixture of benzene-1,4-diboronic acid and 1,2,4,5-tetrahydroxybezene in THF.[19] The authors proposed that the condensation polymerization between these two molecules could be promoted under these conditions, leading to nucleation in the early stages for the particle formation. In their experiments, the ratio of boron molecule to catechol molecule was set as 1:1, resulting in the formation of high M_w polymers via condensation polymerization for the nucleation. In our case however, we hypothesized that the polymerization based on boronate esterification in our particle formation may not be a simple condensation polymerization, but a so-called nucleation-elongation polymerization which greatly enhances the materials tunability. To understand the mechanism of the formation of the nanoparticles, we added different volumes (0.1, 0.3, 0.5, 0.65, 0.8, 1.0 mL) of a solution of **Im-Ca** in methanol (5 mg/mL) dropwise into a 1 mL of **Im-BA** (5 mg/mL in methanol). These solutions could be assumed as intermediate stages of the fast particles formation. As shown in Figure 6.5, DLS measurements and TEM suggest that the nanoparticle size systematically increased with increase in the amount of **Im-Ca** in the mixture. Since the molecular weights of the two monomers are similar, the relative stoichiometry of the first five solutions is below 1:1. It is interesting to note that small nanoparticles were formed even at a 1:10 ratio and that their sizes from all these mixtures were quite uniform. These observations provided the first indication that polymers are likely formed through the nucleation-elongation polymerization, rather than the classical step growth mechanism. At the beginning of the dropwise addition, the polymers formed via this specific polymerization could form the

nucleus that serve as the template for further nanoparticle growth with increasing amounts of **Im-Ca**. To make sure that short oligomers could not lead to the formation of particles, we synthesized molecule mono-**Im-Ca** containing only one catechol groups via reaction between aniline and 3, 4-dihydroxybenzaldehyde. The addition of this molecule should result in shorter oligomers in solution. No particles could be observed, suggesting that short oligomers indeed could not lead to the formation of particles. Note that **Im-BA** and **Im-Ca** in beginning of the **Im-Ca** addition were under sub-stoichiometric conditions. If the mechanism involves a simple step growth formation

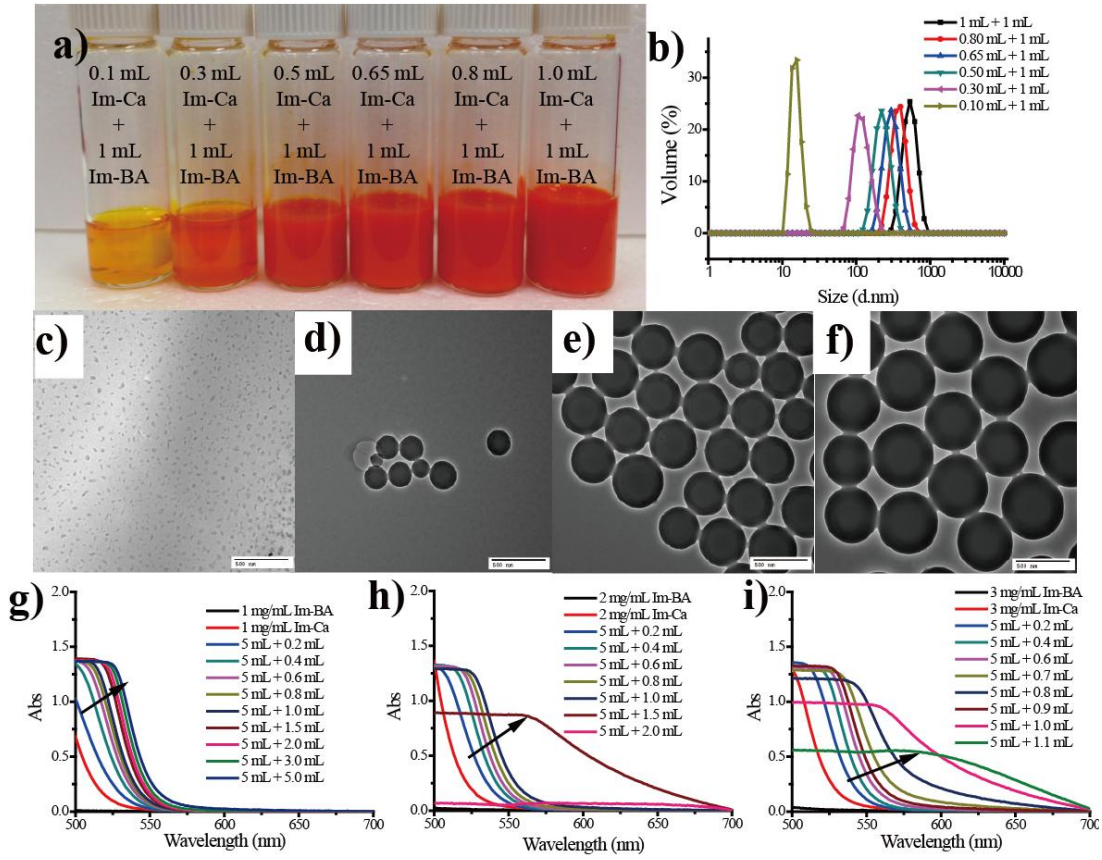

Figure 6.5 Mechanism study of the particle formation. a) Photographs of the **BNP** solution with different ratios of **Im-Ca** into **Im-BA** in methanol. b) DLS of the **BNP** prepared with different addition volumes of **Im-Ca** into 1 mL of **Im-BA** solution. TEM images of the corresponding solutions, c) 0.10 mL **Im-Ca** + 1.0 mL **Im-BA**, d) 0.30 mL **Im-Ca** + 1.0 mL **Im-BA**, e) 0.65 mL **Im-Ca** + 1.0 mL **Im-BA**, f) 1.0 mL **Im-Ca** + 1.0 mL **Im-BA**. The scale bar is 500 nm. Absorption spectra of the reaction mixture with different initial concentrations during the dropwise addition, g) 1 mg/mL, h) 2 mg/mL, i) 3 mg/mL. Note that there were flat lines between 500 and 525 nm, because samples had an absorbance of more than dynamic range of instrument.

of the boronate ester, then only oligomers would form in solution and there should not be significant nanoparticle formation at imbalanced ratios of the starting monomers.

To further determine that it is the polymer formed but not oligomer formation, leading to the nucleation step, we investigated the absorption spectra of these reaction mixtures after small additions of **Im-Ca** into **Im-BA**, since the red shift in absorption likely indicates increase in conjugation, *i.e.* polymer chain length. First, a solution of **Im-Ca** (1 mg/mL) was added in 0.1 mL increments to a 5 mL solution of **Im-BA** (1mg/mL) and the evolution of the absorption spectrum of the resultant solution was monitored after each addition. As shown in Figure 6.5g, **Im-BA** solution with 1 mg/mL did not have any absorption while **Im-Ca** solution with 1 mg/mL had a small absorption from 500 nm to 550 nm. After 0.2 mL **Im-Ca** was added into 5 mL **Im-BA**, a significant absorption was noticed even though the concentration of **Im-Ca** in this mixture was only around 0.04 mg/mL, suggesting the formation of oligomers, which have a much stronger absorption from 500 nm to 550 nm. As more **Im-Ca** was added, the absorption intensity of the low energy peak between 500 nm and 550 nm keeps slowly increasing and red-shifting throughout the addition process. Interestingly however, no particle formation was observed via both DLS and TEM at this monomer concentration. The solution was also clear, although the color became deep orange. This is taken to suggest that the 1 mg/mL concentrations of the monomers are lower than the critical concentration for the nucleation step in the nucleation-elongation polymerization. On the contrary, when the concentrations of the monomers are 2 mg/mL, there was a sharp increase in absorption after 550 nm at a sub-stoichiometric ratio of monomers (2 mL of Im-Ca into 5 mL of **Im-BA**, the ratio of **Im-Ca** to **Im-BA** is 0.4/1), as shown in Figure 6.5h, suggesting the formation of polymers with larger conjugation. At this ratio, the solution became a turbid suspension and small spherical particles were also observed by TEM. Similar results were found at an even lower stoichiometry of **Im-Ca** (only 0.9 mL of **Im-Ca** into 5 mL of **Im-BA**), when the initial concentration was 3 mg/mL (Figure 6.5i).

Several observations are noteworthy in this reaction: (*i*) there is a critical concentration above which nucleation for nanoparticle formation seems to occur (>1 mg/mL in this case). (*ii*) Conjugated polymers with strong absorption above 550 nm are achieved even when there is a significant imbalance in the stoichiometry of the constituent monomers. (*iii*) Uniformly dispersed nanoparticles are formed at these imbalanced stoichiometry conditions, and size of particles increased with the continuing addition of monomer. (*iv*) The sharp increase in low energy absorption at a certain ratio is indicative of the possibility that the reaction rate is much faster after a slower nucleation process. All these observations are consistent with the nucleation-elongation (N-E) polymerization pathway.

The cooperative growth of supramolecular polymers, seen in such a N-E pathway, often has a secondary interaction as its molecular origin. We hypothesized that the possible dative N→B bond from the nitrogen of the imine and the boron from the boronate ester could be the reason for chain fold and collapse, which has been often proposed to drive the high-polymer formation in the reversible polymerization.[37, 38] Similarly, the La Mer model suggests that the common route to achieve monodisperse NPs in the solution phase is to separate nucleation and growth steps during the synthesis.[39] Here, we hypothesize that the N-E polymerization first leads to polymers, inducing particle nucleation in the early stage. Further particle growth continues using the initially formed aggregates as the template. Finally, the resulting particles have to be spherical owing to the requirement for minimization of the interfacial free energy between the particles and solvent used.[40, 41] To first test whether there is a dative interaction between the imine nitrogen and boronate ester boron atoms, we focused on the distinct structural change from trigonal planar to tetrahedral geometry at the boron atom associated with such an interaction.[21] Indeed, a sharp peak was observed at 21 ppm in solid state ^{11}B NMR for the particles, indicative of the tetrahedral geometry. This peak is distinct from the typical signal at ~30 ppm, observed for the trigonal planar boronate esters in the solid state (Figure 6.6).[42] In fact, in the case of the boronate

nanoparticles, a small percentage of the trigonal boronate ester was seen in the NMR, most likely arising from the surface boronate moieties that are not datively satisfied. In addition, we also note that Im-BA by itself exhibits both trigonal-planar and tetrahedral geometries at the boron atom. This is attributed to the fact that boronic acids could also form dative N-B bonds with the imine groups.

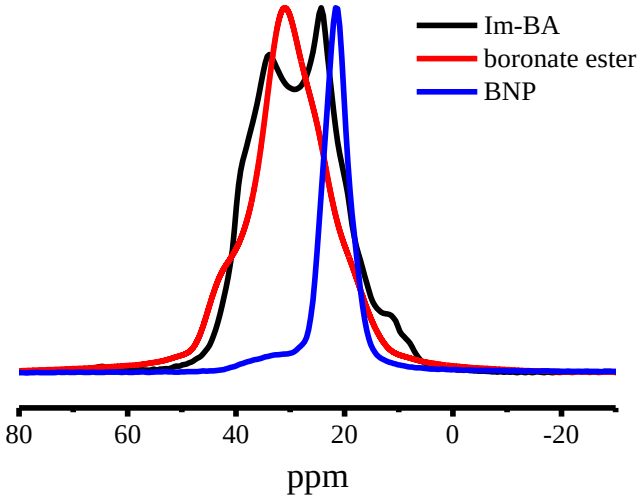

Figure 6.6 Solid ^{11}B-NMR spectra of **Im-BA**, boronate ester from 4-formylphenylboronic acid and 3,4-dihydroxybenzaldehyde, and solid BNP.

To investigate further whether the imine bonds really play an important role in the formation of the nanoparticles, we synthesized two structurally similar stilbene-based monomers **St-BA** and **St-Ca**, wherein the imine bond was replaced with C=C double bond (Scheme 6.1). Since the solubility of **St-BA** in methanol is low, we used ethanol as the solvent in these experiments. No discernible nanoparticles were found, when the experiments were carried out with **St-BA** and **St-Ca**. However, the corresponding imine-based monomers did indeed afford nanoparticles in ethanol, supporting our assertion that the presence of imine is important. Interestingly, mixing the stilbene-based boronic acid monomer with the imine-based catechol monomer or vice versa did not result in any nanoparticle formation (Figure 6.7). These indicate that there seems to be a critical density of the imines that is essential for the observed nanoparticle formation.

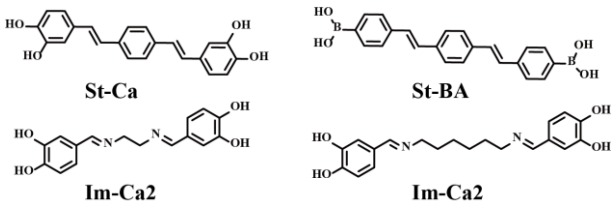

Scheme 6.1 Structure of **St-Ca**, **St-BA**, **Im-Ca2** and **Im-Ca6.**

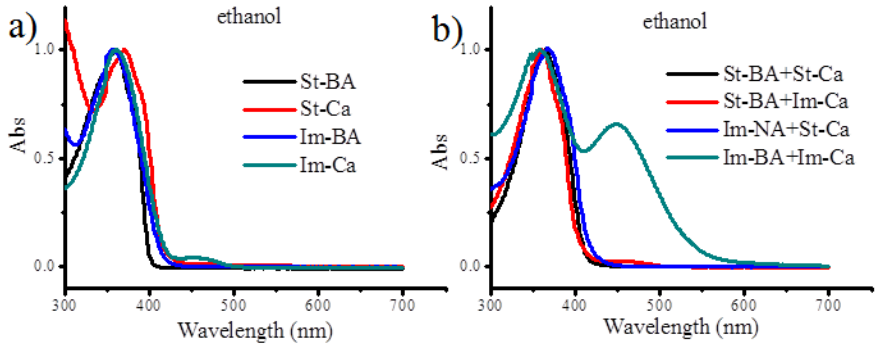

Figure 6.7 UV-vis spectra of a), **St-BA, St-Ca, Im-BA** and **Im-Ca** in ethanol; b), their one to one mixture in ethanol.

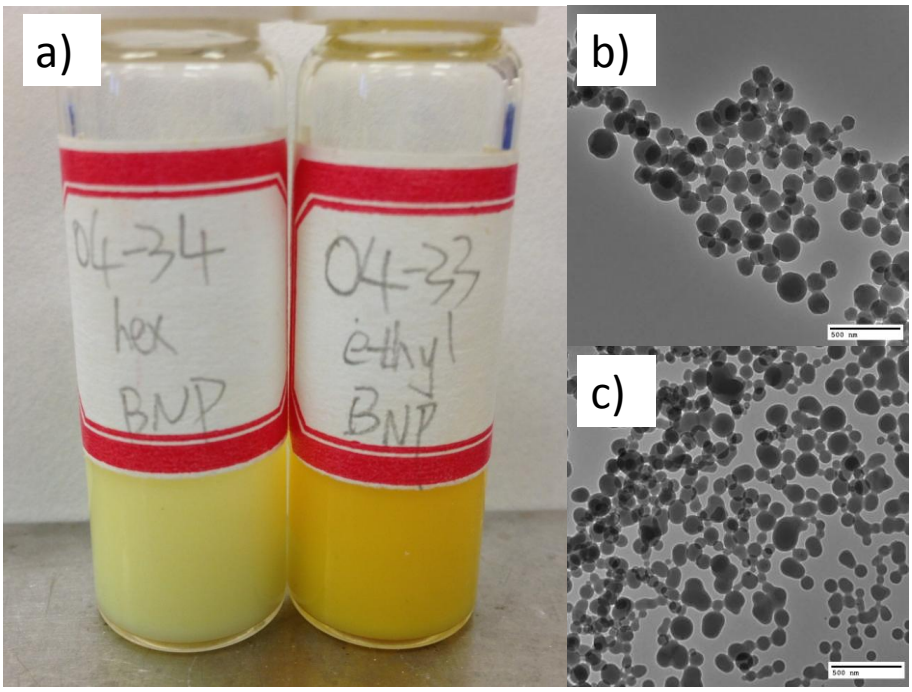

Figure 6.8 a)Typical photos of the mixtures using **Im-BA** react with **Im-Ca2** and **Im-Ca6** in methanol, and their TEM pictures of BNP using b) **Im-Ca2**, c) **Im-Ca6**. The scale bar is 500 nm.

To further test this, we introduced spacers between the catechol moieties by reacting ethylenediamine and hexamethylene diamine to react with 3,4-dihydroxybenzaldehyde to obtain **Im-Ca**2 and **Im-Ca**6 respectively (Scheme 6.1). In these cases, we dilute the nitrogen-boron contacts. Indeed, mixing these molecules with **Im-BA** did afford nanoparticles. However, these nanoparticles were not as well-defined and were less monodisperse compared to those obtained with **Im-BA** and **Im-Ca** (Figure 6.8), supporting our assertion that a critical density of imines might indeed be needed.

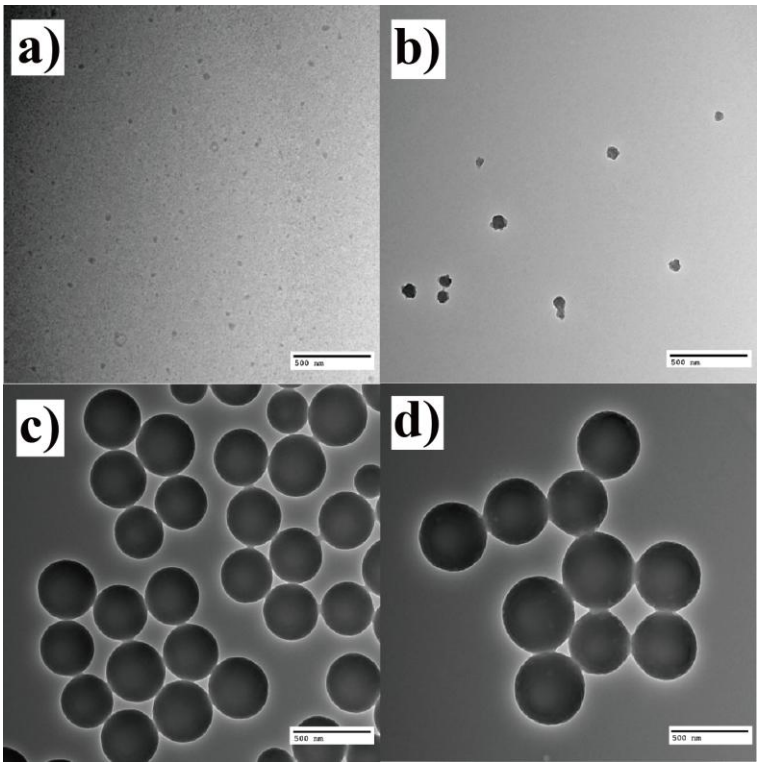

Figure 6.9 Solvent effects on the particle formation. TEM images of the **BNP** prepared with methanol (M) and DMSO (D) mixture solution, a) M/D=4/1, b) M/D=6/1, c) M/D=9/1, d) Pure M. The scale bar is 500 nm.

Next, we were interested in studying the effect of solvent on the formation of the particles to further investigate the effect of interrupting secondary interactions upon the formation of the nanoparticles. Since solvent could significantly influence the rather weak secondary interactions, this could play a critical role on the stability and dynamics of a supramolecular polymer.[43, 44]

While the alcoholic solvents such as methanol, ethanol and isopropanol afforded the nanoparticles, no nanoparticle formation was observed with DMSO as the solvent. It is likely that DMSO interrupts the dative interaction between the imine nitrogen and boron. To empirically test the effect of DMSO, we tested the formation of the boronate ester particles in a mixture of methanol and DMSO. Indeed, particle with around 30 nm diameter formed in the mixture when the ratio of methanol to DMSO is 4/1, while the same mixture afforded a particle size of 450 nm in pure methanol. There were no discernible particle formation, when the presence of DMSO was much higher. In fact, the size of the nanoparticles systematically decreased from pure methanol to mixture solvent with different percentages of DMSO, and the size also decreased with the increasing presence of DMSO (Figure 6.9a-6.9d).

6.2.3 Responsive behavior of BNP based on dative N→B bond

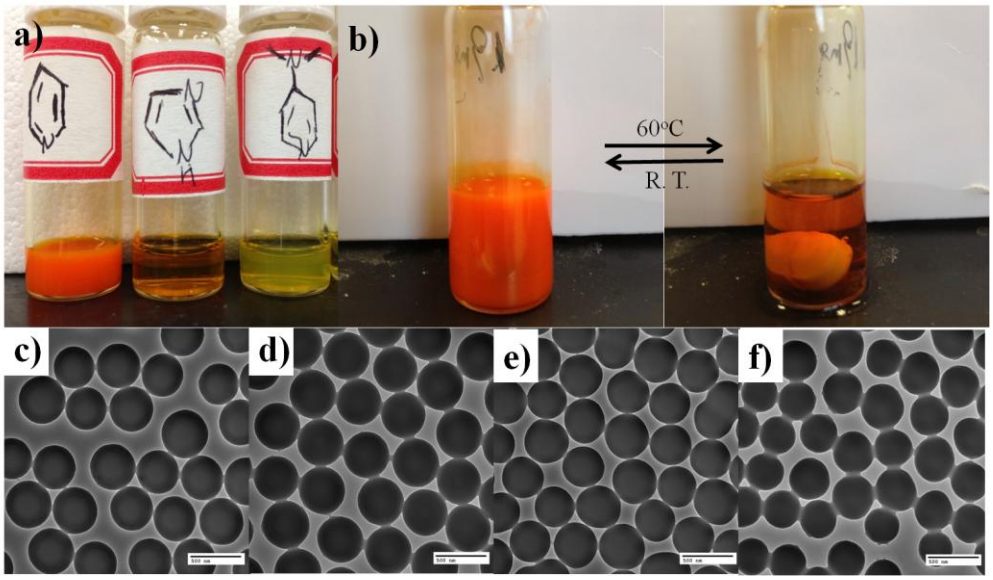

Figure 6.10 Responsive behavior of **BNP** based on dative N→B bond. a) Photographs of the **BNP** with the addition of pyridine, imidazole, 4-dimethylaminopyridine, b) Photographs of the **BNP** with changing temperature and their TEM images of the **BNP**, c) before heating, d) after first heat-cool cycle, e) after second heat-cool cycle, f) after third heat-cool cycle. The scale bars are 500 nm.

To further test whether competing binders for boron could interrupt the dative N→B interaction and thus interrupt the observed cooperative supramolecular assembly, we chose to

study the effect of amine-based Lewis bases, such as pyridine, imidazole, 4-dimethylaminopyridine (DMAP) (Figure 6.10a). We found that the addition of a strong base such as imidazole and DMAP causes the turbid nanoparticle solution to become clear. This is attributed to the possible breakage of the dative N→B interaction by these Lewis bases. Without the secondary interaction, the formed nanoparticles could disassemble. Indeed no particles were observed in these solutions after the addition of these Lewis bases. On the other hand, addition of pyridine did not cause any change to the nanoparticles, most likely because the N→B interactions were unaffected by the rather weak Lewis base.

Finally, we were interested in testing the effect of temperature upon the nanoparticles for two reasons: first, it is possible that the relatively weak N→B dative bond could be broken at higher temperatures[26], which provides an opportunity to test the possibility of thermal reversibility in these nanoparticles. Second, if we were able to disassemble the particles at higher temperature in solution, investigation of the morphology and size of the particles re-formed allows us to test whether the initially formed nanoparticle is the result of equilibrium self-assembly. As shown in Figure 6.10b, the methanolic solution of nanoparticles became clearer upon heating it to 60 ℃ and the solution turned turbid again when cooled down to ambient temperature. This indicates that the nanoparticles could be losing its nanoassembly at higher temperature, but is re-formed upon cooling. To test whether the morphology and size of the nanoparticles were similar before and after the heat-cool cycle, the samples were investigated using TEM. Indeed, both these features remain unchanged even after three heat-cool cycles. We also further tracked the reformation of these nanoparticles by looking at the samples for TEM at different time points during the cooling step (Figure 6.11). It is clear that the nanoparticles are small initially, finally reaching the particle size similar to that observed before heat-cool cycle. These results show that these nanoparticles are thermally reversible and that the formation of the nanoparticles is likely due to equilibrium self-assembly.

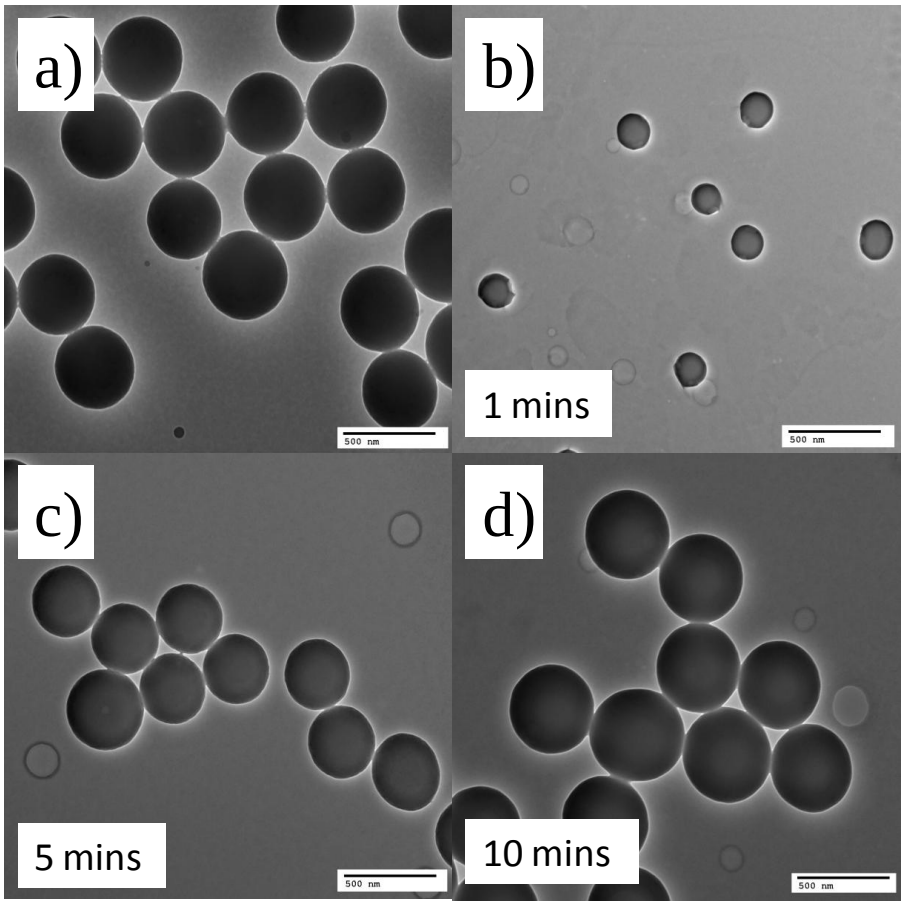

Figure 6.11 TEM images of the **BNP**, a) before the heating and cooling at room temperature for b) 1 min, c) 5 mins, d) 10 mins.

6.3 Summary

In summary, we report on a supramolecular nanoparticle that is autonomously self-assembled by conjugated polymers based on boronate ester. We have shown that: (*i*) the polymers inducing nucleation for the formation of the particle involves a N-E polymerization step; (*ii*) dative bond between the nitrogen in the imine building blocks and the boron in the boronate ester is regarded as the necessary secondary interaction for the specific reaction; (*iii*) their particle size could be easily adjusted by controlling the mixing concentration; (*iv*) imine density and solvent can affect the particle formation; and (*v*) these boronate nanoparticles exhibit thermally responsive disassembly behavior due to the relatively weak dative covalent N→B bond. To our knowledge, this is the first time for a cooperative polymerization to use covalent dative bond as

the driving force. We believe that this will open new doors for autonomous self-assembly strategies to achieve not only monodisperse, but also functionally diverse nanoassemblies.

6.4 Experimental

6.4.1 General Procedures

p-Phenylenediamine, ethylenediamine, hexamethylene diamine, 3,4-dihydroxybenzaldehyde, 4-formylphenylboronic acid, tert-butyldimethylsilyl chloride, imidazole, 4-Dimethylaminopyridine, pinacol, 1,4-bis (bromomethyl) benzene, triethylphosphite and other conventional reagents were obtained from commercial sources and were used as received unless otherwise mentioned. ^{1}H-NMR spectra were recorded on a Bruker 400 MHz NMR spectrometer using the residual proton resonance of the solvent as the internal standard. ^{13}C-NMR spectra were recorded on a Bruker 100 MHz NMR spectrometer using the carbon signal of the deuterated solvent as the internal standard. Solid state ^{11}B-NMR spectra were recorded at 13 kHz on a Bruker DSX300 spectrometer with 4 mm rotor. Mass spectra were taken on Bruker MicrOTOF-II. Dynamic light scattering (DLS) measurements were performed by using a Malvern Nanozetasizer. UV/visible absorption spectra of the samples in solutions were measured on a Unico UV/Vis 2802PCS instrument. Transmission electron microscopy (TEM) images were taken from JEOL 2000FX at 200 KV. FT-IR spectra were acquired in a Bruker Alpha-P Diamond ATR-FTIR. Scanning electron microscopy (SEM) images were taken from FESEM Magellan 400. Thermogravimetric analysis (TGA) was performed in a nitrogen atmosphere on a DuPont TGA 2950 at a heating rate of 10 ℃/min.

6.4.2 Synthesis of Im-Ca

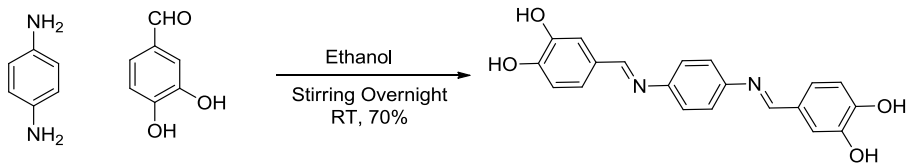

Scheme 6.2 Synthesis of **Im-Ca**.

The preparation of **Im-Ca** was achieved following a literature procedure with a minor modification.[45] The scheme is shown above. To a solution of p-phenylenediamine (0.15 g, 1.39 mmol) in anhydrous ethanol (10 mL) was added 3,4-dihydroxybenzaldehyde (0.40 g, 2.90 mmol). The clear brown mixture was stirred at room temperature under an argon atmosphere and protected from light. The product precipitated out of the reaction mixture. The brown precipitate was filtered and washed with cold ethanol three times. Final product was vacuum dried to obtain a brown solid (yield: 70%) ^{1}H-NMR (400MHz, DMSO-6D) δ(ppm): 9.57 (s, 2H), 9.29 (s, 2H), 8.41 (s, 2H), 7.38 (d, 2H), 7.23 (s, 4H), 7.17 (q, 2H), 6.82 (d, 2H). ^{1}H-NMR (400MHz, CD_3OD and DMSO-6D) δ(ppm): 8.39 (s, 2H), 7.39 (d, 2H), 7.22 (s, 4H), 7.17 (q, 2H), 6.82 (d, 2H). ^{13}C-NMR (100MHz, DMSO-6D) δ(ppm): 159.89, 149.57, 146.09, 128.56, 122.91, 122.30, 115.83, 114.51. ESI/MS m/z 349.11 $[M+H]^+$ (expect m/z=349.35).

6.4.3 Synthesis of Im-BA

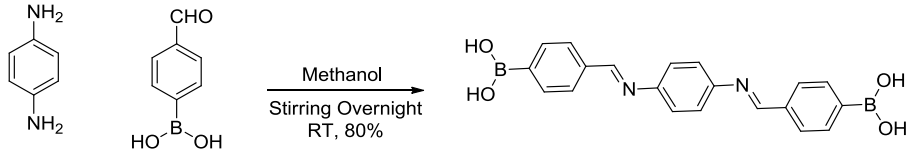

Scheme 6.3 Synthesis of **Im-BA**.

Im-BA was synthesized from condensation reaction between p-phenylenediamine and 4-formylphenylboronic acid according to the synthesis of **Im-Ca**. The scheme is shown above. To a solution of p-phenylenediamine (0.05 g, 0.46 mmol) in 20 mL MeOH was added 4-formylphenylboronic acid (0.15 g, 1.00 mmol). The clear yellow mixture became cloudy after stirring at room temperature overnight. The yellow precipitate was filtered and washed with cool methanol three times. Final product was vacuum dried to obtain a yellowish solid (yield: 80%) ^{1}H-NMR (400MHz, DMSO-6D) δ(ppm): 8.67 (s, 2H), 8.22 (s, 4H), 7.89 (m, 8H), 7.36 (s, 4H). ^{1}H-NMR (400MHz, CD_3OD and DMSO-6D) δ(ppm): 8.65 (s, 2H), 7.88 (m, 8H), 7.34 (s, 4H). ^{13}C-NMR (100MHz, DMSO-6D) δ(ppm): 160.67, 149.83, 137.76, 134.90, 128.06, 122.54.

ESI/MS m/z 431.16 $[M+59]^-$ (expect m/z=431.19), m/z 445.20 $[M+73]^-$ (expect m/z=445.21), m/z 459.22 $[M+87]^-$ (expect m/z=459.23).

6.4.4 Synthesis of mono-Im-Ca

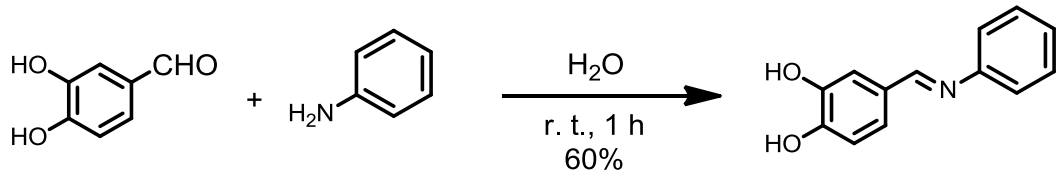

Scheme 6.4 Synthesis of mono-**Im-Ca**.

Mono-**Im-Ca** was synthesized according to a literature procedure.[46] In brif, aniline (0.466 g, 5 mmol) and 3,4-dihydroxybenzaldehyde (0.691 g, 5 mmol) were mixed in water (10 mL) and stirred at room temperature for 1 hour. Then the solid insoluble precipitate was filtered and washed with water for three times. The crude product was recrystallized from toluene to give a pale yellow solid (yield: 60%). 1H-NMR (400MHz, DMSO-6D) δ(ppm): 9.40 (s, 2H), 8.35 (s, 1H), 7.38 (m, 3H), 7.15 (m, 4H), 6.83 (d, 1H). 13C-NMR (100MHz, DMSO-6D) δ(ppm): 160.67, 152.44, 149.69, 146.10, 129.58, 128.45, 125.72, 123.00, 121.33, 115.82, 114.65.

6.4.5 Synthesis of Im-Ca2

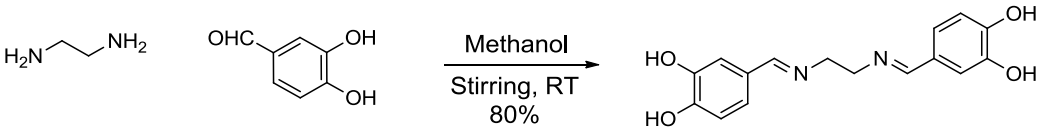

Scheme 6.5 Synthesis of **Im-Ca2**.

The preparation of **Im-Ca**2 is similar to that of **Im-Ca** by using ethylenediamine instead. The scheme is shown above. To a solution of 3,4-dihydroxybenzaldehyde (0.2 g, 1.45 mmol) in methanol (5 mL) was added ethylenediamine (0.046 mL, 0.041 g, 0.68 mmol). The mixture was stirred at room temperature under an argon atmosphere and protected from light. The product precipitated out of the reaction mixture. The precipitate was filtered and washed with cool methanol three times. Final product was vacuum dried to obtain a pale yellow solid (yield: 80%). ^{1}H-NMR (400MHz, CD_3OD) δ(ppm): 8.03 (s, 2H), 7.17 (d, 2H), 7.02 (q, 2H), 6.71 (d, 2H), 3.82

(s, 4H). ^{13}C-NMR (100MHz, DMSO-6D) δ(ppm): 161.75, 148.72, 145.79, 128.55, 121.67, 115.63, 114.07, 61.36, 48.98. ESI/MS m/z 301.11 $[M+H]^+$ (expect m/z=301.31).

6.4.6 Synthesis of Im-Ca6

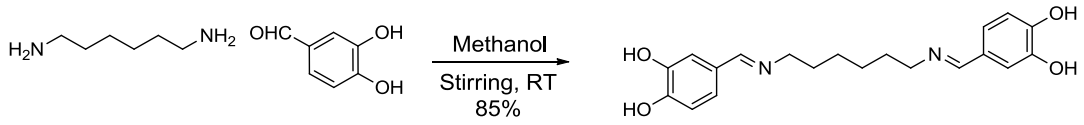

Scheme 6.6 Synthesis of **Im-Ca**6.

The preparation of **Im-Ca**6 is also similar to that of Im-Ca by using hexamethylene diamine instead. The scheme is shown above. To a solution of 3, 4-dihydroxybenzaldehyde (0.2 g, 1.45 mmol) in methanol (5 mL) was added hexamethylene diamine (0.08 g, 0.69 mmol). The mixture was stirred at room temperature under an argon atmosphere and protected from light. The product precipitated out of the reaction mixture. The precipitate was filtered and washed with cool methanol three times. Final product was vacuum dried to obtain a pale yellow solid (yield: 85%). ^{1}H-NMR (400MHz, CD_3OD) δ(ppm): 8.02 (s, 2H), 7.17 (s, 2H), 7.05 (q, 2H), 6.71 (d, 2H), 3.52 (m, 4H), 1.70 (m, 4H), 1.40 (m, 4H). ^{13}C-NMR (100MHz, DMSO-6D) δ(ppm): 160.31, 148.73, 146.06, 128.43, 121.69, 115.79, 113.87, 60.55, 31.12, 27.06. ESI/MS m/z 357.17 $[M+H]^+$ (expect m/z=357.42)

6.4.7 Synthesis of St-BA and St-Ca

Both molecules were prepared through Horner-Wadsworth-Emmons reaction between tetraethyl (1,4-phenylenebis(methylene))bis(phosphonate) and benzaldehyde molecules.[47] Pinacol protected 4-formylphenylboronic acid and TBS protected 3, 4-dihydroxybenzaldehyde were used as the aldehydes in the syntheses of **St-BA** and **St-Ca** respectively.

6.4.8 Synthesis of tetraethyl (1,4-phenylenebis(methylene))bis(phosphonate)

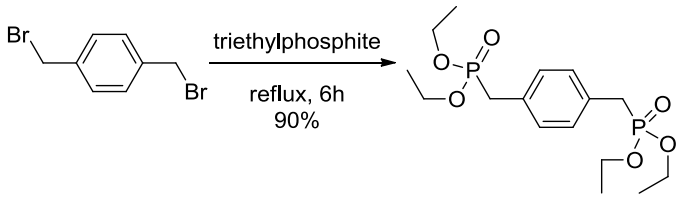

Scheme 6.7 Synthesis of tetraethyl (1,4-phenylenebis(methylene))bis(phosphonate).

The mixture of 1,4-bis (bromomethyl) benzene (1.3 g, 4.93 mmol) and triethylphosphite (20 mL) was heated to reflux for 5 hours. Afterwards, excess triethylphosphite was removed under the reduced pressure. The remaining slurry was poured into a large amount of hexane to extract residual remains of triethylphosphite. The precipitate was filtered and washed with hexane three times. Final product was vacuum dried to obtain a white solid (yield: 90%). ^{1}H-NMR (400 MHz, $CDCl_3$) δ(ppm): 7.24 (s, 4H), 4.00 (m, 8H), 3.12 (d, 4H), 1.23 (t, 12H). ^{13}C-NMR (100 MHz, $CDCl_3$) δ(ppm): 130.25, 129.96, 62.24, 34.13, 32.51, 16.40.

6.4.9 Protection of 4-formylphenylboronic acid

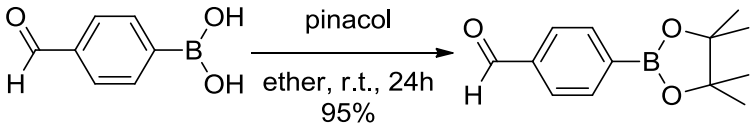

Scheme 6.8 Protection of 4-formylphenylboronic acid.

The boronic acid group was protected using pinacol.[48] At room temperature, 10.0 mmol boronic acid and anhydrous pinacol (11.0 mmol) were mixed in anhydrous diethyl ether (10 mL) and the reaction mixture was stirred for 24 hours. After washing with water, the ether phase was dried with $MgSO_4$ and concentrated to dryness in vacuo to give the final product (yield: 95%). ^{1}H-NMR (400MHz, $CDCl_3$) δ(ppm): 10.05 (s, 1H), 7.95 (d, 2H), 7.87 (d, 2H), 1.36 (s, 12H). ^{13}C-NMR (100 MHz, $CDCl_3$) δ(ppm): 192.83, 138.56, 135.30, 128.86, 84.26, 25.34.

6.4.10 Protection of 3, 4-dihydroxybenzaldehyde

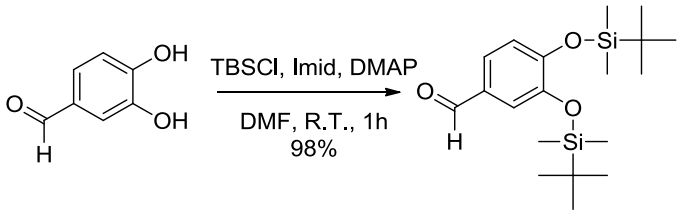

Scheme 6.9 Protection of 3, 4-dihydroxybenzaldehyde.

The hydroxyl groups were protected using tert-butyldimethylsilyl chloride.[49] To a solution of 3, 4-dihydroxybenzaldehyde (2.05 g, 15 mmol) in 25 mL DMF was added imidazole (3.05 g, 45 mmol), DMAP(183 mg, 1.5 mmol) and tert-butyldimethylsilyl chloride (6.80 g, 45 mmol). The mixture was kept stirring at room temperature for 1 hour. Then the solution was extracted with 25 mL diethyl ether for three times. The combined organic solution was washed with brine, and then dried over anhydrous $MgSO_4$. The remaining solvent was removed under reduced pressure. Final product was vacuum dried to obtain a white solid (yield: 98%). ^{1}H-NMR (400MHz, $CDCl_3$) δ(ppm): 9.80 (s, 1H), 7.35 (m, 2H), 6.93 (d, 1H), 0.99 (s, 18H), 0.23 (s, 12H). ^{13}C-NMR (100 MHz, $CDCl_3$) δ(ppm): 190.99, 153.41, 147.77, 130.72, 125.30, 120.43, 25.59, 18.61.

6.4.11 Synthesis of St-BA

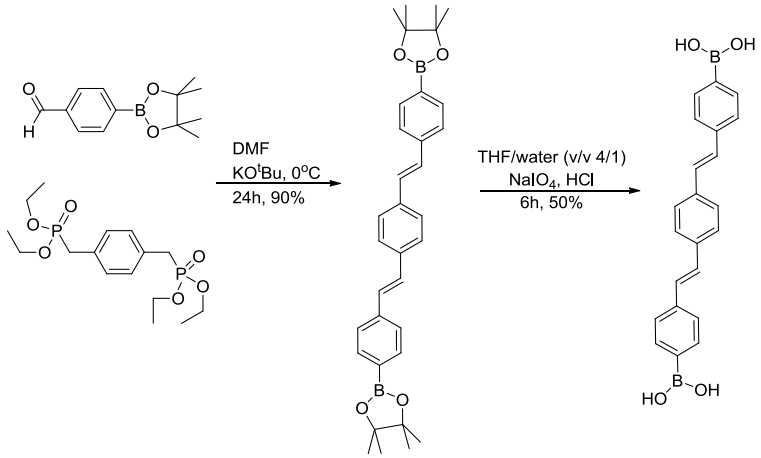

Scheme 6.10 Synthesis of **St-BA**.

First, 1.72 mmol aldehyde was added to a solution of the tetraethyl (1,4-phenylenebis(methylene))bis(phosphonate) in anhydrous DMF (5 mL) under argon atmosphere.

Potassium tert-butanolate (5.17 mmol) was added to the clear solution at 0 ℃. The mixture was stirred for 24 hours and allowed to warm up to room temperature. The reaction mixture was poured into water (20 mL) and neutralized with 1M HCl. The white precipitate formed was collected by filtration, washed thoroughly with water, and dried under vacuum. The residue was recrystallized from petroleum ether to give the pre-product as colorless needles (yield: 90%).

The crude pre-product was dissolved in THF (11mL) and some sodium periodate (2.22 g) and water (2.80 mL) was added. After stirring for 30 mins, 1M HCl (1.1 mL) was added. After 2 more hours, additional sodium periodate (1.17 g) was added and the solution was stirred for another 2 hours. The reaction mixture was diluted with ethyl acetate (20 mL) and washed with water. The organic phase was dried over anhydrous $MgSO_4$. The remaining solvent was removed under reduced pressure. Final product was vacuum dried to obtain a light yellow solid (yield: 50%). ^{1}H-NMR (400MHz, DMSO-6D) δ(ppm): 8.03 (s, 4H), 7.78 (d, 4H), 7.62 (s, 4H), 7.56 (d, 4H), 7.28 (q, 4H). ^{13}C-NMR (100MHz, DMSO-6D) δ(ppm): 139.04, 136.93, 135.03, 129.01, 128.91, 127.41, 125.97. ESI/MS m/z 429.18 $[M+59]^-$ (expect m/z=429.20), m/z 443.21 $[M+73]^-$ (expect m/z=443.22), m/z 457.22 $[M+87]^-$ (expect m/z=457.24).

6.4.12 Synthesis of St-Ca

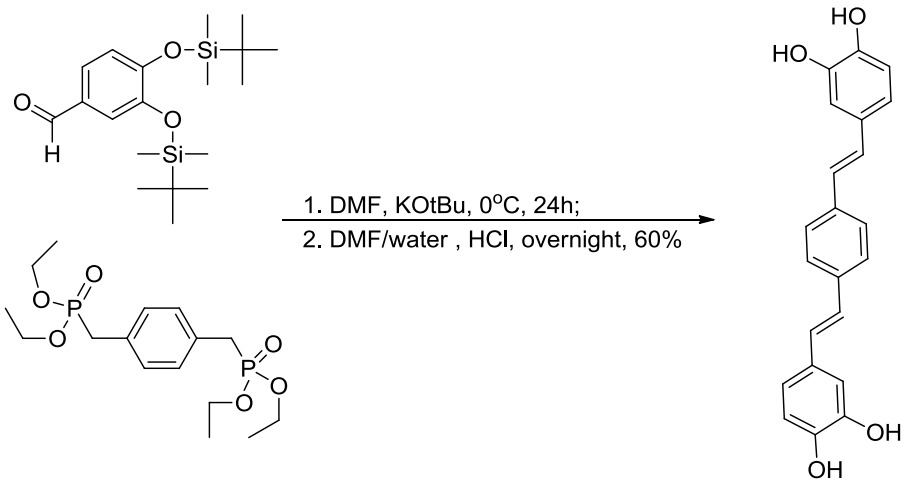

Scheme 6.11 Synthesis of **St-Ca**.

The preparation of **St-Ca** is similar to that of **St-BA** by using protected 3, 4-dihydroxybenzaldehyde instead. 1.06 mmol aldehyde was added to a solution of tetraethyl (1,4-phenylenebis(methylene))bis(phosphonate) in anhydrous DMF (5 mL) under argon atmosphere. Potassium tert-butoxide (3.17 mmol) was added to the clear solution at 0 ℃. The mixture was stirred for 24 hours and allowed to warm up to room temperature. The reaction mixture was poured into water (20 mL) and neutralized with 1M HCl. The mixture was kept stirring overnight. The white precipitate formed was collected by filtration, washed thoroughly with water, and dried under vacuum. The residue was recrystallized from petrolether to give the pre-product as colorless needles (yield: 60%). ^{1}H-NMR (400MHz, DMSO-6D) δ(ppm): 9.10 (s, 2H), 8.94 (s, 2H), 7.49 (s, 4H), 6.90 (m, 8H), 6.72 (d, 2H), ^{13}C-NMR (100MHz, DMSO-6D) δ(ppm): 146.11, 145.84, 136.60, 129.15, 128.85, 126.80, 125.13, 119.10, 116.13, 113.68. ESI/MS m/z 369.10 $[M+Na]^{+}$ (expect m/z=369.38).

6.4.13 Preparation of Nanoparticles via dropwise addition

First, **Im-Ca** and **Im-BA** were dissolved in methanol with the help of heating. After cooling down by setting at room temperature, one solution was added into the solution drop by drop, the mixture solution because deep orange and suspension was finally got. The resultant particles were purified by repeating centrifugation, decantation and resuspension. The composite particles were then dried in a vacuum oven at 50 ^{o}C overnight.

6.4.14 Stability of nanoparticles in solution and in solid state.

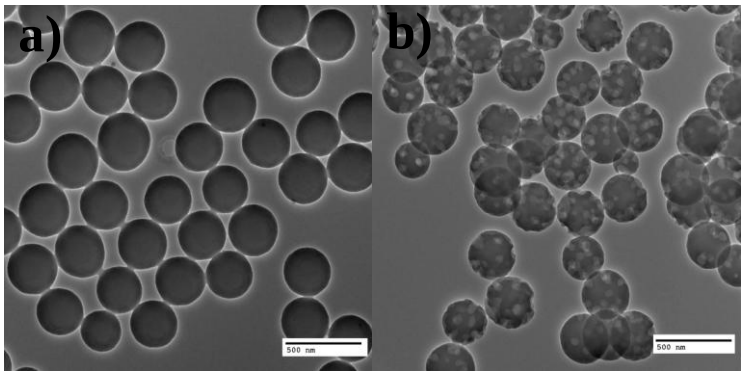

Figure 6.12 Aging of the **BNP** in methanol. TEM images of the samples taken after a) 5 mins after the mixing, size is 330 nm, b) 3 days after the mixing, size is 320 nm. The scale bar is 500 nm.

As noted in the manuscript, the nanoparticles disassemble at large dilutions in solution. Here we compare the stability in solution and dry solid state over a prolonged period. In solution, the particles seem to turn porous after 3 days (Figure 6.12). One possible explanation is that imine bond might hydrolyze, resulting in the disassembly of the particles. In fact, we observed that the imine bond in the **Im-BA** could hydrolyze back to the amine and aldehyde molecules slowly. In the ^{1}H NMR spectra over time, the intensity of the singlet at ~10 ppm, arising from the aldehyde CH proton, increased with a concurrent decrease in the intensity of the singlet at 8.6 ppm from the imine CH proton (Figure 6.13). By contrast, the dried particles retained its spherical morphology and size, when stored under dry conditions and redispersed in methanol for analysis.

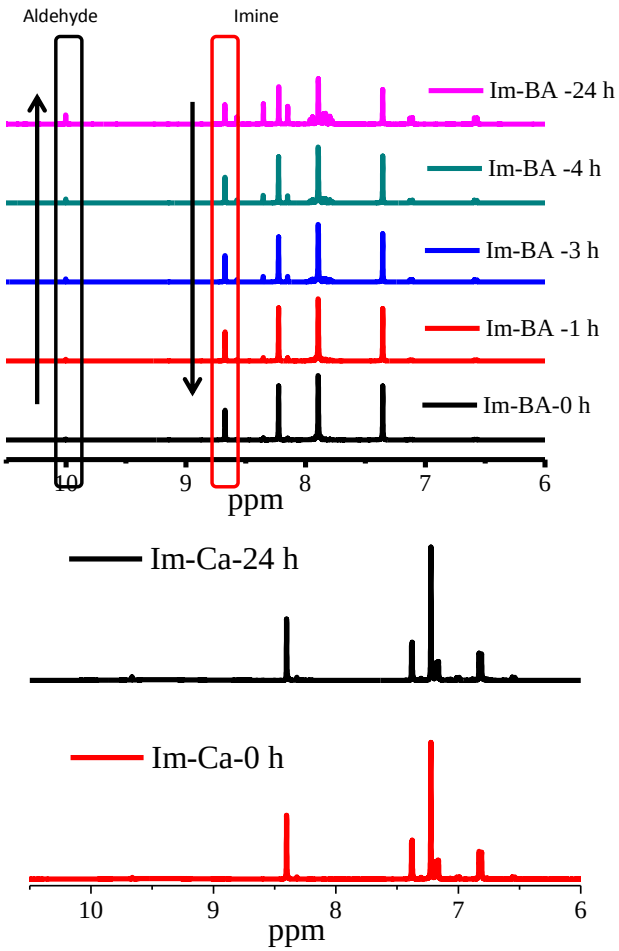

Figure 6.13 NMR spectra showing stability of the imine bond in **Im-BA** and **Im-Ca** as time.

Additionally, we characterized the thermal stability of the particles by TGA (Figure 6.14). The nanoparticles were found to be quite stable thermally with >70% of the residue remaining even at the high temperature of 600 ℃. There was about 10% weight decrease at ~150 ℃ indicating the possibility that there were some solvents trapped in these nanoparticles .

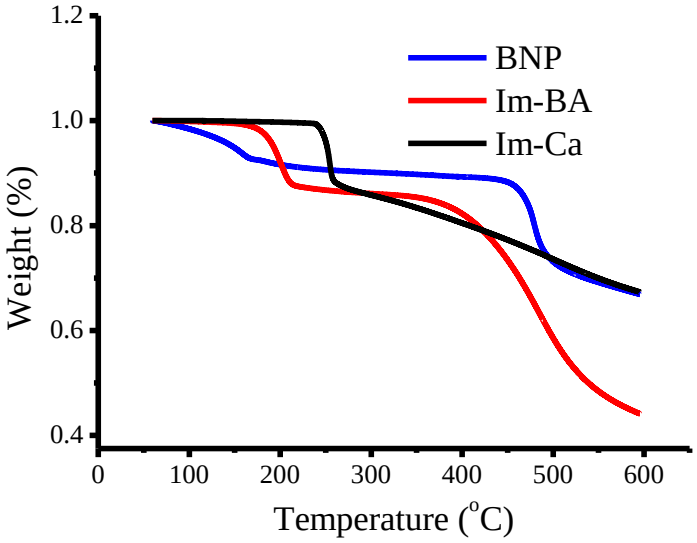

Figure 6.14 TGA curves of **Im-BA, Im-Ca** and solid **BNP**.

6.5 References

1. De Greef, T. F. A.; J. Smulders, M. M.; Wolffs, M.; Schenning, A. P. H. J.; Sijbesma, R. P.; Meijer, E. W. Supramolecular polymerization. *Chem Rev* **2009**, *109*, 5687-5754.

2. Jonkheijm, P.; Van der Schoot, P.; Schenning, A. P.; Meijer, E. W. Probing the solvent-assisted nucleation pathway in chemical self-assembly. *Science* **2006**, *313*, 80-83.

3. Song, Y.; Cheng, P. N.; Zhu, L.; Moore, E. G.; Moore, J. S. Multivalent macromolecules redirect nucleation-dependent fibrillar assembly into discrete nanostructures. *J. Am. Chem. Soc.*, **2014**, *136*, 5233-5236.

4. Caspar, D. L. Movement and self-control in protein assemblies. Quasi-equivalence revisited. *Biophys J.* **1980**, *32*, 103-138.

5. Van Workum, K.; Douglas, J. F. Schematic models of molecular self-organization. *Macromol. Symp.* **2005**, *227*, 1-16.

6. Simic, V.; Bouteiller, L.; Jalabert, M. Highly cooperative formation of bis-urea based supramolecular polymers. *J. Am. Chem. Soc.* **2003**, *125*, 13148-13154.

7. Folmer-Andersen, J. F.; Lehn, J. M. Thermoresponsive dynamers: thermally induced, reversible chain elongation of amphiphilic poly (acylhydrazones). *J. Am. Chem. Soc.* **2011**, *133*, 10966-10973.

8. Korevaar, P. A.; George, S. J.; Markvoort, A. J.; Smulders, M. M.; Hilbers, P. A.; Schenning, A. P.; De Greef, T. F.; Meijer, E. W. Pathway complexity in supramolecular polymerization. *Nature* **2012**, *481*, 492-496.

9. Zhao, D.; Moore, J. S. Nucleation-elongation polymerization under imbalanced stoichiometry. *J. Am. Chem. Soc.* **2003**, *125*, 16294-16299.

10. Iwasawa, N.; Takahagi, H. Boronic esters as a system for crystallization-induced dynamic self-assembly equipped with an on-off switch for equilibration. *J. Am. Chem. Soc.* **2007**, *129*, 7754-7755.

11. Christinat, N.; Scopelliti, R.; Severin, K. Multicomponent assembly of boronic acid based macrocycles and cages. *Angew. Chem. Int. Ed.* **2008**, *47*, 1848-1852.

12. Nishimura, N.; Kobayashi, K. Self-assembly of a cavitand-based capsule by dynamic boronic ester formation. *Angew. Chem. Int. Ed.* **2008**, *47*, 6255-6258.

13. Nishimura, N.; Yoza, K.; Kobayashi, K. Guest-encapsulation properties of a self-assembled capsule by dynamic boronic ester bonds. *J. Am. Chem. Soc.* **2009**, *132*, 777-790.

14. El-Kaderi, H. M.; Hunt, J. R.; Mendoza-Cortes, J. L.; Cote, A. P.; Taylor, R. E.; O'Keeffe, M.; Yaghi, O. M. Designed synthesis of 3D covalent organic frameworks. *Science* **2007**, *316*, 268-272.

15. Colson, J. W.; Woll, A. R.; Mukherjee, A.; Levendorf, M. P.; Spitler, E. L.; Shields, V. B.; Spencer, M. G.; Park, J.; Dichtel, W. R. Oriented 2D covalent organic framework thin films on single-layer grapheme. *Science* **2011**, *332*, 228-231.

16. Nakazawa, I.; Suda, S.; Masuda, M.; Asai, M.; Shimizu, T. pH-Dependent reversible polymers formed from cyclic sugar-and aromatic boronic acid-based bolaamphiphiles. *Chem. Commun.*, **2000**, *10*, 881-882.

17. Niu, W.; Smith, M. D.; Lavigne, J. J. Self-assembling poly (dioxaborole) s as blue-emissive materials. *J. Am. Chem. Soc.* **2006**, *128*, 16466-16467.

18. Bapat, A. P.; Roy, D.; Ray, J. G.; Savin, D. A.; Sumerlin, B. S. Dynamic-covalent macromolecular stars with boronic ester linkages. *J. Am. Chem. Soc.* **2011**, *133*, 19832-19838.

19. Nishiyabu, R.; Teraoka, S.; Matsushima, Y.; Kubo, Y. Fabrication of soft submicrospheres by sequential boronate esterification and their dynamic behavior. *ChemPlusChem* **2012**, *77*, 201.

20. Höpfl, H. J. The tetrahedral character of the boron atom newly defined—a useful tool to evaluate the N→ B bond. *Organomet. Chem.* **1999**, *581*, 129-149.

21. Zhu, L.; Shabbir, S. H.; Gray, M.; Lynch, V. M.; Sorey, S.; Anslyn, E. V. A structural investigation of the NB interaction in an *o*-(N, N-dialkylaminomethyl) arylboronate system. *J. Am. Chem. Soc.* **2006**, *128*, 1222-1232.

22. Franzen, S.; Ni, W.; Wang, B. Study of the mechanism of electron-transfer quenching by boron-nitrogen adducts in fluorescent sensors. *J. Phys. Chem. B* **2003**, *107*, 12942-12948.

23. Ni, W.; Kaur, G.; Springsteen, G.; Wang, B.; Franzen, S. Regulating the fluorescence intensity of an anthracene boronic acid system: a B–N bond or a hydrolysis mechanism? *Bioorg. Chem.*, **2004**, *32*, 571-581.

24. Christinat, N.; Scopelliti, R.; Severin, K. Multicomponent assembly of boron-based dendritic nanostructures. *J. Org. Chem.* **2007**, *72*, 2192-2200.

25. Cruz-Huerta, J.; Salazar-Mendoza, D.; Hernandez-Paredes, J.; Hernandez Ahuactzi, I. F.; Hopfl, H. N-containing boronic esters as self-complementary building blocks for the assembly of 2D and 3D molecular networks. *Chem. Commun.* **2012**, *48*, 4241-4243.

26. Sheepwash, E.; Krampl, V.; Scopelliti, R.; Sereda, O.; Neels, A.; Severin, K. Molecular networks based on dative boron-nitrogen bonds. *Angew. Chem. Int. Ed.* **2011**, *50*, 3034-3037.

27. Zhang, Y.; Li, M.; Chandrasekaran, S.; Gao, X.; Fang, X.; Lee, H. W.; Hardcastle, K.; Yang, J.; Wang, B. A unique quinolineboronic acid-based supramolecular structure that relies on double intermolecular B-N bonds for self-assembly in solid state and in solution. *Tetrahedron*, **2007**, *63*, 3287-3292.

28. Kiviranta, P. H.; Leppänen, J.; Kyrylenko, S.; Salo, H. S.; Lahtela-Kakkonen, M.; Tervo, A. J.; Wittekindt, C.; Suuronen, T.; Kuusisto, E.; Järvinen, T. N, N'-bisbenzylidenebenzene-1, 4-diamines and N, N'-bisbenzylidenenaphthalene-1, 4-diamines as sirtuin type 2 (SIRT2) inhibitors. *J. Med. Chem.* **2006**, *49*, 7907-7911.

29. Spitler, E. L.; Dichtel, W. R. Lewis acid-catalysed formation of two-dimensional phthalocyanine covalent organic frameworks. *Nat. Chem.*, **2010**, *2*, 672-677.

30. Spitler, E. L.; Giovino, M. R.; White, S. L.; Dichtel, W. R. A mechanistic study of Lewis acid-catalyzed covalent organic framework formation. *Chem. Sci.*, **2011**, *2*, 1588-1593.

31. Brewer, S. H.; Allen, A. M.; Lappi, S. E.; Chasse, T. L.; Briggman, K. A.; Gorman, C. B.; Franzen, S. Infrared detection of a phenylboronic acid terminated alkane thiol monolayer on gold surfaces. *Langmuir* **2004**, *20*, 5512-5520.

32. Li, H.; Jäkle, F. Universal scaffold for fluorescent conjugated organoborane polymers. *Angew. Chem. Int. Ed.*, **2009**, *48*, 2313-2316.

33. Jäkle, F.; Lewis acidic organoboron polymers. *Coord. Chem. Rev.*, **2006**, *250*, 1107-1121.

34. Hall, L. W.; Odom, J. D.; Ellis, P. D. Nuclear magnetic resonance investigation of the nature of the boron-carbon bond in some vinylboranes. *J. Am. Chem. Soc.* **1975**, *97*, 4527-4531.

35. Liu, W.; Pink, M.; Lee, D. Conjugated polymer sensors built on π-extended borasiloxane cages. *J. Am. Chem. Soc.* **2009**, *131*, 8703-8707.

36. Bachler, V.; Metzler-Nolte, N. The π-electron-accepting ability of the boron atom in ethynylboranes and related compounds-an approximate weight computation for resonance structures. *Eur. J. Inorg. Chem.* **1998**, *6*, 733-744;

37. Zhao, D.; Moore, J. S. Reversible polymerization driven by folding. *J. Am. Chem. Soc.* **2002**, *124*, 9996-9997.

38. Oh, K.; Jeong, K.-S.; Moore, J. S. Folding-driven synthesis of oligomers. *Nature* **2001**, *414*, 889.

39. LaMer, V. K.; Dinegar, R. H. Theory, production and mechanism of formation of monodispersed hydrosols. *J. Am. Chem. Soc.* **1950**, *72*, 4847-4854.

40. Oh, M.; Mirkin, C. A. Chemically tailorable colloidal particles from infinite coordination polymers. *Nature* **2005**, *438*, 651-654.

41. Maeda, H.; Hasegawa, M.; Hashimoto, T.; Kakimoto, T.; Nishio, S.; Nakanishi, T. Nanoscale spherical architectures fabricated by metal coordination of multiple dipyrrin moieties. *J. Am. Chem. Soc.* **2006**, *128*, 10024-10025.

42. Niu, W.; Smith, M. D.; Lavigne, J. J. Substituent effects on the structure and supramolecular assembly of bis (dioxaborole) s derived from 1, 2, 4, 5-tetrahydroxybenzene. *Cryst. Growth Des.* **2006**, *6*, 1274-1277.

43. Korevaar, P. A.; Schaefer, C.; De Greef, T. F.; Meijer, E. W. Controlling chemical self-assembly by solvent-dependent dynamics. *J. Am. Chem. Soc.* **2012**, *134*, 13482-13491.

44. England, J. L.; Haran, G. Role of solvation effects in protein denaturation: from thermodynamics to single molecules and back. *Annu. Rev. Phys. Chem.* **2011**, *62*, 257-277.

45. Kiviranta, P. H.; Leppänen, J.; Kyrylenko, S.; Salo, H. S.; Lahtela-Kakkonen, M.; Tervo, A. J.; Wittekindt, C.; Suuronen, T.; Kuusisto, E.; Järvinen, T. N, N'-bisbenzylidenebenzene-1, 4-diamines and N, N'-bisbenzylidenenaphthalene-1, 4-diamines as sirtuin type 2 (SIRT2) inhibitors. *J. Med. Chem.* **2006**, *49*, 7907-7911.

46. Cheng, L. X.; Tang, J. J.; Luo, H.; Jin, X. L.; Dai, F.; Yang, J.; Qian, Y. P.; Li, X. Z.; Zhou, B. Antioxidant and antiproliferative activities of hydroxyl-substituted Schiff bases. *Bioorg. Med. Chem. Lett.* **2010**, *20*, 2417-2420.

47. Ha, Y. M.; Lee, H. J.; Park, D.; Jeong, H. O.; Park, J. Y.; Park, Y. J.; Lee, K. J.; Lee, J. Y.; Moon, H. R.; Chung, H. Y. Molecular docking studies of (1E,3E,5E)-1,6-bis(substituted phenyl)hexa-1,3,5-triene and 1,4-bis(substituted *trans*-styryl)benzene analogs as novel tyrosinase inhibitors. *Biol. Pharm. Bull.* **2012**, *36*, 55-65.

48. Oehlke, A.; Auer, A. A.; Jahre, I.; Walfort, B.; Rüffer, T.; Zoufalá, P.; Lang, H.; Spange, S. Nitro-substituted stilbeneboronate pinacol esters and their fluoro-adducts. fluoride ion induced polarity enhancement of arylboronate esters. *J. Org. Chem.* **2007**, *72*, 4328-4339.

49. Uchiyama, M.; Ozawa, H.; Takuma, K.; Matsumoto, Y.; Yonehara, M.; Hiroya, K.; Sakamoto, T. Regiocontrolled intramolecular cyclizations of carboxylic acids to carbon-carbon triple bonds promoted by acid or base catalyst. *Org. Lett.* **2006**, *8*, 5517-5520.

CHAPTER 7

HOLLOW METAL ORGANIC NANOPARTICLES FROM POLYMERIC NANOPARTICLES USING KIRKENDALL EFFECT

7.1 Introduction

The rapidly developing field of nanotechnology depends on versatile strategies that provide access to the next generation of nanomaterials[1-3]. Majority of current nanomaterials are either purely inorganic[4,5], such as silica nanoparticles, metal and metal oxide nanocrystals, or purely organic[6,7], such as polymer nanoparticles and supramolecular assemblies. There is a recent surge in methods for generating hybrid metal-organic coordination materials, constructed from metal ions and polyfunctional organic ligands[8-11]. One of the important determinants of their versatility emanates from the opportunity for diversity in these materials through functional group variations of the inorganic or organic building blocks. This chemical design feature has opened up the opportunities for these materials in a number of diverse applications such as catalysis, gas storage, biosensing, and biomedicine.[12-14]

In all these applications, hollow nanoparticles have increasingly attracted special interest, because of their low density, high surface area, material economy, and lower cost compared to their solid counterparts. Several assembly techniques, including liquid-liquid interfacial growth,[15] spay-drying[16], solvothermal approach[17,18] Ostwald ripening,[19] and template synthesis[20-22], have been used to prepare hollow metal-organic nanoparticles (MOPs). Similarly, hollow inorganic nanoparticles have been accessed using a range of related techniques.[23-26] Among the methods used for hollow inorganic nanoparticles, Kirkendall effect is particularly interesting, as this provides a simple and robust access to pristine and hybrid hollow inorganic materials.[24] Despite the advantages, this non-reciprocal diffusion process has not been used for achieving hollow MOPs.

In this manuscript, we report a simple, rapid, and robust strategy for achieving hollow MOPs from high-quality organic polymer nanoparticles using the Kirkendall effect. The well-defined solid nature of the starting organic polymer nanoparticles translates to well-defined hollow MOPs after the addition of metal ions. We show that (*i*) the underlying mechanism for the formation of the hollow MOP is the Kirkendall effect, which is the first time to be applied for metal-organic composites, rather than for metallic nanocrystals; (*ii*) a variety of metal ions with different coordination geometries can result in the formation of the hollow MOPs, indicating the generality of the methodology; (*iii*) this Kirkendall effect is then conveniently exploited to demonstrate control over the thickness of the nanoparticle walls; and (*iv*) the size of the hollow MOPs can be easily tuned by using the precursor organic polymer nanoparticles of different sizes.

7.2 Results and Discussion

7.2.1 Preparation and characterization of hollow metal organic nanoparticles (MOPs)

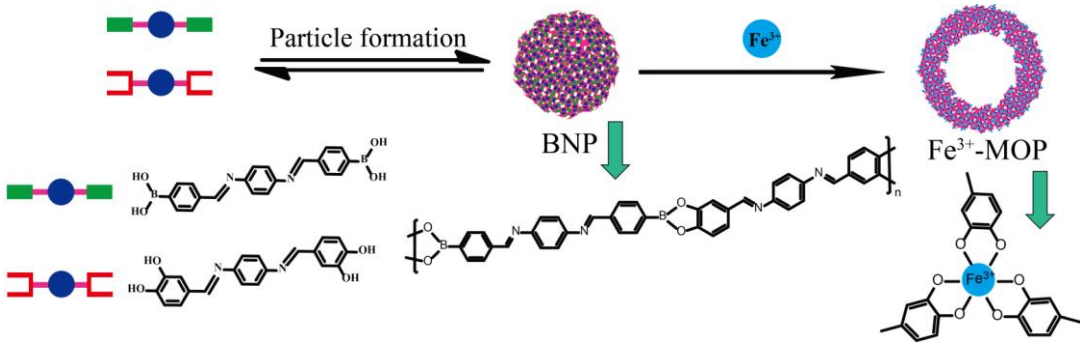

Scheme 7.1 Scheme presents the syntheses of BNP via Im-Ca and Im-BA, and the preparation of hollow MOP by adding metal chloride salts to the BNP solution.

In a typical synthesis, a calculated amount of $FeCl_3$ is simply added to a methanolic suspension of the pre-made organic boronate nanoparticle (BNP). After stirring the solution for about 12 hours, a solid product was collected by centrifugation and washed with methanol. The BNP itself was prepared using a simple condensation-driven cooperative polymerization of a bis-imido boronic acid (Im-BA) molecule and a bis-imido catechol (Im-Ca) molecule in methanol[27]. The reaction scheme and the MOP formation are illustrated in scheme 7.1.

Figure 7.1a shows transmission electron microscopy (TEM) images of BNP with diameter of ~300 nm. Upon addition of $FeCl_3$, the color of the solution immediately changed and the formation of nanoparticles with distinct contrast between the center and corona were evident from TEM (Figure 7.1b). This provided the first indication of the hollow nature of the resultant nanoparticles. The hollow morphology was further investigated using field emission scanning electron microscopy (SEM, Figure 7.1c). Broken nanoparticles indeed showed empty inner spaces (inset of Figure 7.1c), providing direct evidence for the formation of hollow nanoparticles.

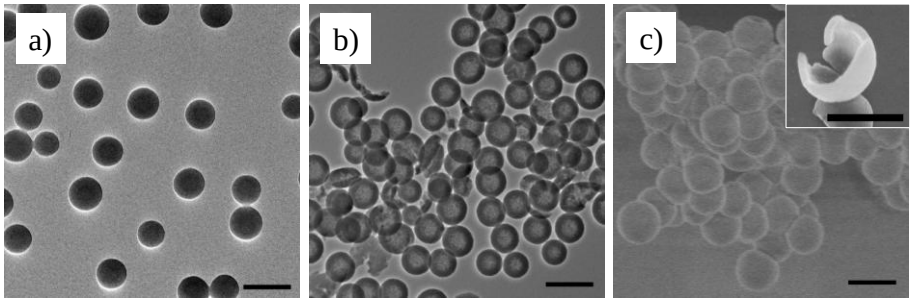

Figure 7.1 a) TEM image of the BNP; b) TEM image of the hollow Fe^{3+}-MOP; c) SEM image of the hollow Fe^{3+}-MOP; Inset is a SEM image of one broken hollow Fe^{3+}-MOP. All the scale bar is 500 nm.

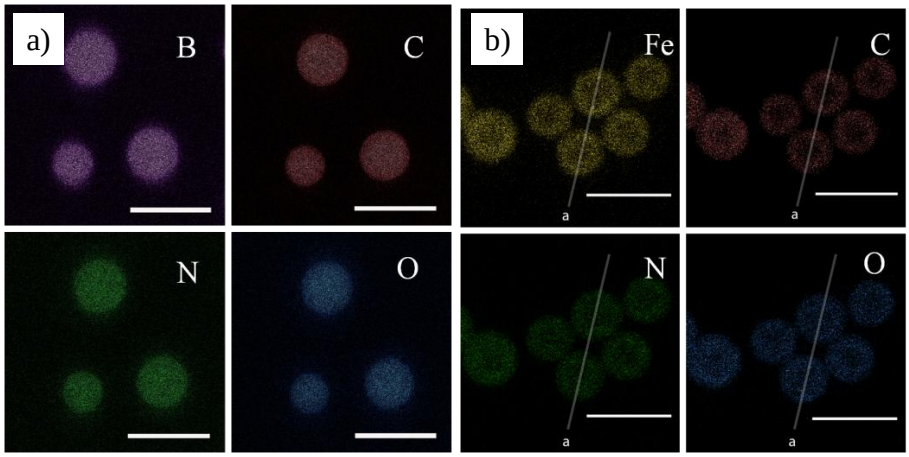

Figure 7.2 a) EELS mapped images of BNP; b) EELS mapped images of hollow Fe^{3+}-MOP. All the scale bar is 500 nm.

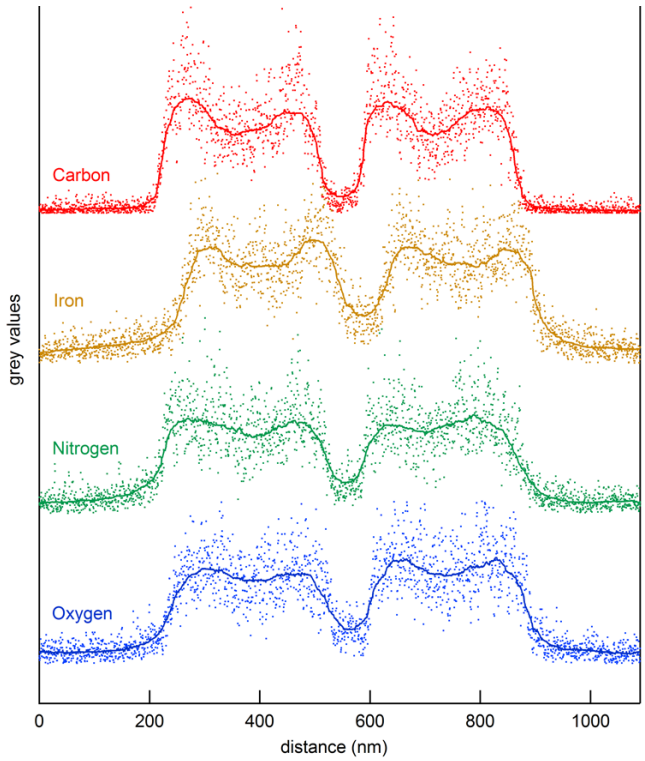

Figure 7.3 Fe, C, N and O line-scanned EELS profiles of two nanoparticles in Figure 1f. EELS images and line-scan profiles confirm the hollow structure of hollow Fe^{3+}-MOP.

The presumption in this experiment is to test the effect of the strong coordination interaction between catechol moieties and Fe^{3+} upon the polymer nanoparticle. This coordination interaction presumably replaces the boronic acid monomer in the polymer to result in a crosslinked nanoparticle. Note that Fe^{3+} complexes are octahedral and therefore require three catechol moieties for binding, which should result in a crosslinked nanoparticle. This possibility was investigated using Energy Filtered Transmission Electron Microscopy (EFTEM). The EFTEM maps show clearly that boron, carbon, nitrogen and oxygen are all homogenously distributed throughout the entire BNP (Figure 7.2a). In contrast however, iron was found along with carbon, nitrogen and oxygen in the hollow nanoparticles (Figure 7.2b). There was no discernible presence of boron in these particles, implying that the hollow nanoparticles might indeed be due to the iron-catechol coordination and thus the observed nanostructures could be hollow MOPs. To further investigate the hollow nature of these MOPs, EFTEM cross-sectional profiles were

analyzed across two individual particles (Figure 7.3). Elemental mapping by energy dispersive X-ray absorption spectroscopy (EDS) further confirmed similar distribution of iron and carbon throughout the entire hollow nanoparticles (Figure 7.4). The intensity of the mapped images shows the characteristic properties of a hollow structure with contrast between the core and shell of the nanoparticles.

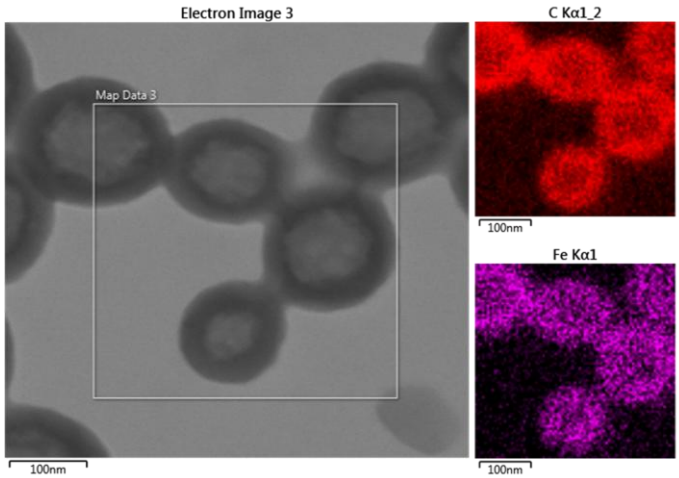

Figure 7.4 Bright-field STEM images and EDS maps of hollow Fe^{3+}-MOP, element C and Fe included.

7.2.2 General method for hollow metal organic nanoparticles (MOP)

The versatility of this method of generating hollow MOPs was investigated using other metal ions, Cu^{2+}, Sn^{4+}, and Al^{3+}. These metal ions were chosen, because they provide not only variations in their preferred coordination geometry (4- or 6-coordinate), but also variations in their ability to crosslink. Since only two catechol units are needed for the 4-coordinate distorted tetrahedral geometry, it is not necessary that the resultant metal organic material is crosslinked. We investigated whether similar hollow MOP formation could be observed for these other metal ions as well. As shown in Figures 7.5a-7.5c, hollow MOPs are also obtained for all of these ions. EDS analysis of the Sn-based MOP also showed the presence of both tin and carbon in the hollow nanoparticles (Figure 7.6a). In addition, the possibility of preparing hollow dual-metal MOPs was

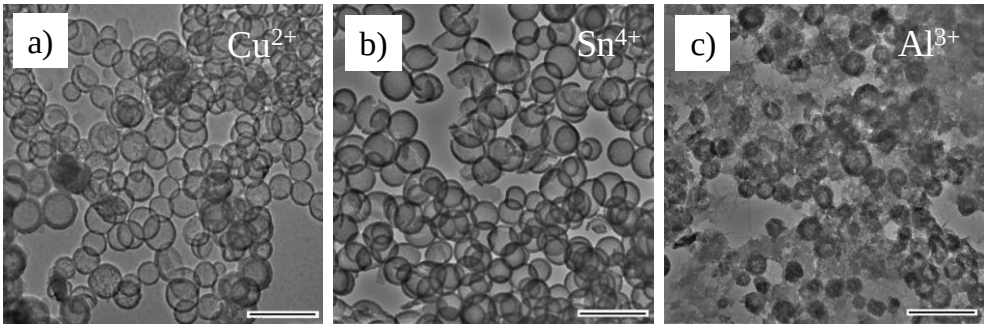

Figure 7.5 a) TEM image of the hollow Cu^{2+}-MOP by adding Cu^{2+}; b) TEM image of the hollow Sn^{4+}-MOP adding Sn^{4+}; c) TEM image of the hollow Al^{3+}-MOP adding Al^{3+}; All the scale bar is 500 nm.

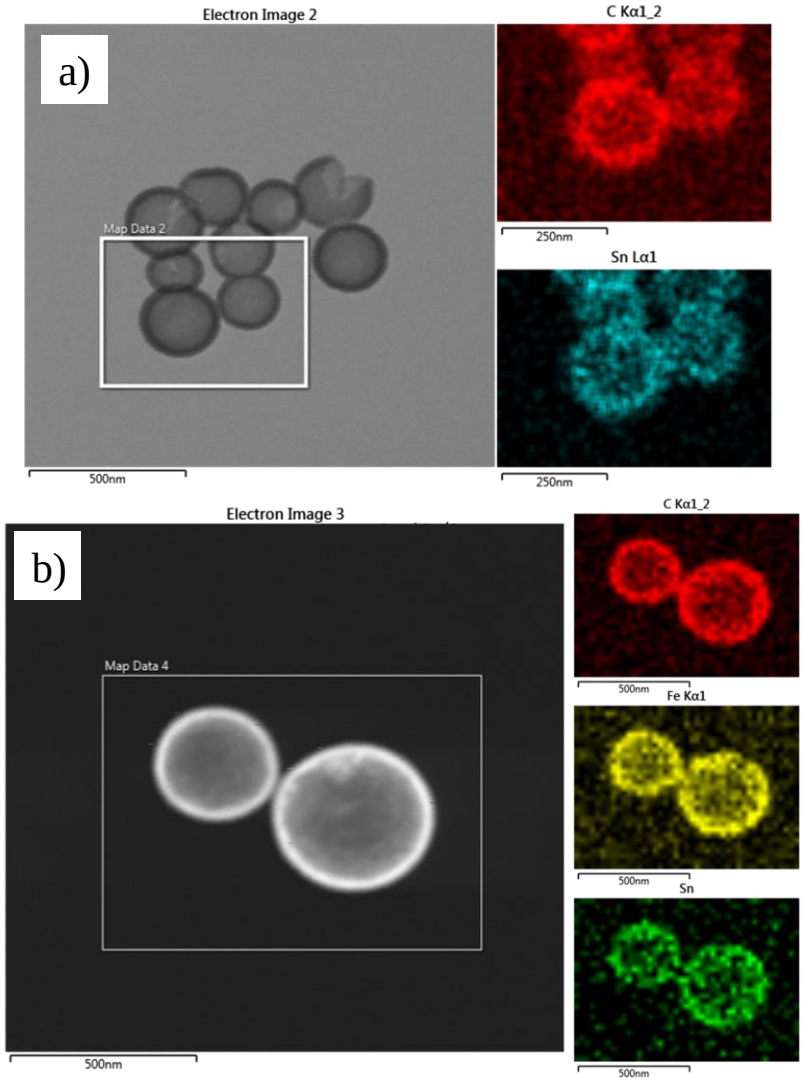

Figure 7.6 a) Bright-field STEM images and EDS maps of hollow Sn^{4+}-MOP, element C and Sn included; b) HAADF STEM images and EDS maps of dual Fe^{3+}/Sn^{4+}-hollow MOP, element C, Fe and Sn included.

also tested by adding a mixture of $FeCl_3$ and $SnCl_4$ in a 1:1 ratio to the BNP solution. EDS of samples indeed showed a homogenous distribution of element Fe and Sn in the hollow nanoparticles (Figures 7.6b).

7.2.3 Electron paramagnetic resonance spectroscopy characterization

The hypothesis for describing the formation mechanism of the hollow MOPs is that the metal ions replace the boronate functionalities to form a stable metal-catecholate complex. Electron paramagnetic resonance (EPR) spectroscopy was used to investigate this ligand field environment around the high-spin (hs, d5) Fe^{3+}. EPR spectroscopy is a sensitive probe of the number of catecholate ligands coordinated to the Fe^{3+} center[28]. Figure 3 shows the EPR spectra of the metal-free BNP and three metal-containing (Fe^{3+}, Al^{3+}, and dual Fe^{3+} - Al^{3+}) hollow MOPs. The spectrum of as-prepared BNP shows a single sharp feature at g = 2.00 that is readily assigned to an organic radical species. The spectrum of the Al^{3+} hollow MOP displays the same g = 2.00 resonance. However, the spectrum of the Fe^{3+} hollow MOP displays two broad features centered at g' = 4.25 and ~ 9.6 in addition to the significantly broadened g = 2.00 resonance. These peaks in the spectrum of pure Fe^{3+}-MOPs are rather broad and indistinguishable from the ferromagnetic resonances that are typical for Fe_2O_3 nanoparticles[29] or mixed-valent iron centers[30]. To conclusively rule out the formation of these undesired phases, we prepared hollow MOPs using only 5 mol % Fe^{3+} diluted in Al^{3+}. The features in the EPR spectrum of these hollow MOPs, containing diluted Fe^{3+} centers, are much narrower which is consistent with the absence of condensed Fe-O phases. Interestingly, an additional weak resonance at g' ~ 9.6 is resolved in the spectrum of the Fe^{3+}-doped Al^{3+} hollow MOPs that is occluded by the broad g' = 4.25 resonance in the pure Fe^{3+} hollow MOPs. The EPR spectrum of the mixed metal hollow MOPs displays the same features of Fe^{3+} with tris(catecholate) coordination[28]. The pseudo-octahedral geometry of $[Fe(catecholate)_3]^{3+}$ produces a rhombic EPR spectrum with resonances at g' = 4.22 and a weak resonance at g' ~ 9.6.[29] In addition to the rhombic Fe^{3+} features at g-values > 3, a rather intense

radical signal (g = 2.00) can also be observed. A similar radical signal was also reported in a paramagnetic Fe^{3+} complex with three substituted catecholate ligand, DOPA (3,4-dihydroxyphenylalanine)[31, 32].

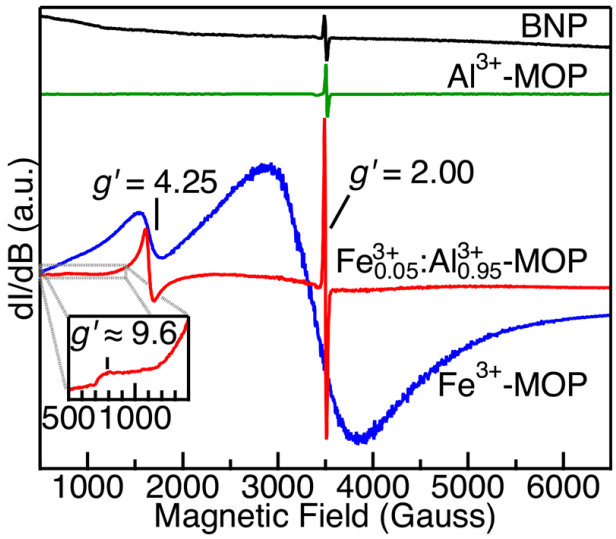

Figure 7.7 EPR spectra of BNP and hollow MOP. 295 K, X-band (9.8 GHz) EPR spectrum measured at room temperature for BNP (black), hollow Al^{3+}-MOP (green), hollow Fe^{3+}-MOP (blue), dual hollow Fe^{3+}/Al^{3+}-MOP (red) (starting composition was 0.05 mol fraction of $FeCl_3/AlCl_3$). Inset: g' ~ 9.6 transition of the dual hollow Fe^{3+}/Al^{3+}-MOPs on an expanded scale.

7.2.4 Mechanism study of the hollow MOP formation

The mechanism of the hollow MOP formation was probed. A reasonable hypothesis is that the formation of hollow MOPs is due to Kirkendall effect, which is a phenomenon that was originally observed in metallurgy[33]. Here, the nonreciprocal mutual diffusion process through an interface of two metals results in the creation of vacancies to compensate from the inequality of the material flow. This feature has been utilized to generate hollow Co_3S_4 and CoO nanocrystals[24] and later to obtain hollow nanoparticles of oxides and chalcogenides[34]. Thus, this effect has previously been limited to the chemical transformation of metallic nanocrystals. To investigate if the Kirkendall effect is responsible for the observed formation organic-inorganic composite nanostructures, we monitored the temporal evolution of the conversion of the BNPs to hollow MOPs after addition of $FeCl_3$. Aliquots were taken from the reaction mixture at various times and

monitored by TEM. A few small cavities in interior of the solid nanoparticles (Figure 7.8b) are clearly observed within 20 minutes. After 1 hour, the particle cores became patchy and the surface of the nanoparticles became concurrently more prominent (Figure 7.8c). Fully hollow nanoparticles were formed after 6 hours (Figure 7.8d) and no further evolution of morphology was observed, suggesting that the formation of hollow nanoparticles before 6 hours. A similar trend in the temporal evolution was also observed for the Sn^{4+}-based hollow MOPs (Figure 7.9).

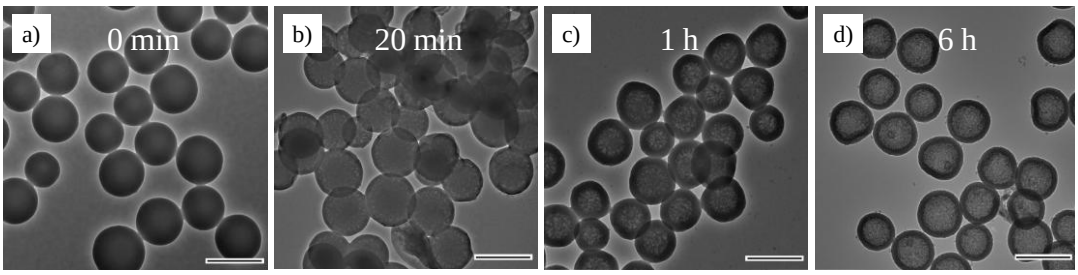

Figure 7.8 TEM images taken at a) 0 min, b) 20 min, c) 1 h and d) 6 h after the addition of $FeCl_3$ into BNP; the scale bar is 500 nm. Conditions: 0.1 mL $FeCl_3$ methanol solution was added into 1 mL BNP methanol solution prepared using 3 mg/mL Im-BA and Im-Ca, the ratio of Fe^{3+} to Im-Ca was 1/2. The TEM samples were taken by drop-casting. The scale bar is 500 nm.

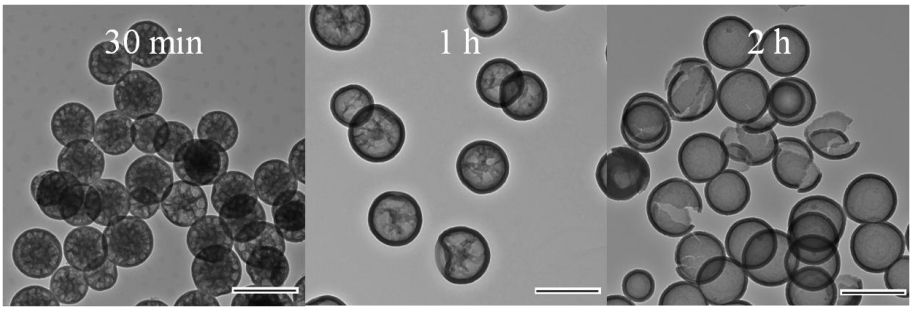

Figure 7.9 Time dependent TEM measurement, taken after 30 min, 1 h, and 2 h. Conditions: 0.1 mL $SnCl_4$ methanol solution was added into 1 mL BNP methanol solution prepared using 3 mg/mL Im-BA and Im-Ca, the ratio of Sn^{4+} to Im-Ca was 1/2. The TEM samples were taken by drop-casting. The scale bar is 500 nm.

An important implication of understanding the operating mechanism is that it offers a pathway for additional control elements. A rendition of the Kirkendall effect to explain the formation of hollow MOPs would suggest that the diffusion of the boronate ester polymer to the surface of the nanoparticle, where the reaction between Fe^{3+} and the boronate ester takes place, is faster than the diffusion of Fe^{3+} from the solution to the interior of the particle (Scheme 7.2). If

the opposite were true (diffusion of Fe^{3+} into the interior of the BNP is faster than boronate ester polymer out-diffusion), then the resultant product will be a solid nanoparticle.

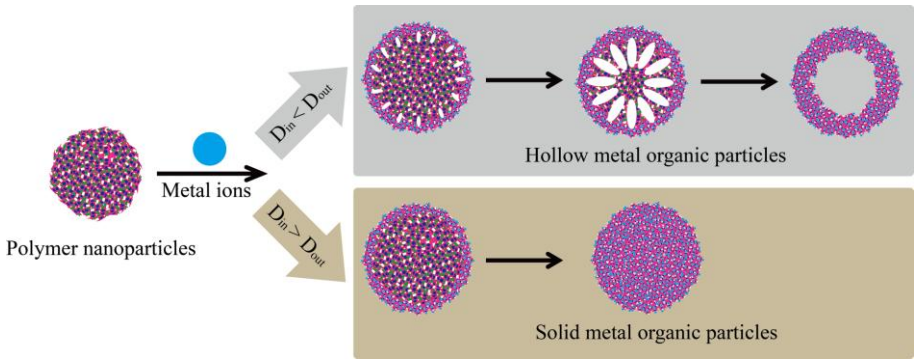

Scheme 7.2 Schematic illustration showing the transformation of solid polymer nanoparticles to hollow or solid metal organic particles, depending on the relative diffusivities.

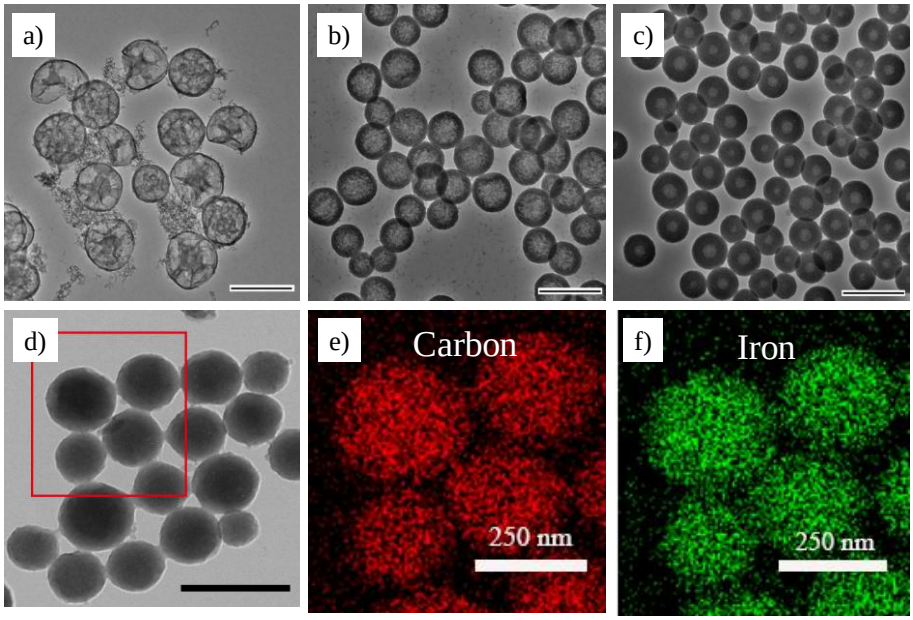

Figure 7.10 The thickness of shell could be tuned by changing the ratio of Fe^{3+} to Im-Ca, a) 1/8, b) 1/2, c) 3/4.However, when the ratio increased up to 1/1, only solid MOPs were observed as shown TEM in figure d). EDS maps of solid Fe^{3+}-MOP, element C (e) and Fe (f) included. , all scale bar is 500 nm except e) and f) with 250 nm scale bar.

We hypothesized then that one can gain control over the thickness of the shell in the hollow MOPs by simply tuning the concentration of Fe^{3+} in solution, as these variations will generate an intermediate scenario between the solid and the hollow nanoparticles. Accordingly, the ratio of

metal ions to the polymer repeat units was varied. Indeed, this variation was found to affect not only the thickness of the shells, but understandably also the rate of the formation of the hollow MOPs. For example, when the concentration of $FeCl_3$ is 1/8th of that of the Im-Ca repeat unit in the polymer, it took more than 12 hours to complete the formation of hollow MOP. However, this process was completed within 2 hours, when this ratio was changed to 1:2. As anticipated, the thickness of the shell was also observed to increase consistently with the increasing ratio of $FeCl_3$/Im-Ca, from about 15 nm to 90 nm when the ratio increased from 1/8 to 3/4 (Figure 7.10a – 7.10c). Similar to Fe^{3+}, both the rate of formation and the thickness of the shell increase with the increasing amount of Sn^{4+} ions. The formation of solid MOPs in the presence of an even higher concentration of Fe^{3+} ions (ratio of $FeCl_3$/Im-Ca is 1:1) further supports that the operating mechanism as one based on Kirkendall effect. EDS analysis of the samples showed a homogenous distribution of Fe in the respective solid nanoparticles (Figure 7.10d – 7.10f).

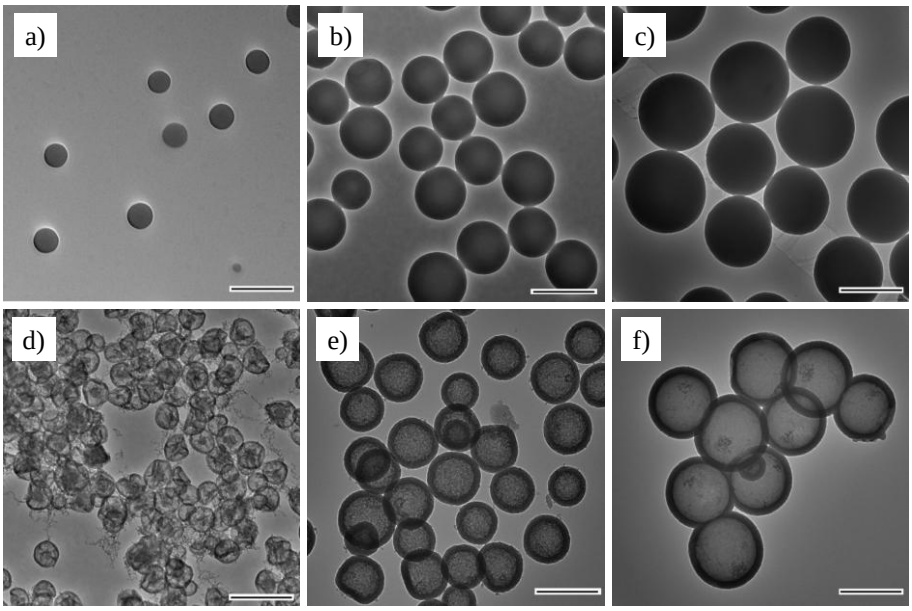

Figure 7.11 The size of hollow MOP could be varied by tuning the size of BNP used, a, d) 1.5 mg/mL monomers, b, e) 3.0 mg/mL monomers, c, f) 5.0 mg/mL monomers. The ratio of Fe^{3+} to Im-Ca was 1/2; all scale bar is 500 nm.

Finally, it is also important to identify whether the starting size of the boronate nanoparticle will be preserved during the transformation to hollow MOPs. The BNPs size can be tuned by

simply varying the concentrations of the monomers[27]. Three BNPs with diameters of 210, 410, and 550 nm were used for the formation of hollow MOPs (Figure 7.11a – 7.11c). Our results indeed show that the resulting size of the hollow MOPs depends on the size of the primary BNP (see Figure 7.11d – 7.11f). Overall, hollow MOPs can be obtained with an excellent control over size, kinetics of formation and shell thickness.

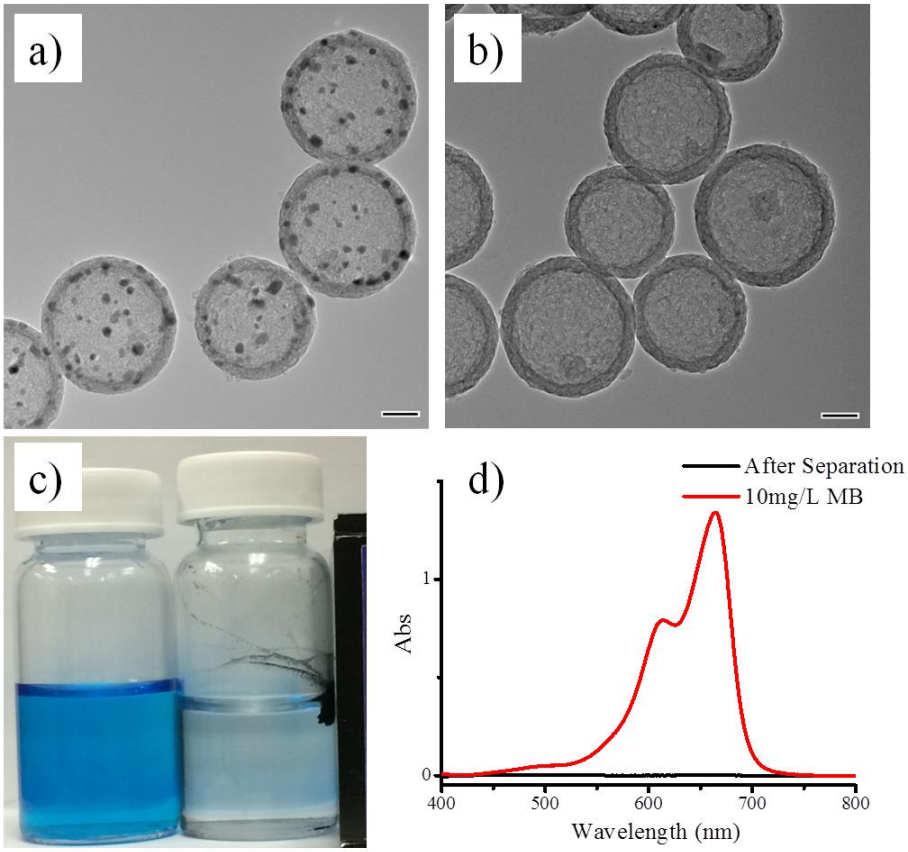

Figure 7.12 Preparation and application of hollow Fe@C particles. TEM measurement of a) hollow Fe@C particles after the temperature thermal treatment of MOPs, b) hollow carbon particles after the acid treatment of Fe@C; c) Optical photograph of the MB solution without (left) and with (right) the addition of Fe@C applying an external magnet; d) UV-vis absorption measurement before and after the magnetic separation.

To demonstrate a potential application of these hollow MOPs, hollow carbon particles loaded with metal nanoparticles (M@C) were prepared by direct pyrolysis. For example, the high temperature thermal treatment of hollow Fe^{3+}-MOPs at 800 ^{o}C under a N_2 atmosphere for 1 hour resulted in the formation of light color hollow carbon spheres loaded with small dark

nanoparticles as shown in TEM of Figure 7.12a. The iron content of the small nanoparticles was confirmed from the EDX line scanning data (Figure 7.13). These small nanoparticles can be removed by the addition of hydrogen chloride with the formation of small bubbles in the solution (Figure 7.12b), further indicating that these small nanoparticles are likely to be pure Fe nanoparticles. These magnetic-functionalized carbon particles with encapsulated Fe nanoparticles have been successfully used as a magnetically separable adsorbent for removing organic waste from aqueous solution using an organic dye (methylene blue, MB).[35] The photograph in Figure 7.12c and the absorption spectra in Figure 6d demonstrate the separation of MB using these hollow Fe@C . Absorption spectra, measured before and after mixing aqueous solutions of MB with Fe@C nanoparticles, indicate that MB has been almost quantitatively removed from the solution (Figure 7.12d). The magnetic property of the Fe@C particles is then utilized to remove them from the aqueous solution. Redistribution of these particles in methanol releases the MB into methanol, which allows for the particles to be reused. We show that MB can be quantitatively removed from the aqueous solution and then released into methanol.

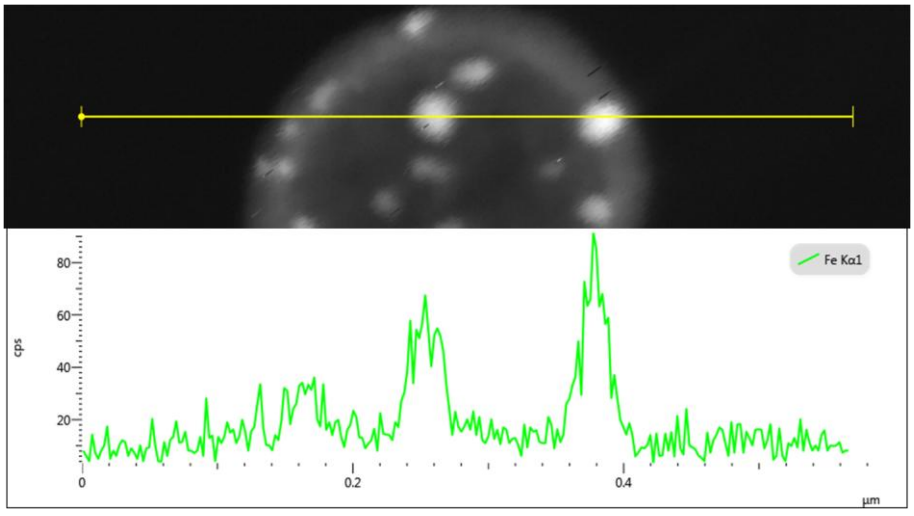

Figure 7.13 HAADF STEM images and EDX line scanning data.

7.3 Summary

In conclusion, a simple and versatile strategy for achieving hollow metal organic nanoparticles has been developed, where boronate ester based solid organic nanoparticles have been used as the precursor. The size of the hollow MOPs is dictated by the size of the precursor BNP, which itself exhibits excellent tunability. The formation of these hollow MOPs seem to be independent of the valence and the geometry of the metal ion, which also allows for the incorporation of more than one type of metal ion into the MOPs. Kirkendall effect has been shown to be the underlying mechanism for the formation of these hollow MOPs. For the first time, Kirkendall effect has been responsible for the formation of hollow metal organic nanoparticles from organic polymer nanoparticles. This understanding further lends itself to control in the shell thickness of the MOPs. Overall, the method reported here for achieving hollow MOPs with a high degree of control has the versatility to impact applications such as catalysis, sensing, storage, and biomedicine, as this approach should be extendable to other organic-inorganic molecular architectures. Moreover, the fields of polymer synthesis and self-assembly are orthogonally and rapidly evolving with its own versatility and control elements[36]. Our ability to reliably generate hollow organic-inorganic hybrid nanoparticles using polymeric nanostructure templates will open up a fount of opportunities for hybrid materials nanotechnology.

7.4 Experimental

7.4.1 General

p-Phenylenediamine, 3,4-dihydroxybenzaldehyde, 4-formylphenylboronic acid, Iron(III) chloride, Copper(II) chloride, Tin(IV) chloride pentahydrate, Aluminum chloride and other conventional reagents were obtained from commercial sources and used as received unless otherwise mentioned. ^{1}H-NMR spectra were recorded on a Bruker 400 MHz NMR spectrometer using the residual proton resonance of the solvent as the internal standard. ^{13}C-NMR spectra were recorded on a Bruker 100 MHz NMR spectrometer using the carbon signal of the deuterated

solvent as the internal standard. Mass spectra were taken on Bruker micrOTOF-II. Convential Bright-Filed Transmission electron microscopy (TEM) images were taken using a JEOL JEM-2000FX operating at 200 KV. Scanning electron microscopy (SEM) images were taken using a FEI Magellan 400 FESEM in SE imaging mode. Engery Filtered Transmission Electron Microscopy was performed using a JEO JEM-2200FS Energy Filtered Field Emission TEM operating at 200kV. Prior to generating the element distribution images (EFTEM maps) the presence of the respective elements was verfiied using Elelectron Energy Lass Spectroscopy (EELS) in the same instrument. Subsequently EFTEM maps were acquired using the three-window method in wide-field mode, which is based on the subtraction of two pre-edge images from one post-edge image for back-ground substraction[1]. The following element edges where used: B_K= 165eV, C_K=284eV, N_K = 401eV, O_K = 532eV, $Fe_{L2,3}$ = 708eV and an Energy Window width of E = 20eV was used for B and C while for N, O and Fe E was set to 30 eV. EDS mapping was performrmed in the same instrument in STEM mode utilizing an Oxford X-MAX 80mm^2 detector and a probe size of 1.5nm. EDS maps were acquired until sufficient cotrast was obtained (typically 15-30 min). Room temperature EPR spectra were collected on powdered samples using the TE102 mode of a X-band resonator (9.81 GHz, Bruker ELEXSYS-500).

7.4.2 Synthesis of Im-Ca

The preparation of Im-Ca was achieved following our previous report[27]. To a solution of p-phenylenediamine (0.15 g, 1.39 mmol) in anhydrous ethanol (10 mL) was added 3,4-dihydroxybenzaldehyde (0.40 g, 2.90 mmol). The clear brown mixture was stirred at room temperature under an argon atmosphere and protected from light. The product precipitated out of the reaction mixture. The brown precipitate was filtered and washed with cold ethanol three times. Final product was vacuum dried to obtain a brown solid (yield: 70%) ^{1}H-NMR (400 MHz, DMSO-6D) δ(ppm): 9.57 (s, 2H), 9.29 (s, 2H), 8.41 (s, 2H), 7.38 (d, 2H), 7.23 (s, 4H), 7.17 (q, 2H), 6.82 (d, 2H). ^{1}H-NMR (400 MHz, CD_3OD and DMSO-6D) δ(ppm): 8.39 (s, 2H), 7.39 (d,

2H), 7.22 (s, 4H), 7.17 (q, 2H), 6.82 (d, 2H). ^{13}C-NMR (100MHz, DMSO-6D) δ(ppm): 159.89, 149.57, 146.09, 128.56, 122.91, 122.30, 115.83, 114.51. ESI/MS *m/z* 349.11 $[M+H]^+$ (expect *m/z* 349.35).

7.4.3 Synthesis of Im-BA

Im-BA was synthesized from condensation reaction between p-phenylenediamine and 4-formylphenylboronic acid. To a solution of p-phenylenediamine (0.05 g, 0.46 mmol) in 20 mL MeOH was added 4-formylphenylboronic acid (0.15 g, 1.00 mmol). The clear yellow mixture became cloudy after stirring at room temperature overnight. The yellow precipitate was filtered and washed with cool methanol three times. Final product was vacuum dried to obtain a yellowish solid (yield: 80%) ^{1}H-NMR (400MHz, DMSO-6D) δ(ppm): 8.67 (s, 2H), 8.22 (s, 4H), 7.89 (m, 8H), 7.36 (s, 4H). ^{1}H-NMR (400MHz, CD_3OD and DMSO-6D) δ(ppm): 8.65 (s, 2H), 7.88 (m, 8H), 7.34 (s, 4H). ^{13}C-NMR (100MHz, DMSO-6D) δ(ppm): 160.67, 149.83, 137.76, 134.90, 128.06, 122.54. ESI/MS *m/z* 431.16 $[M+59]^-$ (expect *m/z*=431.19), *m/z* 445.20 $[M+73]^-$ (expect *m/z*=445.21), *m/z* 459.22 $[M+87]^-$ (expect *m/z*=459.23).

7.4.4 Preparation of Hollow Metal-Organic Particles

The preparation of hollow nanoparticles could be watched as the movie S1. First, Im-Ca and Im-BA were dissolved in methanol with the help of heating. After cooling down by setting at room temperature, one solution was added into the solution drop by drop, the mixture solution because deep orange and suspension was finally got. Then a methanolic solution of metal chloride salts ($FeCl_3$ in this example) was added to the suspension of BNPs once. After stirring for given time, the resultant hollow metal-organic particles were washed with methanol, collected by centrifugation, and dried in a vacuum oven at 50 ^{o}C overnight.

7.4.5 Preparation of Hollow Fe@C particles

Hollow Fe^{3+}-MOPs were placed in a tube furnace and let the nitrogen gas flow for 30 mins at room temperature. Then the furnace was calcined up to 800 ℃ quickly. After 1 hours, the

furnace was turned off and the resulting particles were cooled to room temperature with the nitrogen gas flow.

7.4.6 Adsorption of methylene blue (MB) from aqueus solution

Hollow Fe@C (2 mg) was added to 10 mL of MB aqueous solution (10 mg/L) and was sonticated to form the dispersed solution. After 5 mins, an external magnet was applied to removed the Fe@C particles from the aqueous solutions. UV-Vis spectra were measured before and after the separation.

7.4.7 Release of methylene blue (MB) from Fe@C particles

After collecting the Fe@C particles from the aqueous solution containing MB, methanol was used to wash the MB moelcules out from these carbon based particles for four times. Each time, Fe@C particles were removed from the solution by applying external magnet, and methanol solution containing MB could be collected. The Fe@C particles can then be used for adsorption of MB again.

7.5 References

1. Martin, C. R. Nanomaterials-a membrane-based synthetic approach. *Science* **1994**, *266*, 1961.

2. Huang, Y.; Duan, X.; Wei, Q.; Lieber, C. M. Functional nanoscale electronic devices assembled using silicon nanowire building blocks. *Science* **2001**, *291*, 630.

3. Suteewong, T.; Sai, H.; Hovden, R.; Muller, D.; Bradbury, M. S.; Gruner, S. M.; Wiesner, U. Multicompartment mesoporous silica nanoparticles with branched shapes: An epitaxial growth mechanism. *Science* **2013**, *340*, 337.

4. Wang, X.; Zhuang, J.; Peng, Q.; Li, Y. A general strategy for nanocrystal synthesis. *Nature* **2005**, *437*, 121.

5. Howes, P. D.; Chandrawati, R.; Stevens, M. M. Colloidal nanoparticles as advanced biological sensors. *Science* **2014**, *346*, 1247390.

6. Savić, R.; Luo, L.; Eisenberg, A.; Maysinger, D. Micellar nanocontainers distribute to defined cytoplasmic organelles. *Science* **2003**, *300*, 615.

7. Jones, J. T. A.; Hasell, T.; Wu, X.; Bacsa, J.; Jelfs, K. E.; Schmidtmann, M.; Chong, S. Y.; Adams, D. J.; Trewin, A.; Schiffman, F.; Cora, F.; Slater, B.; Steiner, A.; Day, G. M.; Cooper, A. I. Modular and predictable assembly of porous organic molecular crystals. *Nature* **2011**, *474*, 367.

8. Furukawa, H.; Cordova, K. E.; O'Keeffe, M.; Yaghi, O. M. The chemistry and applications of metal-organic frameworks. *Science* **2013**, *341*, 1230444.

9. Oh, M.; Mirkin, C. A. Chemically tailorable colloidal particles from infinite coordination polymers. *Nature* **2005**, *438*, 651.

10. Spokoyny, A. M.; Kim, D.; Sumrein, A.; Mirkin, C. A. Infinite coordination polymer nano- and microparticle structures. *Chem. Soc. Rev.*, **2009**, *38*, 1218.

11. Carné, A.; Carbonell, C.; Imaz, I.; Maspoch, D. Nanoscale metal–organic materials. *Chem. Soc. Rev.*, **2011**, *40*, 291–305

12. Seo, J. S.; Whang, D.; Lee, H.; Jun, S.I. ; Oh, J.; Jeon, Y. J.; Kim, K. A homochiral metal–organic porous material for enantioselective separation and catalysis. *Nature* **2000**, *404*, 982.

13. Banerjee, R.; Phan, A.; Wang, B.; Knobler, C.; Furukawa, H.; O'Keeffe, M.; Yaghi, O. M. High-throughput synthesis of zeolitic imidazolate frameworks and application to CO_2 capture. *Science* **2008**, *319*, 939.

14. Horcajada, P.; Gref, R.; Baati, T.; Allan, P. K.; Maurin, G.; Couvreur, P.; Ferey, G.; Morris, R. E.; Serre, C. Metal–organic frameworks in biomedicine. *Chem. Rev.* **2011**, *112*, 1232.

15. Ameloot, R.; Vermoortele, F.; Vanhove, W.; Roeffaers, M. B.J. ; Sels, B. F.; De Vos, D. E. Interfacial synthesis of hollow metal–organic framework capsules demonstrating selective permeability. *Nat. Chem.* **2011**, *3*, 382.

16. Carné-Sánchez, A.; Imaz, I.; Cano-Sarabia, M.; Maspoch, D. A spray-drying strategy for synthesis of nanoscale metal–organic frameworks and their assembly into hollow superstructures. *Nat. Chem.* **2013**, *5*, 203.

17. Pang, M.; Cairns, A. J.; Liu, Y.; Belmabkhout, Y.; Zeng, H. C.; Eddaoudi, M. Synthesis and integration of Fe-soc-MOF cubes into colloidosomes via a single-step emulsion-based approach. *J. Am. Chem. Soc.* **2013**, *135*, 10234.

18. Zhang, Z.; Chen, Y.; Zhang, J.; Xu, X.; Yang, Y.; Nosheen, F.; Saleem, F.; He, W.; Wang, X. Hierarchical Zn/Ni-MOF-2 nanosheet-assembled hollow nanocubes for multicomponent catalytic reactions. *Angew. Chem. Int. Ed.* **2014**, *53*, 12517.

19. Huo, J.; Wang, L.; Irran, E.; Yu, H.; Gao, J.; Fan, D.; Li, B.; Wang, J.; Ding, W.; Amin, A. M.; Li, C.; Ma, L. Hollow ferrocenyl coordination polymer microspheres with micropores in shells prepared by Ostwald ripening. *Angew. Chem. Int. Ed.* **2010**, *49*, 9237.

20. Ejima, H.; Richardson, J. J.; Liang, K.; Best, J. P.; van Koeverden, M. P.; Such, G. K.; Cui, J.; Caruso, F. One-step assembly of coordination complexes for versatile film and particle engineering. *Science* **2013**, *341*, 154.

21. Zhang, Z.; Chen, Y.; Xu, X.; Zhang, J.; Xiang, G.; He, W.; Wang, X. Well-defined metal-organic framework hollow nanocages. *Angew. Chem. Int. Ed.* **2014**, *53*, 429.

22. Zhang, F.; Wei, Y.; Wu, X.; Jiang, H.; Wang, W.; Li, H. Hollow zeolitic imidazolate framework nanospheres as highly efficient cooperative catalysts for [3 + 3] cycloaddition reactions. *J. Am. Chem. Soc.* **2014**, *136*, 13963.

23. Caruso, F.; Caruso, R. A.; Möhwald, H. Nanoengineering of inorganic and hybrid hollow spheres by colloidal templating. *Science* **1998**, *282*, 1111.

24. Yin, Y.; Rioux, R. M.; Erdonmez, C. K.; Hughes, S.; Somorjai, G. A.; Alivisatos, A. P. Formation of hollow nanocrystals through the nanoscale Kirkendall effect. *Science* **2004**, *304*, 711.

25. Oh, M. H.; Yu, T.; Yu, S.-H.; Lim, B.; Ko, K.-T.; Willinger, M.-G.; Seo, D.-H.; Kim, B. H.; Cho, M. G.; Park, J.-H. Galvanic replacement reactions in metal oxide nanocrystals. *Science* **2013**, *340*, 964.

26. Lou, X. W.; Wang, Y.; Yuan, C.; Lee, J. Y.; Archer, L. A. Template-free synthesis of SnO2 hollow nanostructures with high lithium storage capacity. *Adv. Mater.* **2006**, *18*, 2325.

27. Li, L.; Yuan, C.; Dai, L.; Thayumanavan, S. Thermoresponsive Polymeric Nanoparticles: Nucleation from Cooperative Polymerization Driven by Dative Bonds. *Macromolecules* **2014**, *47*, 5869.

28. Weisser, J. T.; Nilges, M. J.; Sever, M. J.; Wilker, J. J. EPR investigation and spectral simulations of iron-catecholate complexes and iron-peptide models of marine adhesive cross-links. *Inorg. Chem.* **2006**, *45*, 7736.

29. Koksharov, Y. A.; Gubin, S.P.; Kosobudsky, I. D.; Beltran, M.; Khodorkovsky, Y.; Tishin, A. M. Low temperature electron paramagnetic resonance anomalies in Fe-based nanoparticles. *J. Appl. Phys.* **2000**, *88*, 1587.

30. Nikiforov, V. N.; Koksharov, Y. A.; Polyakov, S. N.; Malakho, A. P.; Volkov, A. V.; Moskvina, M. A.; Khomutov, G. B.; Irkhin, V. Y. Magnetism and Verwey transition in magnetite nanoparticles in thin polymer film. *J. Alloys Compd.* **2013**, *569*, 58.

31. Sever, M. J.; Weisser, J. T.; Monahan, J.; Srinivasan, S.; Wilker, J. J. Metal-mediated cross-linking in the generation of a marine-mussel adhesive. *Angew. Chem. Int. Ed.* **2004**, *43*, 448.

32. Sever, M. J.; Wilker, J. J. Absorption spectroscopy and binding constants for first-row transition metal complexes of a DOPA-containing peptide. *Dalton Trans.* **2006**, 813.

33. Kirkendall, E. Diffusion of zinc in alpha brass. *Aime Trans.* **1942**, *147*, 104.

34. Yin, Y.; Erdonmez, C. K.; Cabot, A.; Hughes, S.; Alivisatos, A. P. Colloidal synthesis of hollow cobalt sulfide nanocrystals. *Adv. Funct. Mater.* **2006**, *16*, 1389.

35. Lee, H. J.; Choi, S. C.; Oh, M. Well-dispersed hollow porous carbon spheres synthesized by direct pyrolysis of core-shell type metal-organic frameworks and their sorption properties. *Chem. Commun.*, **2014**, *50*, 4492.

36. Hawker, C. J.; Wooley, K. L. The convergence of synthetic organic and polymer chemistries. *Science* **2005**, *309*, 1200.

CHAPTER 8

SUMMARY AND FUTURE DIRECTIONS

8.1 Summary

To be an effective drug delivery system, the delivery vehicle should exhibit several key characteristics to achieve four functionalities (Figure 8.1): (*i*) to retain the carriers, which have encapsulated drug molecules, in the blood circulation after the injection, the delivery vehicle should have good drug loading capability, especially for hydrophobic drug, since most cancer drug are hydrophobic. The encapsulation stability should be good enough, so there is no release during the blood circulation; (*ii*) to evade the circulation system and accumulate in the tumor site, the particle size should be around 10-200 nm due to the requirement from the enhanced permeability and retention (EPR) effect; (*iii*) to be selectively taken up by the target cells, the surface should be easily modified with functional groups; (*iv*) finally, the drug should be able to be released upon the stimuli in the tumor cells, such as low pH and redox environment.

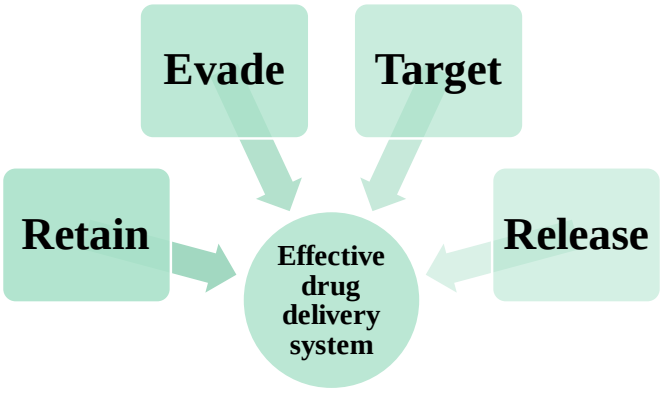

Figure 8.1 Schematic representation of the functionalities for an effective drug delivery system after the injection.

Our group has described the design and application of amphiphilic random copolymer to prepare self-crosslinked nanogels with single- or multi-stimuli responsive behaviors, providing non-covalent hydrophobic encapsulation capabilities with high encapsulation stability and

controlled release of the payload for drug delivery. In this thesis, we further fundamentally studied the structure-property correlations in self-crosslinked polymer nanogels and developed improved functionalities for drug delivery applications. In Chapter 2, we highlight unprecedented control in fine-tuning the sizes and encapsulation stability using Hofmeister ions. The size of the nanogel can be systematically varied with concentration of both kosmotropic and chaotropic anion. Encapsulation stability of guest molecules is also dependent on the nature of the salt used for preparation of the nanogels; chaotropic anions afford nanogels with greater guest encapsulation stability. The guest release kinetics of nanogels made with ions were also consistent with the Hofmeister series.

Fluorescence resonance energy transfer (FRET) based method has been applied to evaluate exchange dynamics of lipophilic guest molecules, providing important sights on the evaluation of the stability of these drug delivery vehicles. In Chapter 3, we have shown that the dominant mechanism for guest exchange in nanogel hosts is collision-based. In addition, the mechanism of guest exchange can change on the basis of the microenvironment of the host. When the nanogel interior is hydrophobic, the collision-based mechanism is the dominant pathway. However, when the interior is sufficiently hydrophilic, the dominant mechanism changes to a diffusion-based one. In drug delivery applications, the drug-loaded nanocarrier experiences both concentration and environmental changes upon bio-distribution to diseased tissues. The mechanistic variations based on environments provide insights into molecular designs that can afford stable encapsulation in one environment and release of the molecules in another.

It is important to have nanocarriers that can be effectively transported across cellular membranes for biomedical applications. In Chapter 4, we have developed a simple method to prepare a nanogel that is capable of transforming from a negatively charged form into a positively charged in the slightly acidic tumor extracellular environment. The reported facile synthetic method for preparing the pH_e-responsive charge conversional nanogels, combined with stable

encapsulation and tunable pI, should open up new avenues in the design of advanced drug carriers for intelligent drug delivery. The study also highlights the opportunities to develop other functional nanogels using units with other functional group.

Reagent-free synthetic methods are needed for nanogel formation due to their simplicity and implications in green chemistry. In Chapter 5, we have demonstrated a new pathway for the preparation of disulfide based self-crosslinking nanogels using photoirradiation. The most important take-home message of this work is that pyridyl disulfide might be used as a photo-crosslinkable functional group, while this crosslinks would be redox responsive, which should play an important role in the design of drug delivery nanocarriers. From the application standpoint, changing the DTT-induced crosslinking method to photo-induced crosslinking method makes our nanogel preparation more cost-effective. The scale up of the process should become possible considering that the diffusion of crosslinking agents into the large volume of solution may result in heterogeneous crosslinking density.

Hybrid metal-organic coordination materials, constructed from metal ions and polyfunctional organic ligands, have received great attention due to their interesting applications. We have developed a simple, rapid, and robust method to produce hollow metal-organic particles with well controlled size and thickness from organic polymer particles. In Chapter 6, we prepared organic polymer particles through boronate esterification. Their size, absorption characteristic can be adjusted by controlling the mixing concentration. We pointed out that the nucleation step involves a nucleation elongation polymerization with N→B interaction as the driving force for the collapsing. In Chapter 7, we have demonstrated that hollow metal organic nanoparticles can be prepared by simply adding metal ions into purely organic nanoparticles. The Kirkendall effect is responsible for the formation of the hollow structure as shown by time dependent TEM measurements. The tunability of the original organic nanoparticles makes it easy to control the size of hollow nanoparticles, while the thickness can be tuned by simply altering the ratio of

metal ions to the catechol monomers. We further showed that various metal ions can be used to form hollow nanoparticles. We believe that this approach can be extended to the development of more diverse hollow metal organic nanoparticles.

8.2 Future directions

In this section future directions for two more projects are described.

8.2.1 Redox-activatable ^{19}F-MRI nanoprobe

Magnetic resonance imaging (MRI) is of great interest in both basic biological research and clinical diagnosis of cancer and other diseases.[1-3] ^{19}F MRI has received significant attention in MR imaging and spectroscopy studies because of two reasons: (*i*) ^{19}F-MRI has little biological background, offering a means to detect diseases in deep tissue since there is low levels of endogenous fluorine in the body; (*ii*) ^{19}F has 100% natural abundance and its gyromagentic ratio (40.06 MHz/T) is second only to ^{1}H, making it more sensitive for detection over other nuclei.[4] Here we are interested in redox-responsive ^{19}F MRI nanoprobe, since it is important to monitor biological redox reactions.[5-8] Actually, biological redox reactions play important roles in many biological processes. Abnormal levels of redox reactions can result in various disease including liver damage, skin lesions, and slow growth.[9-12]

A stimulus-responsive ^{19}F-MRI nanoprobes have been usually prepared based on the strategy of using changes in spin-spin relaxations between the aggregation and free states to turn ON/OFF ^{19}F signals in response to the pH values.[13-15] For example, pH-activatable ^{19}F-MRI nanoprobes were prepared by introducing the fluoro groups into the ionizable block (PR) of amphiphilic copolymers containing a hydrophilic poly(ethylene oxide) (PEO) segment and tertiary amine/ammonium segment (Figure 8.2).[15] At pH > pK_a, the formation of micelle highly restricted chain motions, resulting in short spin–spin relaxation times (almost 0), which effectively broadened and eliminated the ^{19}F signals. However, protonation of ammonium groups

at low pH dissembled the micelles into dissociated polymer chains with conformational flexibility, leading to reappearance of the previous ^{19}F signal.

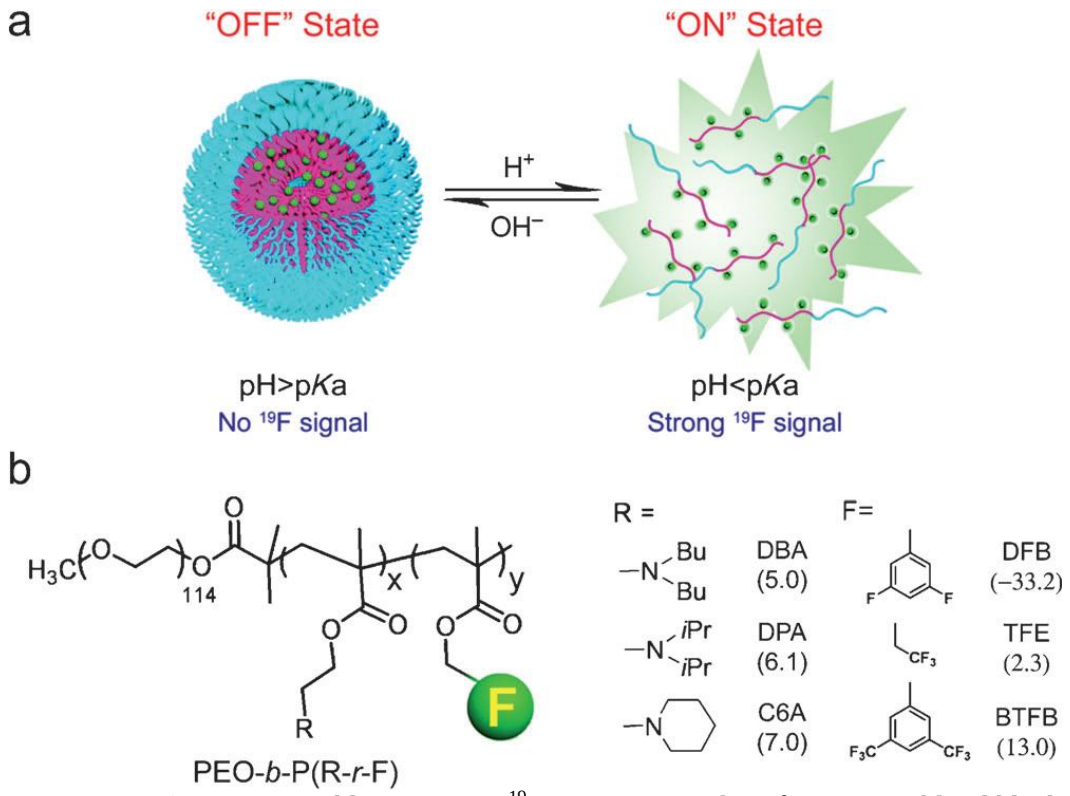

Figure 8.2 a) pH-activatable ON/OFF ^{19}F-MRI nanoprobes from ionizable diblock copolymers. At pH > pK_a, the hydrophobic segments selfassemble into a micelle core leading to ^{19}F signal suppression as a result of restricted polymer chain motion. Upon pH activation (pH < pK_a), micelle disassembly leads to dissociated unimers and a strong ^{19}F signal. b) Structural formula of three representative diblock copolymers containing different pH responsive segments and ^{19}F reporter moieties, their pKa values and ^{19}F chemical shifts (in ppm, relative to trifluoroacetic acid, or TFA), respectively, are shown in parenthesis (reproduced with permission from reference[15]).

We have demonstrated the possibility to make nanogels desired functional behavior by introducing specific functionalities into the amphiphilic random copolymers. Herein, redox-activatable ^{19}F-MRI nanoprobe is achieved by designing a polymeric nanogel containing trifluoroethyl groups. The PEGMA-co-TFEMA-co-PDSMA copolymers were synthesized by a reversible addition–fragmentation chain transfer (RAFT) polymerization reaction (Scheme 8.1). Three different copolymers with varying molecular weight were targeted. Copolymers P1–P3 were synthesized by simply varying the feed ratio of RAFT regent to the monomers during the

polymerization. After polymerization, the polymers were purified by precipitation in hexane, filtered, and washed to remove unreacted monomers. The polymers were characterized by NMR and GPC as shown in Table 1 and Figure 8.3. The relative ratios of the monomer incorporated in the polymer were determined by the characteristic resonances of PDS (δH_a = 8.46, δH_b = 7.67, δH_c = 7.10), PEGMA (δH_d = 3.37 ppm) and TFE (δH_e = 4.4 ppm) moieties to calculate the relative ratios of the monomer incorporated in the polymer (Figure 8.4).

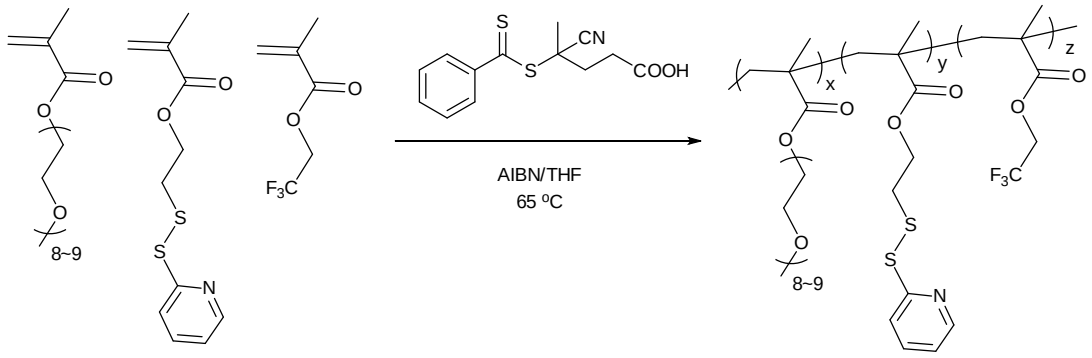

Scheme 8.1 Synthetic scheme of $PEGMA_x$-co-$PDSMA_y$-co-$TFEMA_z$ random copolymer.

Table 8.1 Characteristics of $PEGMA_x$-co-$PDSMA_y$-co-$TFEMA_z$ copolymers (P1–P4)

polymer	PEGMA	PDS	TFE	Mw
P1	28%	56%	16%	7.6 kDa
P2	28%	56%	16%	13 kDa
P3	28%	56%	16%	28 kDa

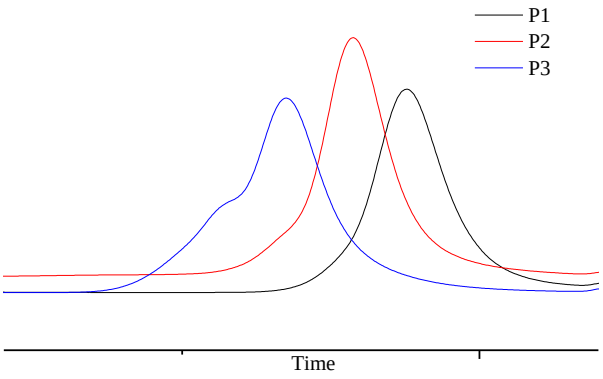

Figure 8.3 GPC results of P1-P3.

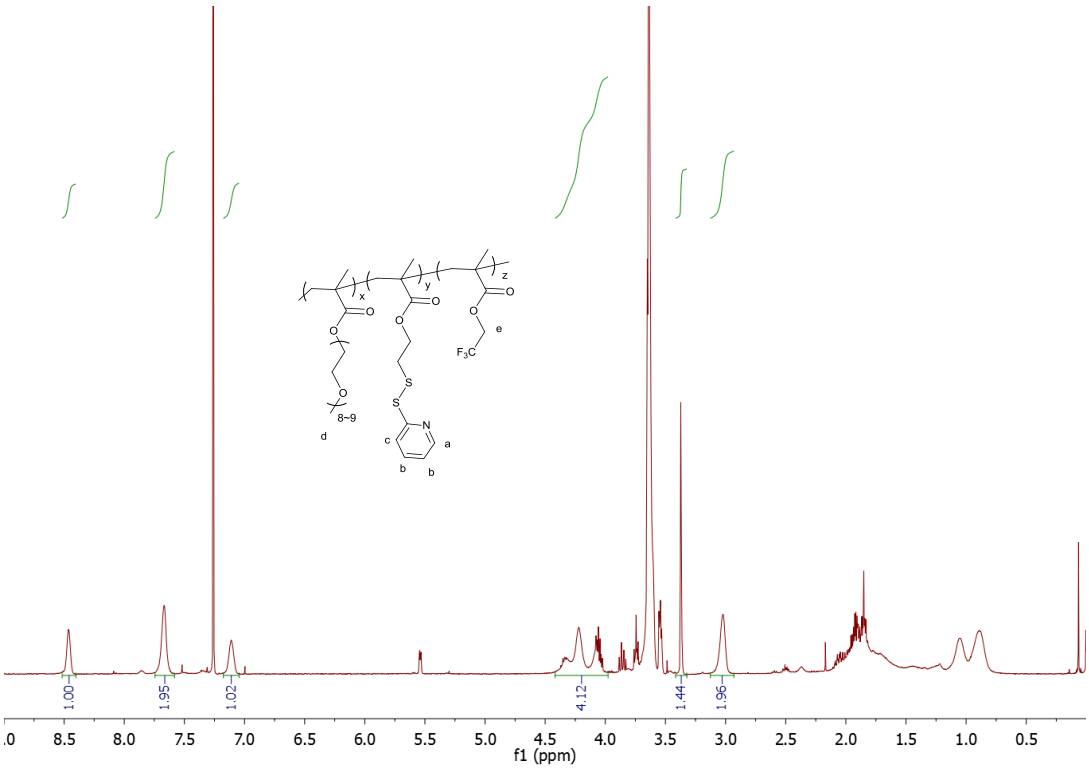

Figure 8.4 Typical NMR spectrum of P2.

To test the possibly of using these polymers for redox-activatable ^{19}F MRI, ^{19}F NMR spectra were taken for all three polymers before and after the addition of GSH in water containing 10% D_2O (Figure 8.5). There were almost no peaks observed due to the formation of micelle aggregates. However, we noticed that significant peaks appeared after adding GSH, since the disulfide bond can be broken, leading to the disassembly of micelle aggregates. The T2 was measured by employing the spin-echo method (Table 8.2). For control, the T2 was also measured for polymers in $CDCl_3$.

Table 8.2 T2 measurement

polymer	T2 in $CDCl_3$	T2 in water with 10% D_2O	T2 in 10 mM GSH
P1	120 ms	~ 0	11 ms
P2	111 ms	~ 0	9 ms
P3	118 ms	~ 0	10 ms

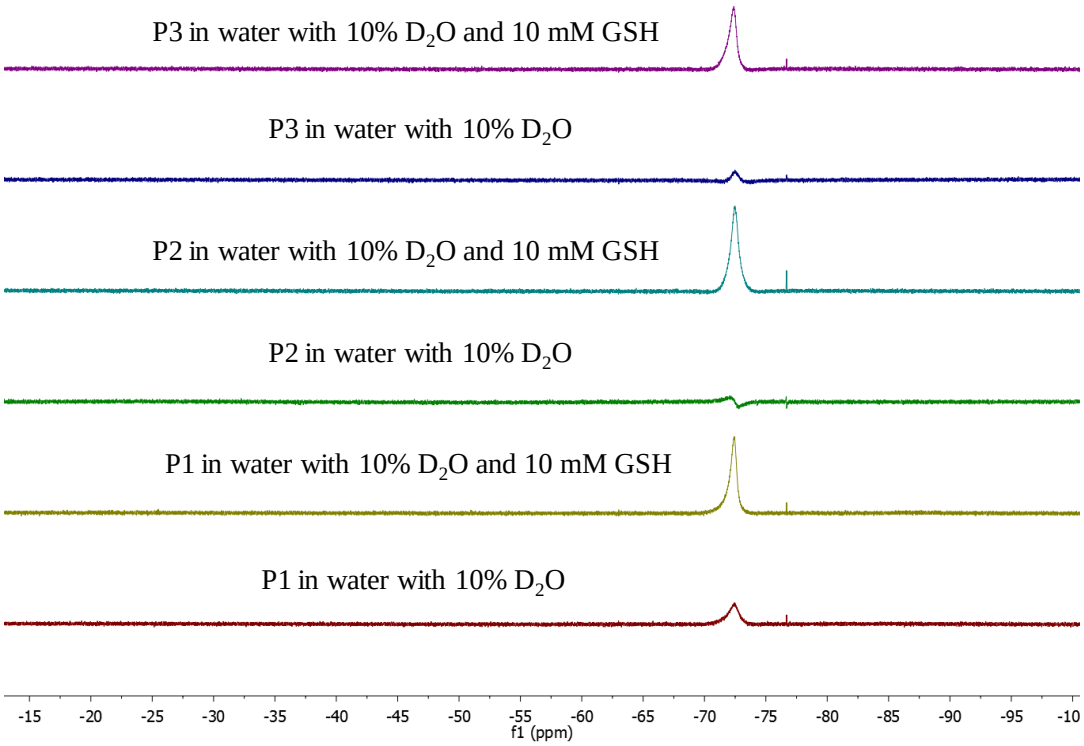

Figure 8. 5 ^{19}F NMR spectra were taken for all three polymers before and after the addition of GSH in water containing 10% D_2O.

The problem until now is that the T2 for the polymer solution with 10 mM GSH are too low to be useful for preclinical ^{19}F imaging.[16] Further step for this project is to increase the T2 number:

(*i*) try to decrease the amount of trifluoroethyl groups in the polymers. It is believed that the interaction between trifluoroethyl groups greatly decrease the motion of these groups, leading to low T2;

(*ii*) introduce another pH-responsive functional groups into the polymers. The protonation of these groups should be able to increase the motion of polymer chains after the disassembly. In addition, the cell-uptake will be also increased.

(*iii*) mix with degradable polymers, resulting in porous aggregation. It might decrease the density of trifluoroethyl groups among the particles, which should avoid the interaction between trifluoroethyl groups.

8.2.2 Hollow carbon particles loaded with metal nanoparticles

Nanoscale carbons is of great interest owing to their performance in various applications such as adsorption, supercapacitors, catalysis and biomedical applications.[17-21] Many methods have been developed to this kind of materials, including carbide-derived carbon (CDC), template carbonization, and chemical or physical activation methods.[22-25] Recently, porous coordination polymer (PCPs) or metal organic framework (MOFs), which are constructed from metal ions and polyfunctional organic ligands, have been demonstrated as novel templates to prepare microporous carbons by direct pyrolysis under an inert atmosphere.[26-30]

Among the various carbon materials, hollow carbon particles have special interest, because of their low density, high surface area, materials economy, and lower cost compared to their solid counterparts. We hypothesize that hollow carbon particles can be easily prepared by direct pyrolysis of hollow metal organic particles (MOFs). Actually, in Chapter 7, hollow carbon particles loaded with iron nanoparticles (Fe@C) have been prepared by direct pyrolysis of hollow Fe^{3+}-MOPs at 800 ^{o}C under a N_2 atmosphere for 1 hour (Figure 8.6a). These magnetic-functionalized carbon particles with encapsulated Fe nanoparticles have been successfully used as a magnetically separable adsorbent for removing organic waste from aqueous solution using an organic dye (methylene blue, MB).

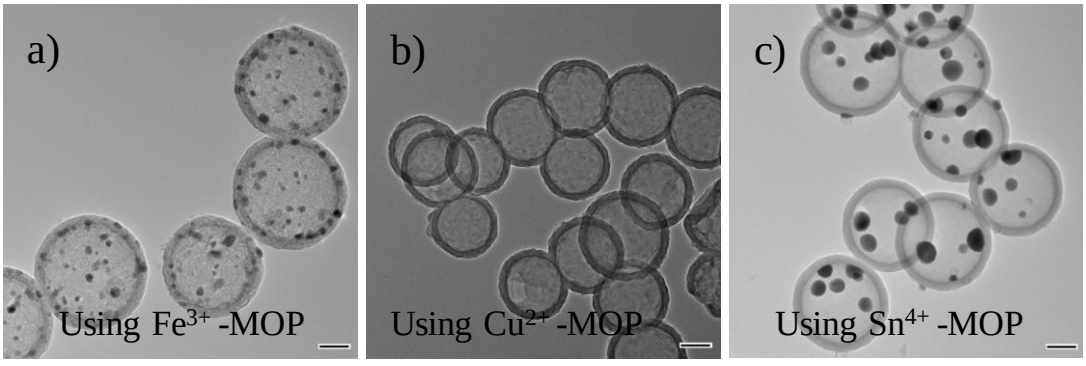

Figure 8. 6 Hollow carbon particles loaded with metal nanoparticles (M@Fe), a) Fe@C, b) Cu@C, c) Sn@C.

As we have demonstrated that hollow Cu^{2+}-MOP and Sn^{4+}-MOP were also prepared using our Kirkendall effect based method, direct pyrolysis of these hollow particles were done at 800 ^{o}C under a N_2 atmosphere for 1 hour. TEM measurement was taken for both samples after the thermal treatment (Figure 8.6). Hollow structures were indeed observed. X-ray powder diffraction (XRD) data were collected to determine the state of metal. As shown in Figure 8.7, typical sharp peaks in all XRD patterns match well with the reported results, indicating the formation of pure Fe, Cu and Sn in these hollow carbon particles.[31-33]

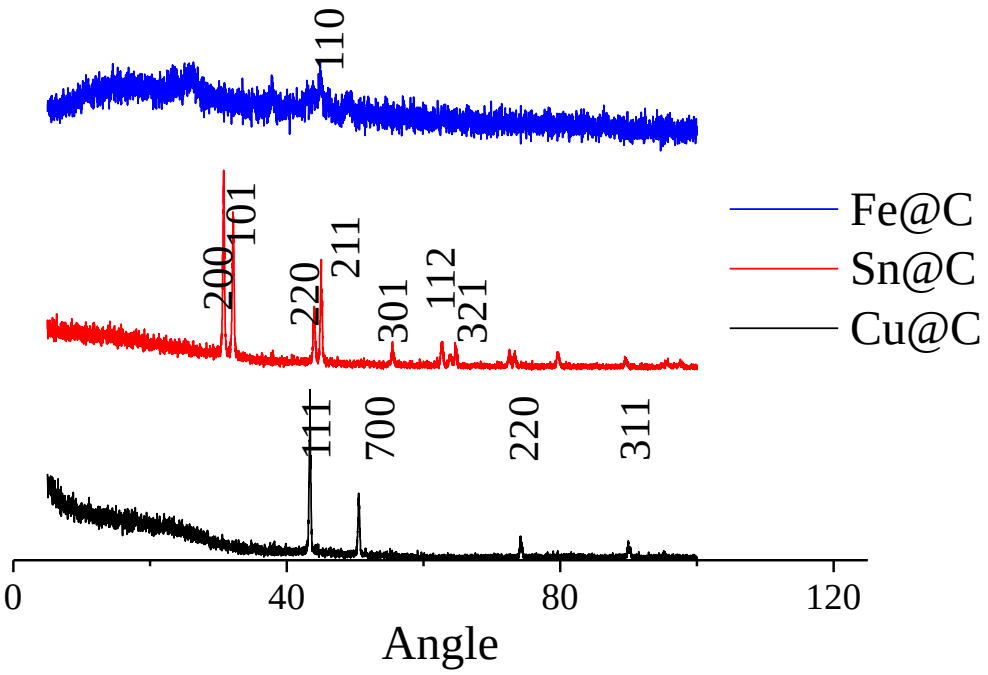

Figure 8.7 XRD results of M@C. Typical peaks were marked.

However, it is interesting to note that nanoscale structure was not observed for samples using only organic polymer particles. We first use thermogravimetric analysis (TGA) in N_2 to determine the thermal stability of hollow MOPs and organic polymer particles (BNP) (Figure 8.8a). There was a fast weight loss stage from 450 ^{o}C to 500 ^{o}C only detected for BNP, which was mainly caused by the decomposition of boronate ester, resulting in the crash of BNP. TGA in air for all M@C were also taken to measure the amount of metal in these carbon based particles

(Figure 8.8b). All samples first have a miss increase from 250 °C to 300 °C, which was caused by the oxidizations. Then they stabilized at a temperature of 700 °C when 20-40 % by mass of the material remains, further showing the present of metal in all samples.

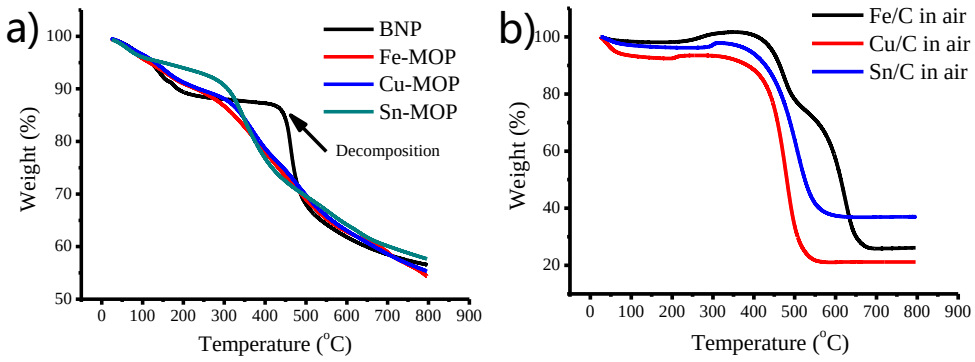

Figure 8.8 TGA result, a) MOPs and BNP in N_2, b) M@C in air.

Future directions for this project are to test the potential applications of these hollow carbon particles loaded with metal nanoparticles.

Cu nanoparticles have been used in various catalytic reactions such as the low-temperature oxidation of carbon monoxide, oxidation of alcohols, carbon–carbon bond formation reactions, carbon–heteroatom bond formation, various coupling reactions and so on.[34-38] Here we studied the reduction of 4-nitrophenol (4-NP) into 4-aminophenol (4-AP) in the presence of $NaBH_4$ using hollow Cu@C particles.[39] In the typical reaction procedure, 1 mL solution of 4-NP (0.3 mg/mL) was added to a 10 mL freshly prepared solution of $NaBH_4$ (1 mg/mL). To this mixture, 0.3 mg hollow Cu@C was added, the color of the solution faded as the reaction proceeded. UV-visible spectra were used to monitor the progress of the reaction. Every several minutes, 1 mL upper solution was transferred to a quartz cuvette for UV-visible spectra measurement. Once a spectrum was recorded, the solution was immediately transferred back to the previous vial and stirred for another few minutes for the sequential catalytic reaction. Blank experiments were also carried out to show that the reactions do not proceed without catalysts only in the presence of $NaBH_4$. When

the reaction with Cu@C contiunes, the absorption peak at 400 nm from 4-NP gradually decreases in intensity while a small shoulder at 300 nm attributed to 4-AP gradually increases (Figure 8.9).

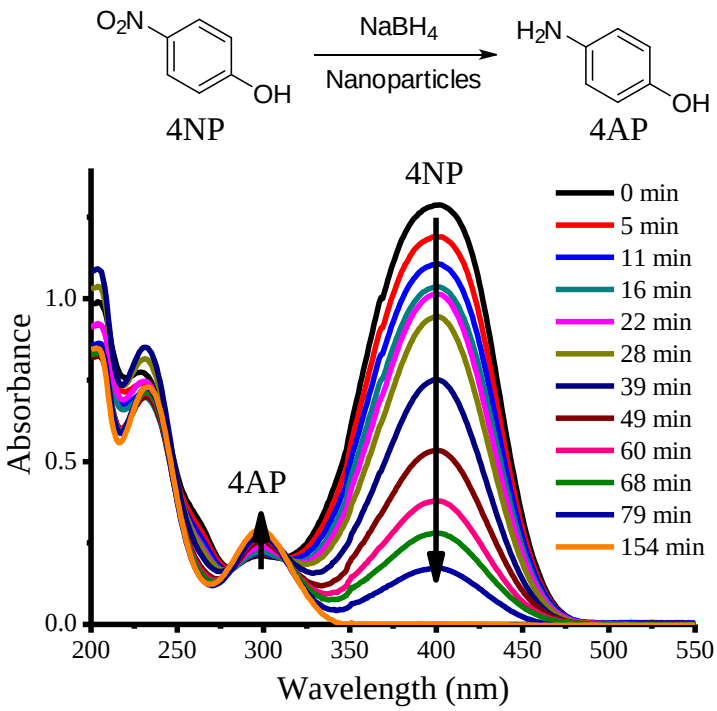

Figure 8.9 The time-dependent absorption spectra of the reaction solution in the presence of 0.3 mg of Cu@C.

Sn nanoparticles have been widely studies as one of the promising anode materials for lithiumbatteies, since they have high theoretical specific capacity (994 994 mAh/g), which exhibit much higher capacity than the commercialized graphite anodes (~372 mAh/g).[40] Unfortunately, the cycle life of Sn-based anode materials is commonly low, which mainly results from the pulverization of active materials caused by the huge volume change of Sn during lithium insertion/ extraction into/from Sn (about 300%).[41] To potentially solve this issue, tin-encapsulated spherical hollow carbon has been designed and prepared, exhibiting higher capacity and better cycle performance than unencapsulated mixture materials.[33, 42, 43] The reasons for that are: (*i*) the carbon shell has itself good electronic conductivity and prevents the aggregation of active Sn materials; (*ii*) the void space accommodates the strain of volume change during Li+ insertion/extraction. In addition, two more potential advantage using our Sn@C could be: (*i*) the

carbon may be nitrogen-doped concerning the molecules used, which can improve the electrochemical performance, exhibiting superhigh capacity and excellent rate capability[44]; (*ii*) Sn-based intermetallic compounds (MxSn; M = Cu, Fe, *etc*) and multiphase Sn–M alloys have been explored to show better performance[45].

8.3 References

1. Caravan, P.; Ellison, J. J.; McMurry, T. J.; Lauffer, Randall B. Gadolinium (III) chelates as MRI contrast agents: structure, dynamics, and applications. *Chem. Rev.* 1999, *99*, 2293-2352;

2. Laurent, S.; Forge, D.; Port, M.; Roch, A.; Robic, C.; Vander Elst, L.; Muller, R. N. Magnetic iron oxide nanoparticles: synthesis, stabilization, vectorization, physicochemical characterizations, and biological applications. *Chem. Rev.* **2008**, *108*, 2064-2110;

3. Thorek, D. L. J.; Ulmert, D.; Diop, N.-F. M.; Lupu, M. E.; Doran, M. G.; Huang, R.; Abou, D. S.; Larson, S. M.; Grimm, J. Non-invasive mapping of deep-tissue lymph nodes in live animals using a multimodal PET/MRI nanoparticle. *Nat. Commun.* **2014**, *5*, 1-9;

4. Ruiz-Cabello, J.; Barnett, B. P.; Bottomley, P. A.; Bulte, J. W. M. Fluorine (19F) MRS and MRI in biomedicine. *NMR Biomed.* **2011**, *24*, 114-129

5. Hwang, C.; Sinskey, A. J.; Lodish, H. F. Oxidized redox state of glutathione in the endoplasmic reticulum. *Science* **1992**, *257*, 1496-1502.

6. Chen, X.; Zhou, Y.; Peng, X.; Yoon, J.; Fluorescent and colorimetric probes for detection of thiols. *Chem. Soc. Rev*. **2010**, *39*, 2120-2135.

7. Yuan, L.; Lin, W.; Zhao, S.; Gao, W.; Chen, B.; He, L.; Zhu, S. A unique approach to development of near-infrared fluorescent sensors for in vivo imaging. *J. Am. Chem. Soc*.**2012**, *134*, 13510-135123.

8. Jung, H. S.; Chen, X.; Kim, J. S.; Yoon, J. Recent progress in luminescent and colorimetric chemosensors for detection of thiols. *Chem. Soc. Rev.* **2013**, *42*, 6019-6031.

9. Herzenberg, L. A.; De Rosa, S. C.; Dubs, J. G.; Roederer, M.; Anderson, M. T.; Ela, S. W.; Deresinski, S. C.; Herzenberg, L. A. Glutathione deficiency is associated with impaired survival in HIV disease. *Proc. Natl. Acad. Sci. U. S. A.* **1997**, *94*, 1967-1972.

10. Shahrokhian, S. Lead phthalocyanine as a selective carrier for preparation of a cysteine-selective electrode. *Anal. Chem.* **2001**, *73*, 5972-5978.

11. Barnham, K. J.; Masters, C. L.; Bush, A. I. Neurodegenerative diseases and oxidative stress. *Nat. Rev. Drug Discov.* **2004**, *3*, 205-214.

12. Valko, M.; Leibfritz, D.; Moncol, J.; Cronin, M. T. D.; Mazur, M.; Telser, J. Free radicals and antioxidants in normal physiological functions and human disease. *Int. J. Biochem. Cell Biol.* **2007**, *39*, 44-84.

13. Oishi, M.; Sumitani, S.; Nagasaki, Y. On-off regulation of 19F magnetic resonance signals based on pH-sensitive PEGylated nanogels for potential tumor-specific smart ^{19}F MRI probes. *Bioconjugate Chem.* **2007**, *18*, 1379-1382;

14. Takaoka, Y.; Sakamoto, T.; Tsukiji, S.; Narazaki, M.; Matsuda, T.; Tochio, H.; Shirakawa, M.; Hamachi. I. Self-assembling nanoprobes that display off/on 19F nuclear magnetic resonance signals for protein detection and imaging. *Nat. Chem.* **2009**, *1*, 557-561;

15. Huang, X.; Huang, G.; Zhang, S.; Sagiyama, K; Togao, O.; Ma, X.; Wang, Y.; Li, Y.; Soesbe, T. C.; Sumer, B. D.; Takahashi, M.; Sherry, A. D.; Gao, J. Multi‐chromatic pH‐activatable ^{19}F‐MRI nanoprobes with binary ON/OFF pH transitions and chemical‐shift barcodes. *Angew. Chem. Int. Ed.*, **2013**, *52*, 8074-8078;

16. Thurecht, K. J.; Blakey, I.; Peng, H.; Squires, O.; Hsu, S.; Alexander, C.; Whittaker, A. K. Functional hyperbranched polymers: toward targeted in vivo 19F magnetic resonance imaging using designed macromolecules. *J. Am. Chem. Soc.* **2010**, *132*, 5336.

17. Zhang, S.; Chen, L.; Zhou, S.; Zhao, D.; Wu. L. Facile synthesis of hierarchically ordered porous carbon via in situ self-assembly of colloidal polymer and silica spheres and its use as a catalyst support. *Chem. Mater.,* **2010**, *22*, 3433-3440;

18. Lee, J. -S.; Kim, S. -I.; Yoon, J. -C.; Jang, J. -H. Chemical vapor deposition of mesoporous graphene nanoballs for supercapacitor. *ACS Nano*, **2013**, *7*, 6047-6055;

19. Wang, L.; Sun, Q.; Wang, X.; Wen, T.; Yin, J.; Wang, P.; Bai, R.; Zhang, X.; Zhang, L.; Lu, A.; Chen, C. Using hollow carbon nanospheres as a light-induced free radical generator to overcome chemotherapy resistance. *J. Am. Chem. Soc.*, **2015**, *137*, 1947–1955;

20. Schaefer, Z. L.; Gross, M. L.; Hickner, M. A.; Schaak, R. E. Uniform hollow carbon shells: nanostructured graphitic supports for improved oxygen-reduction catalysis. *Angew. Chem. Int. Ed.*, **2010**, *49*, 7045-7048;

21. Liu, Z.; Robinson, J. T.; Tabakman, S. M.; Yang, K.; Dai, H. Carbon materials for drug delivery & cancer therapy. *Mater. Today* **2011**, *14*, 316-323.

22. Wang, H.; Gao, Q.; Hu, J. High hydrogen storage capacity of porous carbons prepared by using activated carbon. *J. Am. Chem. Soc.*, **2009**, *131*, 7016-22.

23. Jänes, A.; Thomberg, T.; Lust, E. Synthesis and characterisation of nanoporous carbide-derived carbon by chlorination of vanadium carbide. *Carbon*, **2007**, *45*, 2717-2722.

24. Yang, Z.; Xia, Y.; Mokaya, R. Enhanced hydrogen storage capacity of high surface area zeolite-like carbon materials. *J. Am. Chem. Soc.* **2007**, *129*, 1673-1679.

25. Ania, C. O.; Khomenko, V.; Raymundo‐Piñero, E.; Parra, J. B.; Beguin, F. The large electrochemical capacitance of microporous doped carbon obtained by using a zeolite template. *Adv. Funct. Mater.*, **2007**, *17*, 1828-1836.

26. Hu, J.; Wang, H.; Gao, Q.; Guo, H. Porous carbons prepared by using metal–organic framework as the precursor for supercapacitors. *Carbon*, **2010**, *48*, 3599-3606.

27. Yang, S. J.; Park, C. R. Preparation of Highly Moisture-Resistant Black-Colored Metal Organic Frameworks. *Adv. Mater.*, **2012,** *24*, 4010-4013.

28. Aijaz, A.; Fujiwara, N.; Xu, Q. From metal–organic framework to nitrogen-decorated nanoporous carbons: high CO2 uptake and efficient catalytic oxygen reduction. *J. Am. Chem. Soc.*, **2014**, *136*, 6790-6793.

29. Hu, M.; Reboul, J.; Furukawa, S.; Torad, N. L.; Ji, Q.; Srinivasu, P.; Ariga, K.; Kitagawa, S.; Yamauchi, Y. Direct carbonization of Al-based porous coordination polymer for synthesis of nanoporous carbon. *J. Am. Chem. Soc.*, **2012**, *134*, 2864-2867.

30. Lee, H. J.; Choi, S.; Oh, M.; Well-dispersed hollow porous carbon spheres synthesized by direct pyrolysis of core-shell type metal-organic frameworks and their sorption properties. *Chem. Commun.*, **2014**, *50*, 4492-4495.

31. Wang, H.; Yan, N.; Li, Y.; Zhou, X.; Chen, J.; Yu, B.; Gong, M.; Chen, Q. Fe nanoparticle-functionalized multi-walled carbon nanotubes: one-pot synthesis and their applications in magnetic removal of heavy metal ions. *J. Mater. Chem.*, **2012**, *22*, 9230-9236.

32. Patra, A. K.; Dutta, A.; Bhaumik, A. Cu nanorods and nanospheres and their excellent catalytic activity in chemoselective reduction of nitrobenzenes. *Cataly. Commun.* **2010**, *11*, 651-655.

33. Ni, W.; Wang, Y.; Xu, R. Formation of Sn@ C yolk-shell nanospheres and core-sheath nanowires for highly reversible lithium storage. *Part. Part. Syst. Charact.* **2013**, *30*, 873-880.

34. Tu, C. H.; Wang, A. Q.; Zheng, M. Y.; Wang X. D.; Zhang, T. Factors influencing the catalytic activity of SBA-15-supported copper nanoparticles in CO oxidation. *Appl. Catal., A,* **2006**, *297*, 40-47.

35. Kalbasi, R. J.; Nourbakhsh, A. A.; Zia, M. Aerobic oxidation of alcohols catalyzed by copper nanoparticle-polyacrylamide/SBA-15 as novel polymer-inorganic hybrid. *J. Inorg. Organomet. Polym.*, **2012**, *22*, 536-542.

36. Ranu, B. C.; Dey, R.; Chatterjee T. ; Ahammed, S. Copper nanoparticle-catalyzed carbon carbon and carbon heteroatom bond formation with a greener perspective. *ChemSusChem*, **2012**, *5*, 22-44.

37. Ahammed, S.; Saha, A.; Ranu, B. C. Hydrogenation of azides over copper nanoparticle surface using ammonium formate in water. *J. Org. Chem.*, **2011**, *76*, 7235-7239.

38. Dulle, J.; Thirunavukkarasu, K.; Mittelmeijer-Hazeleger, M. C.; Andreeva, D. V.; Shiju, N. R.; Rothenberg, G. Efficient three-component coupling catalysed by mesoporous copper-aluminum based nanocomposites. *Green Chem.*, **2013**, *15*, 1238-1243.

39. Deka, P.; Deka, R. C.; Bharali, P. In situ generated copper nanoparticle catalyzed reduction of 4-nitrophenol. *New J.Chem.*, **2014**, *38*,1789.

40. Winter, M.; Besenhard, J. O. Electrochemical lithiation of tin and tin-based intermetallics and composites. *Electrochim. Acta* **1999**, *45*, 31.

41. Vaughey, J. T.; O'Hara, J.; Thackeray, M. M. Intermetallic Insertion Electrodes with a Zinc Blende-Type Structure for Li Batteries: A Study of Li x InSb (0≤ x≤ 3). *Electrochem. Solid-State Lett.*, **2000**, *3*,13–16.

42. Lee, K. T.; Jung, Y. S.; Oh, S. M. Synthesis of tin-encapsulated spherical hollow carbon for anode material in lithium secondary batteries. *J. Am. Chem. Soc.*, **2003**, *125*, 5652-5653.

43. Zhang, W.; Hu, J. -S.; Guo, Y. -G.; Zheng, S. -F.; Zhong, L. -S.; Song, W. -G.; Wan, L. -J. Tin-nanoparticles encapsulated in elastic hollow carbon spheres for high-performance anode material in lithium-ion batteries. *Adv. Mater.*, **2008,** *20*, 1160-1165.

44. Qie, L.; Chen, W.; Wang, Z.; Shao, Q.; Li, X.; Yuan, L.; Hu, X.; Zhang, W.; Huang, Y. Nitrogen-doped porous carbon nanofiber webs as anodes for lithium ion batteries with a superhigh capacity and rate capability. *Adv. Mater.*, **2012,** *24*, 2047-2050.

45. Park, C. -M.; Kim, J. -H.; Kim, H.; Sohn, H. -J.; Li-alloy based anode materials for Li secondary batteries. *Chem. Soc. Rev.*, **2010**, *39*, 3115–3141.

BIBLIOGRAPHY

Aathimanikandan, S. V.; Savariar, E. N.; Thayumanavan, S. Temperature-sensitive dendritic micelles. *J. Am. Chem. Soc.* **2005**, 127, 14922-14929.

Adam, W.; Grimm, G. N.; Marquardt, S.; Saha-Möller, C. R. Are pyridinethiones reliable photochemical oxyl-radical sources for photobiological studies? The importance of secondary photolysis products in the guanine oxidation of 2'-deoxyguanosine and cell-free DNA. *J. Am. Chem. Soc.* **1999**, *121*, 1179-1185;

Ahammed, S.; Saha, A.; Ranu, B. C. Hydrogenation of azides over copper nanoparticle surface using ammonium formate in water. *J. Org. Chem.*, **2011**, *76*, 7235–7239.

Aida, T.; Meijer, E. W.; Stupp, S. I. Functional supramolecular polymers. *Science*, **2012**, *335*, 813–817

Aijaz, A.; Fujiwara, N.; Xu, Q. From metal–organic framework to nitrogen-decorated nanoporous carbons: high CO2 uptake and efficient catalytic oxygen reduction. *J. Am. Chem. Soc.*, **2014**, *136*, 6790-6793.

Allen, T. M.; Cullis, P. R. Drug delivery systems: entering the mainstream. *Science* **2004**, *303*, 1818-1822.

Ameloot, R.; Vermoortele, F.; Vanhove, W.; Roeffaers, M. B.J. ; Sels, B. F.; De Vos, D. E. Interfacial synthesis of hollow metal–organic framework capsules demonstrating selective permeability. *Nat. Chem.* **2011**, *3*, 382.

Ania, C. O.; Khomenko, V.; Raymundo‐Piñero, E.; Parra, J. B.; Beguin, F. The large electrochemical capacitance of microporous doped carbon obtained by using a zeolite template. *Adv. Funct. Mater.*, **2007**, *17*, 1828-1836.

Arakawa, T.; Timasheff, S. N. Preferential interactions of proteins with salts in concentrated solutions. *Biochem*istry. **1982**, 21, 6545-6552.

Bachler, V.; Metzler-Nolte, N. The π-electron-accepting ability of the boron atom in ethynylboranes and related compounds-an approximate weight computation for resonance structures. *Eur. J. Inorg. Chem.* **1998**, *6*, 733-744;

Bae, Y.; Fukushima, S.; Harada, A.; Kataoka, K. Design of environment-sensitive supramolecular assemblies for intracellular drug delivery: Polymeric micelles that are responsive to intracellular pH change. *Angew. Chem., Int. Ed.*, **2003,** *42*, 4640–4643.

Bahadur, K. C. R.; Xu, P. Multicompartment intracellular self‐expanding nanogel for targeted delivery of drug cocktail. *Adv. Mater.*, **2012**, *24*, 6479–6483.

Baldwin, R. L. How Hofmeister ion interactions affect protein stability. *Biophys. J.* **1996**, 71, 2056-2063.

Robert-Banchereau, E.; Lacombe, S.; Ollivier, J. Solution reactivity of thiyl radicals with molecular oxygen: Unsensitized photooxidation of dimethyldisulfide. *Tetrahedron Lett.* **1995**, *36*, 8197-8200;

Banerjee, R.; Phan, A.; Wang, B.; Knobler, C.; Furukawa, H.; O'Keeffe, M.; Yaghi, O. M. High-throughput synthesis of zeolitic imidazolate frameworks and application to CO_2 capture. *Science* **2008**, *319*, 939.

Bapat, A. P.; Roy, D.; Ray, J. G.; Savin, D. A.; Sumerlin, B. S. Dynamic-covalent macromolecular stars with boronic ester linkages. *J. Am. Chem. Soc.* **2011**, *133*, 19832-19838.

Barnham, K. J.; Masters, C. L.; Bush, A. I. Neurodegenerative diseases and oxidative stress. *Nat. Rev. Drug Discov.* **2004**, *3*, 205-214.

Barrell, M. J.; Campaña, A. G.; von Delius, M.; Geertsema, E. M.; Leigh, D. A. Light-driven transport of a molecular walker in either direction along a molecular track. *Angew. Chem. Int. Ed.* **2011**, *50*, 285-290;

Basak, D.; Kumar, R.; Ghosh, S. Telechelic poly(disulfide)s and related block copolymer. *Macromol. Rapid Commun.*, **2014**, *35*, 1340–1344.

Bickerton, S.; Jiwpanich, S.; Thayumanavan, S. Interconnected roles of scaffold hydrophobicity, drug loading, and encapsulation stability in polymeric nanocarriers. *Mol. Pharmaceutics* **2012**, *9*, 3569-3578.

Bikram, M; West, J. L. Thermo-responsive systems for controlled drug delivery. *Expert Opin Drug Deliv.* **2008**, *10*, 1077-1091;

Bordello, J.; Novo, M.; Al-Soufi, W. Exchange-dynamics of a neutral hydrophobic dye in micellar solutions studied by fluorescence correlation spectroscopy. *J. Colloid Interface Sci.* **2010**, *345*, 369-376.

Brewer, S. H.; Allen, A. M.; Lappi, S. E.; Chasse, T. L.; Briggman, K. A.; Gorman, C. B.; Franzen, S. Infrared detection of a phenylboronic acid terminated alkane thiol monolayer on gold surfaces. *Langmuir* **2004**, *20*, 5512-5520.

Cantrell, G. K.; Meyer, T. Y. Catalytic CN bond formation by metal-imide-mediated imine metathesis. *J. Am. Chem. Soc.* **1998**, *120*, 8035-8042;

Caravan, P.; Ellison, J. J.; McMurry, T. J.; Lauffer, Randall B. Gadolinium (III) chelates as MRI contrast agents: structure, dynamics, and applications. *Chem. Rev.* 1999, *99*, 2293 – 2352;

Carné, A.; Carbonell, C.; Imaz, I.; Maspoch, D. Nanoscale metal–organic materials. *Chem. Soc. Rev.*, **2011**, *40*, 291–305

Carné-Sánchez, A.; Imaz, I.; Cano-Sarabia, M.; Maspoch, D. A spray-drying strategy for synthesis of nanoscale metal–organic frameworks and their assembly into hollow superstructures. *Nat. Chem.* **2013**, *5*, 203.

Caruso, F.; Caruso, R. A.; Möhwald, H. Nanoengineering of inorganic and hybrid hollow spheres by colloidal templating. *Science* **1998**, *282*, 1111.

Caspar, D. L. Movement and self-control in protein assemblies. Quasi-equivalence revisited. *Biophys J.* **1980**, *32*, 103-138.

Cerritelli, S.; Velluto, D.; Hubbell, J. A. PEG-SS-PPS: reduction-sensitive disulfide block copolymer vesicles for intracellular drug delivery. *Biomacromolecules*, **2007**, *8*, 1966–1972.

Chakravarthi, S.; Jessop, C. E.; Bulleid, N. J. The role of glutathione in disulphide bond formation and endoplasmic-reticulum-generated oxidative stress. *EMBO reports* **2006**, *7*, 271-275;

Chen, X.; Zhou, Y.; Peng, X.; Yoon, J.; Fluorescent and colorimetric probes for detection of thiols. *Chem. Soc. Rev*. **2010**, *39*, 2120–2135.

Cheng, L. X.; Tang, J. J.; Luo, H.; Jin, X. L.; Dai, F.; Yang, J.; Qian, Y. P.; Li, X. Z.; Zhou, B. Antioxidant and antiproliferative activities of hydroxyl-substituted Schiff bases. *Bioorg. Med. Chem. Lett.* **2010**, *20*, 2417-2420.

Choi, S. W.; Zhang, Y.; Xia, Y. N. A temperature-sensitive drug release system based on phase-change materials. *Angew. Chem., Int. Ed.*, **2010**, *49*, 7904–7908.

Christinat, N.; Scopelliti, R.; Severin, K. Multicomponent assembly of boron-based dendritic nanostructures. *J. Org. Chem.* **2007**, *72*, 2192-2200.

Christinat, N.; Scopelliti, R.; Severin, K. Multicomponent assembly of boronic acid based macrocycles and cages. *Angew. Chem. Int. Ed.* **2008**, *47*, 1848-1852.

Chung, J. W.; Lee, K.; Neikirk, C.; Nelson, C. M.; Priestley, R. D. Photoresponsive coumarin-stabilized polymeric nanoparticles as a detectable drug carrier. *Small* **2012**, *8*, 1693-1700;

Chung, M.-K.; Hebling, C. M.; Jorgenson, J. W.; Severin, K.; Lee, S. J.; Gagné, M. R. Deracemization of a dynamic combinatorial library induced by (−)-cytidine and (−)-2-thiocytidine. *J. Am. Chem. Soc.* **2008**, *130*, 11819-11827.

Colson, J. W.; Woll, A. R.; Mukherjee, A.; Levendorf, M. P.; Spitler, E. L.; Shields, V. B.; Spencer, M. G.; Park, J.; Dichtel, W. R. Oriented 2D covalent organic framework thin films on single-layer grapheme. *Science* **2011**, *332*, 228-231.

Connon, S. J.; Blechert, S.. Recent developments in olefin cross-metathesis. *Angew. Chem. Int. Ed.* **2003,** *42*, 1900-1923;

Cruz-Huerta, J.; Salazar-Mendoza, D.; Hernandez-Paredes, J.; Hernandez Ahuactzi, I. F.; Hopfl, H. N-containing boronic esters as self-complementary building blocks for the assembly of 2D and 3D molecular networks. *Chem. Commun.* **2012**, *48*, 4241-4243.

Huang, Y.; Duan, X.; Wei, Q.; Lieber, C. M. Functional nanoscale electronic devices assembled using silicon nanowire building blocks. *Science* **2001**, *291*, 630.

Dan, K.; Rajdev, P.; Deb, J.; Jana, S. S.; Ghosh, S. Remarkably stable amphiphilic random copolymer assemblies: A structure–property relationship study. *J. Polym. Sci. A Polym. Chem.* **2013**, *51*, 4932-4943.

De Greef, T. F. A.; J. Smulders, M. M.; Wolffs, M.; Schenning, A. P. H. J.; Sijbesma, R. P.; Meijer, E. W. Supramolecular polymerization. *Chem Rev* **2009**, *109*, 5687-5754.

Deka, P.; Deka, R. C.; Bharali, P. In situ generated copper nanoparticle catalyzed reduction of 4-nitrophenol. *New J.Chem.,* **2014**, *38*,1789.

Ding, C. X.; Gu, J. X.; Qu, X. Z.; Yang, Z. Z. Preparation of multifunctional drug carrier for tumor-specific uptake and enhanced intracellular delivery through the conjugation of weak acid labile linker. *Bioconjugate Chem.* **2009,** *20*, 1163–1170;

Dirksen, A.; Dirksen, S.; Hackeng, T. M.; Dawson. P. E.. Nucleophilic catalysis of hydrazone formation and transimination: implications for dynamic covalent chemistry. *J. Am. Chem. Soc.* **2006**, *128*, 15602-15603;

Dong, H.; Shu, J. Y.; Dube, N.; Ma, Y.; Tirrell, M. V.; Downing, K. H.; Xu, T. 3-Helix micelles stabilized by polymer springs. *J. Am. Chem. Soc.* **2012**, *134*, 11807-11814.

Dong, W.; Kishimura, A.; Anraku, Y.; Chuanoi, S.; Kataoka, K. Monodispersed polymeric nanocapsules: spontaneous evolution and morphology transition from reducible hetero-PEG PICmicelles by controlled degradation. *J. Am. Chem. Soc.,* **2009**, *131*, 3804–3805.

Du, J. Z.; Tang, Y. Q.; Lewis, A. L.; Armes, S. P. pH-Sensitive vesicles based on a biocompatible zwitterionic diblock copolymer. *J. Am. Chem. Soc.,* **2005**, *127*, 17982–17983;

Du, J. Z.; Sun, T. M.; Song, W. J.; Wu, J.; Wang, J. A tumor-acidity-activated charge-conversional nanogel as an intelligent vehicle for promoted tumoral-cell uptake and drug delivery. *Angew. Chem. Int. Ed.,* **2010**, *49*, 3621-3626.

Du, J. Z.; Du, X. J.; Mao, C. Q.; Wang, J. Tailor-made dual pH-sensitive polymer_doxorubicin nanoparticles for efficient anticancer drug delivery. *J. Am. Chem. Soc.,* **2011**, *133*, 17560–17563;

Dulle, J.; Thirunavukkarasu, K.; Mittelmeijer-Hazeleger, M. C.; Andreeva, D. V.; Shiju, N. R.; Rothenberg, G. Efficient three-component coupling catalysed by mesoporous copper-aluminum based nanocomposites. *Green Chem.*, **2013**, *15*, 1238–1243.

Ejima, H.; Richardson, J. J.; Liang, K.; Best, J. P.; van Koeverden, M. P.; Such, G. K.; Cui, J.; Caruso, F. One-step assembly of coordination complexes for versatile film and particle engineering. *Science* **2013**, *341*, 154.

El-Kaderi, H. M.; Hunt, J. R.; Mendoza-Cortes, J. L.; Cote, A. P.; Taylor, R. E.; O'Keeffe, M.; Yaghi, O. M. Designed synthesis of 3D covalent organic frameworks. *Science* **2007**, *316*, 268-272.

England, J. L.; Haran, G. Role of solvation effects in protein denaturation: from thermodynamics to single molecules and back. *Annu. Rev. Phys. Chem.* **2011**, *62*, 257-277.

Folmer-Andersen, J. F.; Lehn, J.-M. Thermoresponsive dynamers: thermally induced, reversible chain elongation of amphiphilic poly (acylhydrazones). *J. Am. Chem. Soc.* **2011**, *133*, 10966-10973.

Franzen, S.; Ni, W.; Wang, B. Study of the mechanism of electron-transfer quenching by boron-nitrogen adducts in fluorescent sensors. *J. Phys. Chem. B* **2003**, *107*, 12942-12948.

Fu, G. C.; Nguyen, S. T.; Grubbs, G. H. Catalytic ring-closing metathesis of functionalized dienes by a ruthenium carbene complex. *J. Am. Chem. Soc.* **1993,** *115*, 9856-9857;

Fuller, J. M.; Raghupathi, K. R.; Ramireddy, R. R.; Subrahmanyam, A. V.; Yesilyurt, V.; Thayumanavan, S. Temperature-sensitive transitions below LCST in amphiphilic dendritic assemblies: host–guest implications. *J. Am. Chem. Soc.* **2013**, *135*, 8947-8954;

Furukawa, H.; Cordova, K. E.; O'Keeffe, M.; Yaghi, O. M. The chemistry and applications of metal-organic frameworks. *Science* **2013**, *341*, 1230444.

Gao, Y.; Yang, C.; Liu, X.; Ma, R.; Kong, D.; Shi, L. A multifunctional nanocarrier based on nanogated mesoporous silica for enhanced tumor-specific uptake and intracellular delivery. *Macromol Biosci.* **2012**, *12*, 251-259;

Ge, Z.; Liu, S. Functional block copolymer assemblies responsive to tumor and intracellular microenvironments for site-specific drug delivery and enhanced imaging performance. *Chem. Soc. Rev.*, **2013**, *42*, 7289–7325.

Gehlen, M. H.; De Schryver, F. C. Time-resolved fluorescence quenching in micellar assemblies. *Chem. Rev.* **1993**, *93*, 199-221.

Ghosh, S.; Basu, S.; Thayumanavan, S. Simultaneous and reversible functionalization of copolymers for biological applications. *Macromolecules* **2006**, *39*, 5595-5597.

Gjaltema, A.; Van Loosdrecht, M. C. M.; Heijnen, J. Abrasion of suspended biofilm pellets in airlift reactors: Effect of particle size. *J. Biotechnol. Bioeng.* **1997**, *55*, 206-215

Gonz ález-Toro, D. C.; Ryu, J. H.; Chacko, R. T.; Zhuang, J. M.; Thayumanavan, S. Concurrent binding and delivery of proteins and lipophilic small molecules using polymeric nanogels. *J. Am. Chem. Soc.*, **2012**, *134*, 6964–6967;

Griset, A. P.; Walpole, J.; Liu, R.; Gaffey, A.; Colson Y. L.; Grinstaff, M. W. Expansile nanoparticles: synthesis, characterization, and in vivo efficacy of an acid-responsive polymeric drug delivery system. *J. Am. Chem. Soc.*, **2009**, *131*, 2469–2471;

Gu, J.; Cheng, W. P.; Liu, J.; Lo, S. Y.; Smith, D.; Qu, X.; Yang, Z. pH-triggered reversible stealth polycationic micelles. *Biomacromolecules* **2008**, *9*, 255-262;

Gupta, D.; Knight, A. R. Reactions of thiyl radicals. XIII. Photochemically induced exchange reactions of liquid alkyl disulfides. *Can. J. Chem.* **1980**, *58*, 1350-1354;

Ha, Y. M.; Lee, H. J.; Park, D.; Jeong, H. O.; Park, J. Y.; Park, Y. J.; Lee, K. J.; Lee, J. Y.; Moon, H. R.; Chung, H. Y. Molecular docking studies of (1E,3E,5E)-1,6-bis(substituted phenyl)hexa-1,3,5-triene and 1,4-bis(substituted *trans*-styryl)benzene analogs as novel tyrosinase inhibitors. *Biol. Pharm. Bull.* **2012**, *36*, 55-65.

Hall, L. W.; Odom, J. D.; Ellis, P. D. Nuclear magnetic resonance investigation of the nature of the boron-carbon bond in some vinylboranes. *J. Am. Chem. Soc.* **1975**, *97*, 4527-4531.

Hawker, C. J.; Bosman, A. W.; Harth, E. New polymer synthesis by nitroxide mediated living radical polymerizations. *Chem. Rev.*, **2001**, *101*, 3661–3688.

Hawker, C. J.; Wooley, K. L. The convergence of synthetic organic and polymer chemistries. *Science* **2005**, *309*, 1200.

He, J.; Tong, X.; Zhao, Y. Photoresponsive nanogels based on photocontrollable cross-links. *Macromolecules* **2009**, *42*, 4845-4852;

He, Y.; Shao, Q.; Chen, S. F.; Jiang, S. Y. Water mobility: a bridge between the Hofmeister series of ions and the friction of zwitterionic surfaces in aqueous environments. *J. Phys. Chem. C.* **2011**, 115, 15525–15531.

Helmlinger, G.; Schell, A.; Dellian, M.; Forbes, N. S.; Jain, R. K. Acid production in glycolysis-impaired tumors provides new insights into tumor metabolism. *Clin. Cancer Res.* **2002**, *8*, 1284–1291;

Herzenberg, L. A.; De Rosa, S. C.; Dubs, J. G.; Roederer, M.; Anderson, M. T.; Ela, S. W.; Deresinski, S. C.; Herzenberg, L. A. Glutathione deficiency is associated with impaired survival in HIV disease. *Proc. Natl. Acad. Sci. U. S. A.* **1997**, *94*, 1967–1972.

Hilf, S.; Kilbinger, A. F. M. Functional end groups for polymers prepared using ring-opening metathesis polymerization. *Nat. Chem.*, **2009**, *1*, 537–546.

Hirsch, A. K. H.; Buhler, E.; Lehn, J.-M. Biodynamers: self-organization-driven formation of doubly dynamic proteoids. *J. Am. Chem. Soc.* **2012**, *134*, 4177-4183.

Hofmeister, F. On the understanding of the effects of salts, second report. On irregularities in the precipitating effect of salts and their relationship to their physical behavior. *Arch. Exp. Pathol. Pharmocol.* **1888**, 24, 247-260.

Höpfl, H. J. The tetrahedral character of the boron atom newly defined—a useful tool to evaluate the N→ B bond. *Organomet. Chem.* **1999**, *581*, 129-149.

Horcajada, P.; Gref, R.; Baati, T.; Allan, P. K.; Maurin, G.; Couvreur, P.; Ferey, G.; Morris, R. E.; Serre, C. Metal–organic frameworks in biomedicine. *Chem. Rev.* **2011**, *112*, 1232.

Howes, P. D.; Chandrawati, R.; Stevens, M. M. Colloidal nanoparticles as advanced biological sensors. *Science* **2014**, *346*, 1247390.

Hu, J.; Wang, H.; Gao, Q.; Guo, H. Porous carbons prepared by using metal–organic framework as the precursor for supercapacitors. *Carbon*, **2010**, *48*, 3599-3606.

Hu, L. C.; Yonamine, Y.; Lee, S. H.; Van der Veer, W. E.; Shea, K. J. Light-triggered charge reversal of organic–silica hybrid nanoparticles. *J. Am. Chem. Soc.*, **2012**, *134*, 11072–11075;

Hu, M.; Reboul, J.; Furukawa, S.; Torad, N. L.; Ji, Q.; Srinivasu, P.; Ariga, K.; Kitagawa, S.; Yamauchi, Y. Direct carbonization of Al-based porous coordination polymer for synthesis of nanoporous carbon. *J. Am. Chem. Soc.*, **2012**, *134*, 2864-2867.

Hu, Y. Q.; Kim, M. S.; Kim, B. S.; Lee, D. S. Synthesis and pH-dependent micellization of 2-(diisopropylamino)ethyl methacrylate based amphiphilic diblock copolymers via RAFT polymerization. *Polymer*, **2007**, *48*, 3437–3443;

Huang, X.; Huang, G.; Zhang, S.; Sagiyama, K; Togao, O.; Ma, X.; Wang, Y.; Li, Y.; Soesbe, T. C.; Sumer, B. D.; Takahashi, M.; Sherry, A. D.; Gao, J. Multi‐chromatic pH‐activatable 19F‐MRI nanoprobes with binary ON/OFF pH transitions and chemical‐shift barcodes. *Angew. Chem. Int. Ed.*, **2013**, *52*, 8074-8078;

Huo, J.; Wang, L.; Irran, E.; Yu, H.; Gao, J.; Fan, D.; Li, B.; Wang, J.; Ding, W.; Amin, A. M.; Li, C.; Ma, L. Hollow ferrocenyl coordination polymer microspheres with micropores in shells prepared by Ostwald ripening. *Angew. Chem. Int. Ed.* **2010**, *49*, 9237.

Hwang, C.; Sinskey, A. J.; Lodish, H. F. Oxidized redox state of glutathione in the endoplasmic reticulum. *Science* **1992**, *257*, 1496–1502.

Ikkala, O.; ten Brinke, G. Functional materials based on self-assembly of polymeric supramolecules. *Science*, **2002**, *295*, 2407–2409.

Iwasawa, N.; Takahagi, H. Boronic esters as a system for crystallization-induced dynamic self-assembly equipped with an on-off switch for equilibration. *J. Am. Chem. Soc.* **2007**, *129*, 7754-7755.

Jäkle, F.; Lewis acidic organoboron polymers. *Coord. Chem. Rev.*, **2006**, *250*, 1107-1121.

Janata, J.; Josowicz, M. Conducting polymers in electronic chemical sensors. *Nat. Mater*., **2003**, *2*, 19–24.

Janeliunas, D.; van Rijn, P.; Boekhoven, J.; Minkenberg, C. B.; van Esch, J. H.; Eelkema, R. Aggregation-driven reversible formation of conjugated polymers in water. *Angew. Chem. Int. Ed.* **2013**, *52*, 1998-2001;

Jänes, A.; Thomberg, T.; Lust, E. Synthesis and characterisation of nanoporous carbide-derived carbon by chlorination of vanadium carbide. *Carbon*, **2007**, *45*, 2717-2722.

Jiang, J.; Qi, B.; Lepage, M.; Zhao, Y. Polymer micelles stabilization on demand through reversible photo-cross-linking. *Macromolecules* **2007**, *40*, 790-792.

Jiwpanich, S.; Ryu, J.-H.; Bickerton, S.; Thayumanavan, S. Noncovalent encapsulation stabilities in supramolecular nanoassemblies. *J. Am. Chem. Soc.* **2010**, *132*, 10683-10685.

Johnson, J. A.; Lu, Y. Y.; Burts, A. O.; Lim, Y.-H.; Finn, M. G.; Koberstein, J. T.; Turro, N. J.; Tirrell, D. A.; Grubbs, R. H. Core-clickable PEG-branch-azide bivalent-bottle-brush polymers by ROMP: grafting-through and clicking-to. *J. Am. Chem. Soc.*, **2010**, *133*, 559–566.

Jones, J. T. A.; Hasell, T.; Wu, X.; Bacsa, J.; Jelfs, K. E.; Schmidtmann, M.; Chong, S. Y.; Adams, D. J.; Trewin, A.; Schiffman, F.; Cora, F.; Slater, B.; Steiner, A.; Day, G. M.; Cooper, A. I. Modular and predictable assembly of porous organic molecular crystals. *Nature* **2011**, *474*, 367.

Jonkheijm, P.; Van der Schoot, P.; Schenning, A. P.; Meijer, E. W. Probing the solvent-assisted nucleation pathway in chemical self-assembly. *Science* **2006**, *313*, 80-83.

Jung, H. S.; Chen, X.; Kim, J. S.; Yoon, J. Recent progress in luminescent and colorimetric chemosensors for detection of thiols. *Chem. Soc. Rev.* **2013**, *42*, 6019-6031.

Kabanov, A. V.; Vinogradov, S. V. Nanogels as pharmaceutical carriers: finite networks of infinite capabilities. *Angew. Chem. Int. Ed.* **2009**, *48*, 5418-5429.

Kakizawa, Y.; Harada, A.; Kataoka, K. Environment-sensitive stabilization of core-shell structured polyion complex micelle by reversible cross-linking of the core through disulfide bond. *J. Am. Chem. Soc.* **1999**, *121*, 11247-11248;

Kalbasi, R. J.; Nourbakhsh, A. A.; Zia, M. Aerobic oxidation of alcohols catalyzed by copper nanoparticle-polyacrylamide/SBA-15 as novel polymer-inorganic hybrid. *J. Inorg. Organomet. Polym.*, **2012**, *22*, 536–542.

Kalyanasundaram, K.; Thomas, J. Environmental effects on vibronic band intensities in pyrene monomer fluorescence and their application in studies of micellar systems. *J. Am. Chem. Soc.* **1977**, *99*, 2039-2044.

Kim, H.-C.; Park, S.-M.; Hinsberg, W. D. Block copolymer based nanostructures: materials, processes, and applications to electronics. *Chem. Rev.*, **2009**, *110*, 146–177.

Kim, J. K.; Yang, S. Y.; Lee, Y.; Kim, Y. Functional nanomaterials based on block copolymer self-assembly. *Prog. Polym. Sci.*, **2010**, *35*, 1325–1349.

Kim, J. S.; Youk, J. H. Preparation of core cross-linked micelles using a photo-cross-linking agent. *Polymer* **2009,** *50*, 2204-2208.

Kim, K.; Bae, B.; Kang, Y. J.; Nam, J.-M.; Kang, S.; Ryu, J.-H. Natural polypeptide-based supramolecular nanogels for stable noncovalent encapsulation. *Biomacromolecules* **2013**, *14*, 3515-3522.

Kirkendall, E. Diffusion of zinc in alpha brass. *Aime Trans.* **1942**, *147*, 104.

Kiviranta, P. H.; Leppänen, J.; Kyrylenko, S.; Salo, H. S.; Lahtela-Kakkonen, M.; Tervo, A. J.; Wittekindt, C.; Suuronen, T.; Kuusisto, E.; Järvinen, T. N, N'-bisbenzylidenebenzene-1, 4-diamines and N, N'-bisbenzylidenenaphthalene-1, 4-diamines as sirtuin type 2 (SIRT2) inhibitors. *J. Med. Chem.* **2006**, *49*, 7907-7911.

Koh, M. J.; Khan, R. K. M.; Torker, S.; Hoveyda, A. H. Broadly applicable Z- and diastereoselective ring-opening/cross-metathesis catalyzed by a dithiolate Ru complex. *Angew. Chem. Int. Ed.* **2014**, *53*, 1968-1972.

Koksharov, Y. A.; Gubin, S.P.; Kosobudsky, I. D.; Beltran, M.; Khodorkovsky, Y.; Tishin, A. M. Low temperature electron paramagnetic resonance anomalies in Fe-based nanoparticles. *J. Appl. Phys.* **2000**, *88*, 1587.

Korevaar, P. A.; George, S. J.; Markvoort, A. J.; Smulders, M. M.; Hilbers, P. A.; Schenning, A. P.; De Greef, T. F.; Meijer, E. W. Pathway complexity in supramolecular polymerization. *Nature* **2012**, *481*, 492-496.

Korevaar, P. A.; Schaefer, C.; De Greef, T. F.; Meijer, E. W. Controlling chemical self-assembly by solvent-dependent dynamics. *J. Am. Chem. Soc.* **2012**, *134*, 13482-13491.

Kuang, H.; He, H.; Hou, J.; Xie, Z.; Jing, X.; Huang, Y. Thymine modified amphiphilic biodegradable copolymers for photo-cross-linked micelles as stable drug carriers. *Macromol. Biosci.* **2013**, *13*, 1593-1600.

Kumar, R.; Chen, M. H.; Parmar, V. S.; Samuelson, L. A.; Kumar, J.; Nicolosi, R.; Yoganathan, S.; Watterson, A. C. Supramolecular assemblies based on copolymers of PEG600 and functionalized aromatic diesters for drug delivery applications. *J. Am. Chem. Soc.*, **2004**, *126*, 10640-10644.

La, D. S.; Alexander, J. B.; Cefalo, D. R.; Graf, D. D.; Hoveyda, A. H.; Schrock, R. R. Mo-catalyzed asymmetric synthesis of dihydrofurans. Catalytic kinetic resolution and enantioselective desymmetrization through ring-closing metathesis. *J. Am. Chem. Soc.* **1998,** *120*, 9720-9721;

LaMer, V. K.; Dinegar, R. H. Theory, production and mechanism of formation of monodispersed hydrosols. *J. Am. Chem. Soc.* **1950**, *72*, 4847-4854.

Laurent, S.; Forge, D.; Port, M.; Roch, A.; Robic, C.; Vander Elst, L.; Muller, R. N. Magnetic iron oxide nanoparticles: synthesis, stabilization, vectorization, physicochemical characterizations, and biological applications. *Chem. Rev.* **2008**, *108*, 2064 – 2110;

Lee, H. J.; Choi, S.; Oh, M.; Well-dispersed hollow porous carbon spheres synthesized by direct pyrolysis of core-shell type metal-organic frameworks and their sorption properties. *Chem. Commun.*, **2014**, *50*, 4492-4495.

Lee, H. J.; Pardridge, W. M. Monoclonal antibody radiopharmaceuticals: cationization, pegylation, radiometal chelation, pharmacokinetics, and tumor imaging. *Bioconjugate Chem.* **2003**, *14*, 546-553;

Lee, J. -S.; Kim, S. -I.; Yoon, J. -C.; Jang, J. -H. Chemical vapor deposition of mesoporous graphene nanoballs for supercapacitor. *ACS Nano,* **2013**, *7*, 6047–6055;

Lee, K. T.; Jung, Y. S.; Oh, S. M. Synthesis of tin-encapsulated spherical hollow carbon for anode material in lithium secondary batteries. *J. Am. Chem. Soc.*, **2003**, *125*, 5652-5653.

Lee, Y. R.; Chiu, C. L.; Lin, S. M. Ultraviolet photodissociation study of CH_3SCH_3 and CH_3SSCH_3. *J. Chem. Phys.* **1994**, *100*, 7376-7384;

Lee, Y.; Fukushima, S.; Bae, Y.; Hiki, S.; Ishii, T.; Kataoka, K. A protein nanocarrier from charge-conversion polymer in response to endosomal pH. *J. Am. Chem. Soc.* **2007,** *129*, 5362 – 5363;

Li, H.; Jäkle, F. Universal scaffold for fluorescent conjugated organoborane polymers. *Angew. Chem. Int. Ed.*, **2009**, *48*, 2313-2316.

Li, J.; Carnall, J.; Stuart, M. C. A.; Otto, S. Hydrogel formation upon photoinduced covalent capture of macrocycle stacks from dynamic combinatorial libraries. *Angew. Chem. Int. Ed.* **2011**, *50*, 8384-8386;

Li, L.; Raghupathi, K.; Song, C.; Prasad, P.; Thayumanavan, S. Self-assembly of random copolymers. *Chem. commun.* **2014**, *50*, 13417-13432.

Li, L.; Raghupathi, K.; Yuan, C.; Thayumanavan, S. Surface charge generation in nanogels for activated cellular uptake at tumor-relevant pH. *Chem. Sci.* **2013**, *4*, 3654-3660;

Li, L.; Ryu, J.-H.; Thayumanavan, S. Effect of hofmeister ions on the size and encapsulation stability of polymer nanogels. *Langmuir* **2013**, *29*, 50-55.

Li, L.; Song, C.; Jennings, M.; Thayumanavan, S. Photoinduced heterodisulfide metathesis for reagent-free synthesis of polymer nanoparticles. *Chem. commun.* **2015**, *51*, 1425-1428.

Li, L.; Thayumanavan, S. Environment-dependent guest exchange in supramolecular hosts. *Langmuir* **2014,** *30*, 12384-12390.

Li, L.; Yuan, C.; Dai, L.; Thayumanavan, S. Thermoresponsive Polymeric Nanoparticles: Nucleation from Cooperative Polymerization Driven by Dative Bonds. *Macromolecules* **2014**, *47*, 5869.

Li, Y.; Song, Y.; Zhao, L.; Gaidosh, G.; Laties, A. M.; Wen, R. Direct labeling and visualization of blood vessels with lipophilic carbocyanine dye DiI. *Nat. Protoc.*, **2008,** *3*, 1703–1708.

Liu, J. Y.; Pang, Y.; Huang, W.; Zhu, Z. Y.; Zhu, X. Y.; Zhou, Y. F.; Yan, D. Y. Redox-responsive polyphosphate nanosized assemblies: a smart drug delivery platform for cancer therapy. *Biomacromolecules,* **2011**, *12*, 2407–2415;

Liu, K. C.; Yeo, Y. Extracellular stability of nanoparticulate drug carriers. *Arch. Pharmacal Res.* **2014**, *37*, 16-23.

Liu, S.; Weaver, J. V. M.; Tang, Y.; Billingham, N. C.; Armes, S. P.; Tribe. K. Synthesis of shell cross-linked micelles with pH-responsive cores using ABC triblock copolymers. *Macromolecules*, **2002,** *35*, 6121–6131.

Liu, W.; Pink, M.; Lee, D. Conjugated polymer sensors built on π-extended borasiloxane cages. *J. Am. Chem. Soc.* **2009**, *131*, 8703-8707.

Liu, X. Y.; Mu, X. R.; Liu, Y.; Liu, H. J.; Chen, Y.; Cheng, F.; Jiang, S. C. Hyperbranched polymers with thermoresponsive property highly sensitive to ions. *Langmuir* **2012**, 10, 4867-4876.

Liu, Z.; Robinson, J. T.; Tabakman, S. M.; Yang, K.; Dai, H. Carbon materials for drug delivery & cancer therapy. *Mater. Today* **2011**, *14*, 316-323.

Nostro, P. L.; Ninham, B. W. Hofmeister phenomena: an update on ion specificity in biology. *Chem. Rev*. **2012**, 112, 2286-2322.

Lobana, T. S.; Kinoshita, I.; Kimura, K.; Nishioka, T.; Shiomi, D.; Isobe, K. Pyridine-2-sulfonates as versatile ligands for the synthesis of novel coordinative and hydrogen-bonded supramolecules. *Eur. J. Inorg. Chem.* **2004**, *2004*, 356-367;

Lou, X. W.; Wang, Y.; Yuan, C.; Lee, J. Y.; Archer, L. A. Template-free synthesis of SnO2 hollow nanostructures with high lithium storage capacity. *Adv. Mater.* **2006**, *18*, 2325.

Lu, J.; Owen, S. C.; Shoichet, M. S. Stability of self-assembled polymeric micelles in serum. *Macromolecules* **2011**, *44*, 6002-6008.

Lu, Y.-X.; Guan, Z. Olefin metathesis for effective polymer healing via dynamic exchange of strong carbon–carbon double bonds. *J. Am. Chem. Soc.* **2012,** *134*, 14226-14231;

Luo, Z.; Cai, K.; Hu, Y.; Zhao, L.; Liu, P.; Duan, L.; Yang, W. Mesoporous silica nanoparticles end‐capped with collagen: redox‐responsive nanoreservoirs for targeted drug delivery. *Angew. Chem. Int. Ed.* **2011**, *50*, 640-643;

Lutz, J.-F. Thermo-switchable materials prepared using the OEGMA-platform. *Adv. Mater.* **2011**, 23, 2237-2243.

Lutz, J. F.; Akdemir, O.; Hoth, A. Point by point comparison of two thermosensitive polymers exhibiting a similar LCST: is the age of poly(NIPAM) Over? *J. Am. Chem. Soc.* **2006**, 128, 13046-13047.

Maeda, H.; Fang, J.; Inutsuka T.; Kitamoto, Y. Vascular permeability enhancement in solid tumor: various factors, mechanisms involved and its implications. *Int. Immunopharmacol.*, **2003**, *3*, 319–328.

Maeda, H.; Hasegawa, M.; Hashimoto, T.; Kakimoto, T.; Nishio, S.; Nakanishi, T. Nanoscale spherical architectures fabricated by metal coordination of multiple dipyrrin moieties. *J. Am. Chem. Soc.* **2006**, *128*, 10024-10025.

Maeda, H.; Wu, J.; Sawa, T.; Matsumura Y.; Hori, K. Tumor vascular permeability and the EPR effect in macromolecular therapeutics: a review. *J. Controlled Release,* **2000**, *65*, 271–284.

Magnusson, J. P.; Khan, A.; Pasparakis, G.; Saeed, A. O.; Wang, W. X.; Alexander, C. Ion-sensitive isothermal responsive polymers prepared in water. *J. Am. Chem. Soc.* **2008**, 130, 10852–10853.

Mai, Y.; Eisenberg, A. Self-assembly of block copolymers. *Chem. Soc. Rev.,* **2012**, *41*, 5969–5985.

Markus, G.; Karush, F. The disulfide bonds of human serum albumin and bovine γ-globulin1. *J. Am. Chem. Soc.* **1957**, *79*, 134-139;

Martin, C. R. Nanomaterials-a membrane-based synthetic approach. *Science* **1994**, *266*, 1961.

Matsumoto, N. M.; Gonz âlez-Toro, D. C.; Chacko, R. T.; Maynard, H. D.; Thayumanavan. S. Synthesis of nanogel–protein conjugates. *Polym. Chem.,* **2013**, *4*, 2464-2469.

Matyjaszewski, K.; Tsarevsky, N. V. Macromolecular engineering by atom transfer radical polymerization. *J. Am. Chem. Soc.*, **2014,** *136*, 6513–6533.

McCoy, C. P.; Rooney, C.; Edwards, C. R.; Jones, D. S.; Gorman, S. P. Light-triggered molecule-scale drug dosing devices. *J. Am. Chem. Soc.*, **2007**, *129*, 9572–9573;

Meyer, C. D.; Joiner, C. S.; Stoddart, J. F. Template-directed synthesis employing reversible imine bond formation. *Chem. Soc. Rev.* **2007,** *36*, 1705-1723;

Milligan, B.; Rivett, D. E.; Savige, W. E. The photolysis of dialkyl sulphides, disulphides, and trisulphides. *Aust. J. Chem.* **1963**, *16*, 1020-1029;

Moad, G.; Rizzardo, E.; Thang, S. H. Living radical polymerization by the RAFT process–a third update. *Aust. J. Chem.*, **2012**, *65*, 985–1076.

Mutlu, H.; de Espinosa, L. M.; Meier, M. A. R. Acyclic diene metathesis: a versatile tool for the construction of defined polymer architectures. *Chem. Soc. Rev.* **2011**, *40*, 1404-1445;

Mutsaers, S. E.; John M. P. Surface charge of macrophages and their interaction with charged particles. *J. Leukocyte Biol.*, **1988**, *44*, 17–26.

Nakase, I.; Takeuchi, T.; Tanaka, G.; Futaki, S. Methodological and cellular aspects that govern the internalization mechanisms of arginine-rich cell-penetrating peptides. *Adv. Drug Delivery Rev.* **2008**, *60*, 598−607.

Nakatani, K.; Ogura, Y.; Koda, Y.; Terashima, T.; Sawamoto, M. Sequence-regulated copolymers via tandem catalysis of living radical polymerization and in situ transesterification. *J. Am. Chem. Soc.*, **2012,** *134*, 4373–4383.

Nakayama, M.; Okano, T.; Miyazaki, T.; Kohori, F.; Sakai, K.; Yokoyama, M. Molecular design of biodegradable polymeric micelles for temperature-responsive drug release. *J. Controlled Release*, **2006**, *115*, 46–56.

Nakazawa, I.; Suda, S.; Masuda, M.; Asai, M.; Shimizu, T. pH-Dependent reversible polymers formed from cyclic sugar-and aromatic boronic acid-based bolaamphiphiles. *Chem. Commun.*, **2000**, *10*, 881-882.

Nelander, B.; Sunner, S. Cogwheel effect in dialkyl disulfides. *J. Am. Chem. Soc.* **1972**, *94*, 3576-3577;

Ni, W.; Kaur, G.; Springsteen, G.; Wang, B.; Franzen, S. Regulating the fluorescence intensity of an anthracene boronic acid system: a B–N bond or a hydrolysis mechanism? *Bioorg. Chem.*, **2004**, *32*, 571-581.

Ni, W.; Wang, Y.; Xu, R. Formation of Sn@ C yolk-shell nanospheres and core-sheath nanowires for highly reversible lithium storage. *Part. Part. Syst. Charact.* **2013**, *30*, 873–880.

Nikiforov, V. N.; Koksharov, Y. A.; Polyakov, S. N.; Malakho, A. P.; Volkov, A. V.; Moskvina, M. A.; Khomutov, G. B.; Irkhin, V. Y. Magnetism and Verwey transition in magnetite nanoparticles in thin polymer film. *J. Alloys Compd.* **2013**, *569*, 58.

Nishimura, N.; Kobayashi, K. Self-assembly of a cavitand-based capsule by dynamic boronic ester formation. *Angew. Chem. Int. Ed.* **2008**, *47*, 6255-6258.

Nishimura, N.; Yoza, K.; Kobayashi, K. Guest-encapsulation properties of a self-assembled capsule by dynamic boronic ester bonds. *J. Am. Chem. Soc.* **2009**, *132*, 777-790.

Nishinaga, T.; Tanatani, A.; Oh, K.; Moore, J. S. The size-selective synthesis of folded oligomers by dynamic templation. *J. Am. Chem. Soc.* **2002**, *124*, 5934-5935;

Nishiyabu, R.; Teraoka, S.; Matsushima, Y.; Kubo, Y. Fabrication of soft submicrospheres by sequential boronate esterification and their dynamic behavior. *ChemPlusChem* **2012**, *77*, 201.

Niu, W.; Smith, M. D.; Lavigne, J. J. Self-assembling poly (dioxaborole) s as blue-emissive materials. *J. Am. Chem. Soc.* **2006**, *128*, 16466-16467.

Niu, W.; Smith, M. D.; Lavigne, J. J. Substituent effects on the structure and supramolecular assembly of bis (dioxaborole) s derived from 1, 2, 4, 5-tetrahydroxybenzene. *Cryst. Growth Des.* **2006**, *6*, 1274-1277.

Novo, M.; Felekyan, S.; Seidel, C. A.; Al-Soufi, W. Dye-exchange dynamics in micellar solutions studied by fluorescence correlation spectroscopy. *J. Phys. Chem. B* **2007**, *111*, 3614-3624.

Oehlke, A.; Auer, A. A.; Jahre, I.; Walfort, B.; Rüffer, T.; Zoufalá, P.; Lang, H.; Spange, S. Nitro-substituted stilbeneboronate pinacol esters and their fluoro-adducts. fluoride ion induced polarity enhancement of arylboronate esters. *J. Org. Chem.* **2007**, *72*, 4328-4339.

Oh, J. K.; Drumright, R.; Siegwart, D. J.; Matyjaszewski, K. The development of microgels/nanogels for drug delivery applications. *Prog. Polym. Sci.* **2008**, *33*, 448-477.

Oh, J. K.; Siegwart, D. J.; Lee, H.; Sherwood, G.; Peteanu, L.; Hollinger, J. O.; Kataoka, K.; Matyjaszewski, K. Biodegradable nanogels prepared by atom transfer radical polymerization as potential drug delivery carriers: synthesis, biodegradation, in vitro release, and bioconjugation. *J. Am. Chem. Soc.*, **2007**, *129*, 5939–5945.

Oh, K.; Jeong, K.-S.; Moore, J. S. Folding-driven synthesis of oligomers. *Nature* **2001**, *414*, 889-893;

Oh, M.; Mirkin, C. A. Chemically tailorable colloidal particles from infinite coordination polymers. *Nature* **2005**, *438*, 651-654.

Oh, M. H.; Yu, T.; Yu, S.-H.; Lim, B.; Ko, K.-T.; Willinger, M.-G.; Seo, D.-H.; Kim, B. H.; Cho, M. G.; Park, J.-H. Galvanic replacement reactions in metal oxide nanocrystals. *Science* **2013**, *340*, 964.

Oishi, M.; Sumitani, S.; Nagasaki, Y. On-off regulation of 19F magnetic resonance signals based on pH-sensitive PEGylated nanogels for potential tumor-specific smart 19F MRI probes. *Bioconjugate Chem.* **2007**, *18*, 1379 – 1382;

Otsuka, H.; Nagano, S.; Kobashi, Y.; Maeda, T.; Takahara, A. A dynamic covalent polymer driven by disulfide metathesis under photoirradiation. *Chem. Commun.* **2010**, *46*, 1150-1152;

Otto, S.; Furlan, R. L. E.; Sanders, J. K. M. Dynamic combinatorial libraries of macrocyclic disulfides in water. *J. Am. Chem. Soc.* **2000**, *122*, 12063-12064;

Otto, S.; Furlan, R. L. E.; Sanders, J. K. M. Selection and amplification of hosts from dynamic combinatorial libraries of macrocyclic disulfides. *Science* **2002**, *297*, 590-593;

Pan, L.; He, Q.; Liu, J.; Chen, Y.; Ma, M.; Zhang, L.; Shi, J. Nuclear-targeted drug delivery of TAT peptide-conjugated monodisperse mesoporous silica nanoparticles. *J. Am. Chem. Soc.* **2012**, *134*, 5722-5725.

Pang, M.; Cairns, A. J.; Liu, Y.; Belmabkhout, Y.; Zeng, H. C.; Eddaoudi, M. Synthesis and integration of Fe-soc-MOF cubes into colloidosomes via a single-step emulsion-based approach. *J. Am. Chem. Soc.* **2013**, *135*, 10234.

Park, C. –M.; Kim, J. –H.; Kim, H.; Sohn, H. -J.; Li-alloy based anode materials for Li secondary batteries. *Chem. Soc. Rev.*, **2010**, *39*, 3115–3141.

Patra, A. K.; Dutta, A.; Bhaumik, A. Cu nanorods and nanospheres and their excellent catalytic activity in chemoselective reduction of nitrobenzenes. *Cataly. Commun.* **2010**, *11*, 651–655.

Peer, D.; Karp, J. M.; Hong, S.; Farokhzad, O. C.; Margalit, R.; Langer, R. Nanocarriers as an emerging platform for cancer therapy. *Nat. Nanotechnol.* **2007**, *2*, 751-760.

Piñeiro, L.; Freire, S.; Bordello, J.; Novo, M.; Al-Soufi, W. Dye exchange in micellar solutions. Quantitative analysis of bulk and single molecule fluorescence titrations. *Soft Matter* **2013**, *9*, 10779-10790.

Pinna, M. C.; Bauduin, P.; Touraud, D.; Monduzzi, M.; Ninham, B. W.; Kunz, W. Hofmeister effects in biology: effect of choline addition on the salt-induced super activity of horseradish peroxidase and its implication for salt resistance of plants. *J. Phys. Chem. B*, **2005**, 109, 16511-16514.

Poon, Z.; Chang, D.; Zhao, X. Y.; Hammond, P. T. Layer-by-layer nanoparticles with a pH-sheddable layer for in vivo targeting of tumor hypoxia. *ACS Nano.*, **2011**, *5*, 4284-4292.

Qie, L.; Chen, W.; Wang, Z.; Shao, Q.; Li, X.; Yuan, L.; Hu, X.; Zhang, W.; Huang, Y. Nitrogen-doped porous carbon nanofiber webs as anodes for lithium ion batteries with a superhigh capacity and rate capability. *Adv. Mater.*, **2012,** *24*, 2047-2050.

Qin, S.; Geng, Y.; Discher, D. E.; Yang, S. Temperature-controlled assembly and release from polymer vesicles of poly(ethylene oxide)-*block*- poly(*N*-isopropylacrylamide). *Adv. Mater.* **2006**, 18, 2905-2909.

Quémener, D.; Davis, T. P.; Barner-Kowollik, C.; Stenzel, M. H. RAFT and click chemistry: A versatile approach to well-defined block copolymers. *Chem. Commun.*, **2006**, *42*, 5051–5053.

Radovic-Moreno, A. F.; Lu, T. K.; Puscasu, V. A.; Yoon, C. J.; Langer, R.; Farokhzad, O. C. Surface charge-switching polymeric nanoparticles for bacterial cell wall-targeted delivery of antibiotics. *ACS Nano,* **2012,** *6*, 4279–4287.

Raghupathi, K.; Li, L.; Ventura, J.; Jennings M.; Thayumanavan, S. pH responsive soft nanoclusters with size and charge variation features. *Polym. Chem.*, **2014**, *5*, 1737–1742.

Ranu, B. C.; Dey, R.; Chatterjee T. ; Ahammed, S. Copper nanoparticle-catalyzed carbon carbon and carbon heteroatom bond formation with a greener perspective. *ChemSusChem*, **2012**, *5*, 22–44.

Rharbi, Y.; Chen, L.; Winnik, M. A. Exchange mechanisms for sodium dodecyl sulfate micelles: high salt concentration. *J. Am. Chem. Soc.* **2004**, *126*, 6025-6034.

Rharbi, Y.; Li, M.; Winnik, M. A.; Hahn, K. G. Temperature dependence of fusion and fragmentation kinetics of Triton X-100 Micelles. *J. Am. Chem. Soc.* **2000**, *122*, 6242-6251.

Rharbi, Y.; Winnik, M. A. Solute exchange between surfactant micelles by micelle fragmentation and fusion. *Adv. Colloid Interface Sci.* **2001**, *89*, 25-46.

Richard, J. P.; Melikov, K.; Vives, E.; Ramos, C.; Verbeure, B.; Gait, M. J.; Chernomordik, L. V.; Lebleu, B. Cell-penetrating peptides A reevaluation of the mechanism of cellular uptake. *J. Biol. Chem.*, **2003**, *278*, 585–590.

Robert-Banchereau, E.; Lacombe, S.; Ollivier, J. Unsensitized photooxidation of sulfur compounds with molecular oxygen in solution. *Tetrahedron* **1997**, *53*, 2087-2102.

Rosebrugh, L. E.; Marx, V. M.; Keitz, B. K.; Grubbs, R. H. Synthesis of highly *cis*, syndiotactic polymers via ring-opening metathesis polymerization using ruthenium metathesis catalysts. *J. Am. Chem. Soc.*, **2013**, *135*, 10032–10035.

Rösler, A.; Vandermeulen, G. W. M.; Klok, H.-A. Advanced drug delivery devices via self-assembly of amphiphilic block copolymers. *Adv. Drug Delivery Rev.*, **2012**, *64*, 270–279.

Rothbard, J. B.; Jessop, T. C.; Lewis, R. S.; Murray, B. A.; Wender, P. A. Role of membrane potential and hydrogen bonding in the mechanism of translocation of guanidinium-rich peptides into cells. *J. Am. Chem. Soc.* **2004**, *126*, 9506−9507.

Rueping, M.; Jaun, B.; Seebach, D. NMR Structure in methanol of a β-hexapeptide with a disulfide clamp. *Chem. Commun.* **2000**, *22*, 2267-2268;

Ruiz-Cabello, J.; Barnett, B. P.; Bottomley, P. A.; Bulte, J. W. M. Fluorine (19F) MRS and MRI in biomedicine. *NMR Biomed.* **2011**, *24*, 114 – 129

Ruzette, A.-V.; Leibler, L. Block copolymers in tomorrow's plastics. *Nat. Mater.*, **2005**, *4*, 19–31.

Ryu, J. –H.; Bickerton, S.; Zhuang, J.; Thayumanavan, S. Ligand-decorated nanogels: fast one-pot synthesis and cellular targeting. *Biomacromolecules* **2012**, *13*, 1515-1522.

Ryu, J. H.; Chacko, R. T.; Jiwpanich, S.; Bickerton, S.; Babu, R. P.; Thayumanavan, S. Self-cross-linked polymer nanogels: a versatile nanoscopic drug delivery platform. *J. Am. Chem. Soc.* **2010**, 132, 17227-17235.

Ryu, J. H.; Jiwpanich, S.; Chacko, R.; Bickerton, S.; Thayumanavan, S. Surface-functionalizable polymer nanogels with facile hydrophobic guest encapsulation capabilities *J. Am. Chem. Soc.* **2010**, *132*, 8246-824;

Ryu, J. –H.; Roy, R.; Ventura, J.; Thayumanavan, S. Redox-sensitive disassembly of amphiphilic copolymer based micelles. *Langmuir* **2010**, *26*, 7086–7092.

Savic, R.; Eisenberg, A.; Maysinger, D. Block copolymer micelles as delivery vehicles of hydrophobic drugs: Micelle–cell interactions. *J. Drug Target.* **2006**, *14*, 343-355.

Savić, R.; Luo, L.; Eisenberg, A.; Maysinger, D. Micellar nanocontainers distribute to defined cytoplasmic organelles. *Science* **2003**, *300*, 615.

Schaefer, Z. L.; Gross, M. L.; Hickner, M. A.; Schaak, R. E. Uniform hollow carbon shells: nanostructured graphitic supports for improved oxygen-reduction catalysis. *Angew. Chem. Int. Ed.*, **2010**, *49*, 7045-7048;

Seo, J. S.; Whang, D.; Lee, H.; Jun, S.I. ; Oh, J.; Jeon, Y. J.; Kim, K. A homochiral metal–organic porous material for enantioselective separation and catalysis. *Nature* **2000**, *404*, 982.

Sever, M. J.; Weisser, J. T.; Monahan, J.; Srinivasan, S.; Wilker, J. J. Metal-mediated cross-linking in the generation of a marine-mussel adhesive. *Angew. Chem. Int. Ed.* **2004**, *43*, 448.

Sever, M. J.; Wilker, J. J. Absorption spectroscopy and binding constants for first-row transition metal complexes of a DOPA-containing peptide. *Dalton Trans.* **2006**, 813.

Shahrokhian, S. Lead phthalocyanine as a selective carrier for preparation of a cysteine-selective electrode. *Anal. Chem.* **2001**, *73*, 5972–5978.

Sheepwash, E.; Krampl, V.; Scopelliti, R.; Sereda, O.; Neels, A.; Severin, K. Molecular networks based on dative boron-nitrogen bonds. *Angew. Chem. Int. Ed.* **2011**, *50*, 3034-3037.

Shen, Y.; Jin, E.; Zhang, B.; Murphy, C. J.; Sui, M.; Zhao, J.; Wang, J.; Tang, J.; Fan, M.; Kirk, E. V.; Murdoch, W. J. Prodrugs forming high drug loading multifunctional nanocapsules for intracellular cancer drug delivery. *J. Am. Chem. Soc.*, **2010**, *132*, 4259-4265.

Simic, V.; Bouteiller, L.; Jalabert, M. Highly cooperative formation of bis-urea based supramolecular polymers. *J. Am. Chem. Soc.* **2003**, *125*, 13148-13154.

Song, Y.; Cheng, P. N.; Zhu, L.; Moore, E. G.; Moore, J. S. Multivalent macromolecules redirect nucleation-dependent fibrillar assembly into discrete nanostructures. *J. Am. Chem. Soc.*, **2014**, *136*, 5233-5236.

Spitler, E. L.; Dichtel, W. R. Lewis acid-catalysed formation of two-dimensional phthalocyanine covalent organic frameworks. *Nat. Chem.*, **2010**, *2*, 672-677.

Spitler, E. L.; Giovino, M. R.; White, S. L.; Dichtel, W. R. A mechanistic study of Lewis acid-catalyzed covalent organic framework formation. *Chem. Sci.*, **2011**, *2*, 1588-1593.

Spokoyny, A. M.; Kim, D.; Sumrein, A.; Mirkin, C. A. Infinite coordination polymer nano-and microparticle structures. *Chem. Soc. Rev.*, **2009**, *38*, 1218.

Suteewong, T.; Sai, H.; Hovden, R.; Muller, D.; Bradbury, M. S.; Gruner, S. M.; Wiesner, U. Multicompartment mesoporous silica nanoparticles with branched shapes: An epitaxial growth mechanism. *Science* **2013**, *340*, 337.

Suwa, K.; Yamamoto, K.; Akashi, M.; Takano, K.; Tanaka, N.; Kunugi, S. Effects of salt on the temperature and pressure responsive properties of poly(N-vinylisobutyramide) aqueous solutions. *Colloid Polym. Sci.* **1998**, 276, 529-533.

Swaminathan, S.; Fowley, C.; McCaughan, B.; Cusido, J.; Callan, J. F.; Raymo. F. M. Intracellular guest-exchange between dynamic supramolecular hosts. *J. Am. Chem. Soc.*, **2014**, *136*, 7907-7913.

Swann, J. M. G.; Bras, W.; Topham, P. D.; Howse, J. R.; Ryan, A. J. Effect of the Hofmeister anions upon the swelling of a self-assembled ph-responsive hydrogel. *Langmuir* **2010**, 26, 10191–10197.

Takaoka, Y.; Sakamoto, T.; Tsukiji, S.; Narazaki, M.; Matsuda, T.; Tochio, H.; Shirakawa, M.; Hamachi. I. Self-assembling nanoprobes that display off/on 19F nuclear magnetic resonance signals for protein detection and imaging. *Nat. Chem.* **2009**, *1*, 557 – 561;

Taynton, P.; Yu, K.; Shoemaker, R. K.; Jin, Y.; Qi, H. J.; Zhang, W. Heat- or water- driven malleability in a highly recyclable covalent network polymer. *Adv. Mater.* **2014**, *26*, 3938–3942.

Thorek, D. L. J.; Ulmert, D.; Diop, N.-F. M.; Lupu, M. E.; Doran, M. G.; Huang, R.; Abou, D. S.; Larson, S. M.; Grimm, J. Non-invasive mapping of deep-tissue lymph nodes in live animals using a multimodal PET/MRI nanoparticle. *Nat. Commun*. **2014**, *5*, 1-9;

Thurecht, K. J.; Blakey, I.; Peng, H.; Squires, O.; Hsu, S.; Alexander, C.; Whittaker, A. K. Functional hyperbranched polymers: toward targeted in vivo 19F magnetic resonance imaging using designed macromolecules. *J. Am. Chem. Soc.* **2010**, *132*, 5336.

Tong, R.; Hemmati, H. D.; Langer, R.; Kohane, D. S. Photoswitchable nanoparticles for triggered tissue penetration and drug delivery. *J. Am. Chem. Soc.*, **2012**, *134*, 8848–8855;

Tu, C. H.; Wang, A. Q.; Zheng, M. Y.; Wang X. D.; Zhang, T. Factors influencing the catalytic activity of SBA-15-supported copper nanoparticles in CO oxidation. *Appl. Catal., A*, **2006**, *297*, 40–47.

Uchiyama, M.; Ozawa, H.; Takuma, K.; Matsumoto, Y.; Yonehara, M.; Hiroya, K.; Sakamoto, T. Regiocontrolled intramolecular cyclizations of carboxylic acids to carbon-carbon triple bonds promoted by acid or base catalyst. *Org. Lett.* **2006**, *8*, 5517-5520.

Ulbrich, K.; Subr, V. Polymeric anticancer drugs with pH-controlled activation. *Adv. Drug Delivery Rev*. **2004**, *56*, 1023-1050;

Valko, M.; Leibfritz, D.; Moncol, J.; Cronin, M. T. D.; Mazur, M.; Telser, J. Free radicals and antioxidants in normal physiological functions and human disease. *Int. J. Biochem. Cell Biol.* **2007**, *39*, 44-84.

Van Workum, K.; Douglas, J. F. Schematic models of molecular self-organization. *Macromol. Symp.* **2005**, *227*, 1-16.

Vander, H. M. G.; Cantley, L. C.; Thompson, C. B. Understanding the Warburg effect: the metabolic requirements of cell proliferation. *Science*, **2009**, *324*, 1029–1033;

Vaughey, J. T.; O'Hara, J.; Thackeray, M. M. Intermetallic Insertion Electrodes with a Zinc Blende-Type Structure for Li Batteries: A Study of Li x InSb ($0 \leq x \leq 3$). *Electrochem. Solid-State Lett.*, **2000**, *3*,13–16.

Von Hippel, P. H.; Wong. K. Y. Neutral salts: the generality of their effects on the stability of macromolecular conformations. *Science* **1964**, 145, 577-580.

Wagener, K. B., Boncella, J. M.; Nel, J. G. Acyclic diene metathesis (ADMET) polymerization. *Macromolecules* **1991**, *24*, 2649-2657;

Wang, C.; Chen, Q.S.; Wang, Z. Q.; Zhang, X. An enzyme-responsive polymeric superamphiphile. *Angew. Chem. Int. Ed.,* **2010**, *49*, 8612-8615;

Wang, H.; Gao, Q.; Hu, J. High hydrogen storage capacity of porous carbons prepared by using activated carbon. *J. Am. Chem. Soc.*, **2009**, *131*, 7016–22.

Wang, H.; Yan, N.; Li, Y.; Zhou, X.; Chen, J.; Yu, B.; Gong, M.; Chen, Q. Fe nanoparticle-functionalized multi-walled carbon nanotubes: one-pot synthesis and their applications in magnetic removal of heavy metal ions. *J. Mater. Chem.*, **2012**, *22*, 9230-9236.

Wang, H.; Zhuang, J.; Thayumanavan, S. Functionalizable Amine-Based Polymer Nanoparticles. *ACS Macro Lett.* **2013**, *2*, 948−951.

Wang, X.; Liu, G.; Hu, J.; Zhang, G.; Liu, S. Concurrent block copolymer polymersome stabilization and bilayer permeabilization by stimuli-regulated traceless crosslinking. *Angew. Chem. Int. Ed.*, **2014,** *53*, 3138-3142.

Wang, X.; Zhuang, J.; Peng, Q.; Li, Y. A general strategy for nanocrystal synthesis. *Nature* **2005**, *437*, 121.

Wedemeyer, W. J.; Welker, E.; Narayan, M.; Scheraga, H. A. Disulfide bonds and protein folding. *Biochemistry* **2000**, *39*, 4207-4216.

Weisser, J. T.; Nilges, M. J.; Sever, M. J.; Wilker, J. J. EPR investigation and spectral simulations of iron-catecholate complexes and iron-peptide models of marine adhesive cross-links. *Inorg. Chem.* **2006**, *45*, 7736.

Winter, M.; Besenhard, J. O. Electrochemical lithiation of tin and tin-based intermetallics and composites. *Electrochim. Acta* **1999**, *45*, 31.

Wong, C.-H.; Zimmerman, S. C. Orthogonality in organic, polymer, and supramolecular chemistry: from Merrifield to click chemistry. *Chem. Commun.*, **2013**, *49*, 1679–1695.

Xiong, M. H.; Bao, Y.; Yang, X. Z.; Wang, Y. C.; Sun, B. L.; Wang, J. lipase-sensitive polymeric triple-layered nanogel for on-demand drug delivery. *J. Am. Chem. Soc.*, **2012**, *134*, 4355–4362;

Yamagata, M.; Hasuda, K.; Stamato, T.; Tannock, I. F. The contribution of lactic acid to acidification of tumours: studies of variant cells lacking lactate dehydrogenase. *Br. J. Cancer,* **1998**, *77*, 1726–1731;

Yang, S. J.; Park, C. R. Preparation of Highly Moisture-Resistant Black-Colored Metal Organic Frameworks. *Adv. Mater.*, **2012,** *24*, 4010-4013.

Yang, Z.; Xia, Y.; Mokaya, R. Enhanced hydrogen storage capacity of high surface area zeolite-like carbon materials. *J. Am. Chem. Soc.* **2007**, *129*, 1673–1679.

Yin, Y.; Erdonmez, C. K.; Cabot, A.; Hughes, S.; Alivisatos, A. P. Colloidal synthesis of hollow cobalt sulfide nanocrystals. *Adv. Funct. Mater.* **2006**, *16*, 1389.

Yin, Y.; Rioux, R. M.; Erdonmez, C. K.; Hughes, S.; Somorjai, G. A.; Alivisatos, A. P. Formation of hollow nanocrystals through the nanoscale Kirkendall effect. *Science* **2004**, *304*, 711.

Yuan, C.; Luo, W.; Zhong, L.; Deng, H.; Liu, J.; Xu, Y.; Dai, L. Au @ polymer nanostructures with tunable permeability shells for selective catalysis. *Angew. Chem. Int. Ed.* **2011**, *51*, 3515-3519.

Yuan, C.; Raghupathi, K.; Popere, B. C.; Ventura, J.; Dai, L.; Thayumanavan, S. Composite supramolecular nanoassemblies with independent stimulus sensitivities. *Chem. Sci.*, **2014**, *5*, 229-234.

Yuan, L.; Lin, W.; Zhao, S.; Gao, W.; Chen, B.; He, L.; Zhu, S. A unique approach to development of near-infrared fluorescent sensors for in vivo imaging. *J. Am. Chem. Soc*.**2012**, *134*, 13510–135123.

Yuan, Y. Y.; Mao, C. Q.; Du, X. J.; Du, J. Z.; Wang, F.; Wang, J. Surface charge switchable nanoparticles based on zwitterionic polymer for enhanced drug delivery to tumor. *Adv. Mater.*, **2012**, *24*, 5476–5480;

Zhang, F.; Wei, Y.; Wu, X.; Jiang, H.; Wang, W.; Li, H. Hollow zeolitic imidazolate framework nanospheres as highly efficient cooperative catalysts for [3 + 3] cycloaddition reactions. *J. Am. Chem. Soc.* **2014**, *136*, 13963.

Zhang, Q.; Ko, N. R.; Oh, J. K. Recent advances in stimuli-responsive degradable block copolymer micelles: synthesis and controlled drug delivery applications. *Chem. Commun.*, **2012**, *48*, 7542–7552.

Zhang, S.; Chen, L.; Zhou, S.; Zhao, D.; Wu. L. Facile synthesis of hierarchically ordered porous carbon via in situ self-assembly of colloidal polymer and silica spheres and its use as a catalyst support. *Chem. Mater.*, **2010**, *22*, 3433–3440;

Zhang, W.; Hu, J. –S.; Guo, Y. –G.; Zheng, S. -F.; Zhong, L. -S.; Song, W. -G.; Wan, L. -J. Tin-nanoparticles encapsulated in elastic hollow carbon spheres for high-performance anode material in lithium-ion batteries. *Adv. Mater.*, **2008,** *20*, 1160-1165.

Zhang, Y. J.; Cremer, P. S. Chemistry of Hofmeister anions and osmolytes. *Ann. Rev. Phys. Chem.* **2010**, 61, 63-83.

Zhang, Y. J.; Furyk, S.; Bergbreiter, D. E.; Cremer, P. S. Specific ion effects on the water solubility of macromolecules: PNIPAM and the Hofmeister Series. *J. Am. Chem.Soc.* **2005**, 127, 14505–14510.

Zhang, Y.; Furyk, S.; Sagle, L. B.; Cho, Y.; Bergbreiter, D. E.; Cremer, P. S. Effects of Hofmeister anions on the LCST of PNIPAM as a function of molecular weight. *J. Phys. Chem. C.* **2007**, 111, 8916-8924.

Zhang, Y.; Li, M.; Chandrasekaran, S.; Gao, X.; Fang, X.; Lee, H. W.; Hardcastle, K.; Yang, J.; Wang, B. A unique quinolineboronic acid-based supramolecular structure that relies on double intermolecular B-N bonds for self-assembly in solid state and in solution. *Tetrahedron*, **2007**, *63*, 3287-3292.

Zhang, Z.; Chen, Y.; Zhang, J.; Xu, X.; Yang, Y.; Nosheen, F.; Saleem, F.; He, W.; Wang, X. Hierarchical Zn/Ni-MOF-2 nanosheet-assembled hollow nanocubes for multicomponent catalytic reactions. *Angew. Chem. Int. Ed.* **2014**, *53*, 12517.

Zhang, Z.; Chen, Y.; Xu, X.; Zhang, J.; Xiang, G.; He, W.; Wang, X. Well-defined metal-organic framework hollow nanocages. *Angew. Chem. Int. Ed.* **2014**, *53*, 429.

Zhao, D.; Moore, J. S. Reversible polymerization driven by folding. *J. Am. Chem. Soc.* **2002**, *124*, 9996-9997.

Zhao, D.; Moore, J. S. Nucleation-elongation polymerization under imbalanced stoichiometry. *J. Am. Chem. Soc.* **2003**, *125*, 16294-16299.

Zhu, J.; Tan, M.; Zhang, L.; Yin, Q. Elongation flow-triggered morphology transitions of dendritic polyethylene amphiphilic assemblies: host−guest implications. *Soft Matter*, **2014**, *10*, 6506-6513.

Zhu, L.; Shabbir, S. H.; Gray, M.; Lynch, V. M.; Sorey, S.; Anslyn, E. V. A structural investigation of the NB interaction in an *o*-(N, N-dialkylaminomethyl) arylboronate system. *J. Am. Chem. Soc.* **2006**, *128*, 1222-1232.

Zhuang, J.; Chacko, R. T.; Amado Torres, D. F.; Wang, H.; Thayumanavan, S. Dual Stimuli–Dual Response Nanoassemblies Prepared from a Simple Homopolymer. *ACS Macro Lett.* **2014**, *3*, 1−5.

Zhuang, J.; Jiwpanich, S.; Deepak, V. D.; Thayumanavan, S. Facile preparation of nanogels using activated ester containing polymers. *ACS Macro Lett.*, **2012**, *1*, 175−179.

Zotti, G.; Vercelli, B.; Berlin, A. Monolayers and multilayers of conjugated polymers as nanosized electronic components. *Acc. Chem. Res.*, **2008**, *41*, 1098–1109.

Zou, P.; Chen, H.; Paholak, H. J.; Sun, D. Noninvasive fluorescence resonance energy transfer imaging of in vivo premature drug release from polymeric nanoparticles. *Mol. Pharmaceutics* **2013**, *10*, 4185-4194.